MULTI-PARAMETER QUANTITATIVE MAPPING OF MICROFLUIDIC DEVICES

Mathieu A. BENNET

Degree of Doctor in Philosophy

The University of Edinburgh

– 2011 –

Abstract

Fluorescence lifetime imaging microscopy (FLIM) is a powerful technique to non-invasively map the physical and chemical environment within microfluidic devices. In this work FLIM has been used in conjunction with a variety of other techniques to provide a greater insight into flow behaviour and fluid properties at the microscale.

The pH-sensitive fluorescent dyes, fluorescein and C-SNARF 1, have been used to generate pH maps of microfluidic devices with a time-gated camera and a time-and-space-correlated single photon counting (TSCSPC) detector, respectively. Using time-gated detection and fluorescein, the fluorescence lifetime images allow for direct reading of the pH. The relative contribution to fluorescence of the acid and basic forms of C-SNARF 1 was spatially resolved on the basis of pre-exponential factors, giving quantitative mapping of the pH in the microfluidic device.

Three dimensional maps of solvent composition have been generated using 2-photon excitation FLIM (2PE-FLIM) in order to observe the importance of gravitational effects in microfluidic devices. Two fluidic systems have been studied: glycerol concentration in the microfluidic device was measured using Kiton red; water concentration in a methanolic solution was measured using ANS. The density mismatch between two solutions of different composition induced a rotation of the interface between two streams travelling side by side in a microchannel. The experiment has provided evidence of non-negligible gravitational effects in microflows. 2PE-FLIM has superior capability than methods used previously to assess similar phenomena.

FLIM and micro-particle imaging velocimetry (μ-PIV) have been implemented on a custom-built open frame microscope and used simultaneously for multimodal mapping of fluid properties and flow characteristics. It has been shown that viscosity mismatch between two streams induces a non-constant advective transport across the channel and results in a flow profile that deviates from the usual Poiseuille profile, characteristic of pressure driven flow in microfluidic devices.

An aqueous solution of the temperature-sensitive fluorescent dye Kiton red has been encapsulated in an oil microdroplet using the in-vitro compartmentalisation (IVC) double emulsion method. A microdroplet has been trapped in an operating microfluidic device using optical tweezers and its fluorescence lifetime image has been recorded using FLIM. This permits measurement of the local temperature on the micron scale in a chemically non-invasive fashion.

Declaration

I declare that the work presented in this thesis is my own unless stated by reference.

Signed:

Date:

Acknowledgements

First of all, I would like to thank my supervisor, Anita Jones, for her incommensurable support. I could not have thought better supervisor for my PhD, and I mean it.

I also want to thank David Mendels for the plethora of ideas that secured my entertainment in the vicinity of optical benches and microfluidic devices for the whole duration of my PhD.

I would also like to thank Gerald Buller, my first academic supervisor, for invariably supporting my will to further my experience in academia.

I would still be hands on in the lab without the *savoir faire* of Andy Garrie, Nhan Pham, Aongus McCarthy, Jochen Arlt, Juanita Cardenas, Rosario Sanchez, Robert Neely, and Patricia Richardson. I am deeply grateful for their help and for sharing their special powers with me. Thanks also to Bill Gibbons, for helping with grammar and spelling.

It has been a pleasure to share the office with Diana and Xiaohua. Away from the lab and the office, Cristina, Nathalie, Trish and Guilhem have always achieved quality banters around a meal, a brew or a cigarette. They have brought some daily sunshine in the nicest damp country in the world.

Finally, words cannot say how thankful I am to the people I love the most: my parents; my brother; and Ioanna.

Table of Contents

1 Introduction

The scaling down or miniaturisation of devices is a strong trend that kicked off in the 1950's with the important advances in space technology. Presently, this trend is also driven by consumers' desires for ever smaller devices. Most advantages that result from scaled down devices are obvious. Small size means objects are less bulky, more mobile, more convenient to use and require less material to make. A universal example is the miniaturisation of computers. However, scaling down devices does not only mean having to cope with smaller dimensions: although the fundamental physics and chemistry describing phenomena at the macroscale are usually the same as at the microscale, some parameters which are dominant in the latter are unimportant in the former and vice versa. Therefore, miniaturising devices implies dealing with phenomena that were unknown from previous observation of macroscopic systems.

Thanks to the development of Micro Electrical Mechanical Systems (MEMS), microtechnology has developed rapidly in a viable fashion, self-sustained by emerging applications since 1954. However, it was only in the 1980's that an interest in reducing the size of fluidic systems emerged. There is currently no standard in microfluidic development and where MEMS have allowed microtechnology to become ubiquitous, microfluidic-technology-based devices are still only found sporadically. This is due to a lack of understanding of fluid phenomena at the microscale. A boom in microfluidic technologies is therefore impeded by the lack of computational fluid dynamic (CFD) models adapted to the microscale. Consequently, engineers are faced with developing microfluidic devices by trial and error, which is costly and time consuming. Although key features of the effects governing flow in a microchannel can be gained by scaling analysis, a reliable development of CFD models for the microscale depends upon their results being

assessed and validated by experimental observations[1]. Because conventional techniques used to map macroscale phenomena are not adapted, or simply not suitable, to be used to probe micrometer-size, monolithic devices, scientists had to find means of collecting spatial, quantitative information about fluid and flow properties in microchannels.

Microfluidic devices were first implemented by engineers in inkjet technology 20 years ago. It is therefore not a surprise that the first visualisation techniques that emerged were the ones already used by engineers in fluid dynamics prior to miniaturisation. Among those techniques, Particle Imaging Velocimetry (PIV) has had greater success than other particle-based flow visualisation methods because it is the most accurate and can provide more information per interrogation area [1]. First used in 1998 and renamed Micro-Particle Imaging Velocimetry (μ-PIV), it is a much more powerful tool than fluorescence based (mainly caged fluorescence imaging) flow visualisation methods which are limited to bulk flow measurement [2].

With microfluidic technologies gaining interest from life scientists, especially from molecular biologists, more microscopic techniques entered the pool of visualisation tools used to image microfluidic devices. Probably the most widespread imaging tool in biology is fluorescence microscopy. First limited to staining species, it quickly became clear that scientists could use the emission from fluorescent molecules not only to localise biological organelles but also to collect information about the chemical and environmental vicinity of the fluorophore. This is possible because the fluorescence characteristics of a fluorophore are sensitive to their

[1] The author has to stress here that the degree of quantification obtained from a model is a subjective notion. Some of the results presented in this work could therefore be to some extent tractable from established models. In this respect, the quantification of the diffusion of a species across a microfluidic channel can be obtained with some level of good agreement between experimental results and numerical solution [5]. However, this is only true when the two fluids that are brought in contact at the T-junction and their mixture have similar physical properties (i.e.: viscosity, density). This is the case in chapter 4 of this manuscript where two saline buffers are mixed and where the fluidic system can be approximated to diffusion of chemical species from one side of the microchannel to the other.

surroundings. In microfluidic devices, researchers have exploited the response of fluorophores to the surrounding medium to map the environment in the device.

At first, techniques based on changes in fluorescence intensity were used because they are cheap, easy to set up and provide good contrast [3]. However, the fluorescence intensity of a sample does not reflect only the surroundings of the molecule. It is dependent on fluorophore concentration, photobleaching, and temporal instability of the excitation source. Furthermore, the affinity of molecules to a specific environment and the spatial heterogeneity of the illumination source are detrimental to quantitative mapping of the sample. For example, when imaging microfluidic devices, these shortcomings are ostensible at the wall of the device where adsorption of the dye generates an increase of the fluorescence intensity.

Conventional fluorescence microscopy is therefore mostly useful to localise fluorescent species in samples. In order to gain information about the chemical and environmental factors of a sample, time-resolved fluorescence is used. In time-resolved fluorescence the fluorescence lifetime of the sample rather than its intensity is measured. The fluorescence lifetime is an intrinsic property of a fluorescent molecule and is typically insensitive to the fluorophore concentration in the sample. Therefore, recording the response of fluorescence lifetime to environmental variations provides measurements that are independent of fluorophore concentration. Time-resolved fluorescence measures the sensitivity of the fluorophore to chemical and environmental factors such as pH, ion concentration, temperature, and polarity. Combining the measurement of fluorescence lifetime using time-resolved fluorescence with 2D imaging using the basic setup of conventional fluorescence microscopy techniques allows for quantitative maps of the sample to be created [4]. In the images created, the fluorescent lifetime rather than the intensity is used as contrast. This technique, Fluorescent Lifetime Imaging Microscopy (FLIM), overcomes the aforementioned problems associated with intensity based techniques. It was first applied to quantitatively map mixing in microfluidic devices [3] and it is now accepted as a powerful tool to quantitatively map chemical and environmental factors in microfluidic devices. To date and to the best of our knowledge, it has been

used to map solvent concentration [3, 5], temperature [6-8], viscosity [9], and ion concentration [10, 11].

In continuation of the work published so far, Chapter 4 of this thesis will demonstrate the use of FLIM to map pH. The importance of mapping pH in terms of biochemical applications, assessment of micromixers and as validation for CFD models is discussed. Along with conventional wide-field time-gated FLIM technique, we have also evaluated the capability of a Time-and Space-Correlated Single Photon Counting (TSCSPC) FLIM technique to map pH gradient in a microfluidic device. It is the first time to date, to the best of our knowledge, that such a technique has been used for generating fluorescence lifetime images of microfluidic devices.

Scaling analysis of flow behaviour can give great insight into the change in fluid dynamics between the macroscale and microscale. Actually the same equations stand true in both cases. Scaling analysis is made as a function of the typical length l of the system studied and allows for the forces applied on the system to be assessed and when appropriate neglected. Microfluidic devices have a large surface-to-volume ratio compared to macroscopic devices. Therefore, recessive and hidden phenomena in macroscale systems can become dominant and ostensible at the microscale. For example, surface forces scale with l whereas gravitational forces scale with l^3. It is therefore predictable, that whereas gravity will play a major role in macroscale analysis, it will be overpowered by surface forces in microscale analysis. The pitfall here is to imagine a boundary between the laws ruling the fluid dynamics between the microscale and the macroscale. This boundary would mislead the modeller who would, for the sake of simplification and correctly for many cases, neglect gravitational forces when studying fluid dynamics at the microscale. The laws of fluid dynamics are continuous. It is the change in the relative importance of each factor in the equations describing the laws that reflect the change of flow behaviour. In the case of two miscible liquids with different density, discrepancies between CFD results and experimental data obtained using FLIM were found. Taking into account gravitational and buoyancy effects corrected for the discrepancies [7]. In Chapter 5, it is shown how 2-Photon excitation FLIM was used to generate 3D maps of solvent

composition showing the rotation of the interface between two solvents of different density. The results confirm the importance of gravitational effects when assessing flow behaviour in microfluidic devices.

The work presented in Chapter 4 and Chapter 5, demonstrates the capability of FLIM as an imaging technique to provide detailed spatially-resolved quantitative information about the bulk properties in a microfluidic device. In order to fulfil the need for ever more accurate measurements of flow parameters, FLIM has been combined with μ-PIV to generate simultaneously quantitative spatial information about the bulk properties, using FLIM, and detailed flow field parameters, using μ-PIV. The two techniques have different requirements in terms of illumination sources, detection wavelength and camera. Commercial microscopes are intrinsically unsuitable to perform these two tasks simultaneously. Therefore, an open frame platform microscope has been employed to provide the adequate flexibility in the optical setup. In Chapter 6, the use of this optical setup to observe the influence of a temperature and viscosity gradient across a microchannel on the flow field parameters is described.

Because of their many inherent advantages, microfluidic devices have attracted attention from almost every discipline in natural sciences. They are used for diagnostics and drug delivery in medicine, study of flow behaviour in physics, miniaturisation in engineering, sample analysis in chemistry, and cell handling in biology, to name just a few examples. As the different fields find new and promising applications to develop, scientists are facing the challenges of becoming acquainted with concepts and techniques/tools that did not originally belong to their background knowledge and skills. Developing tools, methods and techniques accessible by scientists from different backgrounds is a crucial step in the popularisation of the technology. In this regard, fabrication of microfluidic chips by soft-lithography has provided the scientific community with a cheap and easy way of producing their own devices [12]. Chapter 3 includes a description of the use of soft-lithography to develop a microfluidic chip with flow rate independent temperature control. In Chapter 7, it is shown how the open frame microscope provides a user-friendly

optical platform that enables optical tweezers and FLIM to be used in tandem. These features were used to trap a novel local fluorescent probe fabricated using the in-vitro compartmentalisation method [13]. Encapsulation of an aqueous solution of a temperature sensitive fluorescent molecule permits chemically non-invasive detection of local temperature in a microfluidic device.

2 THEORY

The work presented in this thesis requires the understanding of principles and techniques which are presented in this chapter.

2.1 Fluorescence

Luminescence takes place when an atom/molecule undergoes excitation resulting in a transition from ground to excited state, and emits light by returning to its ground state energy level. The excitation source can be inherent to the system, i.e. chemiluminescence (chemical reactions), or require an outside source of energy, e.g. electroluminescence (electrical discharges), sonoluminescence (sound), triboluminescence (crushing) [14].

Fluorescence and phosphorescence occur after excitation of a molecule by a photon and are classified as photoluminescent phenomena. Photoluminescence is the property of molecules to absorb light at a wavelength (referred to as excitation wavelength) and to subsequently re-emit light at longer wavelength (referred to as emission wavelength) after an average time called fluorescent/phosphorescent lifetime.

2.1.1 Principles of fluorescence

2.1.1.1 Excitation

The photon is the quantum of energy of electromagnetic radiations. The energy of a photon is given by Planck's law:

$$E_{\varphi} = \frac{h \cdot c}{\lambda} \qquad \textbf{(2-1)}$$

where h is Planck's constant, c the speed of light, λ the wavelength of the light. Specific wavelengths, known as absorption wavelengths, are absorbed by molecules. When a molecule absorbs a photon with energy E_{φ}, an electron in the ground

electronic state (energy E_m) is promoted to a higher electronic state of energy E_n given by:

$$E_n = E_m + E_\varphi \qquad \textbf{(2-2)}$$

A molecule possesses quantised states of energy and the absorption of energy occurs when the energy of a photon matches the energy difference between those states. At room temperature, usually only the lowest vibrational state of the electronic ground state ($E_{m,\ v=0}$) is populated. Therefore, the absorption of a photon results in a transition between $E_{0,v=0}$ and a vibronically excited state ($E_{n,v1}$) as shown Figure 2-1.

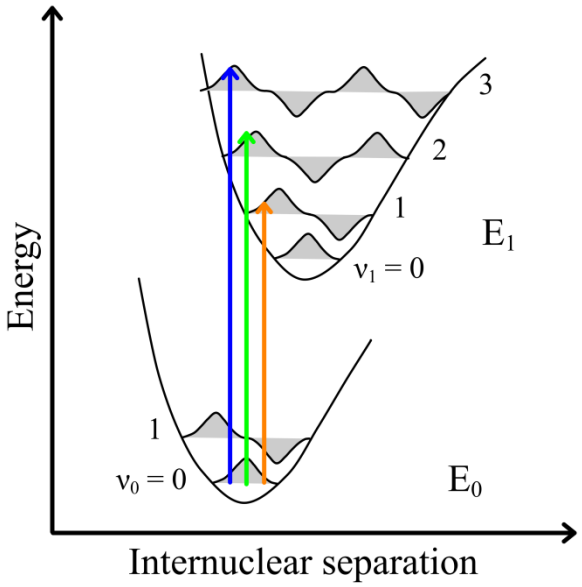

Figure 2-1: Schematic representation of the potential energy curves and vibrational energy levels of ground and excited electronic states.

The coloured arrows on Figure 2-1 indicate the most intense vibronic transition that would take place in this case. Their intensity is determined by the Franck-Condon principle that states that electronic transitions are so fast in comparison to the nuclear motion that immediately after the transition, the nuclei have nearly the same relative position and momentum as they did before the transition [15]. Therefore, the arrows representing a vibronic transition are represented vertically in Figure 2-1 and the probability of a transition is proportional to the overlap of the wave functions

between the lowest vibrational state of E_0 and a vibronically excited state. The overlap is given by:

$$\int \psi_{0,v=0} \psi_{1,v1} dxdydz \qquad \textbf{(2-3)}$$

where $\psi_{0,v=0}$ and $\psi_{1,v}$ are the wavefunctions of vibronic state having energies $E_{0,v=0}$ and $E_{1,v1}$ in Figure 2-1.

The absorption of radiation is caused by the interaction of the electric field of the radiation with electrons. The electric moment induced by the radiation in an atom/molecule is referred to as transition dipole moment. It is given by a vector, the amplitude of which is referred to as transition moment that gives the strength of the interaction. The direction of the vector in the molecular framework defines the direction of transition polarisation. The transition dipole moment is given by:

$$d_{m,n} = \int \psi_{m,v} \mu \psi_{n,v_n} dxdydz \qquad \textbf{(2-4)}$$

where μ is the dipole moment operator.

If the transition dipole moment is non-zero, then the probability of the transition is finite and the transition is said to be allowed. If the transition dipole moment is zero, the transition is formally forbidden. The factors that determine whether a transition is allowed or forbidden are expressed in terms of the selection rules for transition. Two main selection rules are: the spin selection rule that states that a transition between two states of different multiplicity, such as singlet-triplet, is forbidden; the symmetry selection rule that states that transitions between states of the same symmetry are forbidden. The intensities of transitions are measured by absorption spectroscopy and the characteristic extinction coefficient of a molecule is defined by the Beer-Lambert law:

$$A = \log \frac{I_0}{I} = \varepsilon \cdot c \cdot l \qquad \textbf{(2-5)}$$

where I_0 is the intensity of a light beam incident to a sample of length *l*, concentration c and extinction coefficient ε. The logarithmic of the incident beam intensity over the intensity of the transmitted beam is referred to as absorption, A.

2.1.1.2 De-excitation

Following the absorption of a photon several processes compete to de-excite the molecule. The main processes underlying photoluminescence are depicted on a Jabłoński diagram, Figure 2-2. They are classified as 'radiative' (straight arrows) and 'non-radiative' (wavy arrows) decays depending on whether or not they result in the emission of a photon on de-excitation.

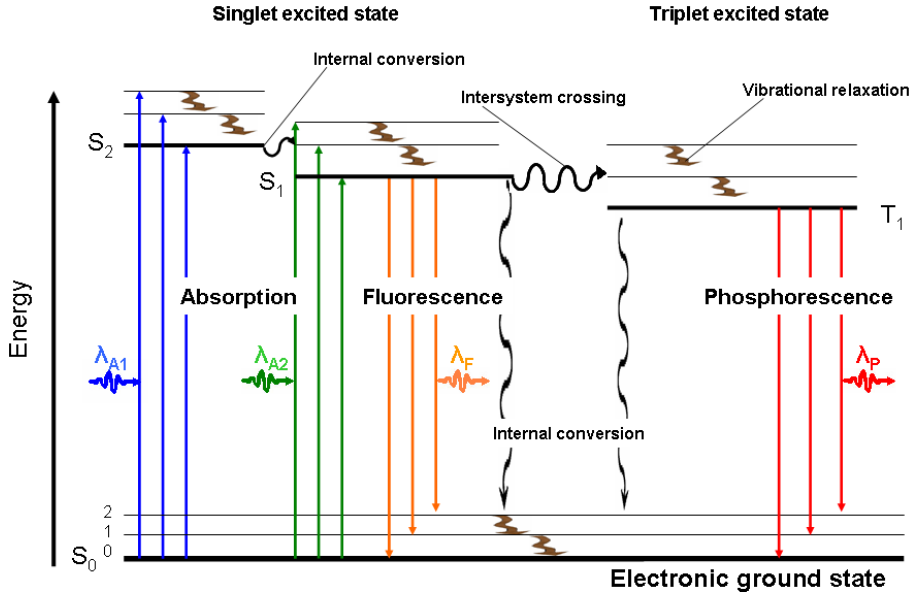

Figure 2-2: A Jabłoński diagram for a photoluminescent system showing pathways for the deactivation of an excited state. The lowest vibrational energy level for each electronic state is indicated by the thicker line.

Following excitation (blue and green arrows on Figure 2-2, a molecule will relax to a lower vibrational state by vibrational relaxation and to a lower electronically excited state by internal conversion. These processes occur in approximately 10^{-12} seconds. Once the molecule is at the lowest vibrational state of S_1, it can undergo: non-radiative decay by internal conversion (black wavy arrows on Figure 2-2); relaxation to the ground state with emission of a photon (this is fluorescence, orange arrows in Figure 2-2 and occurs in the nanosecond range); intersystem crossing to a triplet state

from which a relaxation to the ground state with emission of a photon will be delayed due to the forbidden nature of the spin change (this phenomenon is called phosphorescence (red arrows in Figure 2-2) and occurs in the millisecond to second range.

2.1.1.3 Stokes shift

Generally, the absorption of a photon by a fluorescent molecule occurs between the electronic ground state and an electronically (or vibronically) excited state of the molecule. Some energy will therefore be lost in the non-radiative processes described above. A photon emitted from the lowest vibrational state of S_1 will therefore have less energy than the photon previously absorbed. This leads to a shift of the emission spectrum toward longer wavelengths (lower energy) compared to the excitation/absorption spectrum. This shift is referred to as *Stokes shift* an illustration of which is shown Figure 2-3.

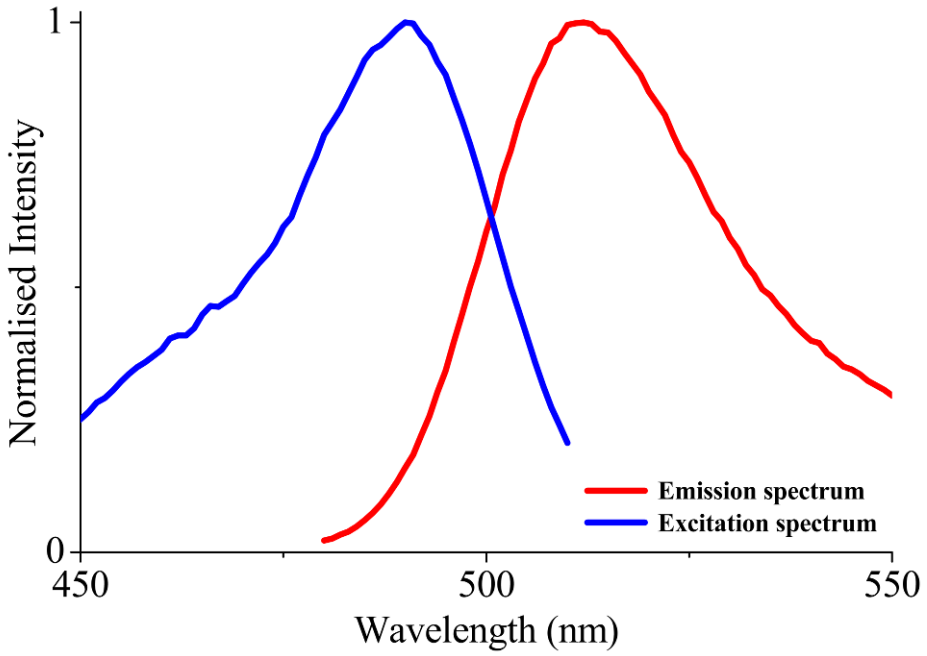

Figure 2-3: Emission and excitation spectra of fluorescein showing the Stokes shift

The Stokes shift is very useful for the detection of emitted photons by fluorescent molecules as it allows elimination of the excitation signal by spectral filtering. Another rule resulting from the fact that fluorescence occurs generally between the

lowest vibrational state of S_1 and S_0 states that the emission spectrum is independent of the excitation wavelength. This rule is referred to as Kasha's rule.

2.1.2 Fluorescence Lifetime and Quantum yield

2.1.2.1 Fluorescence quantum yield

The fluorescence quantum yield is an important characteristic of a fluorophore. It quantifies the emission efficiency: the number of photons emitted relative to the number of photons absorbed.

$$Q = \frac{photons \cdot emitted}{photons \cdot absorbed} \qquad \textbf{(2-6)}$$

Equation (2-6) can be expressed in terms of radiative and non radiative decay rates. The non-radiative decays include internal conversion, intersystem crossing, and quenching. The number of photons absorbed is proportional to the sum of the radiative and non-radiative rate constants ($k_r + k_{nr}$) while the number of photons emitted is proportional to the radiative rate constant (k_r). Equation (2-6) then becomes:

$$Q = \frac{k_r}{k_r + k_{nr}} \qquad \textbf{(2-7)}$$

The quantum yield ranges from 0 ($k_{nr} >> k_r$, no fluorescence) to 1 ($k_r >> k_{nr}$, 100% efficiency).

2.1.2.2 Fluorescence lifetime

The fluorescence lifetime is the inverse of the decay rate constant as described by Equation (2-8).

$$\tau = \frac{1}{k_r + k_{nr}} \qquad \textbf{(2-8)}$$

From Equation (2-7) and Equation (2-8), an expression for the quantum yield as a function of lifetime is obtained:

$$Q = k_r \cdot \tau \qquad \textbf{(2-9)}$$

After excitation, fluorophores will not all re-emit at a time equal to the lifetime but will follow first-order kinetics:

$$S_1(t) = S_1(0)\exp(-(k_r + k_{nr})t) \qquad \textbf{(2-10)}$$

where S_1 is the excited state population. Using Equation (2-8), a relation between population and lifetime is derived:

$$\Leftrightarrow S_1(t) = S_1(0)\exp\left(-\frac{t}{\tau}\right) \qquad \textbf{(2-11)}$$

The time resolved intensity I(t) of a fluorescing solution follows the same kinetics as the excited state population $S_1(t)$. They are related by the radiative decay constant of the fluorescence molecule:

$$I(t) = k_r \cdot S_1(t) = k_r \cdot S_0 \exp\left(-\frac{t}{\tau}\right) = I_0 \exp\left(-\frac{t}{\tau}\right) \qquad \textbf{(2-12)}$$

Equation (2-12) relates the time resolved intensity to the fluorescence lifetime. This relation permits the calculation of the fluorescence lifetime from the recorded fluorescence decay.

2.1.3 Influence of molecular environment on fluorescence lifetime

The fluorescence lifetime is affected by the interaction of the fluorophore in its excited state with its environment. The fluorescence lifetime is the time given to the fluorophore to interact. The factors that affect the fluorescence lifetime are the solvent polarity, the temperature and intermolecular interactions. While intermolecular interactions promote additional non-radiative decay channels, environmental factors such as temperature affect the rate of intramolecular non-

radiative processes. Solvent polarity is probably the most common factor in environmental sensitivity of fluorescence. However, the factors that affect fluorescence are multiple. They include, for example, solvent viscosity, pH, and temperature. These multiple influencing factors provide many environmental properties that can be probed. A change in one of the environmental properties can affect several decay processes. For example, a change in temperature can induce changes in more than one quenching phenomenon. It is responsible for some intramolecular quenching phenomena but also affects e.g. collisional quenching and solvent interaction because solvent properties such as viscosity and diffusivity are sensitive to temperature. Therefore, it may be difficult to fully determine what effect is responsible for the change of fluorescence properties since more than one effect will simultaneously affect fluorophores.

The influence of temperature and pH on the fluorescence lifetime of the probes used in this thesis will be discussed in relevant chapters.

2.2 Time-Correlated Single Photon Counting

Time-correlated single photon counting (TCSPC) is based on the detection of single photons of a periodic light signal, the measurement of the detection time of an individual emitted photon, and the reconstruction of the waveform from the individual time measurements [16, 17]. It is utilised in many different applications such as fluorescence lifetime measurements, optical tomography, detection and identification of single molecules, DNA sequencing, fluorescence lifetime imaging and time-of-flight systems.

2.2.1 Principle

The emission of a photon following excitation is a random event characterised by the fluorescence lifetime. Currently, electronics do not allow the recording and time-correlation of all the photons emitted following excitation by a laser pulse. TCSPC makes use of the fact that for very low detection probability (up to 1%) one can built up the photon emission distribution corresponding to the

intensity against time distribution. This is achieved by recording the arrival time of the first photon detected following a large number of excitation pulses. A diagram is shown Figure 2-4 to describe a typical TCSPC setup.

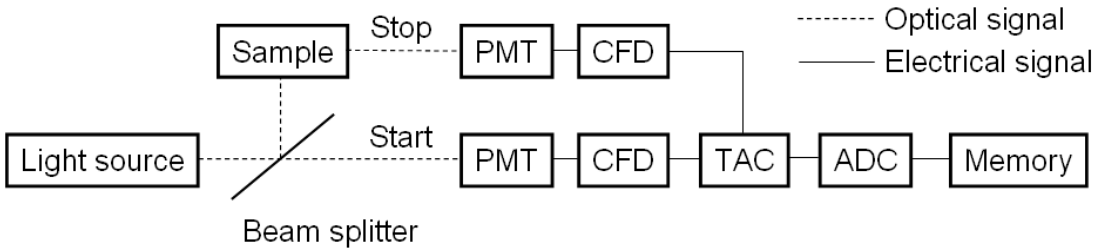

Figure 2-4: Diagram of a time-correlated single photon counting system

The light source (e.g.: a pulsed laser) is split. A small portion of the light is directed to a photodetector that produces the start signal. This start signal is used to trigger the voltage ramp of the time to amplitude converter (TAC). The amplitude of the TAC output voltage is proportional to the time between the start signal and the first photon detected by the PMT on the sample side. An analogue to digital converter (ADC) reads the output of the TAC and increments a memory location corresponding to the time of arrival of the first photon detected. A large number of events are recorded in this fashion (≥10000 for a single exponential decay) until a suitable photon emission distribution is obtained for analysis. A description of each module is given hereafter.

2.2.2 Light sources

An ideal light source for single photon counting would work at high intensity, be tuneable from the UV to 600nm (where most fluorescent excitation lies), have a variable repetition rate from kHz (enabling the recording of ms decay) to 100 MHz (enabling the recording of ns decay). The pulse used for excitation also requires several characteristics such as: wavelength-independent shape, reproducibility, and narrow width (sub-ns). Although flash lamps were very common in the early stages of TCSPC, their lack of intensity in a narrow spectral bandwidth, long pulse duration and the instability of the pulse profile made them obsolete for fluorescence measurements after the introduction of the laser [17]. In the work presented in this thesis a mode-locked frequency doubled Ti:Sapphire and a picosecond pulsed diode laser were used.

2.2.3 Constant Fractional Discriminator

The fact that the time at which a fluorescence photon is incident on the detector can be defined with picosecond resolution is critical to the operation and precision of TCSPC. In order to extract timing information from pulses such as the one produced by PMTs, discriminators are used. There are two main types of discriminator: the leading edge discriminator and the constant fraction discriminator. The leading edge discriminator is the simpler. This produces an output pulse at the time when the input signal crosses a given threshold. The lack of sufficient timing resolution with leading edge discriminator arises from the fact that the output pulses from a photomultiplier, corresponding to individual photon detection, have a significant spread in pulse height. This implies that timing based on a leading edge discriminator would be subject to considerable jitter as shown Figure 2-5.

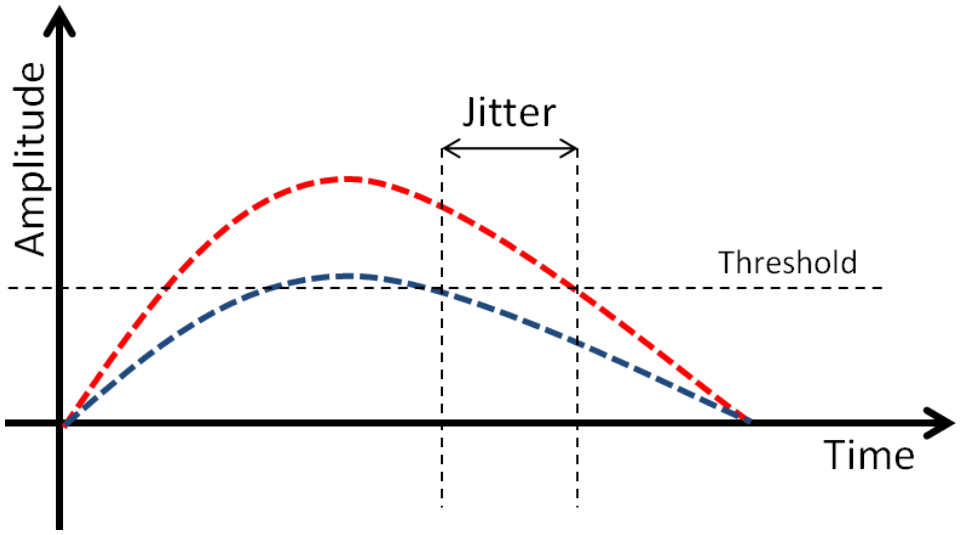

Figure 2-5: Fluctuation in the detection time induced by leading edge triggering.

Instead, a Constant Fraction Discriminator (CFD) is used to extract precise timing information from the detector pulse output using a method that is largely independent of the amplitude of the pulse [18]. Figure 2-6 shows the basic functionality of a CFD.

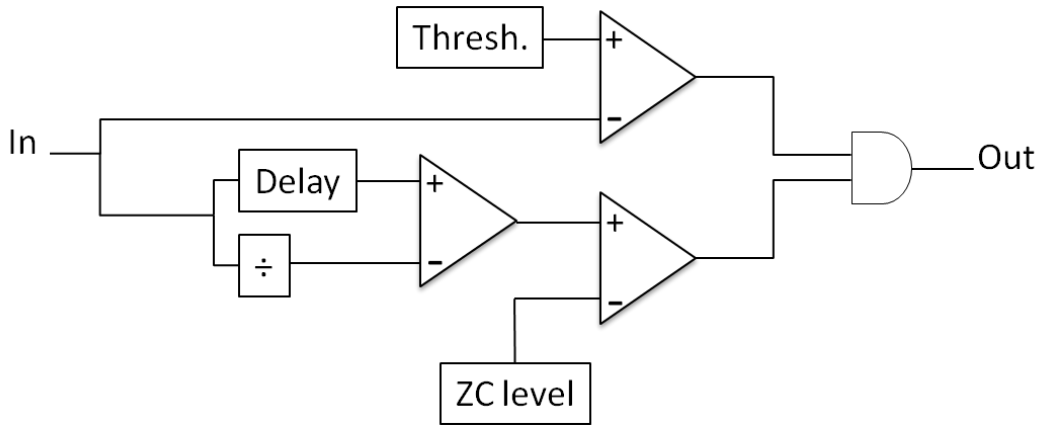

Figure 2-6: Basic functionality of a CFD

The input pulse coming from the PMT is fed to a leading edge discriminator and a constant fraction discriminator. One part of the latter is delayed, while the other is attenuated by a constant fraction. The attenuated signal is subtracted from the delayed signal resulting in a bipolar pulse that crosses the baseline at an amplitude-independent time as shown Figure 2-7.

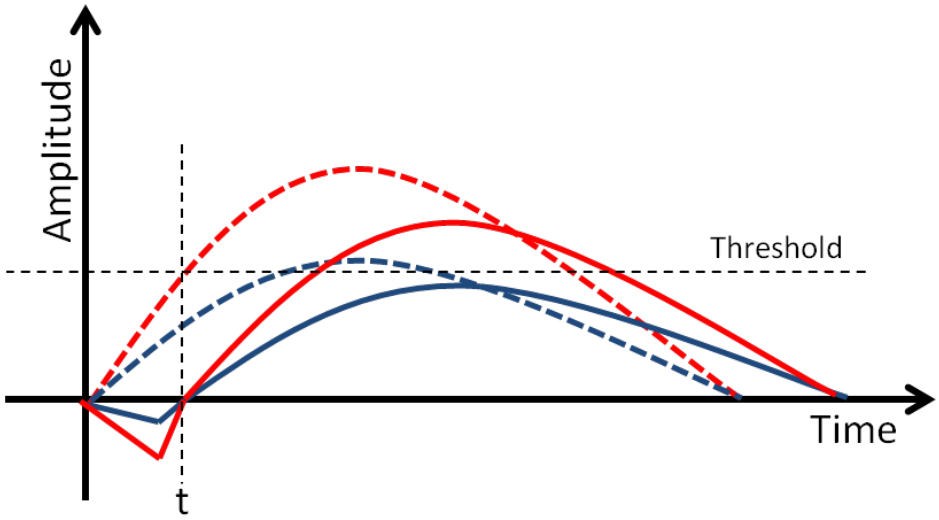

Figure 2-7: Incoming pulses (dashed lines) and transformed pulses (plain lines) that result from the operation of a CFD.

Figure 2-7, the dashed red and blue lines correspond to two incoming pulses of different amplitude. The plain lines represent the transformation of these pulses through the operation of the CFD. In the schematic graph Figure 2-7, the transformed

pulses appear to cross on the x-axis. However, due to some DC noise in the input signal, small variations leading to an offset of this crossing point occur. In order to compensate for this DC noise, the level at which the pulses are detected is set by the users. This level is referred as to zero-cross level or Z/C.

2.2.4 Time to Amplitude Converter

The TAC is used to measure the time passed between the excitation pulse and the first photon detected. When the start pulse is detected, a capacitor is charged proportionally to the time interval between the start and stop signal. For example, if the capacitor is charged from 0 to 5V, the TAC range set to 100 ns and a photon detected 60ns after the excitation pulse, the TAC charge will be 3V (the charge is linearly proportional to time interval). The main limiting factor for the TAC is the so-called *dead-time*; i.e. the time it requires resetting [19]. The TAC can be run in an inverted mode (charge starts on photon detected) in order to minimise the frequency of the dead-time, but this is not necessary for modern systems with low dead-time.

It is important for the system to record all the photons detected by the detector. However, if two photons arrive in a TAC period, only the first one will be taken into account resulting in pulse pile-up. This phenomenon biases the photon distribution detection towards a shorter time. In order to reduce the probability of detecting two photons in a TAC period, the stop signal rate is kept below 1% of the start signal rate.

2.2.5 Analogue to Digital Converter

The ADC converts the amplitude of the TAC signal into an address in the memory. When a photon is detected at a certain relative arrival time, the address is incremented. After many ‘photon detected’ events, the distribution of photon emission over time is built-up. The ADC addresses up to 4096 channels each corresponding to a fraction of the TAC range; e.g.: if the TAC range is 50 ns and the ADC is working on 4096 channels, each channel corresponds to 12.2 ps.

2.2.6 Detectors

2.2.6.1 Photomultiplier Tube

TCSPC technique requires single photon detection. The most frequently used detectors for low level detection of light are photomultiplier tubes [19]. Microchannel plates (MCP) are used to reduce the transit time, i.e. give shorter instrument response function. They consist of an array of electron multipliers orientated parallel to each other. Microchannels are usually about 10 μm in diameter and are orientated at a small angle (~8°) from the input window of the MCP [20]. Figure 2-8 below shows the operating mode of a microchannel from a MCP.

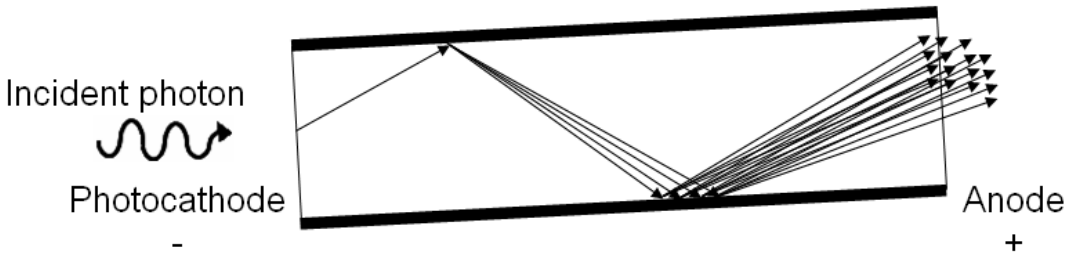

Figure 2-8: Electron amplification in an MCP PMT

The MCP PMT consists of a photocathode, a microchannel plate and an anode. The photocathode is a thin layer of metal held at high negative potential, typically -1000V to 2000V [21]. When a photon strikes the photocathode surface, a photoelectron (or primary electron) is emitted and accelerated toward the anode. When an electron strikes the wall of the microchannel, an avalanche of electrons is created, leading to an exponential amplification of the signal. MCP PMT typically shows 10^4-10^7 gain.

There are three important parameters affecting the instrument response of a TCSPC system: the excitation pulse width, the timing jitter of the electronics and the spread in transit time in the MCP PMT. The transit time is the time between the creation of the primary electron and the bunch of electrons arriving at the anode. The transit time spread is due to electrons following slightly different paths. Another time figure of the MCP PMT is the rising time of the anode. It is defined as the time the

anode takes to get from 10% to 90% of its final level. These characteristics influence the shape and width of the instrument response function (IRF).

2.2.6.2 Single-Photon Avalanche Diode

Single photons can be detected by semiconductor diodes, which can operate in the triggered avalanche mode [22]. Although the investigation of the avalanche processes in silicon date back from 1964 [23], the first practical device was devised by Cova et al in 1981[24]. The fast improvement of single-photon avalanche diode (SPAD) immediately after its successful development has made this detector an attractive alternative to MCP PMT in TCSPC [25]. It is now use in combination with TCSPC technique for Time-of-Flight [26, 27] and time-resolved fluorescence systems [28-30]. Herein is presented a brief description of the working principle of avalanche photodiodes.

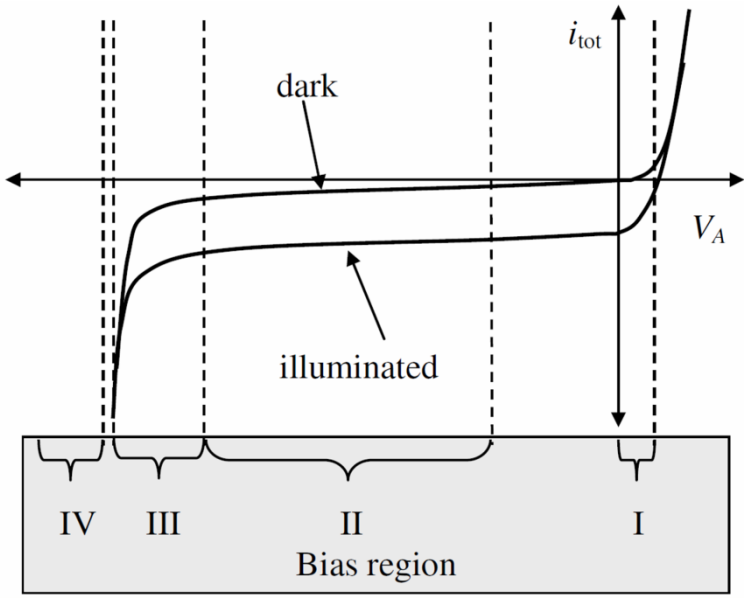

Figure 2-9: Current-Voltage characteristic of an APD structure [31]

Figure 2-9 represents the characteristic working mode of an avalanche photodiode. The schematic has been divided into four bias regions which correspond to the four different working modes of the device. In the forward bias mode region I, current is constantly flowing through the device. In Bias region II, the increase of current

between the curve labelled “dark” and the curve labelled “illuminated” is due to the current generated by the creation of electron-hole pairs following the absorption of photons (photoelectric effect) by the semiconducting material. Bias region III is referred to as the linear mode. In this region, the high electric field will accelerate the electrons and holes created by the absorption of photons. The electrons and holes are accelerated in opposite direction and gather enough energy to ionise other atoms in the crystal lattice. Upon ionisation, more electron-hole pairs are created resulting in a gain factor of ca. 10-1000. SPADs are working in bias region IV. In this region the electric field is such that the creation of an electron-hole pair by absorption of a single photon will engender a self-sustained amplification of the creation of electron-hole pairs by impact ionisation. This mode called “Geiger mode” is characterised by an infinite gain amplification taking the form of an avalanche process. It results in the generation of a detectable current following the absorption of a single photon by the semiconducting material. The avalanche current continues to flow until the process is quenched, usually by lowering the bias below breakdown voltage. The process by which the absorption of a single photon leads to a measurable current is shown Figure 2-10.

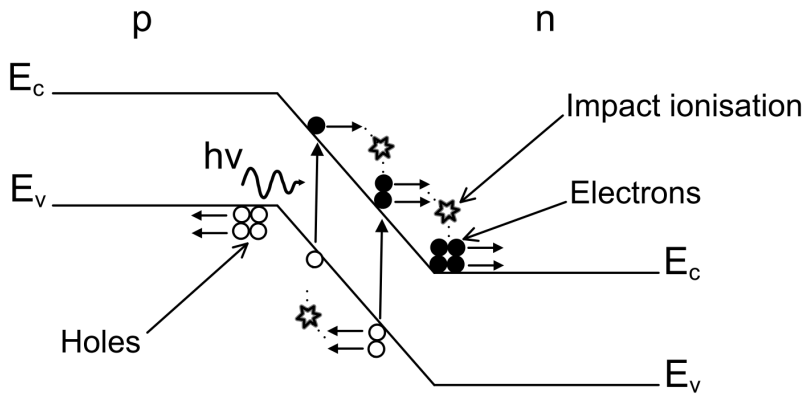

Figure 2-10: Creation of an electron-hole pair by absorption of a photon in the depletion region of the p-n junction. The electron is promoted to the conduction band. The accelerated electron gains enough energy to cause impact ionisation by collision with the lattice resulting in a self-sustained multiplication process referred to as avalanche.

Figure 2-11 shows a cross-section of a thin junction SPAD.

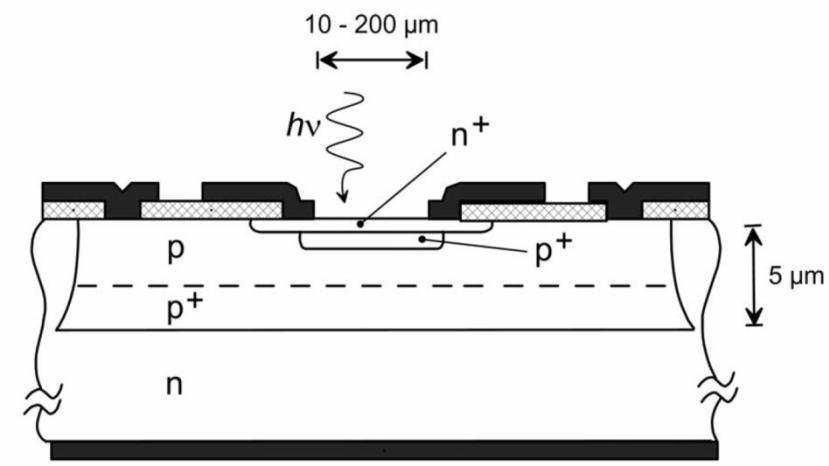

Figure 2-11: Cross-section of a thin junction SPAD showing approximate dimension and doped regions [32].

The p-doped region is lightly doped and is the region where an incoming photon will be absorbed. The multiplication process takes placed in the highly doped region p^+ and at the interface between p^+ and n^+ where the electric field is high.

When using SPADs for time-resolved measurements that require high resolution timing, a drawback arises because the time response of the device has two components. One due to the photons absorbed in the depletion layer and one due to the photon absorbed in the neutral region. The absorption process followed by diffusion and the photon arrival distribution are shown Figure 2-12.

Photons absorbed in the neutral region (Figure 2-12(a),2) beneath the active junction generate carriers that move around by diffusion and eventually reach the depletion layer with a statistically fluctuating delay [32]. This delay causes the diffusion-tail in the distribution of arrival time Figure 2-12(b). Furthermore, the distribution of arrival times is wavelength dependent, with the diffusion tail becoming more prominent at longer wavelengths.

The problem diffusion imposes on the measurements of time-resolved fluorescence spectra has been characterised in the early years of the development of SPADs [25, 33]. In order to reduce the generation of diffusive carriers in the neutral region, researchers have worked on improving the structure of the device. Some devices considerably reduce the effect of carriers' diffusion on the arrival time

distribution [32]. However, their colour-dependence characteristics have only been tested in the range 750nm-900nm [34] which does not guarantee the successful implementation of such a device in TCSPC setup for fluorescence decay measurement since most of the dyes used have their maximum emission between 500nm and 600nm. The fabrication of devices free of diffusion was devised, fabricated and tested [35, 36]. Their main drawbacks are the complex fabrication process and the reduced detection efficiency due to the reduction of the depth of the device.

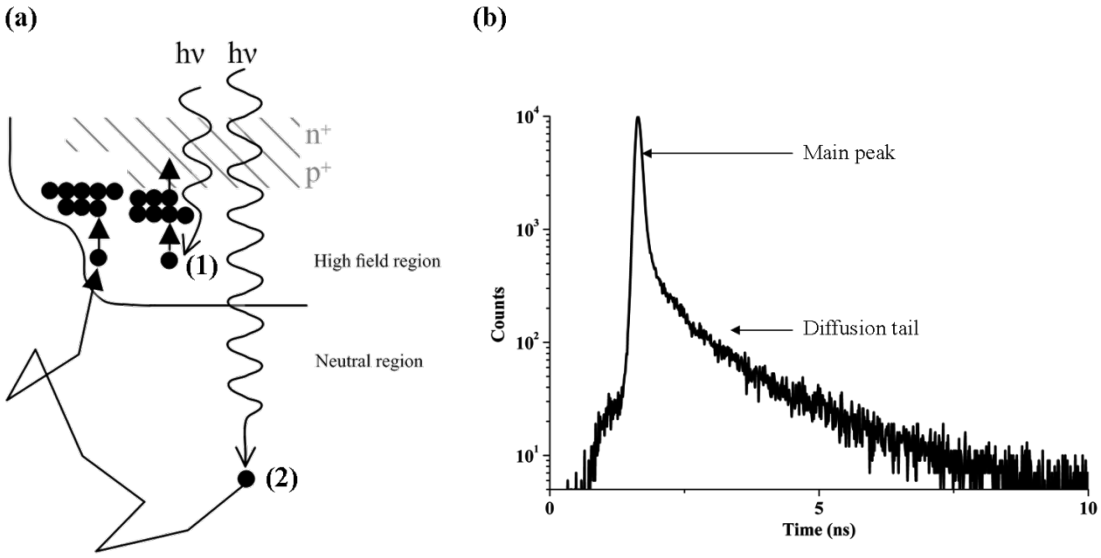

Figure 2-12: Outline of avalanche generation by photons absorbed in the depletion region (a1) and in the neutral region (a2). Photon arrival time distribution measured in a TCSPC setup and commercial silicon SPAD (b).

The wavelength dependence of photon detector is the principal reason for poor fits in TCSPC fluorescence decay measurements. Several correction methods have been developed to account for or correct this effect. Their comparison [37] demonstrates that one of them is superior. It involves the measurement of the fluorescence decay of a reference compound under identical conditions as used for the sample [37]. Recently the method was further developed and used for direct measurement of the instrument response of the SPAD which can be used for fitting with deconvolution. Briefly, it makes use of the short lifetime of quenched fluorescent dyes to record the instrument response of the device under identical

conditions (emission wavelength, optical path) as used for the recording of the sample fluorescence lifetime decay [29, 30]. This work is further discussed in Section 6.3.1.

2.3 Fluorescence Microscopy

The end of the 20th and beginning of the 21st century have seen massive technological advances in every conceivable area. Fluorescence microscopy has benefited from imaging hardware, development of new fluorescent probes, increase in the performance of computers and evolution of software tools [38]. Such improvements have made fluorescence microscope easier to use and more versatile, hence increasing the number of investigators, whose main aim is to obtain characteristics of specimens or phenomena at the microscale through qualitative or quantitative fluorescence measurements.

2.3.1 Fluorescence microscopy for environmental mapping

Most of the work related to fluorescence microscopy uses fluorescence as a contrast agent to produce images. However, using the sensitivity of fluorescent dyes to their surrounding environment, researchers have developed methods that provide spatially resolved quantitative information about some biologically, chemically or physically relevant properties to the system imaged.

In order to produce quantitative images using fluorescence microscopy, the sample is commonly stained with a fluorescent dye, and then illuminated with light at an appropriate excitation wavelength [38]. The fluorescence of the dye, that is dependent on its molecular environment, is detected, localised and analysed to generate a quantitative map of the system studied. The three main schemes used to generate quantitative mapping of samples using fluorescence are based on the three main characteristics of fluorescence. The change of quantum yield is used in intensity-based imaging, the change of relative importance of the emission at specific wavelength is measured in wavelength-ratiometric imaging and the fluorescence lifetime is spatially-resolved in fluorescence lifetime imaging microscopy.

Intensity-based methods are the easiest to implement because they do not require sophisticated equipment and because many probes change intensity with changing environment. However, when it comes to quantitative imaging, intensity-based methods are often inadequate [39]. This is because the measurements depend on uncontrollable factors such as the spatial heterogeneity of the probe concentration, and temporal, spatial, and spectral fluctuations of the light source.

The problems of intensity-based imaging can be avoided by using *wavelength-ratiometric* probes. These probes exhibit changes of emission spectrum as a response to environmental change. The analyte properties are therefore measured as a relative change of intensity at two separate wavelengths. Wavelength-ratiometric methods provide a straightforward way to overcome the limitation of intensity-based techniques. However, the difficulty in creating suitable probes is a clear drawback of the technique [40].

Fluorescence lifetime is an intrinsic property of a fluorescent molecule and is therefore insensitive to the problems associated with intensity-based imaging. Fluorescence lifetime imaging microscopy is the technique used to spatially resolve the distribution of fluorescent lifetime values in a sample. The fluorescence image relates the position to the fluorescence lifetime of the probe in the sample. The fluorescence lifetime of the probe is then related to its local molecular environment and hence to the properties of the sample.

2.3.2 Fluorescence Lifetime Imaging Microscopy

There are two methods used for mapping fluorescence lifetime: time-domain and frequency-domain fluorescence lifetime imaging microscopy (TD-FLIM and FD-FLIM).

2.3.2.1 Frequency-domain FLIM

In frequency-domain fluorescence lifetime imaging microscopy (FD-FLIM), the illumination is provided by an intensity-modulated source. Because of the time lag between excitation and emission, the emission is delayed relative to the excitation. This delay is described as a phase shift which varies as a function of the

modulation frequency. Additionally, the response of the sample results in the demodulation of the emission relative to excitation which also varies as a function of the modulation frequency. This factor is commonly referred to as *modulation*. The phase shift and the modulation are separate measurements each of which depend on the relative values of the lifetime and the light modulation frequency [41]. Without going into details, the theory behind FD-FLIM is not as straightforward as for TD-FLIM. At the genesis of time-resolved fluorescence microscopy, FD-FLIM was a good alternative to TD-FLIM because it allowed simplified instrumentation and cheaper implementation. Later, this became only true when with *a priori* knowledge of the probe characteristics, the system was designed and constructed to operate at single wavelength and single frequency. However, quantitative time-resolved measurement and imaging of fluorescence bearing a complex decay requires a wide range of excitation frequencies and wavelengths. Furthermore, since the advent of cheap and reliable laser sources (e.g. diode lasers) and time-gated cameras, FD-FLIM is not significantly cheaper to implement than TD-FLIM. In the present work TD-FLIM has been used exclusively.

2.3.2.2 Time-Domain FLIM

The most common method of wide-field TD-FLIM uses a time-gated intensifier. In time-gated detection, the collected signal is amplified and recorded by a CCD camera for shorts period of time at several time intervals after the excitation pulse. This technique requires high gain and fast gate time. A schematic of a time-gated intensified CCD camera is shown Figure 2-13 [42].

When a photon strikes the photocathode, a photoelectron is emitted and accelerated by a high voltage towards a microchannel plate. In the MCP, the electron striking the wall will generate secondary electrons. At the output of the channels, the bunch of electrons will be accelerated by a high voltage towards a phosphor screen from which high energy photons (green photons) will be emitted and coupled to the CCD surface through a lens coupling system.

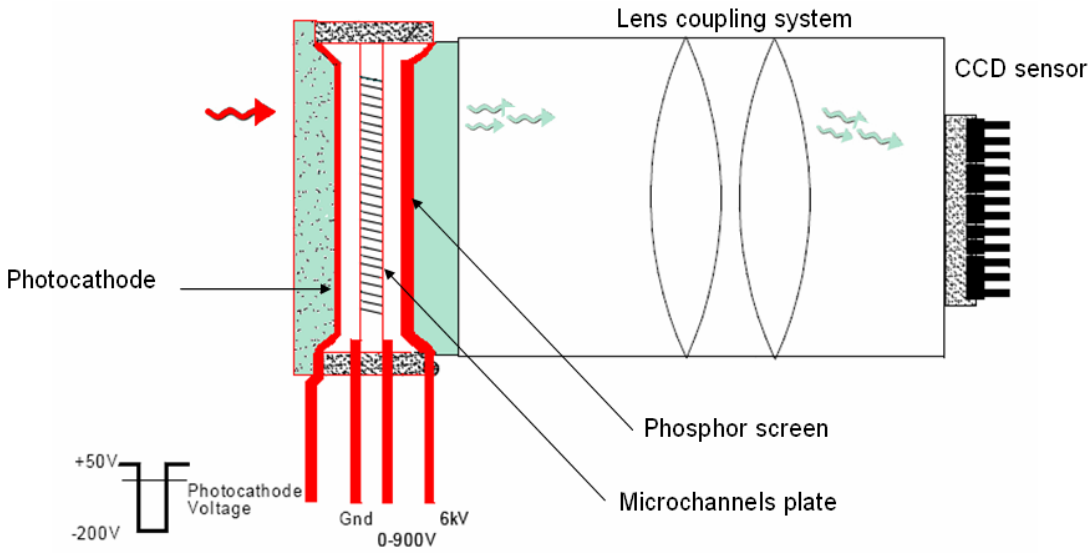

Figure 2-13: Schematic representation of a time-gated intensified CCD camera [42]. The red wavy arrow represents a photon coming from the fluorescence of the sample. The green arrows are the photoelectron emitted by the phosphor screen.

As for TCSPC, a photodiode (Figure 2-4) gives a triggering signal to the system. On reception of the trigger signal a delay will be imposed. After this delay the photocathode voltage will be set for the photons striking the photocathode surface to generate the emission of photoelectrons. The photocathode will remain 'active' according to user specification. While the photocathode is active, the green photons screened on the CCD accumulate charges on a 2Dwise array of sensor. The charges are then collected row by row and column by column and converted into voltage for a 2D map of intensity to be created within the gate time. The delay after triggering is then increased and the process is repeated until construction of the full decay as illustrated Figure 2-14.

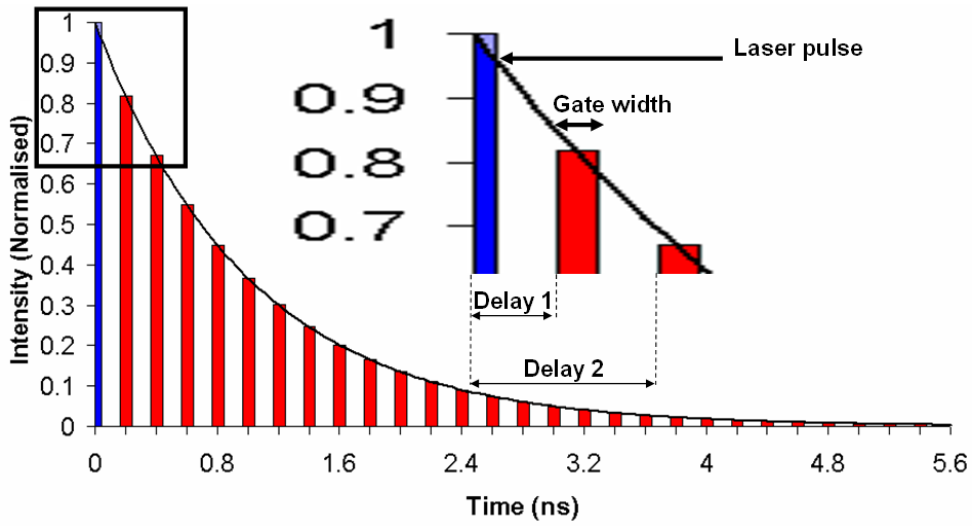

Figure 2-14: Fluorescence intensity decay constructed using a time-gated system.

In order to generate the FLIM map, the intensity decay from each pixel is fitted by non-linear regression to an exponential decay function and the spatially-resolved lifetime values converted into an image using a colour-coded scale. The lifetime resolution of a system is typically determined from the interval time between gates and the complexity of the system of interest. FLIM images can be generated with as little as two gates which makes the technique an ideal candidate for pseudo-real time imaging. One of the limitations of the technique comes from the lack of depth resolution. In wide-field FLIM, the whole field of view is illuminated and the fluorescence signal is collected throughout the depth of the sample. When imaging a microfluidic channel filled with a fluorescent solution, the investigator is prevented from observing buoyancy effects. In order to overcome this limitation, 2-photon excitation FLIM has been used. The technique is described hereafter.

2.3.2.3 2-Photon excitation fluorescence lifetime imaging microscopy

The most common method of confocal microscopy is the laser scanning technique where a diffraction-limited excitation spot is scanned across the sample and the collected signal is spatially filtered using pinholes to remove out-of-plane fluorescence. The main difference between wide-field and laser scanning techniques is the delivery of the excitation beam which is collimated in the former and focused in the latter. Therefore, whereas the information from the full field of view is

acquired at once in wide-field, the images are created by sequentially measuring all the pixels when using laser scanning. Confocal microscopy can also be achieved using 2-photon excitation (2PE). The basic principles of 2PE-FLIM are discussed hereafter.

The absorption of two photons by a molecule was first predicted in 1931 [43]. Two-photon molecular excitation is a nonlinear process in which a chromophore simultaneously absorbs two incident photons [44]. The sum of the energy of the two photons should be equal to the energy required for excitation. A Jabłoński diagram describing the absorption of two photons of the same energy is shown Figure 2-15.

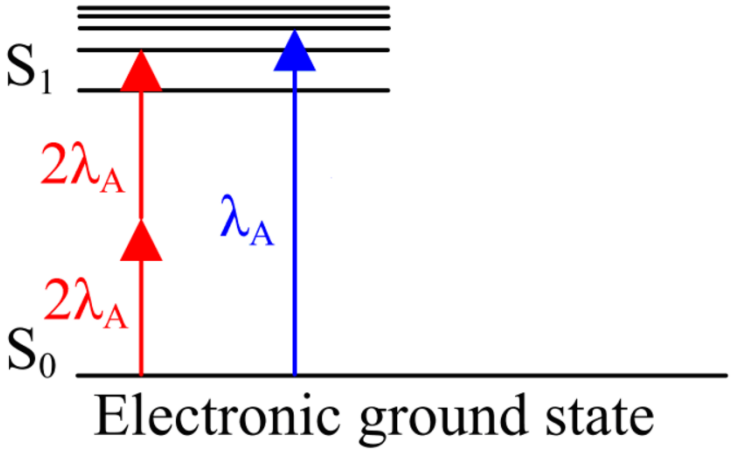

Figure 2-15: Form of a Jabłoński. Simultaneous absorption of two photons by a chromophore (red arrow), One photon process (blue arrow).

Since molecular cross-sections for two photon-absorption are small, high light fluxes are required [45]. This implies the use of laser having high power and short pulse length to reach the peak power required for 2PE to occur. 2PE is superior to conventional confocal because the absorption of the excitation beam is limited to a very small volume at the focus of the objective. The resolution is given by the size of the spot at focus where the photon density is high enough for fluorescent molecules to absorb two photons quasi-simultaneously. The depth- or z-sectioning comes from the quadratic dependence of the fluorescence intensity on the incident photon flux [44, 46]. Approximations for the lateral and axial full widths at half maximum of the two photon excitation spot size are given Equation (2-13) and Equation (2-14) [47]:

$$\Phi_r = \frac{0.37\lambda}{n\sin\theta} \quad \textbf{(2-13)}$$

$$\Delta z = \frac{0.32\lambda}{n\sin^2\frac{\theta}{2}} \quad \textbf{(2-14)}$$

where λ is the excitation wavelength, n the immersion medium and θ the observation angle. The numerical aperture of the objective is given by nsin(θ). With a 1.25 NA objective operated at 960 nm, typical 2PE axial resolution of 0.9 μm and radial resolution of 0.3 μm can be achieved [44].

2.4 Flow dynamic in microfluidic devices

Microfluidics refers to the control and manipulation of fluids that are constrained in devices with sub-millimetre length scales. The ability to fabricate devices with such length scales has attracted much interest from diverse research communities. The miniaturisation of conventional macroscale devices allows smaller volumes (nL scale) of reagent to be used in analytical sciences; cheaper fabrication cost; the development of portable devices; and the manipulation and detection at the cellular length scale [48]. The scaling down of devices lead to a scaling down of the forces that rule the fluid behaviour. While some effects scale linearly with typical lengths *l*, others are nonlinear and scale with l^2 or l^3. Therefore, the development of microfluidic devices is accompanied by phenomena that are unknown from observation of the fluid behaviour at the macroscale. A detailed analysis of fluid dynamics is beyond the scope of this thesis. However, it is necessary to understand the key aspects of flow dynamics at the microscale. Down to microflows, i.e. not valid for nanoflows, a scaling analysis reveals the change in dominant transport phenomena.

2.4.1 Scaling analysis

The most important factor determining the flow regime in a fluidic system is the Reynolds number (Re). At high Re, the system is in a turbulent regime

characterised by chaotic behaviour of the flow field. A low Re means that the fluidic system is in the laminar regime in which the flow behaviour is ordered. Re is defined as:

$$Re \propto \frac{ul\rho}{\mu} \qquad \textbf{(2-15)}$$

where u (in m/s) is a characteristic velocity, l (m) a characteristic length, ρ (kg/m^3) the density of the fluid and μ its dynamic viscosity (Pa.s). In the case of a rectangular channel, the characteristic length is taken to be the hydraulic diameter, defined as:

$$D_H = \frac{4A}{P} \qquad \textbf{(2-16)}$$

where A is the cross section of the channel (m^2) and P its wetted perimeter (m). In a pipe, the transition between laminar and turbulent flow occurs around Re = 2300. The Reynolds number is the ratio of inertial forces that scale with $1/l$, to viscous forces that scale with $1/l^2$. Therefore, it is expected that reducing the size of a fluidic system will result in a smaller Re. Typical hydraulic diameter in microfluidic devices is of the order of 100 μm. Typical flow velocities are of the order of 1 cm/s, the density of an aqueous solution is about 1000 kg/m^3 and the viscosity about 10^{-3} Pas. Such features result in a Reynolds number of 1 characteristic of a flow in the deep laminar regime. Thus, as opposed to the macroscale system where transport processes such as heat and mass are enhanced by turbulences, at the microscale, transport processes happen much more slowly because they are mostly diffusive. The Péclet number is the ratio between advective mass transport and diffusive mass transport. It is defined as:

$$Pe \propto \frac{ul}{D} \qquad \textbf{(2-17)}$$

where D (m^2/s) is the diffusion coefficient. Typical diffusivity in water is of the order of $1\text{x}10^{-5}$ cm^2/s[1]. Entering this number in Equation (2-17) gives a Péclet number of 10000. This means that advective mass transport dominates in microfluidic devices. In most microfluidic devices, advection is parallel to the flow direction. Therefore,

mixing only occurs by diffusion. The ratio between the channel length required to fully mix two solutions after a T-junction and channel width is:

$$\frac{L_{mixing}}{W} \propto F_0 Pe \qquad \textbf{(2-18)}$$

where F_0 is the Fourier number with typical values from 0.1 to 1 [49]. Entering the Péclet number calculated before and a typical width of 100 μm, leads to a possible required length for two streams to mix of up to 1 metre, which is not acceptable for a miniaturised device. One of the techniques used to improve this situation is the generation of chaotic advection by placing periodic mixing structures or patterns in the microchannel [50, 51] .

2.4.2 Pressure-driven flow

In most microfluidic applications an active process is used to transport the fluid in the device. Pressure-driven flow is the method used throughout the work presented in this thesis to transport the fluid through the devices. The pressure difference between the inlet(s) and outlet(s) is generated by syringe pumps. Pressure-driven flow exhibits a characteristic Poiseuille profile. A fundamental law of fluid mechanics is the no-slip boundary condition that states that, at a solid boundary, the fluid will have zero velocity relative to the boundary. A typical velocity profile of a pressure-driven flow is shown Figure 2-16.

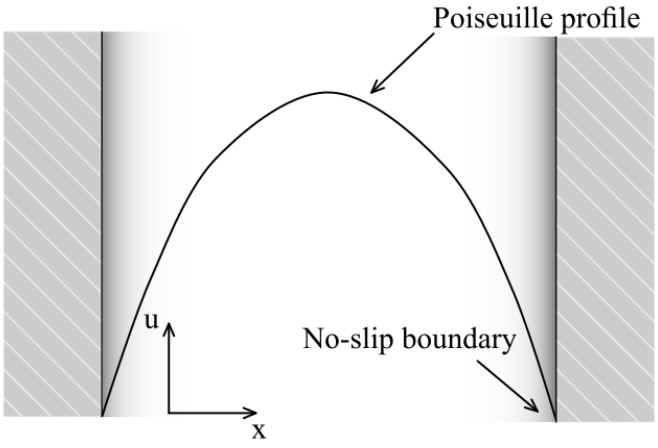

Figure 2-16: Characteristic velocity profile of a pressure driven flow in a microchannel

The velocity gradient across the channel generates spatial heterogeneity in the residence time of the fluid. Whereas fluids at the middle of the channel have high velocity, in the thin layer close to the wall, fluids have a virtual infinite residence time, hence more time to diffuse. Whereas at the macroscale the boundary only affects the fluid in a relatively thin layer close to the wall of the system, in microfluidic systems the influence of the boundary extends over the whole device. Therefore, in microfluidic devices, the boundary can be used to determine flow profiles and control temperature in a much better way than in macroscopic vessels [52].

The parabolic velocity profile shown in Figure 2-16 is characteristic of the laminar flow of a Newtonian fluid in a rectangular channel. An analytic solution to the flow of a Newtonian fluid in a duct of rectangular cross-section with sides located at x = ±a and y = ±b, where a ≥ b, is obtained by solving the governing equation [53]:

$$\frac{\partial^2 w}{\partial x^2}+\frac{\partial^2 w}{\partial y^2}=\frac{1}{\mu}\frac{\mathrm{d}p}{\mathrm{d}z} \qquad \textbf{(2-19)}$$

where w(x,y) is the downstream velocity, μ is the viscosity, and dp/dz the constant pressure gradient down the channel. With the boundary conditions: w(±a,y) = w(x, ±b) = 0, a solution is found of the form:

$$\frac{w}{(-1/2\mu)(\mathrm{d}p/\mathrm{d}z)b^2}=1-\frac{y^2}{b^2}-\frac{32}{\pi^3}\sum_{n=0}\frac{(-1)^n}{(2n+1)^3}\frac{\cosh\lambda_n x}{\cosh\lambda_n a}\cosh\lambda_n y \qquad \textbf{(2-20)}$$

where $\lambda_n = (2n+1)\pi/2b$. The through thickness average $\overline{w}(x)=(1/2b)\int_{-b}^{b} w\,\mathrm{d}y$ is then given by:

$$\frac{\overline{w}}{-(1/3\mu)(\mathrm{d}p/\mathrm{d}z)b^2}=1-\frac{96}{\pi^4}\sum_{n=0}\frac{1}{(2n+1)^4}\frac{\cosh\lambda_n x}{\cosh\lambda_n a} \qquad \textbf{(2-21)}$$

And the volume flow rate Q is obtained by integrating over the channel cross-section $Q=\int_{-a}^{+a}\int_{-b}^{+b} w\,\mathrm{d}x\,\mathrm{d}y$:

$$\Rightarrow \frac{Q}{Q_0} = 1 - \frac{192}{\pi^5}\frac{b}{a}\sum_{n=0}\frac{\tanh \lambda_n a}{(2n+1)^5} \qquad \textbf{(2-22)}$$

where $Q_0 = -4ab^3(\mathrm{d}p/\mathrm{d}z)/3\mu$.

2.5 Microscale Flow Visualization Techniques

The growing interest in miniaturisation of fluidic systems that emerged in the late 80's has encouraged scientists to develop microscale visualisation methods. Although the flow regime in microscale structure is laminar and should *a priori* bestow privileges to accurate computational fluid dynamic calculations, microscale flow visualisation has played a central role in the development of microfluidics technology for several reasons: initial uncertainty about the geometry of the device, about the chemical and physical properties of the boundaries of the microchannels, and about the chemical and physical characteristics of the flowing media result in unpredictable flow behaviour in microfluidic devices. Furthermore, in cases of chemical reaction, the interaction between mass transport and conversion are not calculable to date [54]. Therefore, flow visualisation is important to investigate the flow behaviour at the microscale, provide experimental data to computation fluid dynamics modellers and assess novel microfluidic systems.

In order to visualise fluid transport, the fluid needs to be locally altered for its motion to be detectable. Whereas they all share this particularity, microscale visualisation methods are divided into two subgroups: scalar-based flow velocimetry, where the motion of the bulk fluid is inferred from the observed velocity of a conserved scalar, and particle-based flow velocimetry, where the motion of the bulk fluid is inferred from the observed velocity of marker particles [2, 55].

2.5.1 Scalar-based methods

In scalar-based methods, alteration of the properties of a small volume in the device allows for its dispersion to be monitored along the channel. Photophysical alterations are realised by the introduction of fluorescent or phosphorescent tracers.

The bulk fluid properties can also be altered by IR heating or photochromic reaction (change of colour).

Tracking a locally excited fluorescent tracer is practically unfeasible because fluorescence is a fast decaying process (ns range). Therefore, researchers use fluorescence in conjunction with photobleaching, caging molecules or change of the quantum yield of the fluorescence process.

Photobleached-fluorescence imaging of microflows was developed by Mosier and Santiago [56]. They used a 0.5 W focused argon laser beam across a microchannel, to photobleach a stripe in the fluorescent solution. The motion of the stripe that appears dark on a bright background was imaged using the transmitted light of a mercury lamp and monitored by a CCD camera on a standard epi-fluorescence microscope [57]. A characteristic result obtained using the photobleached-fluorescence imaging method is shown Figure 2-17.

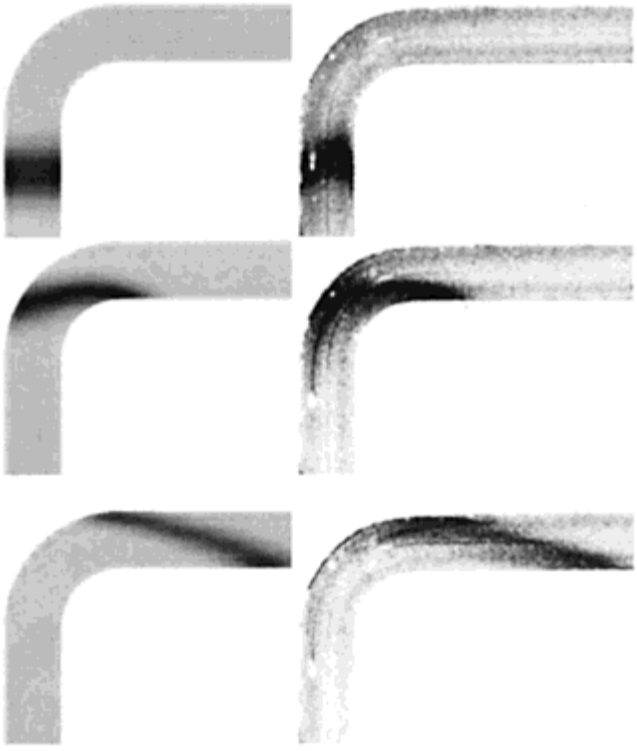

Figure 2-17 : Simulation (left column) and photobleached-fluorescence visualization (right column) of an analyte band travelling around a constant radius corner [57].

The first application of caged fluorescence to microscale flow visualisation was reported by Paul *et al.* in 1998 [58]. Caged-fluorescent dyes are fluorophores with additional chemical groups that render the molecules non-fluorescent [2]. Locally resolved uncaging of the fluorophores by photolysis allows their dispersion to be monitored. Paul *et al.* used a tripled Nd:YAG laser at 355nm to produce a sheet of light having a thickness of 20 μm and a width of 500 μm for the uncaging step. The plane of this sheet was oriented perpendicular to the axis and directed to section the capillary. A second laser was used to excite the uncaged dye at 473 nm. The fluorescence was collected on an epi-fluorescent microscope by a CCD camera [58].

As opposed to fluorescence, phosphorescence lifetime can be long enough (ms range) to track the dispersion of tracers in microfluidic devices [59]. Furthermore, the technique requires only one light source for excitation. However, due to the short timing scale (ms), its use is limited to studying high flow rate in microfluidic devices. The limitations of the technique are too restrictive for it to be widely used. Other scarcely used techniques include photochromic reaction where the absorption spectra of the flow is locally altered by exposure to UV light [60], and infrared heating where a CO_2 laser is used for heating and an infrared camera for detection [61].

2.5.2 Particle-based methods

To date, three particle-based methods have been implemented for microscale flow visualisation. They were all existing methods for the visualisation at the macroscale before being adapted to study microscale flow behaviour.

In laser Doppler velocimetry (LDV) two coherent laser beams are used to generate an interference pattern in the sampling volume. The sample is seeded with particles. As a particle travels at the intersection of the two laser beams, it reflects or scatters light from the positive interference region. The Doppler frequency-shift of the light is used to determine the flow velocity. It has been successfully applied to obtain velocity data in a microfluidic channel [62]. The implementation of LDV to study flow in microfluidic devices requires increased optical control and infrastructure to match the characteristic length of the beam with the microscale.

Furthermore, sampling is based on the probability of a particle crossing the interrogation area. This probability is decreased with decreasing volume where the introduction of higher particle concentration would alter the flow behaviour.

In particle streak velocimetry (PSV), the displacement of particles is imaged on a single frame. The resulting image is a bright background with dark lines representing the displacement of particles. The main advantage of the technique is that it requires little equipment to provide quantitative data. It has been successfully applied to microscale flow visualisation [63]. Whereas PSV images are useful to characterise the profile of the flow, the technique lacks reliability and accuracy [55].

2.5.3 Principles of Micro-Particle Imaging Velocimetry

First introduced in 1998 by Santiago et al. [1], micro-particle imaging velocimetry (μ-PIV) is to date the most well-developed microscale flow visualisation method. The Santiago *et al.* paper has become a pivotal work with over 400 citations (Web of Knowledge as of October 2010).

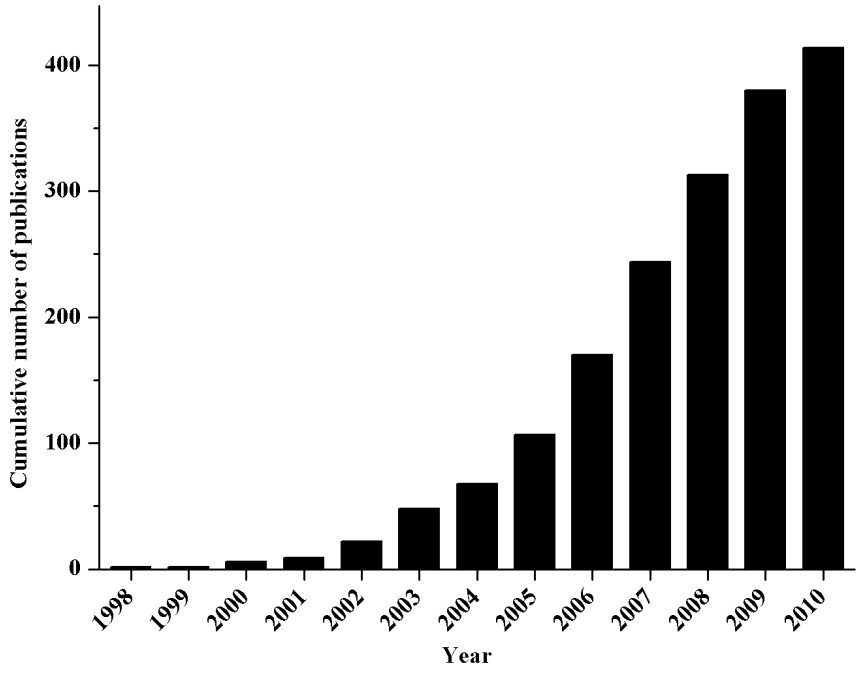

Figure 2-18: Cumulative number of articles reporting the use of μ-PIV as imaging technique, data as of October 2010 obtained from Web of knowledge.

Since its first report, the use of μ-PIV has been constantly expanding (as shown in Figure 2-18) with the emergence of ever novel configurations. The technique has been extensively reviewed in recent publications and books [2, 64-67].

In μ-PIV, two successive images of the seeded flow are taken at a known time interval, Δt. The images are subdivided into interrogation areas which are cross-correlated to determine the most probable local displacement, Δx. The flow velocity (u) in an interrogation area is obtained by dividing the measured displacement by the time interval as defined by:

$$u = \frac{\Delta x}{\Delta t} \qquad \textbf{(2-23)}$$

As opposed to streak imaging, where a long exposure camera is used to record the displacement on a single frame, μ-PIV requires the capability to record discrete particles at two known times. Therefore, the light collected to generate the two images needs to be gated. When continuous illumination is used, the detector must be gated or a shutter must be introduced into the light path. For better time resolution some researchers have used the frequency-doubled emission from two Nd:YAG lasers. This allows the interval between two recordings to be varied from tens of nanoseconds to a few seconds [66].

The particles used in μ-PIV range from 200 nm to 2μm in diameter. They are often fluorescently-labelled and mostly made of polystyrene or latex. Fluorescent beads are used in epi-fluorescence mode and their positions are determined by the emission of light following excitation. The position of non-fluorescent tracers is determined from the light scattered from the beads. Quantum dots have also been used and exhibit several advantages: they are small (nm), have a broad excitation band and are not susceptible to photobleaching. However, due to their small size, they are more susceptible to Brownian motion. The effect of Brownian motion sets the lower limit on the choice of particle size. It is quantified by:

$$\varepsilon_B = \frac{1}{u}\sqrt{\frac{2D}{\Delta t}} \qquad \textbf{(2-24)[1]}$$

where D is the diffusivity of a spherical particle. In 1905, Einstein predicted that Brownian motion of a particle in a fluid at temperature T is characterised by a diffusion coefficient [68]. The diffusivity of a spherical particle is given by Equation (2-25):

$$D = \frac{k_B T}{3\pi\mu d_p} \qquad \textbf{(2-25)}$$

where k_B is Boltzmann's constant, T is the temperature of the fluid, and μ its dynamic viscosity. The error due to Brownian motion increases with $d^{-1/2}$, and $\Delta t^{-1/2}$. It becomes significant (20% error due to Brownian motion) for particles with diameter smaller than 500 nm, flow velocities lower than 0.5 mm/s and time interval of 100 μs [66]. Error due to Brownian motion, which is a random process, can be reduced by looking at several particles or averaging over many sets of images. Therefore, in order to correctly calculate the velocity field map, there are several factors to take into account. Firstly, the tracer particles need to be small enough to faithfully follow the flow motion and not to block the channel, but not too small, to avoid large errors due to Brownian motion. Secondly, the number of detected particles per interrogation area needs to be sufficiently high for averaging purposes but not too high to disturb the flow. This can be realised by collecting a sufficient number of image pairs for enough particles to be detected in each interrogation area.

As opposed to macroscopic PIV where a sheet of light is used, μ-PIV uses wide field illumination in which the entire depth of the device is flooded by light. The measurement plane in μ-PIV is defined by the depth of field of the collecting optics. The measurement depth for volume illumination has been calculated [69, 70]. It allows for the depth of correlation to be estimated. The depth of correlation is defined as the depth over which particles significantly contribute to the correlation function. An expression for the depth of correlation is:

$$z_{corr} = 2\left\{\frac{\left(1-\sqrt{\varepsilon}\right)}{\varepsilon}\cdot\left[\frac{n_0^2 d_p^2}{4NA^2} + \frac{5.95(M+1)^2\lambda^2 n_0^4}{16M^2NA^4}\right]\right\}^{1/2} \qquad \textbf{(2-26)}$$

where $\varepsilon \approx 0.01$, n_0 is the immersion medium, d_p the diameter of the tracer particle, NA and M, the numerical aperture and the magnification of the collecting objective, respectively, and λ the wavelength of the light collected by the objective. The depth of correlation has a quadratic dependence on the NA of the optics used. It becomes small when high NA objectives are used. High NA objectives are used to image small particles, which are susceptible to Brownian motion. Therefore, in such a configuration, the particle can quickly move between in-focus and out-of-focus plane resulting in an increase in the measurement noise. However, it is desirable to minimise the correlation depth when there is a strong velocity gradient in the z-direction in order to reduce biasing of velocity measurements due to particles far from the focal plane [1].

2.5.4 Extension and improvement of μ-PIV

A review of the over 400 papers dedicated to μ-PIV is beyond the scope of this thesis. However, there have been some interesting works reported which overcome characteristic shortcomings of the conventional technique or extend the use of μ-PIV to other purposes than characterising flow fields.

Conventional μ-PIV requires at least one transparent optical window to deliver the illumination light and record the position of moving particles. Although most of the microfluidic prototypes are made of relatively transparent materials, either micro-machined PMMA or cast PDMS sealed with a microscope coverslip, some applications require characterising fluid flow in opaque conditions. X-ray μ-PIV has been used to investigate blood flow in opaque materials [71]. IR μ-PIV has been used to characterise the flow behaviour in a silicon heat sink [72].

The nature of the illumination used for μ-PIV also presents some limits. The measurements allow only for 2-dimensional (2D) maps to be generated and two components (2C) fields to be calculated. This means that the measurements are not spatially resolved in depth, and out of plane velocity components are not measured. In order to limit the depth of measurement, evanescent wave illumination was used to study flow near the wall of microchannels [73]. To resolve the measurement in 3D, researchers have adapted fast scanning confocal microscopes to investigate flow

behaviour in a thin plane of a device [74]. Stereoscopic μ-PIV has been attempted to obtain 2D-3C measurements [75]. However, due to the contradictory requirements of these two techniques (low NA for stereoscopy, high NA for μ-PIV) and the difficulty in separating the two cameras by a large enough angle to obtain good accuracy in the out of focus velocity components, stereoscopy did not encounter the same success at the microscale as at the macroscale. Algorithms can also be used to retrieve in-depth information of the position of the particles. For example, fluorescent particles smaller than the diffraction limit of the imaging system can create a ring pattern that is a function of their distance from the focal plane [76].

In biology, μ-PIV has been used *in-vivo* to track the motion of red blood cells in the arteriole of a rat [77]. μ-PIV has also been used as a thermometry technique in microfluidic devices [78]. By detecting the Brownian motion of particles the temperature can be determined by:

$$\left\langle s^2 \right\rangle = 2D\Delta t = \frac{2k\Delta t}{3\pi d_p} \cdot \frac{T}{\mu} \qquad \textbf{(2-27)}$$

where s^2 is the mean square displacement of a particle.

The growing interest in developing microfluidic applications has encouraged scientists to develop microscale flow visualisation methods. At the end of the 90's, several major methods emerged. The choice of the method is mainly determined by the application of interest. However, thanks to its versatility and its superior capability for high spatial and temporal resolution data, μ-PIV is the most well developed microscale flow visualisation method to date. In this work it has been chosen to generate velocity field maps of microflows.

2.6 Physics of optical tweezers

The manipulation of particles by radiation pressure dates back to 1970 as first reported by Ashkin [79]. His group first demonstrated optical trapping using radiation pressure from a tightly focused laser beam 16 years later [80]. The features of optical tweezers make them the ideal tool for micromanipulation in microfluidic

devices. The principles of the technique are presented herein along with a short review of the different tasks optical tweezers can perform in microfluidic devices.

2.6.1 Principles and characteristics

Interaction between light and particles in the Mie regime (where the diameter of the particle is large compared to the wavelength of light) can be analysed by ray optics [80]. A photon has energy and momentum. When light is refracted by a bead, its momentum is changed. In order to satisfy Newton's third law, an equal and opposite momentum change is imparted to the bead. Therefore, for the force resulting from refraction to work towards trapping, the bead has to have an index of refraction higher than its surrounding medium. By convention, the forces resulting in trapping an object are divided into scattering forces in the direction of the beam and gradient forces perpendicular to the beam direction or in the axial intensity gradient. Figure 2-19 shows the forces experienced by a bead placed in a laser beam.

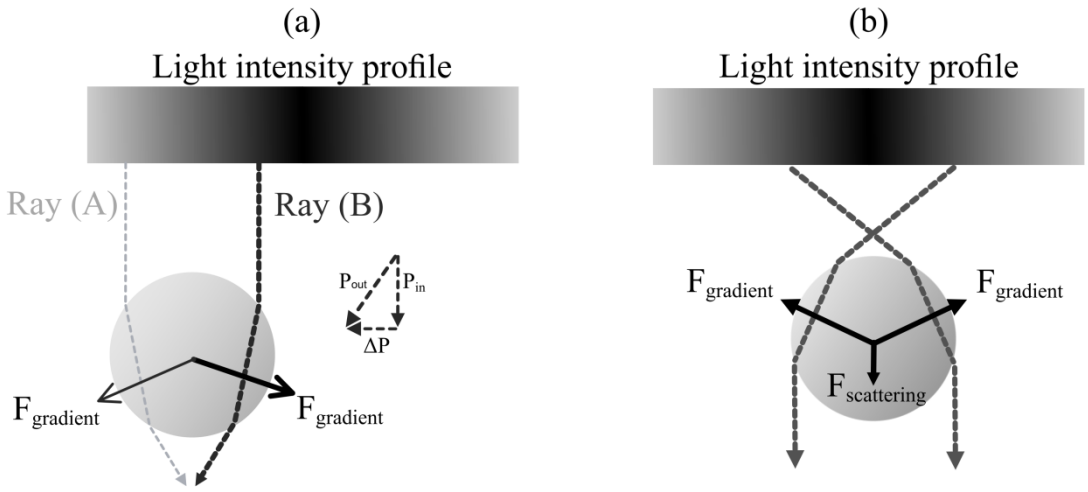

Figure 2-19: Ray diagrams of a transparent bead subjected to optical pressure exerted by a laser. Gradient forces and change of momentum of ray B resulting in the bead being attracted toward higher intensity region of the laser beam (Figure 2-19(a)). Tightly focused laser beam resulting in the bead being trapped (Figure 2-19(b)).

For the sake of clarity, only two rays have been drawn on the representation in Figure 2-19. In Figure 2-19(a), the bead is on the left of the axis of maximum intensity. Due to heterogeneity of the change in photon momentum after refraction, the bead will be subjected to a net force pushing it towards region of higher intensity.

This force is called gradient force. When the bead is in the axis of highest intensity, the net resulting gradient force will be pushing the bead towards the laser focus. However, reflection and absorption by the bead are responsible for the scattering force that acts in the beam propagation direction. The scattering force decreases with increasing distance from the focus. In order for the gradient force to counter interact sufficiently for the bead to be trapped in 3D, the optical setup necessitates the use of a high NA objective to obtain a steep gradient of light. As a result of trapping by equilibrium of the gradient and scattering forces, the bead is held slightly below the laser focus (further from the laser focus in the beam propagation direction). A displacement of the bead outward from its equilibrium position will induce an imbalance of the forces that will bring it back to its trapping position. In the vicinity of the focus, the optical trap behaves like a spring exerting a force on the bead proportional to its displacement from the centre of the trap. Like a spring, the trap is characterised by its stiffness, given by:

$$F_{trap} = \frac{nQP}{c} \qquad \textbf{(2-28) [81]}$$

where n is the refractive index of the surrounding medium, Q is the efficiency of the trap, P the laser power, and c the speed of light. The efficiency of the trap Q ranges between 0 and 1. For a small dielectric particle, Q typically lies in the range between 0.03 and 0.1 [81]. It refers to the amount of momentum transferred to the trapping force.

The force of the trap is an important parameter when using optical tweezers in a microfluidic device because it will determine under which flow conditions and fluid characteristics the laser tweezers will be effective in trapping. The force required for the laser to hold a bead in a stream of flow rate u is characterised by:

$$F_{drag} \approx 6\pi\rho\upsilon r u \qquad \textbf{(2-29) [82]}$$

where ρ is the fluid density, υ its dynamic viscosity and r the radius of the bead. In order for a bead to be trapped, F_{trap} has to be greater than F_{drag}.

2.6.2 Use of optical tweezers

With the generalisation of the use of optical tweezers, ever more applications emerge to manipulate micro-objects in microfluidic devices.

A circularly polarised beam can be used to rotate a trapped object [83]. In that case, the angle of the birefringent plate controlling the laser polarisation is used to control the rate of rotation. Similarly, a birefringent object can rotate and be aligned due to the forces exerted by a linearly polarised laser beam [84]. The shape of microfabricated micro-objects can also be used to generate rotation [85]. In that case it is the anisotropic geometry of the objects that induces a torque as a result of the heterogeneous momentum transfer at their surfaces. Microfabricated microstructures with form birefringence are easily applied to various applications such as light-driven microelectromechanical systems (MEMS) and microfluidic control devices such as micropumps and micro-stirrers [86].

In order to trap multiple objects, the laser focus can be scanned at high speed using galvano scanners equipped with mirrors. The scanning can be performed either continuously and induce a movement of the particles [87] or discretely in which case the laser is irradiating the particle intermittently before the Brownian motion brings the particle away from the laser focus [88]. The capability of galvano scanners are limited by their scanning rate. However, it is possible to trap and manipulate many more particles using piezoelectric mirrors [89]. As opposed to time distribution of the laser light, researchers have also used the shape of the beam to adapt the trapping capabilities. Several techniques have been employed: Bessel beams allow the depth of trapping, usually limited to the objective working distance (ca 100 μm) to be extended, hence exhibiting multi-trapping capability [90]; the use of a computer-controlled spatial light modulator (SLM) allows the generation of 3D arrays of laser foci and their independent movement [91]; recently, the use of a SLM to create two foci to trap an object has shown trapping capabilities using low NA and long working distance objectives [92]. This is particularly valuable when high laser power is not desired on the trap and for imaging applications that require trapping and a large field of view.

Finally, laser tweezers have been used to measure forces in microfluidic devices. They can be used to generate 3D maps of flow fields by looking at a bead intermittently trapped and released in a flow. By looking at the displacement of the bead from the laser focus, the flow field can be determined locally [93]. Looking at the displacement of a bead from the laser focus leads to force measurements with sensitivity of 27 fN in a range of 5.2 pN [94]. Optical trapping in the pN range is useful to study the mechanical properties of biomolecules. Two counter propagating beams can be used to stretch a cell [95] or two beads can be attached at both ends of a biomolecule and pulled away from each other to study the specimen elasticity [96].

3 EXPERIMENTAL

The main experimental setups and methods used in order to achieve the aims of this work are presented in this chapter. These were steady-state and time-resolved fluorescence spectroscopy, wide-field and 2-photon excitation fluorescence lifetime imaging microscopy, micro-particle imaging velocimetry, the fabrication of microfluidic devices and the development of an open-frame microscope. A description of the materials used is given. The experimental details relative to specific work are given in relevant chapters.

3.1 Steady state measurements

The absorption spectra of the optical filters and of the solutions were recorded using a UV-visible spectrophotometer (CARY 300 Conc, Varian). The fluorescence spectra were recorded using a spectrofluorometer (Fluoromax™, SPEX®). Typical settings were 2 nm bandwidth slits for emission and excitation monochromator arms, 0.1 s integration time, and increment of 1 nm. The solutions were contained in 1 cm pathlength microcuvettes (108.002F-QS, Hellma®) made of Quartz SUPRASIL®.

3.2 Time-resolved fluorescence measurements

3.2.1 Experimental setup

The equipment Figure 3-1 was used to record fluorescent decays using the time-correlated single photon counting (TCSPC) technique. The equipment is set up in the Collaborative Optical Spectroscopy Micromanipulation & Imaging Centre (COSMIC).

The laser system is a commercial system supplied by Coherent Inc. It consists of the Verdi V-10 Nd:YVO_4 laser delivering 10 W at 532 nm, used to pump the Mira 900-F Ti:Sapphire laser, tuneable from 700 nm to 1000nm, and delivering pulses at 76 MHz of about 200 fs duration.

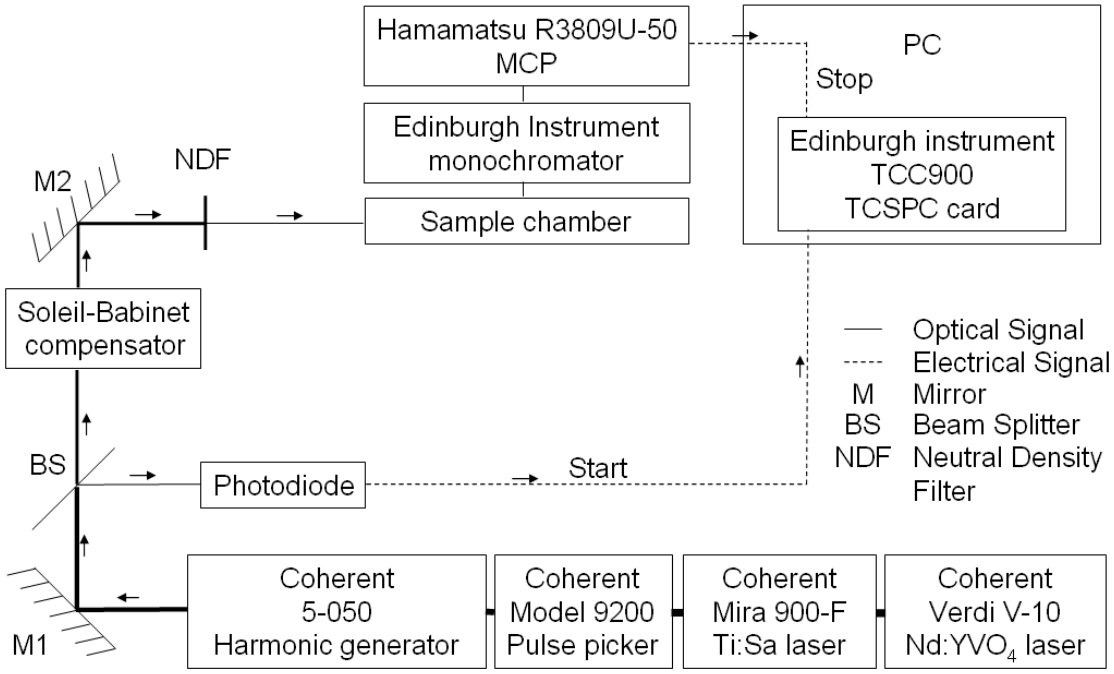

Figure 3-1: Schematic of the experimental setup used for fluorescence lifetime measurement using TCSPC.

A frequency of 76 MHz corresponds to a pulse every 13 ns. Most of the useful fluorophores have a fluorescence that extends beyond 13 ns. Therefore some of the pulses emitted by the Ti:Sapphire have to be rejected. This is done using a pulse picker (Model 9200, Coherent Inc.) which consists of an acousto-optic modulator. The acousto-optic modulator deflects some of the pulses, resulting in a tuneable useful output repetition rate that ranges from 9.5 kHz to 4.75 MHz. Most of the fluorophores absorb light in the UV-visible region, therefore, the Ti:Sapphire emission wavelengths are not appropriate. In order to reach useful wavelengths, the system also incorporates a second (and third) harmonic generator (Model 5-050). The second harmonic is produced through a non-centrosymetric medium (Lithium Triborate and Beta Barium Borate) [97] which has a non-zero second order tensor $\chi^{(2)}$. Under an applied electric field, this tensor implies a dipole oscillating in the crystal at 2 times the original frequency. Assuming an incident light with high power density, some of it will be frequency doubled by the crystal. The maximum output power was measured to be 9 mW at 400 nm (second harmonic). The output of the second harmonic is split using a beam splitter. The reflected part is directed towards

a photodiode that delivers the start signal to the single-photon counting card (TCC-900). The reflected beam is used for the photodiode to give about -600 mV (measured with an oscilloscope) output voltage on detection of a pulse. The threshold of the constant fractional discriminator for start pulse detection is typically set to -300 mV. The beam transmitted through the beam splitter is directed towards the sample chamber through a Soleil-Babinet compensator and a pair of neutral density filter wheels. The Soleil-Babinet compensator is a pair of opposed birefringent crystal wedges the optical axis of which lies at 45° to the polarisation of the incident laser beam. The laser beam, originally horizontally polarised, is vertically polarised at the output of the compensator. A vertically polarised excitation beam together with a collection of the fluorescence emission at the magic angle prevent anisotropy from affecting the recorded data. The distance the beam needs to travel across the crystal is wavelength dependent. It is adjusted before each experiment through the control software (F900 Edinburgh Instrument) using the simplified relation (Equation (3-1)):

$$Q = \frac{41.62}{\lambda} \qquad \textbf{(3-1)}$$

where Q is the calibration factor and λ is the wavelength in nm of the incident beam.

The neutral density filter pairs are used to control the intensity of the fluorescence and hence the stop rate of the TAC. In order to avoid pulse pile-up in the emission distribution and deterioration of the MCP PMT, the filters were set for a maximum stop rate of 40 kHz.

The instrument response was recorded before and after every experiment using light scattered from the excitation beam by a suspension of colloidal silica (Ludox, Aldrich), at a stop rate up to 2 kHz. In the sample chamber (FL920 series spectrometer, Edinburgh Instruments), the beam was focused to the sample (f ~ 10 cm) and directed toward a beam dump. The samples were contained in 1 cm path length Quartz SUPRASIL® cuvettes (Type No. 108.002F-QS, Hellma®) and the emission collected perpendicular to the excitation. An adjustable iris (2 mm to 37 mm) separated the sample chamber from the monochromator. It allowed the volume of the sample from which emission is collected to be controlled. The larger

the aperture, the greater the range of path lengths to the anode of the microchannel plate photomultiplier tube (MCP PMT), the longer the transit time spread and the broader the instrument response. The emission was focused by a lens (f ~ 10 cm) and passed through the emission polariser set at 54.7 degrees relative to the excitation beam polarisation. The entrance and exit slits of the monochromator control the bandpass (usually set to 10 nm) of the emission. The detector, a MCP PMT (Hamamatsu R3809-50) was sensitive over the range 160 nm to 850 nm, with a gain of up to 2.0×10^5 and a transit time spread of 25 ps (manufacturer specification) [98]. The TCSPC electronics are integrated onto a single photon counting card (TCC 900, Edinburgh Instrument). The time-to-amplitude converter has a time range from 2.5 ns to 50 μs, over a maximum of 4096 channels (minimum time per channel: 610 fs) and a dead time of 112.5 ns [99].

3.2.2 Data analysis

Decays are recorded and analysed using F900 (Edinburgh Instrument Ltd.) software. Using initial parameters set by the software user, F900 iteratively fits the exponential decay function given Equation (3-2):

$$I(t) = B + \sum_{i=1}^{n} A_i \exp\left(-\frac{t}{\tau_i}\right) \qquad \textbf{(3-2)}$$

where B accounts for a constant background (dark counts of the detector) and A_i represents the amplitudes of components having a lifetime τ_i.

The recorded data can be fitted regardless of the instrument response from data points situated away in time from the instrument response function. This simple analysis method is referred as to 'tail-fitting' and uses the best fit of Equation (3-2) to the decay curve. However, short lifetime components are not resolved by this method. In order to compensate for the instrument response, an instrument response function (IRF) must be convoluted with the fitted decay function. The shape of the IRF is representative of the excitation pulse and the time response of the detector. Figure 3-2 shows a typical IRF.

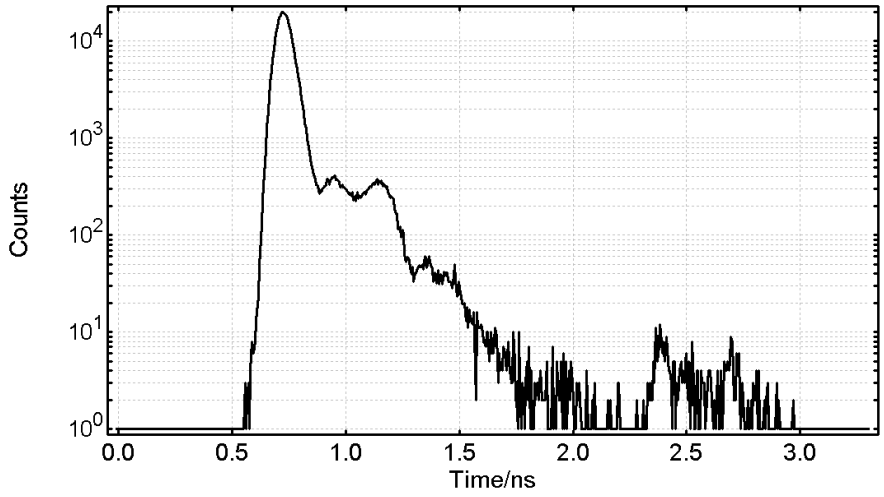

Figure 3-2: Typical instrument response function recorded with the experimental setup Figure 3-1.

The instrument response function is characterised by its shape and its width at full width half maximum (FWHM). The system used in this work shows an instrument response as a pulse of ~70 ps FWHM. The raw data S(t) recorded using TCSPC represents a convolution of the instrument response E(t) with the sample function R(t). The mathematical relationship between the sample response function R(t), the IRF E(t) and the sample function S(t) is given by the convolution integral [100]:

$$S(t) = \int_0^\infty E(t') \cdot R(t - t') \cdot dt' \qquad \textbf{(3-3)}$$

With knowledge of R(t) and E(t'), S(t) can be calculated and the fluorescence lifetime values are determined by iterative non-linear least squares fitting. The quality of the fit is evaluated using the Chi-Square (χ^2) criterion and the residual data. χ^2 is defined by Equation (3-4) [100]:

$$\chi^2 = \sum_{k=1}^{n} w_k \frac{(S_k - F_k)^2}{n} \qquad \textbf{(3-4)}$$

where k is the index for each data point, w_k is the weighting factor, F_k are the experimental values and S_k the calculated values. Lifetime data acquired using TCSPC follow a Poisson distribution, for which the mean count is equal to the variance. Hence the weighting factor is given by Equation (3-5):

$$w_k = \frac{1}{\sqrt{F_k}} \quad \textbf{(3-5)}$$

Mathematically speaking, a perfect fit is characterised by a χ^2 of 1.0. For the experimental system used here, χ^2 values between 1.0 and 1.2 were indicative of acceptable fits. However, systematic errors in the data can result in χ^2 values in excess of 1.5 [101]. This does not mean that the model used is incorrect but rather that the quality of the data is poor. A χ^2 smaller than 1 is out of the theoretical limit for Poissonian distribution. This can be due to an inappropriate fitting range. Obtaining a good χ^2 is necessary but not sufficient to assess the quality of curve fitting. A visual inspection of how the fitted curve matches with the experimental data is also required. A visual inspection of the residuals has also to be performed to validate a fit. The residual function (R_k) is the difference between the weighted calculated intensities and the weighted experimental intensities at each point. It is given by Equation (3-6):

$$R_k = w_k(S_k - F_k) \quad \textbf{(3-6)}$$

For an acceptable fit, the residual data should look like a random distribution of points around zero.

In solution, a fluorophore may exist in more than one emitting state, e.g. multiple conformational forms, resulting in a multi-exponential decay. In the case where two conformational forms, C_1 and C_2 are present, the decay would be bi-exponential with exponential factors τ_1 and τ_2 corresponding to the fluorescence of C_1 and C_2, respectively. With respect to Equation (3-2), the pre-exponential factors A_1 and A_2 represent the contribution of the species C_1 and C_2 to the overall fluorescence decay. Unfortunately, this only works conceptually because mathematically, in Equation (3-2), A_i and τ_i are correlated parameters. This problem can be overcome by recording a series of decays that describe the system under different conditions (e.g. changing the excitation or emission wavelength) and perform simultaneously a global analysis on all the decay curves recorded. In the case of species C_1 and C_2, the lifetime values τ_1 and τ_2 should be independent of the changing conditions. It is

therefore possible to calculate the A-factors (which will vary) independently from τ_1 and τ_2. Furthermore, because it is based on a larger number of data points, global analysis of statistically independent measurements results in an increase of the certainty of the calculated fluorescence lifetimes.

3.3 Wide-field fluorescence lifetime imaging microscopy

Wide-field fluorescence lifetime imaging microscopy (FLIM) was used in conjunction with two different microscopes. More attention will be paid to the implementation of wide-field FLIM onto a custom-built microscope in Chapter 6. FLIM uses the same principle as TCSPC except that spatial information is acquired. The light source used is the same as described in Chapter 3.2.1. The remainder of the equipment is shown Figure 3-3.

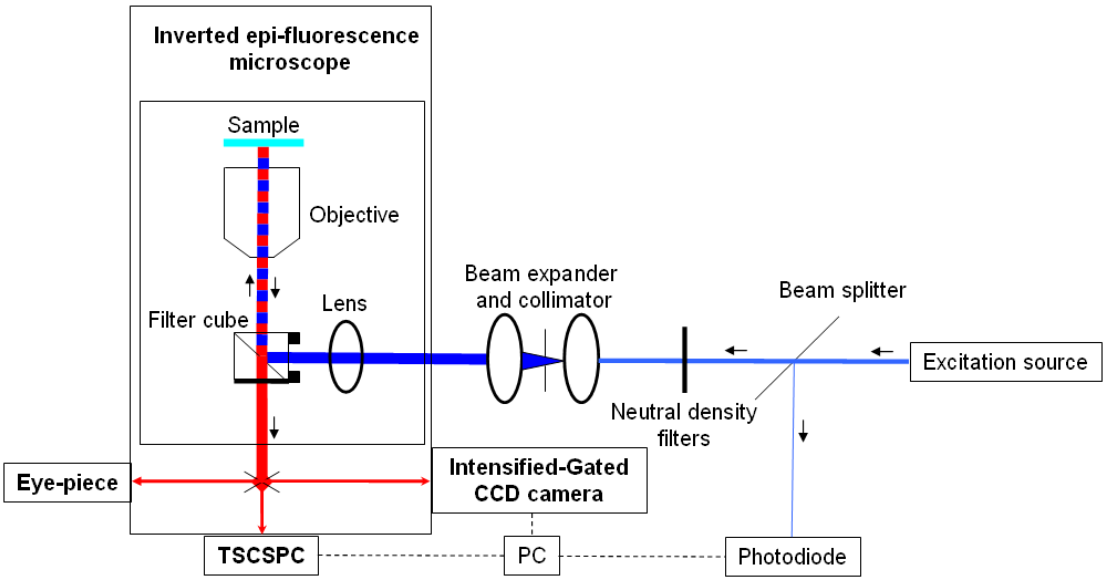

Figure 3-3: Schematic of the FLIM setup on a commercial inverted epi-fluorescence microscope.

As for TCSPC, a portion of the excitation beam is diverted toward a photodiode which gives the triggering signal to the electronics. The rest of the beam is attenuated through three neutral density filter wheels (from fine to high

attenuation), expanded and collimated through a lens pair, spatially filtered by an aperture, and delivered into an inverted epifluorescence microscope (Nikon TE300). The filter cube holds a dichroic mirror and two integrated filter holders. The dichroic mirror reflects the excitation light to the sample. The emission is collected as epifluorescence through the objective and the emission filter and directed toward either the eye-piece or one of the detectors.

3.3.1 Time-gated technique

The time-gated intensified camera used in this study is a Picostar HR-12QE (LaVision GmbH, Germany). The delay is given by a DEL150 picosecond delay module (Becker and Hickl GmbH, Germany). The camera is peltier cooled, 12bit, progressive scan interline sensor with 1376 horizontal by 1040 vertical pixels (6.45 μm x 6.45 μm). Each pixel saturates at 4050 counts. A maximum count between 3000 and 4000 was achieved using neutral density filters and by varying the exposure time of the camera (usually set to 200 ms). The gate width and delay steps were usually set to 500 ps. In order to obtain good image quality, an average of 5 exposures was recorded. Once recorded, the images were analysed using the software provided by the manufacturer (DaVis 6.2). This software allows the construction of single exponential decay images by non-linear regression of the time-correlated data recorded in each pixel and extraction of data from regions of interest for further analysis of the decay curves.

3.3.2 Time- and space-correlated single photon counting

TSCSPC technique was first reported in 2003 [102]. It is based on a space-correlated TCSPC detector (Europhoton GmbH). A schematic diagram of the detector is shown Figure 3-4.

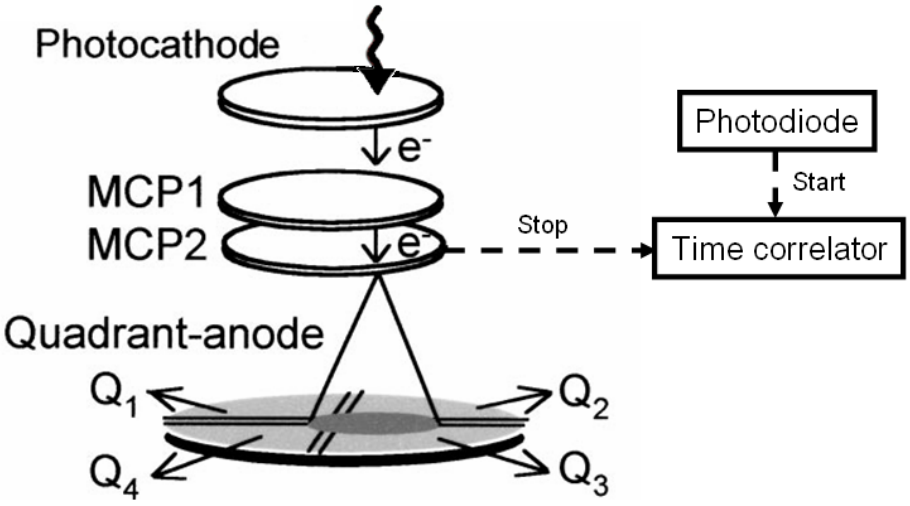

Figure 3-4: Schematic of the TSCSPC detector and working principle [102].

When a photon hits the photocathode, a photoelectron is emitted and a cone-shaped cloud of electrons is created by a pair of MCPs. The electrons are then collected by four independent detectors, the quadrant anode. The centre of the disk created on the quadrant-anode by the cloud of electrons corresponds to the position at which the photon has struck the photocathode. The X and Y coordinates of the incident photon are obtained as combinations of the four output voltages provided by the quadrant anode [103]. The time correlation is given by a TAC operating between the photodiode and the second MCP.

The time correlation of the TSCSPC works in the same fashion as the TCSPC, i.e. detection count rate has to be kept low over the whole sample, the arrival times are addressed to 4096 channels each of 27 ps width. The channels can be binned: binning 10 channels will result in a channel width of 270 ps and a proportional increase in counts. The spatial resolution is limited by the image digitalisation of the pixel size. It has been approximated to be 250 nm with a 100x objective magnification [102]. The control software (QAcapture) is provided by the manufacturer. It allows visualisation of the intensity distribution while recording data. Once recorded, data are analysed using QAAnalyis5. QAAnalysis5 allows: mapping of individual A-factor (Equation (3-2)) for fluorescence systems having up

to 4-component exponential decays; the generation of FLIM images; the extraction of decay curves from regions of interest (ROI) for further analysis.

3.4 Two-photon excitation FLIM

3.4.1 Optical setup

Figure 3-5 shows a schematic of the setup used for 2-photon excitation FLIM (2PE FLIM).

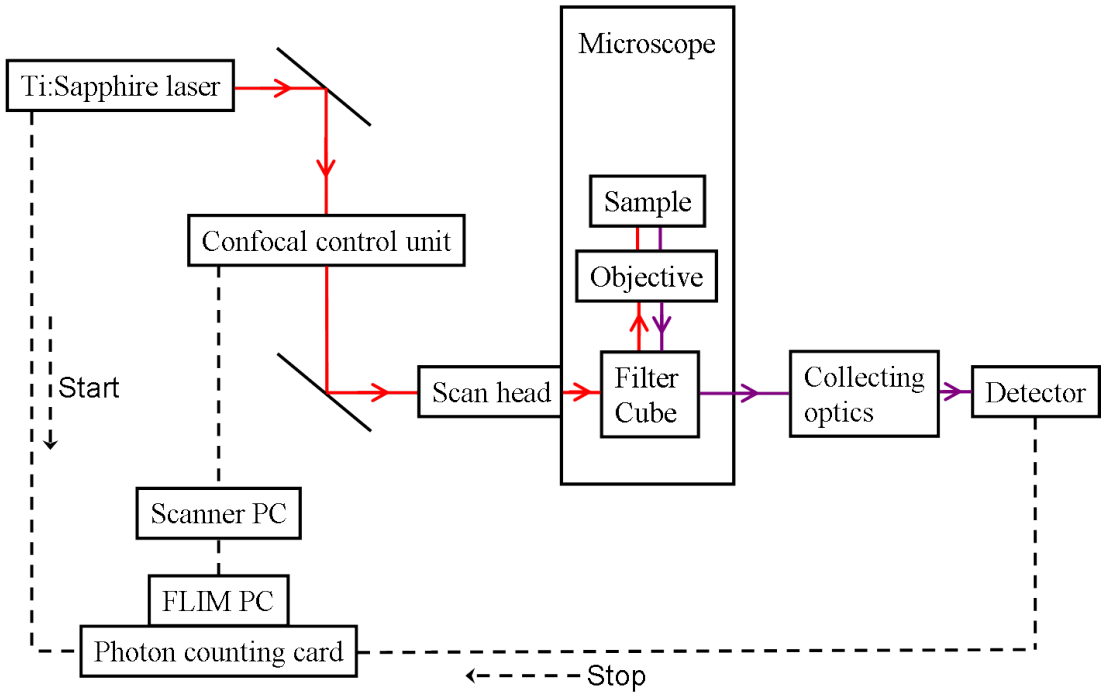

Figure 3-5: Schematic of the experimental setup used for 2PE-FLIM

The laser used is the same model as the one described Chapter 3.2. Its output, at 720 nm and 76 MHz is used to excite the sample. The beam was reflected by a dichroic mirror and focused in the sample using a microscope objective (Nikon, x20 Dry, 0.5NA). The focus was scanned in the sample using a scan head controlled by a software (Biorad Radiance 2100). The fluorescence was collected by a lens and filtered through a pair of fluorescence filters (shortpass 680 nm and 525 nm bandpass, Semrock). The light detector was a fast PMT (PMH100, Becker & Hickl GmbH) with response time of about 150 ps at FWHM [104]. The start signal was

given by the laser through a pulse inverter, and the stop signal from the PMT output. The TAC of the photon counting card (SPC-730, Becker & Hickl GmbH) is activated on reception of a stop signal and measures the time interval until the next laser pulse (reverse mode operation). X and Y synchronising pulses from the scanning unit feed the photon counting card to synchronise data collection. The accumulation of arrival times of photons are registered pixel-by-pixel with the laser scanning.

3.4.2 Experimental parameters

The photon counting card is installed with a software package (SPCM, Becker & Hickl GmbH) preset by the manufacturer to operate the desired module (SPC-730, Becker & Hickl GmbH). Figure 3-6 is a screenshot of the control system parameters used in this work together with the user interface showing the raw image of a microfluidic T-junction.

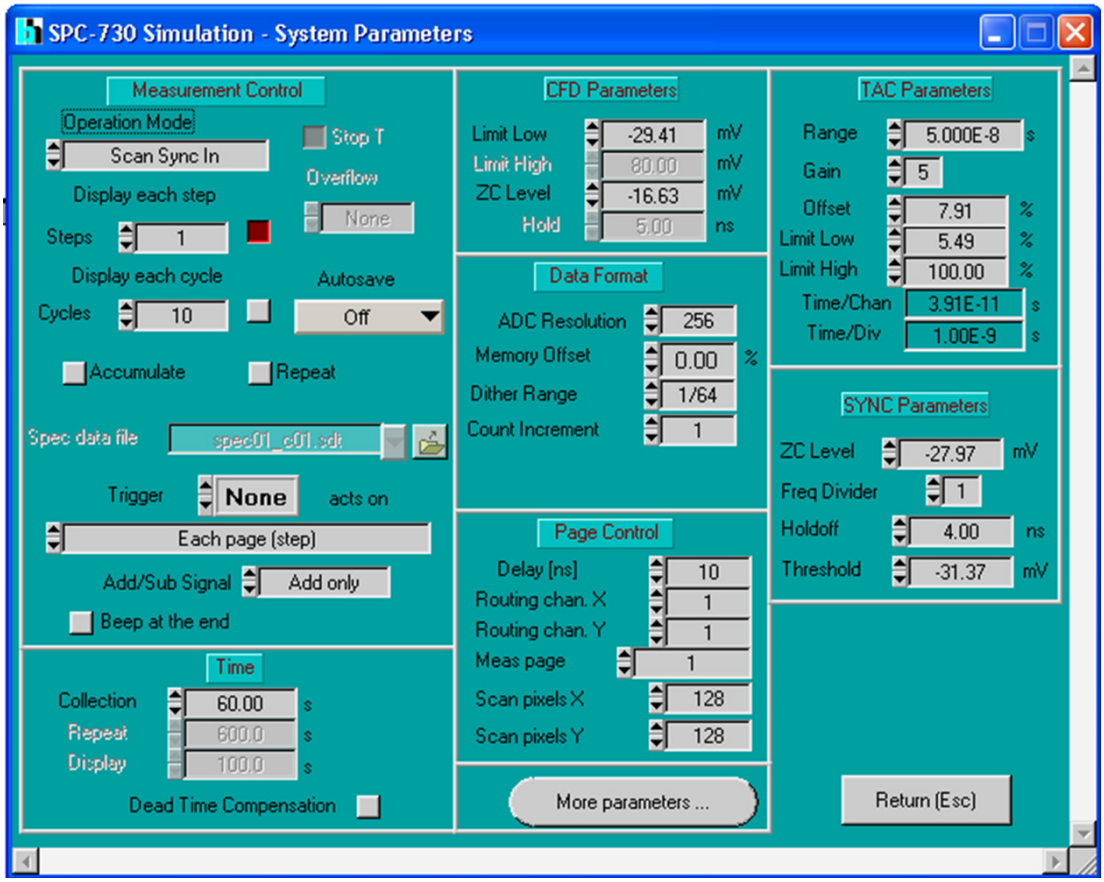

Figure 3-6: System parameters of the photon counting module.

The TAC was operated with a 10 ns range and the arrival times of photons accumulated in 256 channels resulting in a resolution of 0.04 ns per channel. A final image was generated after averaging 10 times the arrival time of photons for 60 s in a 128x128 pixels grid. The number of pixels in the x and y range was set to match the number of point the scanner scans. On the top left of the window shown Figure 3-6, the operation mode 'Scan Sync In' indicates that the counting module was triggered by the pixel clock of the scanner control unit Figure 3-5. A pseudo-real time operation mode is also available ('Oscilloscope') and was used while setting up the experiment to make sure there was no ostensible anomaly in the photon arrival time distribution.

In the main panel of the software (not shown), the synchronisation count rate must match the repetition rate of the laser (76.1MHz) and the TAC detection frequency was kept below 300kHz to ensure: a sustained count rate (preventing saturation of data transfer); protection of the PMT (by placing neutral density filters in the collection arm of the beam path); and to cope with the timing required to correctly record photon arrival time distribution (Stop rate $\leq$ 1% x Start rate).

3.4.3 Fluorescence lifetime maps

Fitting of the decay pixel-by-pixel was performed as described chapter 3.2 by a data analysis software (SPCImage, Becker & Hickl GmbH). The raw data are displayed as an intensity image, spatially resolving the sum of photons recorded on each pixel and pseudo-coloured to show the variation of intensity across the image. The decay curve at each pixel was tail-fitted to a single exponential decay and the FLIM image was displayed using a pseudo-coloured scale according to the curve fitting results.

3.4.4 3D image stacking using ImageJ

FLIM images of the devices were generated at different depth. In order to generate a 3D map of the microfluidic device, the images were stacked using a Java image processing program (ImageJ, [105]).

3.5 Micro-Particle Imaging Velocimetry

Micro-PIV measurements were performed using a Dantec system. The setup consisted of three main parts, the hub (FlowMap System HUB, Dantec), the camera (HiSense PIV/PLIF, 12 bit, Double frame, Dantec), and the illumination source (Micro-Strobe, Dantec). The microfluidic device used was a custom-built device described in Chapter 3.7. The tracking particles were polystyrene microspheres of 2 μm diameter kindly fabricated and donated by Dr. Rosario Sanchez-Martin and Juan Manuel Cardenas-Maestre [106].

3.5.1 Illumination

The seeded flow in the microfluidic device was imaged using transmitted light from a pulsed green LED emitting at λ_{max} = 530 nm with a FWHM of 35 nm (retailer specifications). A band pass filter (FF01-514/30-25, Semrock) was used in front of the source in order to attenuate the wings of the spectrum. The normalised LED emission spectrum and the emission filter normalised transmission are presented Figure 3-7.

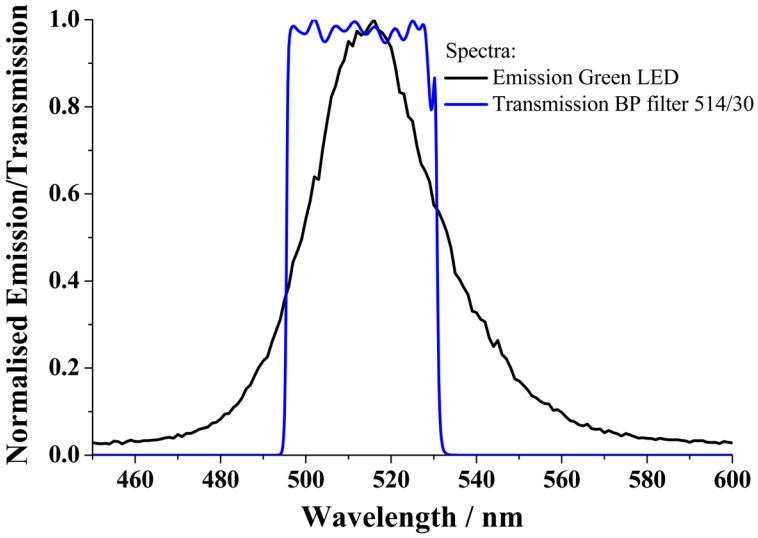

Figure 3-7: Normalised emission spectrum of the illumination source used in the μ-PIV setup (green line), and normalised transmission spectrum of the emission filter (red line) used to filter out the wing of the illumination spectrum.

As observed, the actual emission maximum of the LED is around 515 nm. Although the FWHM is quite narrow, the wings of the illumination spectrum are broad and need to be filtered for the µ-PIV illumination to avoid interference with fluorescence measurements.

A schematic representation of the µ-PIV setup is presented Figure 3-8.

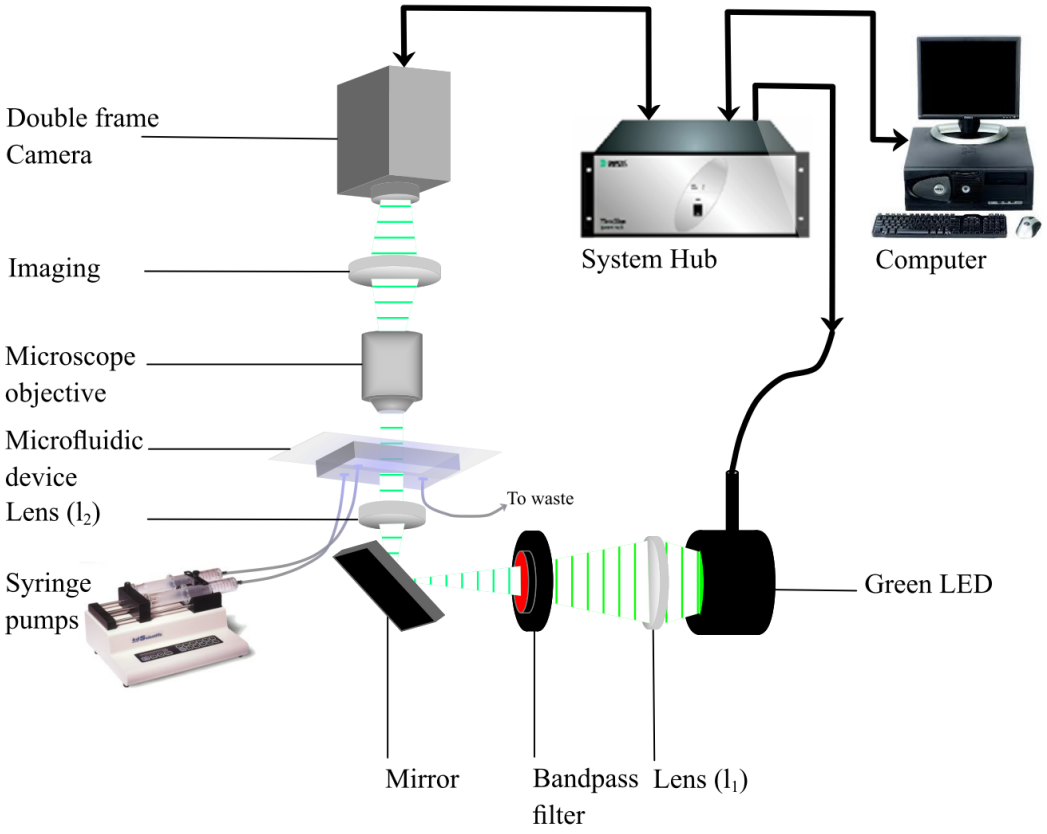

Figure 3-8: Schematic representation of the µ-PIV experimental setup.

The LED source is mounted underneath the 'xyz' microscope stage used to support and position the microfluidic device. An image of the source is created by a lens l_1 at the back focal plane of lens l_2. The lens l_2 image the source at infinity. The light is collected by a microscope objective (x20, NA0.4, LMPlanFI, Olympus). An achromatic lens, l_3 (EFL300, BFP298, NT45-125, Edmundoptics) was used to create an image of the microfluidic device on the camera.

3.5.2 Timing setup

The camera and the illumination source are controlled by the hub the parameters of which were setup before operation. The camera is mounted on the microscope using a C-mount. It is a double-frame CCD camera with a detector consisting of 1280x1024 pixels. The double frame consists of 1280x1024 light-sensitive cells and an equal number of storage cells. The CCD is exposed to the first LED pulse. As soon as the exposure time of frame 1 is finished, the resulting charge of the CCD is transferred to the storage cells. The CCD is exposed to the second LED pulse. The two frames are then transferred to the PIV processor. The exposure starting time and the delay between frame 1 and frame 2 is set up on the computer prior to recording. A schematic of the timing of the system is presented Figure 3-9.

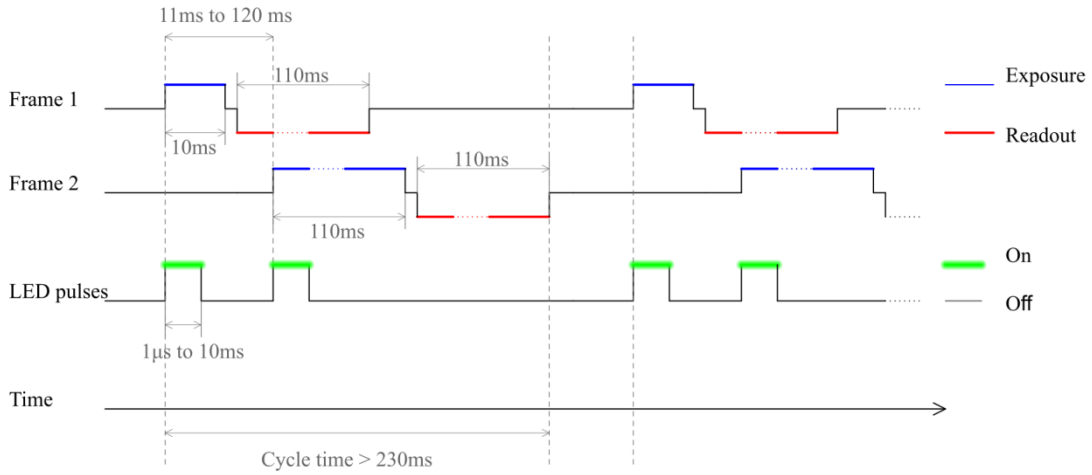

Figure 3-9: Double frame camera and LED timing.

The pulse length (from 10 µs to 10 ms) and the repetition rate (1 Hz to 4.3 Hz) of the LED as well as the time interval between two pulses forming a pair are set by the user on the computer. The length of the pulse determines the contrast and the sharpness of the tracked particles of the image. While long pulses can be used to image relatively slow flow and give a large contrast, short pulses need to be used for faster flow in order to resolve the particle.

The exposure time of frame 1 and frame 2 are fixed. They are 10.9 ms and 110 ms respectively. Therefore, it is important to set the timing for an equal amount

of light to reach the two frames. Background light should be kept to a minimum and the first pulse has to entirely reach the detector within the exposure time of frame 1. Unacceptable amounts of background light or problem in the timing setup results in frame 2 being overexposed (white image) and frame 1 underexposed (black image). The time interval between two pulses is set for the seeded particles to move by a maximum of 20% of the interrogation area. The size of the interrogation area is determined when generating the flow field map. A cycle corresponds to the time it takes for the two frames to be recorded and read. The minimum cycle time is 230 ms which corresponds to the sum of the exposure time of frame 1 (10.9ms), the exposure time of frame 2 (110ms) and the readout time of frame 2 (110ms). Therefore, the maximum repetition rate is 4.3Hz.

3.5.3 Image Recording and Processing

An image set consists of 80 image pairs (160 images). Figure 3-10 illustrates the principal steps required to generate a flow field map. The contrast of the recorded images is adjusted by calibration of the greyscale until the particles are visible. A mean image is created by averaging the value of each pixel over the 160 images. The mean image is then subtracted from each image. The result is a map where the particles appear as black dots on a white background (Figure 3-10.b). The size of the interrogation areas has to be determined for the software to be able to correctly map the flow field. A particle should not move by more than 20% of the interrogation area within the time interval between two pulses.

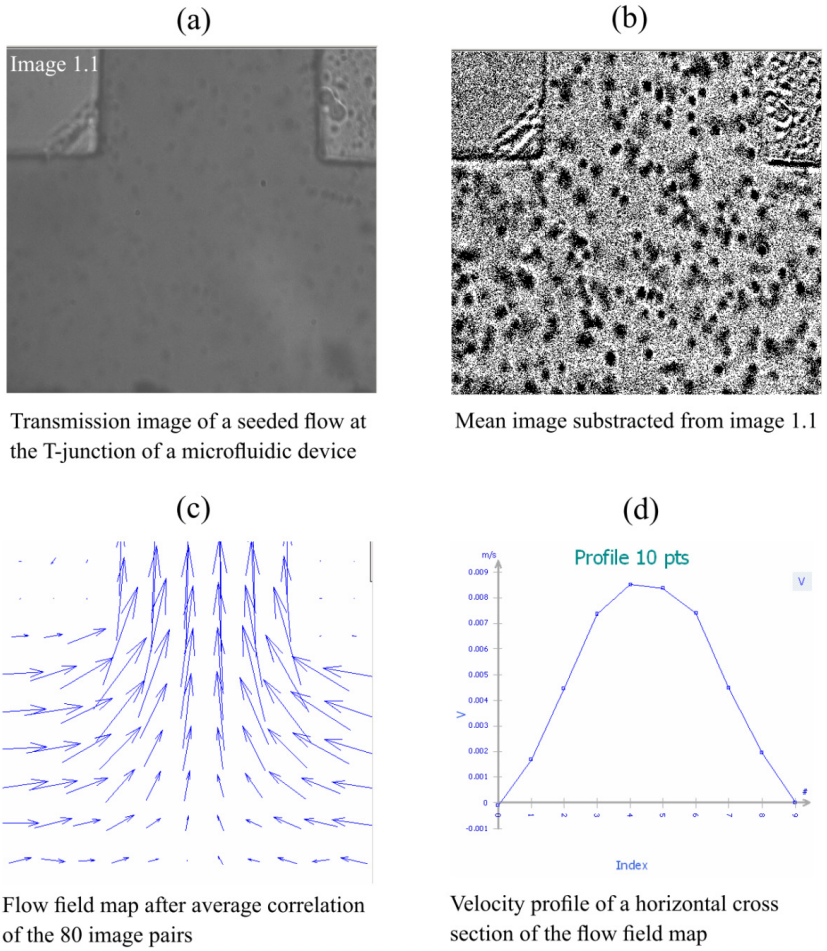

Figure 3-10 Generation of a flow field map. Raw image (a), image filtered by subtraction of a mean image (b), flow field map (c), velocity profile across the channel (d).

The displacement of the particle is approximated from knowledge of the flow rate, device cross section dimensions and time interval between two pulses using Equation (3-7):

$$d_p = \frac{16.7 \times FR \times \Delta t_p}{W \times H} \qquad \textbf{(3-7)}$$

where d_p (in µm) is the approximate distance that a particle will have travelled during the time interval Δt_p (in µs), the time between two pulses generating an image pair, FR is the flow rate imposed by the syringe pumps (µl.min^{-1}), W the width of the microchannel (in µm) and H its height (in µm).

The distance in micrometers is then converted into distance in number of pixels. The interrogation area is a rectangle the horizontal and vertical dimensions of which can be chosen between 16, 32, 34, 128 or 256 pixels. Because some particles will move from one interrogation area to the other, the interrogation areas need to be overlapped by at least the maximum displacement of a particle, ca. 20%. Once those parameters are correctly calculated, the program performs an average correlation for each interrogation area on the 80 images pair and generates a flow field map (Figure 3-10.c) from which the flow velocity across the device can be extracted (Figure 3-10.d). When necessary, filtering of the images and of the flow field maps can be applied such as range confirmation, averaging filters, and spatial masks. Finally, the flow is seeded with polystyrene beads so that at least 20 of them are seen in one interrogation area over the entire image set.

3.6 Open-frame microscope

Multimodal imaging microscopy is increasingly required to gather complimentary set of data. It has already been extensively used by researcher to gain multi-parametric insight into the system under study: multimodal imaging has been used in biology for the study of convective oxygen transport by microvessels using fluorescence laser scanning microscopy, spectral imaging and red blood cells flux imaging [107]; the successful combination of holographic optical tweezers and coherent anti-Raman spectroscopy has been demonstrated for the manipulation and imaging of cholesteric liquid crystals [108]; a system integrating total-internal-reflection fluorescence, epifluorescence, differential interference contrast and 3-D deconvolution imaging modalities with TCSPC and optical tweezer has been developed for the study of molecular dynamics in cell membranes [109]. The development of a microscope that allows nearly simultaneous measurements has also been reported [110].

Although it is of interest to a wide scientific community, multimodal microscopy has not been accompanied by the commercialisation of suitable microscopes. Therefore, multi-parametric experiments require: the development of

optical setup on a floating table around the microscope body [107-110], or the sample to be moved between different microscopes having different capabilities [111]. Furthermore, the rigidity of the microscope usually impedes the simultaneous use of microscopic techniques requiring different illumination sources, detectors, cameras and detection wavelengths. Finally, the complexity of experiment-specific setup requires the expertise of optical scientist each and every time a new modality is implemented. In order to overcome the aforementioned limitation of commercially available apparatus, an open-frame microscope platform that permits: flexibility of the setup; simultaneous use of multiple techniques; and ease of optical alignments, has been fabricated. The use of the platform to combine optical tools and microscopic techniques will be discussed in Chapter 6 and 7 of this thesis. The principal fixtures of the microscope are presented below.

The microscope is designed around a high-precision slotted aluminium platform mounted 20 cm above the optical bench. A schematic of the platform is shown Figure 3-11.

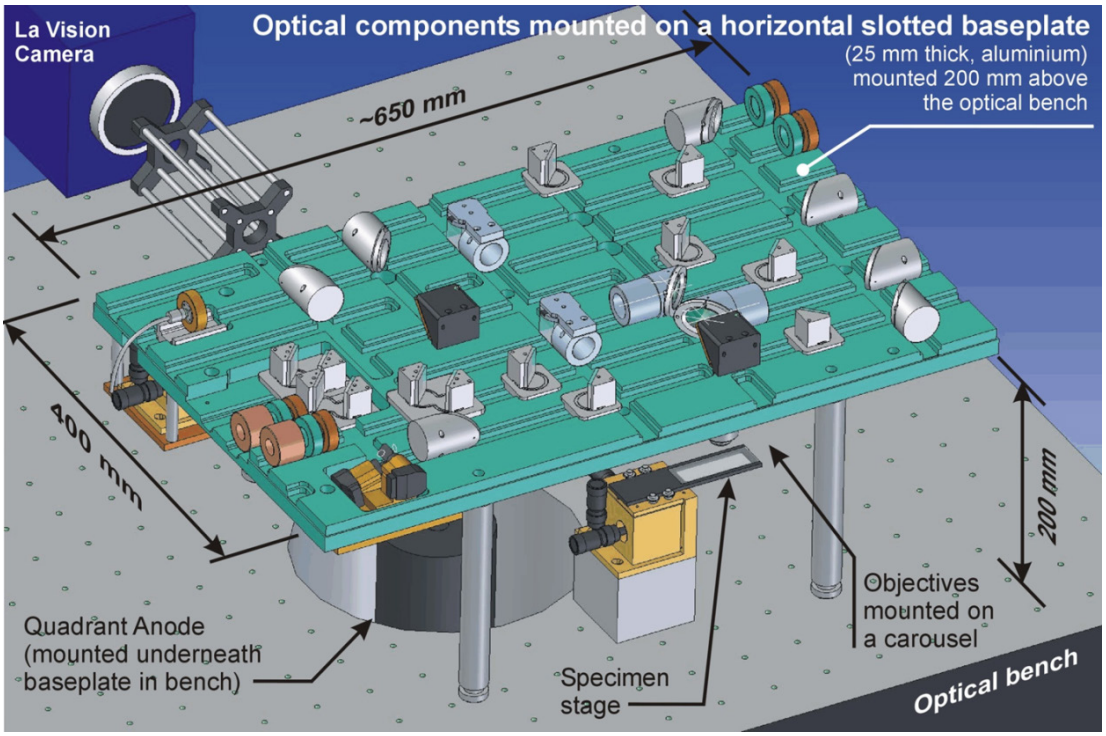

Figure 3-11: CAD image of the open-frame microscope [112].

The light sources and the microscope stage are mounted on the optical bench and the light coupled onto the microscope using telescopic mirrors. The cameras and detectors are held on the edge of the platform by cage plate adapter (SP05, Thorlabs), assembly rods (Thorlabs) and C-mount adapters (Adapter C-Mount/Microbench, Linos). A carrousel is mounted on the platform and accommodates up to three microscope objectives. On the platform, the optical components are held in slots by magnets (Figure 3-12) providing a convenient and robust semi-kinematic mounting system, flexibility in component location and ease of alignment.

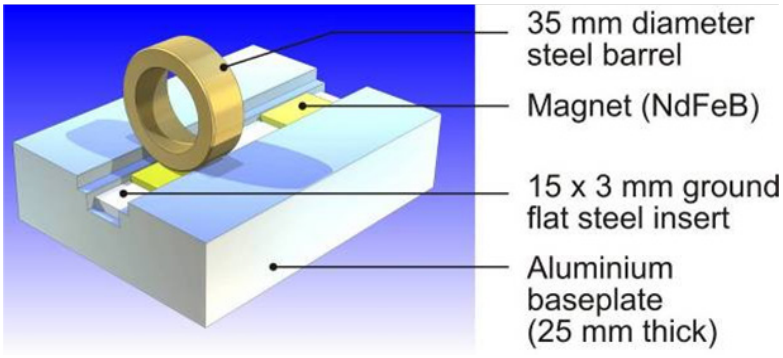

Figure 3-12: Schematic a barrel held in place by a magnet in the slot [112].

On the platform, mirrors are mounted on customised commercially available kinematic mirror mounts (KMS, Thorlabs) or on custom-build kinematic mirror mounts as shown Figure 3-13.

Figure 3-13: Pictures of custom-made kinematic mirror mounts.

Different setups have been implemented on the platform. They are described in details in relevant chapters.

3.7 Microfluidic device design and fabrication

3.7.1 Design of the chip

Early microfluidic devices were made from hard materials such as silicon or glass. Among the drawbacks these characteristics impose, the techniques required to fabricate devices presented some large technical and financial barriers for the rapid development of prototypes by researchers outside electronic engineering. In 1998, Whitesides and Xia [12] published a paper that would revolutionise the fabrication of microfluidic prototypes. Their technique, *soft lithography*, allows the fabrication of chemically inert, optically transparent (240 nm to 1100 nm) and disposable microfluidic devices with control over the chemistry of the surfaces. In this work, soft lithography has been used for the development of a microfluidic device that allows the control of the temperature gradient across the channel independently of analyte flow rate. As will be discussed in Chapter 6, the limitations of the micro-particle imaging velocimetry system used and the prominence of heat flux due to convection in microfluidic devices motivated the development of a custom device.

The microfluidic device design was drawn using CAD software (Autodesk®, Autodesk, Inc.). A few limitations must be taken into account when designing the device. The features size cannot be smaller than the resolution of the lithography technique used to fabricate the mould (~1μm). The feature aspect ratio, width divided by depth or length divided by depth, must be between 0.2 and 2 [113]. When the aspect ratio is too high or too low, the elastomeric character of the polymer used will cause the microstructures in the device to deform or distort and generate defects in the pattern [12]. Finally, sufficient space must be left around inlets and outlets to accommodate tubings feeding the device and support the pressure imposed by the syringe pumps. Figure 3-14 shows the design of a microfluidic chip and the corresponding mask used, as described hereafter.

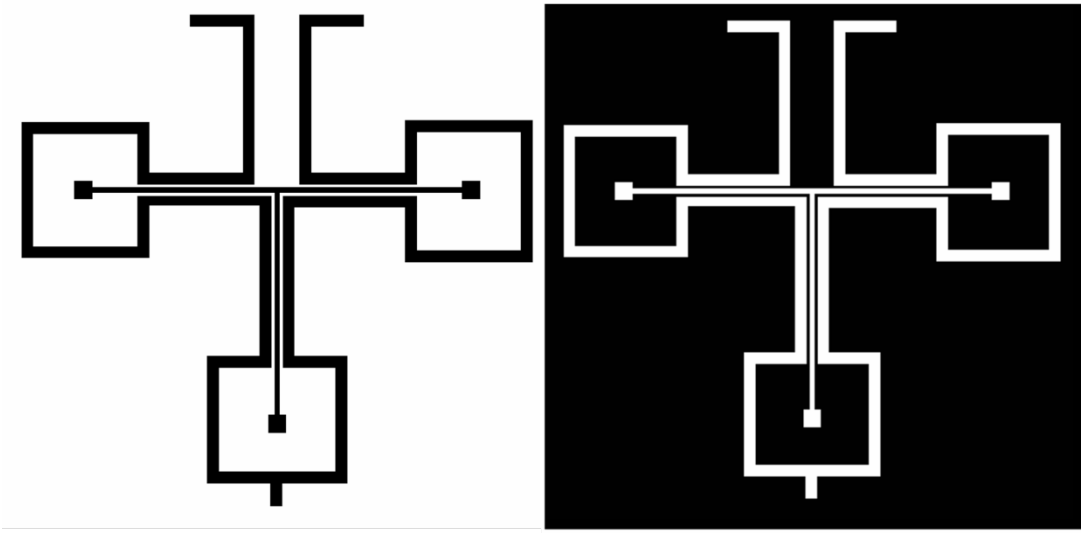

Figure 3-14: Design of the chip (left) and mask used for photolithography (right) of the mould.

3.7.2 Fabrication of the microfluidic device

A master used as a stamp to pattern the microfluidic device is fabricated by photolithography of a negative photoresist polymer (SU8-2025, Microchem, Newton, MA) spin-coated onto a silicon wafer. The photoresist is patterned by UV-light exposure through the mask shown Figure 3-14 (right). The exposed regions harden and the wafer is developed (Propylen Glycol Monomethyl Ether acetate, Microchem). The wafer is then cleaned using isopropanol, dried using a nitrogen gun, and treated with fluorosilane (1H,1H,2H,2H-Perfluorodecylthriethoxysilane, Sigma-Aldrich) to prevent adhesion onto its surface. The master is then placed in a glass Petri dish. The next steps of the fabrication are shown Figure 3-15.

A silicon polymer (Polydimethylsiloxane (PDMS), Sylgard 184, Dow Corning Midland, MI) is poured into the dish containing the master as shown Figure 3-15 (top right). The PDMS is first mixed with a hardener in a 10:1 ratio, the mixture is homogenised by manual mixing and then degassed in vacuum until all trapped air bubble are removed. The vacuum step is repeated after pouring the PDMS mixture onto the master. PDMS is then cured for 2 hours at 65ºC, peeled from the master and cut to size. Holes are punched (Harris Uni-Core) for future connection with tubing. The device is finally exposed to oxygen plasma together with a microscope coverslip (L4239-1, Agar Scientific Ltd, England). After oxygen plasma exposure, the

coverslip is irreversibly bound with the exposed side of the PDMS chip (the side with engraved features).

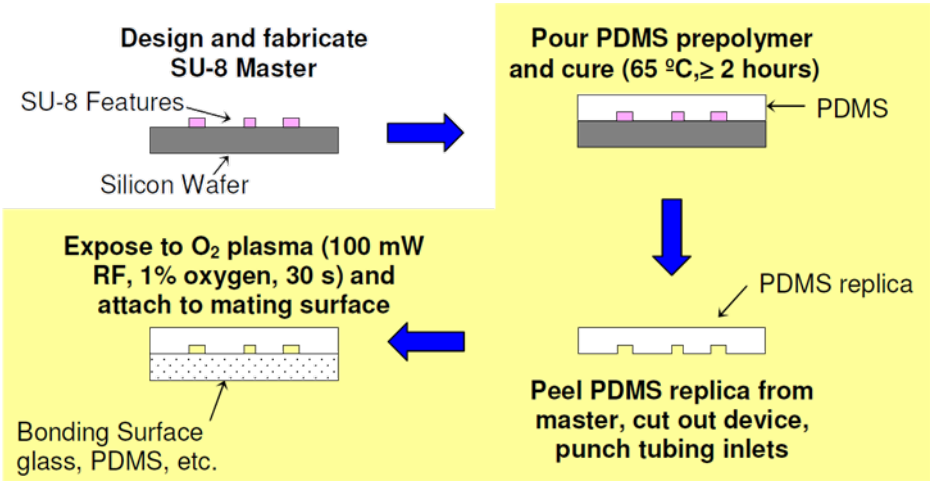

Figure 3-15: Step-by-step fabrication of a microfluidic device made of PDMS.

After oxygen plasma treatment, PDMS is very hydrophilic but gradually recovers hydrophobic properties after a few hours [114]. In order to stabilise the hydrophilicity of the surfaces, the device is treated with APTES (3-aminopropyltriethoxysilane, Sigma-Aldrich). The treatment (0.1 ml APTES in 0.5 ml HPLC grade water and 9.5 ml ethanol) is flowed in the device for 30 min. The device is then rinsed for 30 min with pure ethanol. The final composition of the device surface is shown Figure 3-16.

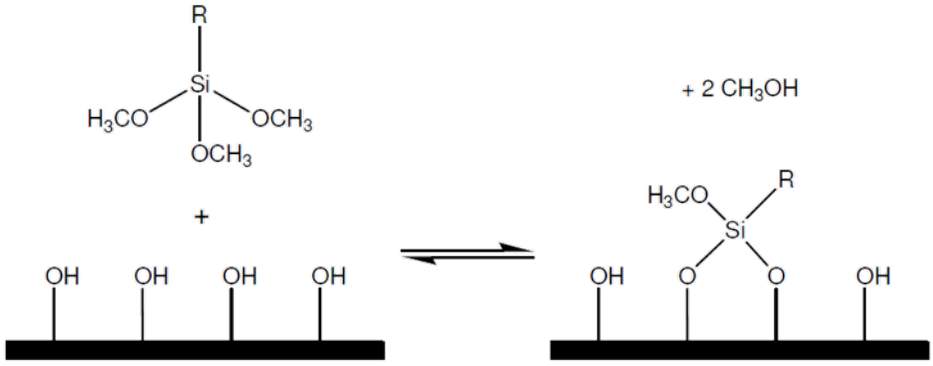

Figure 3-16: Surface treatment of the microfluidic channels. PDMS after oxygen plasma (left), PDMS after APTES treatment (right).

3.7.3 Device operation

Once mounted, the device was filled with the sample solutions and the liquids controlling the temperature across the microchannel by two double-barrel syringe pumps so that the flow rate in the microchannel is independent from the flow rate in the channel controlling the temperature. Details of the device operation are given in Chapter 6.

4 PROBING pH IN A MICROFLUIDIC DEVICE USING WIDE-FIELD FLUORESCENCE LIFETIME IMAGING MICROSCOPY

4.1 Introduction

Mapping of pH in microfluidic devices is of particular importance for the control of biochemical processes [115-117], the evaluation of the mixing properties of a device [51] and the study of flow dynamic properties at the microscale [118]. The present chapter describes the fluorescence of fluorescein (fluorescein sodium, Fluka) and C-SNARF (5-(and-6)-carboxy SNARF®-1, Invitrogen) in phosphate buffer saline (PBS) solutions from pH 6 to pH 8. Use of these dyes in combination with FLIM allows the imaging of pH gradient in a T-injection microfluidic device. Two different FLIM detection techniques are evaluated: time- and space-correlated single photon counting (TSCSPC) for the mapping of pH gradient in a microchannel using C-SNARF as pH indicator and time-gated detection when using fluorescein as pH indicator. The TSCSPC technique has been used to map the relative contribution of the acidic and basic forms of C-SNARF and its capability compared with the more commonly used time-gated technique.

4.1.1 Importance of pH measurement in microfluidic devices

Because of their scaled down size and their monolithic properties, microfluidic devices do not permit access of conventional apparatus for pH measurements. The pH is nevertheless a critical factor for controlled chemical reactions. It is of uppermost importance in microfluidic devices for the synthesis of nanoparticles [117], detection of protein-ligand binding [116], biofabrication of membranes [115], chemical synthesis [119], and the generation of monodisperse

microbubbles [120]. The potential practical applications that require the measurement of pH, especially in medicine, are numerous. Foetal blood tests are performed to determine the well-being of a baby, and blood pH tests are utilised to evaluate the susceptibility of blood cells to cancer development. Furthermore, urine pH tests can be utilised to investigate problems of gastric suction, kidney failure, kidney tubular acidosis, urinary tract infection, diabetic ketoacidosis, alkalosis, interstitial nephritis, acidosis, and sepsis. The implementation of microfluidic technology in diagnostic devices requiring the measurement of pH would reduce the sample volume and the analysis time. Due to their small size, miniaturised systems incorporating microfluidics have potential in field analysis either as handheld devices or as components of mobile laboratories for both point-of-care and forensic applications [121].

4.1.2 Previous measurement of pH in microfluidic devices

The challenge of pH sensing in microfluidic devices has been tackled by researchers from different backgrounds with different techniques. However, two main categories of detection prevail. Electrochemistry is used by one section of the scientific community, while the other section favours fluorescence detection techniques. Measurement of pH by electrochemistry is realised by the implementation of micro-electrodes or ion-sensitive field-effect transistors (ISFET) in the microfluidic system. They are the miniaturised equivalent of electrodes and FETs used in conventional apparatus. The size of the detector has simply been reduced to cope with the size of microfluidic devices.

Lin *et al.* [122] fabricated microelectrodes by sputtering an oxide-sensing layer onto platinum (Pt) electrodes and a reference electrode by deposition of AgCl onto a silver coated glass substrate. The reaction between the sample and the sensing electrode produces a change in chemical energy which produces a change in the potential between the two electrodes. Sensitivity close to conventional apparatus was observed. The main inconvenience of this technique is the dependence of the sensitivity on the size of the electrode (width needs to be controlled to ±20 nm). Furthermore, different pH values are obtained depending on whether the pH is

ramped from basic to acidic or acidic to basic. Finally, the sample reacts with the micro-electrode making the technique invasive, and the fabrication process is much more complex than for standard PDMS chips.

Douglas *et al.* use a difference in acidification rate to discriminate between cancerous and healthy mammalian cells. They used microelectrodes in a microarray to capture and analyse the cells [123].

Difficulties encountered when scaling down microelectrodes [124] has encouraged scientific workers such as Cheng *et al.* to develop ISFET for microfluidics based on metal-oxyde-semiconductor field-effect transistor technology (MOSFET). In the case of back-gated ISFET, the system does not need a reference electrode and the gate is not in electrical contact with the analyte, only a SnO_2 nanobelt channel is actually in contact with the solution. Upon protonation/deprotonation of the belt, the field effect response of the device is proportional to the pH [125]. Although much less invasive than the electrochemistry based on microelectrodes, ISFETs are based on a reaction with the chemical environment. Furthermore, as for microelectrodes, the fabrication of microfluidic devices with an integrated FET based technology is relatively complex. Finally, the semiconductor does not have a linear response to pH over its operating range and has strong dependence of its response on ion concentration.

Electrochemistry at the microscale requires micro-engineering, is invasive and is not able to resolve point measurement or map pH in microfluidic devices. In order to overcome some of these problems, researchers chose to use fluorescence techniques to probe pH at the microscale. Colorimetry has also been used, although rarely, to show the generation of pH gradient [115] or as proof of concept for inkjet-printed microfluidic sensing paper [126]. The most common fluorescent techniques reported use a variation of the fluorophore intensity upon pH change [117-119, 127, 128]. Fluorescence ratiometry [129, 130] and anisotropy [131] have also been used.

Lee *et al.* [127] have developed a fluorescent hydrogel microarray that allows the measurement of pH and oxygen. Sensitivity of the fluorescence intensity of carboxyfluorescein-dextran conjugate to pH was calibrated. Images of the microarray

were recorded using a CCD camera. In order to determine a final pH value, intensity data from a rectangular region (50 x 70 pixels) at the centre of three wells were extracted and averaged. Thete *et al*. [119] reported a microarray that allows the assessment of solvent polarity and pH. The pH was assessed by the change of fluorescence intensity of fluorescein and rhodamine with change of pH. These studies show that fluorescence intensity is suitable for pH measurement in micro-arrays. However, it is not appropriate for spatially resolving the pH values in each individual well.

Shinohara *et al.* [118] used quinine in a laser-induced fluorescence (LIF) setup to measure the pH at the Y-junction of a microfluidic device. The main drawback of the intensity technique can be observed from their work with a pH map dependent on the homogeneity of the excitation beam and the need for averaging images to obtain consistent results. Their experimental results diverge from CFD simulation, especially at low flow rate.

To study the change of pH induced by microelectrodes in a microchannel, Klauke *et al.* [130] used the relative fluorescence of C-SNARF-1-labelled beads that were optically-trapped at discrete points. The sensitivity of the technique is very limited due to the small relative change of the fluorescence intensity (0.08±0.01 for 1 pH unit) with pH and low signal-to-noise ratio (SNR).

To sense the pH in a microchannel, Mela *et al.* [128], immobilised rhodamine B and Oregon Green 514 onto a glass surface modified with 3-aminopropyltriethoxysilane (APTES). This leads to a less invasive probing of the analyte but limits the study to the fraction of solution which is in contact with the glass wall of the device. Furthermore, the use of a confocal setup with intensity-based detection does not allow the generation of an accurate quantitative mapping of the pH.

Abou-Hassan *et al.* [117] used fluorescence confocal laser-scanning microscopy along with fluorescein to map the pH in a microreactor. Although computational and experimental results shown agree well with each other, this technique, which is based on spatially resolving the concentration of fluorescein di-

anion in the device, exhibits low SNR and only allows identification of the region of high pH. Change in local concentration of the probe and of the acid and base (present in the device at high concentration) would seriously hamper quantitative mapping of pH in the entire channel.

Fluorescence intensity-based techniques are impeded by variation in the optical path, uncertainty in the dye concentration, lack of spectral stability or spatial homogeneity of the excitation source and photobleaching effects. Ratiometry techniques can circumvent some of the aforementioned problems. However, this requires a cumbersome and time-consuming calibration procedure [132]. Electrochemical based techniques can only achieve micro-bulk measurements and are invasive.

FLIM is a particularly attractive alternative for quantitative pH imaging in micro-systems. The probes available for intensity or ratiometric pH imaging are not all suitable for pH imaging using FLIM. However, a few of them have been identified, characterised and successfully used to quantitatively image pH distribution in cells [132-134].

4.1.3 Photophysical properties of the fluorescence lifetime pH probes

The protonation OH group of fluorescein observed on the structure of the monoaniom form, shown Figure 4-3 leads to large change in fluorescence intensity. The geometrical structure of the two forms of fluorescein present in solution in the pH range relevant to this work is very similar. However, in the deprotonated state, fluorescein is symmetric while the protonation of the oxygen leads to an asymmetric molecule. Tamulis et al. [135] have shown using quantum mechanical *ab initio* Hartree-Fock and density functional theory investigations applied with the Berny geometry optimisation that despite of the similarity of the geometrical structure, the monoanion and dianion forms exhibit completely different electronic structures. Upon excitation, the dianion will dissipate energy by molecular rotation and vibration until the molecule returns to the first excited state from which de-excitation to the ground state by emission of a photon is more probable than relaxation of the

rotation and vibration. Due to symmetry lowering, the forbidden transition states of the dianion are allowed in the monoanion and as a consequence, the absorbed energy will be distributed between them. Furthermore, the oscillator strength of the first excited state of monoanion is smaller than that of dianion and the energy gap between the second and first excited state is larger in the monoanion than that in dianion. Therefore, the fluorescence quantum yield of the monoanion is smaller than that of the dianion because of the larger radiationless energy dissipation. Although there are no accounts in the literature to how this may affect the fluorescence lifetime of the monoanion, the increase of radiationless de-excitation paths will lead to an increase non-radiative rate constant which is typically accompanied by a decrease of the fluorescence lifetime of fluorophores according to Equation 2.8.

The difference in fluorescence properties between the protonated and deprotonated forms of C-SNARF dyes, shown Figure 4-9, has been attributed to a larger delocalisation of the electron density on the 10-position nitrogen into the π-electron system of the fluorophore in the acidic form than in the basic form. This results in the twisted molecular charge transfer complex in the excited state playing a larger role in the quenching of the acidic form than in the basic form [136].

4.2 Experimental setup and procedures

4.2.1 Solution preparation

For the calibration of the fluorescence lifetime of the dyes against pH, PBS buffers in the range pH 6 to pH 8 were prepared at 5 mM by dissolution of monobasic sodium phosphate dihydrate (Sigma-Aldrich) and dibasic sodium phosphate (Sigma-Aldrich) in HPLC grade water. Aliquots of dye solution were then added to the buffers to reach a concentration of 10μM for the fluorescein (Sigma-Aldrich) and 20μM for SNARF (Invitrogen - Molecular Probe). The pH of the solutions was then measured using a 3-point calibrated pH-meter (Orion 3-Star pH benchtop meter, Thermoscientific).

In order to image the generated pH gradient in the T-mixer, fluorescein solutions were prepared at 200 μM and appropriate masses of the monobasic and dibasic salts were added to reach a concentration of 5 mM of PBS in the solution. Buffer concentration was deliberately chosen to be low to avoid a monoanion-dianion excited state proton transfer reaction that would render the fluorescence lifetime of the monoanion and dianion forms of fluorescein pH-dependent [137]. The acidic solution was measured as pH 6.6 and the basic as pH 7.6. C-SNARF solutions were prepared at 400 μM in 5 mM PBS buffers at pH 6.4 and pH 7.6.

4.2.2 Microfluidic device

The microchannels are made of silicon and covered with a silica coverslip for optical access. A schematic of the device used is given Figure 4-1.

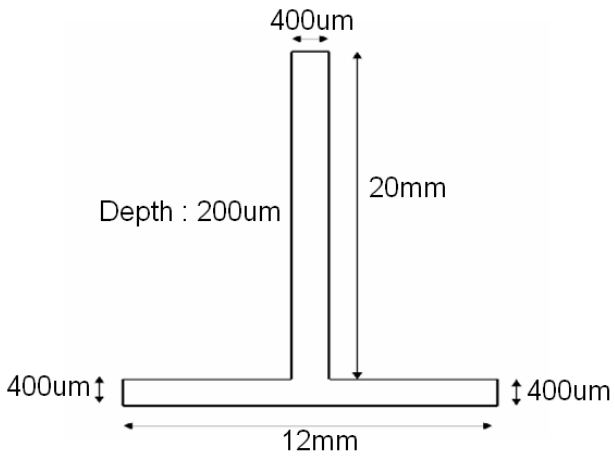

Figure 4-1: Schematic representation of the microfluidic device

Solutions of C-SNARF and fluorescein were loaded in 3 ml syringes and pressure driven through silicone tubing in the two inlets of the device. The syringes were attached to the tubing using dispensing tips (EFD) and the silicone tubing (AlteSil™ High Strength Silicone Tubing, Altec Products Ltd, UK) was attached to the nanoports of the device using the corresponding threaded tips. The acidic solution was pumped through one of the two arms of the T-junction and the basic solution through the other arm. Tubing, tips and syringes were disposed of after each experiment. The device was rinsed thoroughly before and after any experiment using ethanol and water. The cleanliness of the device was assessed by recording FLIM

images when the channel was filled with a solvent alone and ensuring no fluorescence could be detected.

4.2.3 Calibration of the fluorescence lifetime of the probes

Calibration of the fluorescence lifetime of the dyes against the pH of the PBS buffers was performed using the time-correlated single-photon counting setup described in Section 3.2. The fluorescence lifetimes of the solutions were measured in 10 mm pathlength cuvettes (10x2 mm^2 precision cells made of quartz SUPRASIL®, Hellma®). The monochromator was set for a 10 nm bandwidth at 535 nm for fluorescein and 585 nm for C-SNARF-1. Decays were recorded to a maximum of 20000 counts in the peak channel, on 20 and 50 ns range and the count rate was kept below 40 kHz (1% of the excitation repetition rate) using neutral density filters. Global analyses (GA) were performed using FAST (Edinburgh Instruments) and the quality of the fit assessed by the reduced chi-squared parameter and visual inspection of residuals. Because they are constant, the different lifetime components were linked (common parameters to all the decays recorded for the solutions with the same fluorophore) to best model the contribution of the protonated and deprotonated forms of the dye to the fluorescence.

4.2.4 FLIM

4.2.4.1 Laser and fluorescence filters

The laser was tuned to 390 nm and 9 mW output power. A third of this power reached the back of the microscope. No excitation filters were used. The dichroic mirror was a DM455 (Nikon). Two objectives were used for this work: a x40 plan fluor and a x20 apochromatic.

4.2.4.2 TSCSPC

The data acquisition was performed in reverse mode, with each of the photon assigned to one of 4096 channels each of 27 ps width. The count rate was kept below 30 kHz for an acquisition time of ca. 10 min. Lifetime and A-factors maps were generated using QA-Analysis software (Europhoton GmbH, Berlin). The image was

set to have 200 x 200 points. After acquisition, time channels were binned to obtain 54 ps channels and twice as many counts in the peak channel. Decays were fitted from 300 ps after the peak of the decay to the channel where the signal to background ratio ≥ 10. The background was estimated by looking at area outside the channel where no fluorescence could be detected. The FLIM image is only a semi-quantitative representation of the fluorescence lifetime in the channel as it is limited to mono-exponential decay analysis. However, decay curves were exported from the FLIM image and analysed using FAST for quantitative determination of the pH at discrete points across the microchannel. The lifetime components determined by global analysis were subsequently used in the image analysis software to generate A-factor maps.

4.2.4.3 Time-gated camera

The exposure time of the camera was set to 200 ms, the gate width and delay steps 500 ps on a 45 ns range. An image results from averaging 5 separate exposures employing 4 x 4 hardware binning. The lifetime value assigned to a pixel is the average value of 9 pixels (8 surrounding pixels plus the assigned pixel). The excitation intensity was adjusted using neutral density filters to give a maximum of 3500 counts per pixel. The fluorescence images were analysed using the software running the camera module (Davis 6.2, LaVision GmbH, Berlin). FLIM images were obtained by constructing a decay curve for each pixel, taking into account the background counts ca. 50, starting the fitting 1 ns after the peak and stopping it when the decay had reached 10% of its peak value. The lifetime map was produced by assigning a colour on a 16-bit pseudo-color scale to the fitted single exponential decay times. Decay curves were exported from the FLIM image and analysed using FAST for quantitative determination of the pH at discrete points across the microchannel.

4.3 Results

4.3.1 Fluorescence characteristics of fluorescein

Fluorescein is one of the most commonly used fluorophores in microscopy. In solution, it can exist in four prototropic forms in the pH range 1-10 [137, 138]. As shown Figure 4-2, fluorescein has a maximum absorption intensity at 490 nm and a maximum fluorescence emission at 512 nm.

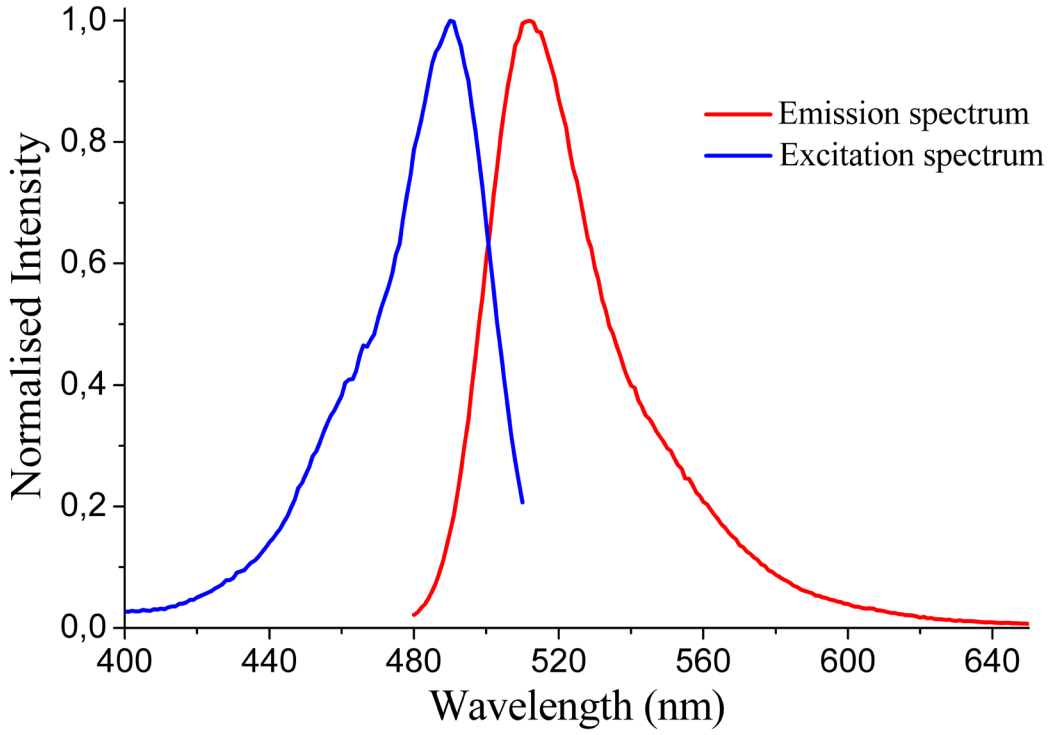

Figure 4-2: Excitation and emission spectra of fluorescein in an aqueous solution.

In the pH range 6-10, only the monoanion and dianion forms contribute to fluorescence emission [137]. The chemical structures of these two forms of fluorescein are shown in Figure 4-3.

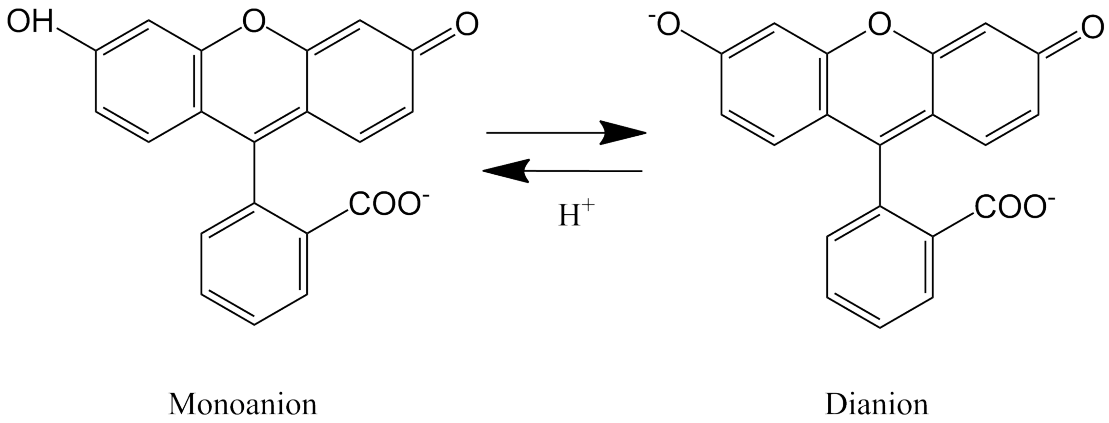

Figure 4-3: Chemical structure and ground-state proton reaction of the fluorescein monoanion and dianion.

Their presence can be determined by an analysis of the spectra shown in Figure 4-4.

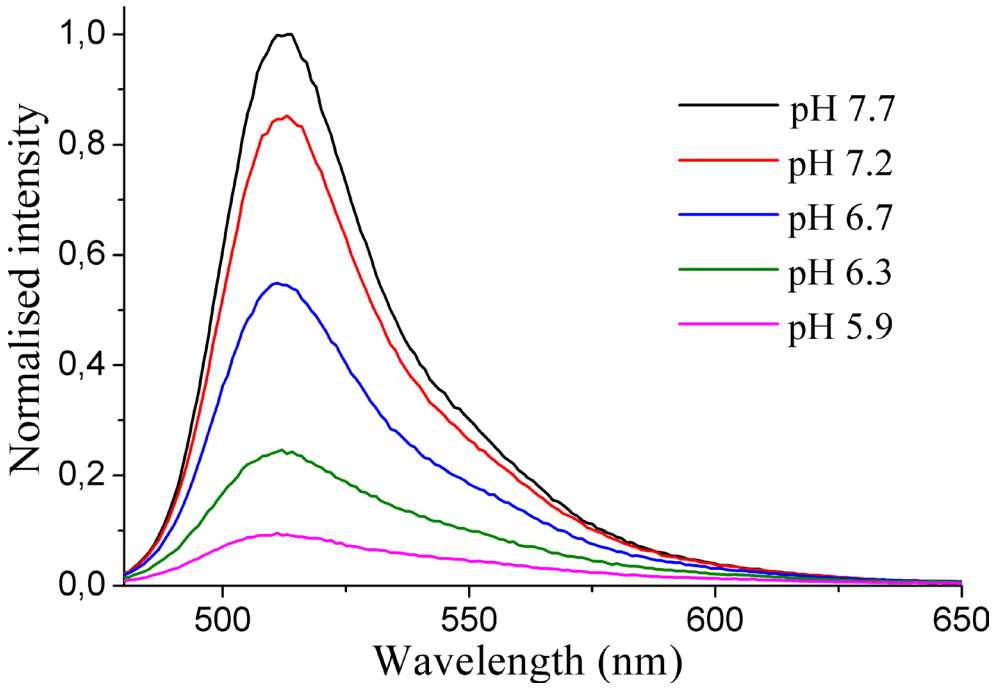

Figure 4-4: Emission spectra of fluorescein at different pH.

The maximum emission occurs at 512 nm independently of the pH. As the pH is decreased, the contribution of the dianion becomes less than the contribution of the monoanion. The quantum yield of the monoanion and dianion are 0.38 and 0.97, respectively [138]. The decrease of intensity at lower pH is therefore related to the increasing contribution of the monoanion and the decreasing contribution of the dianion.

At low buffer concentration, the fluorescence lifetimes of the monoanion and dianion forms of fluorescein are independent of pH. A pH-dependence of those lifetimes was found for PBS buffers of concentrations higher than 20 mM [137]. This pH-dependence is due to excited-state proton exchanges that are too slow to occur at low buffer concentrations. Global analysis of the fluorescence lifetime decay curves of fluorescein in the pH range 6-8 revealed the contribution of the monoanion and dianion forms. Their fluorescence lifetimes were 3.25 ns and 4.21 ns, respectively. These values are in agreement with previous work published on the photophysical properties of fluorescein by Klonis *et al.* (τ_m= 3.4 ns; τ_d = 4.1 ns) [138] and Alvarez *et al.* (τ_m= 3.7 ns; τ_d = 4.3 ns) [137]. Figure 4-5 shows the fractional contribution of the monoanion and dianion to the fluorescence decay.

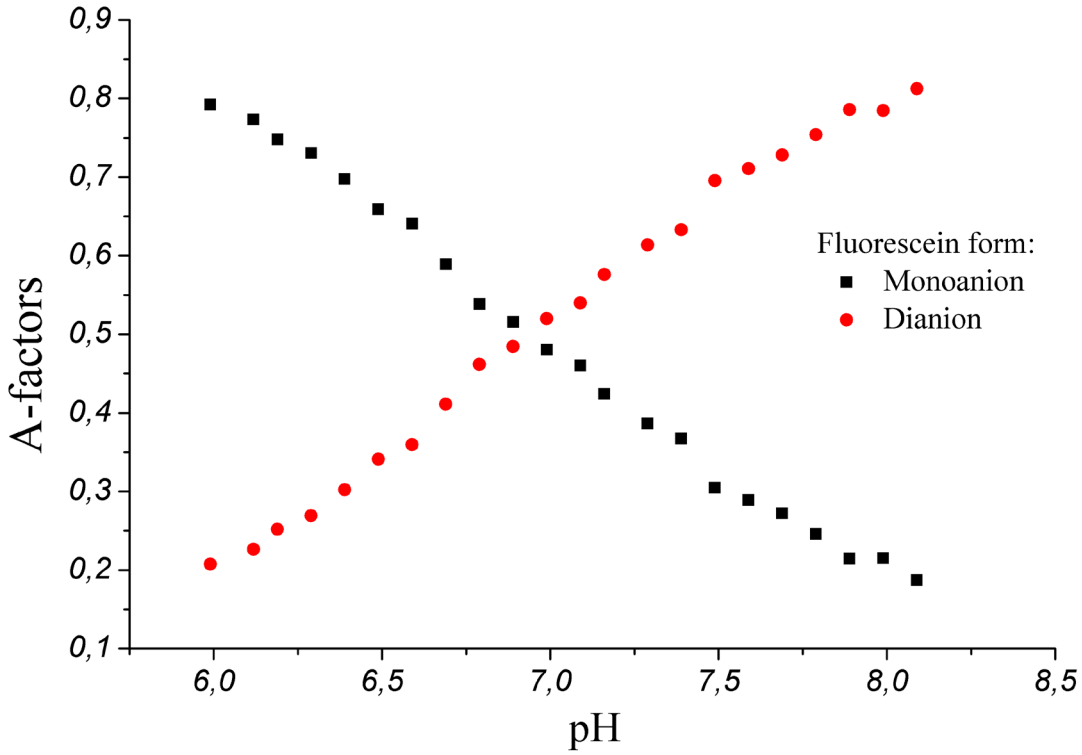

Figure 4-5: Fractional contribution of the monoanion and the dianion forms of fluorescein in the pH range 6-8.

The monoanion and dianion fractional contributions to the fluorescence decay vary from ca. 0.2 to 0.8 in the pH range 6-8. The average fluorescence lifetime is 3.45 ns at pH 6 and increases to 4.04 ns at pH 8.2. The calibration used to read FLIM

images was performed by fitting the TCSPC data with the same initial parameters used for the analysis of FLIM images. The decay curves were tail-fitted to a monoexponential decay function from 1 ns after the maximum channel. The values calculated from the fluorescence decay curves are summarised in Table 4-1.

The results in Table 4-1 show that the fluorescence lifetime of fluorescein becomes decreasingly dependent on pH when pH values tend to pH 7.9. The χ^2 values obtained from tail-fitting the data are in the range 1-1.2 which means that, with the initial parameters used, the fitting of a monoexponential function to the decay curves is satisfactory.

In order to obtain a calibration curve to map the pH in the device, the pH values have been plotted as a function of the lifetimes obtained by tail-fitting. The plot is shown in Figure 4-6.

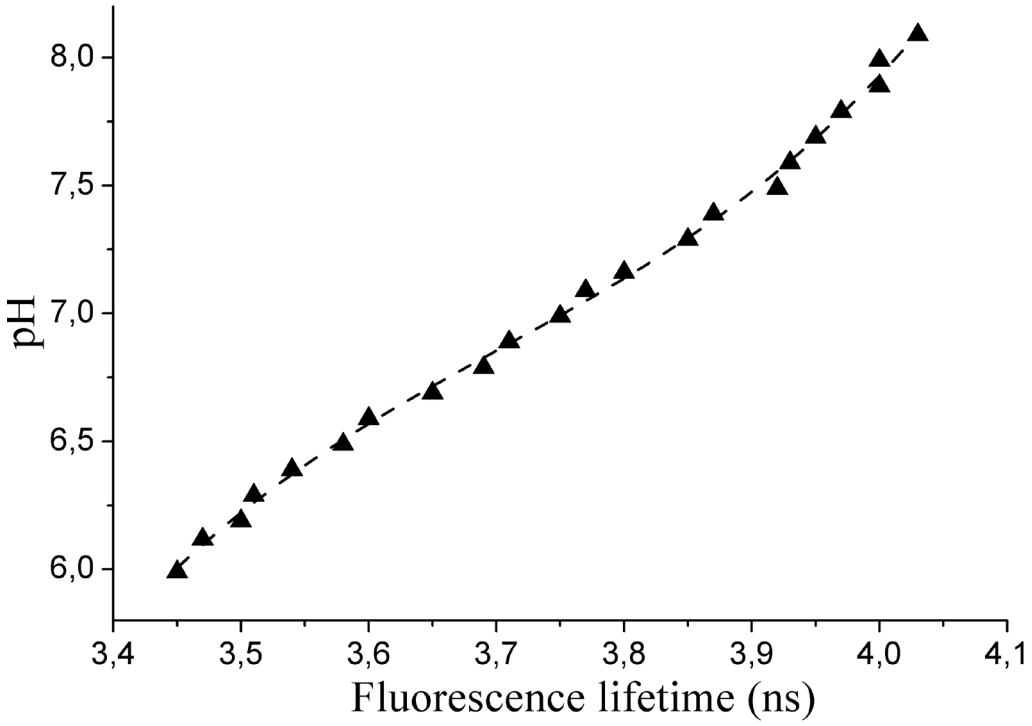

Figure 4-6: Calibration curve of the pH of the solution as a function of fluorescein fluorescence lifetime.

	Global Analysis				Tail Fitting	
pH	A_m	A_d	τ_{av} / ns	χ^2	τ_{TF} / ns	χ^2
5.99	0.79	0.21	3.45	1.05	3.47	1.05
6.12	0.77	0.23	3.47	1.07	3.49	1.06
6.19	0.75	0.25	3.49	1.08	3.52	1.06
6.29	0.73	0.27	3.51	1.01	3.53	1.02
6.39	0.70	0.30	3.54	1.07	3.57	1.07
6.51	0.66	0.34	3.58	1.1	3.61	1.09
6.59	0.64	0.36	3.60	1.04	3.63	1.05
6.69	0.59	0.41	3.65	1.06	3.68	1.06
6.79	0.54	0.46	3.69	1.11	3.71	1.11
6.89	0.52	0.48	3.72	1.13	3.75	1.14
6.99	0.48	0.52	3.75	1.13	3.79	1.08
7.09	0.46	0.54	3.77	1.09	3.81	1.03
7.16	0.42	0.58	3.80	1.2	3.85	1.1
7.27	0.39	0.61	3.85	1.03	3.88	1.05
7.39	0.37	0.63	3.87	1.03	3.92	1.01
7.49	0.30	0.70	3.92	1.02	3.94	1.02
7.61	0.29	0.71	3.93	1.05	3.96	1
7.69	0.27	0.73	3.95	1.13	3.99	1
7.79	0.25	0.75	3.97	1.08	3.99	1.07
7.90	0.21	0.79	4	1.06	4.03	1.05
7.99	0.22	0.78	4	1	4.03	1
8.07	0.19	0.81	4.03	1.1	4.04	1.02

Table 4-1: Fluorescence lifetimes and relative A-factors calculated by global analysis and convolution of the decay curves; fluorescence lifetimes of fluorescein calculated by tail-fitting of the decay curves.

The calibration of the dye fluorescence lifetime as function of pH can be thought of as a titration curve and it is questionable whereas the data could be

satisfactorily fitted to a Handerson-Hasselbach function. Although at first sight, this seems to be a genuine assumption, the trend of the curve presented Figure 4-6 significantly diverges from that of a titration in the fact that around pH = pK_a, a minute addition of a base results in a large change of pH whereas a minute change of the fluorescence lifetime results in a small change of pH. Therefore, the data points were fitted with a 3rd order polynomial function. The calibration of pH as a function of fluorescence lifetime is given by Equation (4-1):

$$pH = 9.81 \times \tau^3 - 109.10 \times \tau^2 + 406.98 \times \tau - 502.55 \qquad \textbf{(4-1)}$$

Equation (4-1) is used to read FLIM images directly and produce quantitative imaging of pH.

4.3.2 Quantitative mapping of pH in a microfluidic device using time-gated intensified CCD camera and fluorescein

Figure 4-7 shows the FLIM images (2a, 2b, 2c) of the pH gradient generated at three positions in the T-mixer when fluorescein solutions at pH 7.6 (left) and pH 6.6 (right) were pumped into the T-mixer (Figure 4-7(1)). The FLIM images clearly show the lifetime gradient resulting from the pH gradient. The flow rate in the mixing channel was 100 μl/min. At this flow rate, the two streams do not have time to fully mix before they reach the channel outlet. However, in the middle of the channel, diffusion is taking place, ironing out the sharp interface between the two streams observed in Figure 4-7 (2.a). This results in an expansion of the diffusion strip materialised by an increasingly larger yellow and turquoise regions from Figure 4-7 (2.a) to Figure 4-7 (2.c).

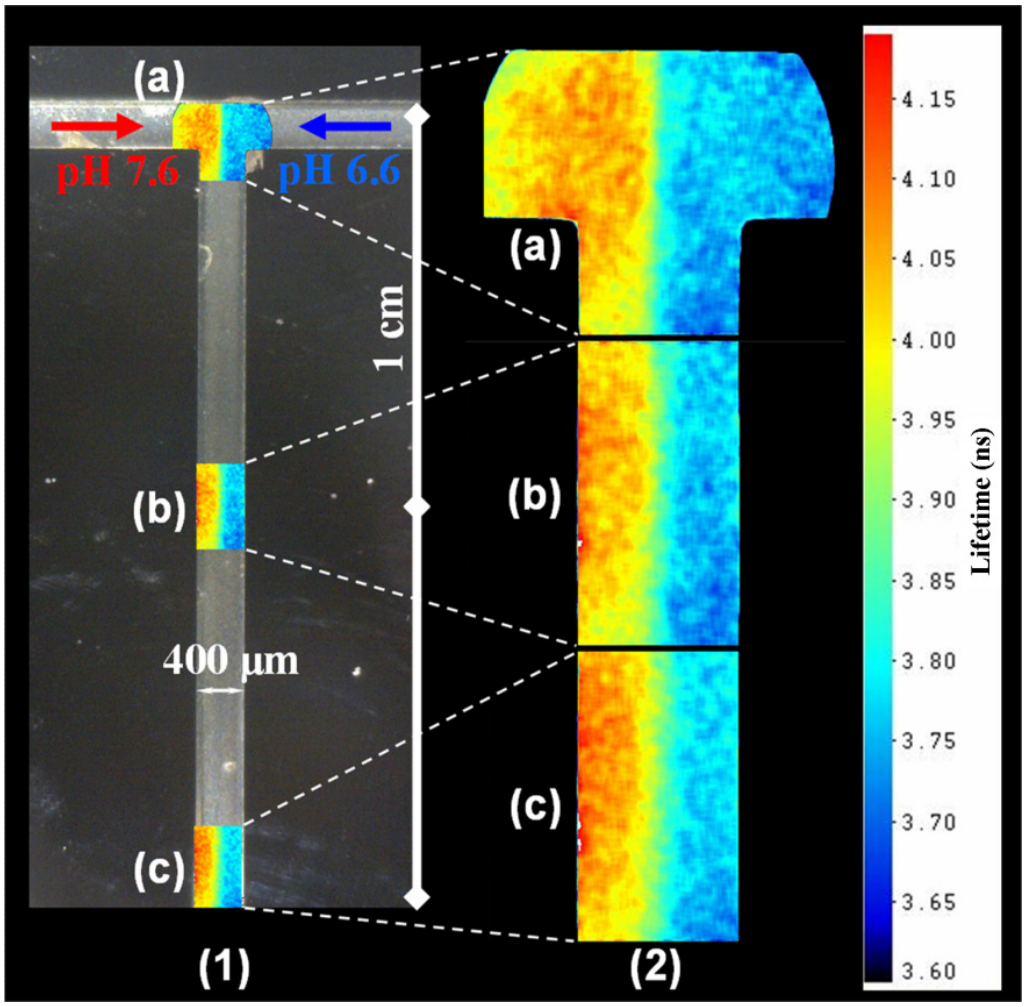

Figure 4-7: Image and dimensions of the T-mixer (1); positions of the area of interest (AOI): T-junction (1a), middle of the channel (1b) and channel outlet (1c). FLIM maps of the AOI (2a, 2b and 2c) recorded using x20 objective and colour coding of the lifetimes of fluorescein from pH 6.6 (τ = 3.7 ns, blue) to pH 7.6 (τ = 4.1 ns, red).

A comparison between fluorescence lifetime image and intensity image of the T-junction is shown Figure 4-8. T he intensity image was obtained by summing all the time-gated images. According to the fluorescent emission spectra shown Figure 4-4, the fluorescence intensity of fluorescein exhibits an ca. 100% increase between pH 6.6 and pH 7.6 whereas the fluorescence lifetimes change by only 9%. Therefore, if fluorescence intensity imaging had the same capability as FLIM, it would generate much better quantitative maps of pH. However, due to the heterogeneity of the excitation beam and disparity in the optical path across the

image, the intensity image shown in Figure 4-8 does not resolve the pH across the channel.

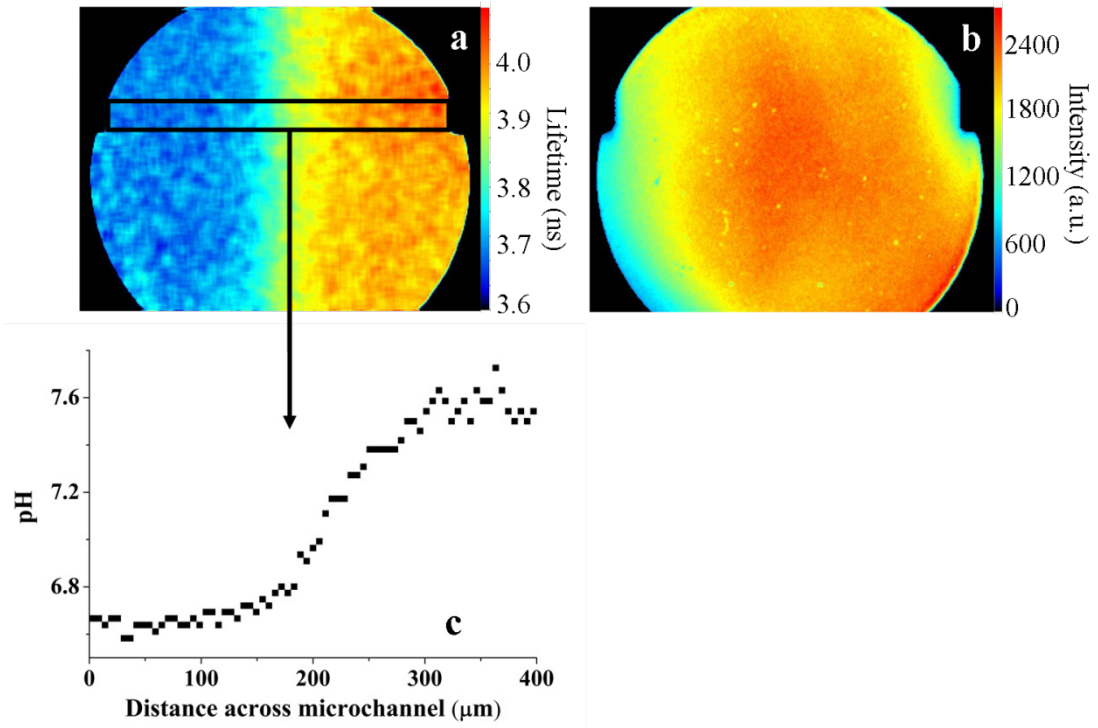

Figure 4-8: (a) FLIM image of the T-junction recorded with x40 objective, lifetime from 3.65 ns (blue) to 4.1 ns (red); (b) Intensity image corresponding to (a), red shows high intensity and blue low intensity; (c) extraction of lifetime data from the FLIM image 3(a) and corresponding pH as function of position across the channel.

The graph in Figure 4-8(c) shows the gradient of lifetime across the chamber. The lifetime corresponding to one of the 71 points was calculated using F900 by analysing the data collected in an area of 10 vertical by 4 horizontal pixels corresponding to an area of 5.6 x 14.1 μm^2. The pH values were calculated using Equation (4-1). From Figure 4-8(c), the accuracy and precision of the pH measurements can be approximated. Statistical analysis of the spread of the values across the first and last 100 μm of the microchannel are summarised in Table 4-2. The range to which the statistical analysis was applied has been chosen by visual estimation of the extent to which there is no pH gradient in the device. In the blue region of the channel in Figure 4-8, the mean pH is 6.64 with a standard deviation of 0.03 pH unit. In the red region, the mean pH is 7.57 with a standard deviation of 0.06 pH unit. The higher standard deviation in the red region can be partly explained

by the decrease sensitivity of the lifetime on pH and partly by a slightly larger spread of the lifetime values (0.12 ns between the minimum and maximum in the red region versus 0.09 ns in the blue region).

Range (μm)	pH from pH-meter	Mean pH from FLIM image	Min. pH from FLIM image	Max. pH from FLIM image	Standard deviation
0-100 (18pts)	6.6	6.64 (3.66 ns)	6.58 (3.64 ns)	6.67 (3.67 ns)	0.027 (0.009 ns)
300-400 (18pts)	7.6	7.57 (3.96 ns)	7.50 (3.94 ns)	7.72 (3.99 ns)	0.059 (0.013 ns)

Table 4-2: Statistical analysis of the spread of pH measurements across gradient free region across the channel.

4.3.3 Fluorescence lifetime characteristics of C-SNARF 1

C-SNARF 1 has been used by researchers as a ratiometric fluorescence pH probe [139-142]. The chemical structure of the acid and basic forms of C-SNARF 1 is given Figure 4-9.

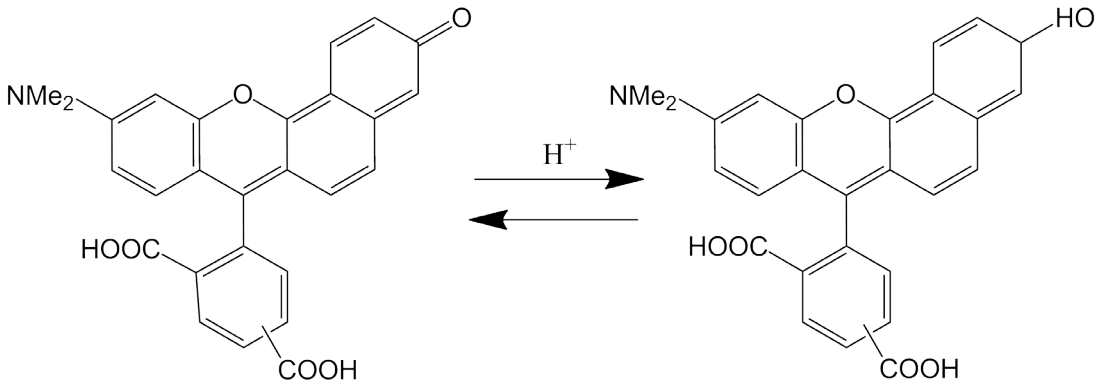

Figure 4-9: Chemical structure of the basic form (left) and acid form (right) of C-SNARF 1.

The presence of the two forms of C-SNARF is obvious from observation of the emission spectra recorded at different pH around the pK_a of the dye shown Figure 4-10. C-SNARF 1 emission spectra exhibit a maximum intensity at 585nm and 638nm for the acid and base forms, respectively, and an isosbestic point at 600nm. The fluorescence lifetime decays were recorded at 585 nm allowing a quasi-equal intensity contribution of the two forms of C-SNARF 1 across the pH range 6.4 to 7.6.

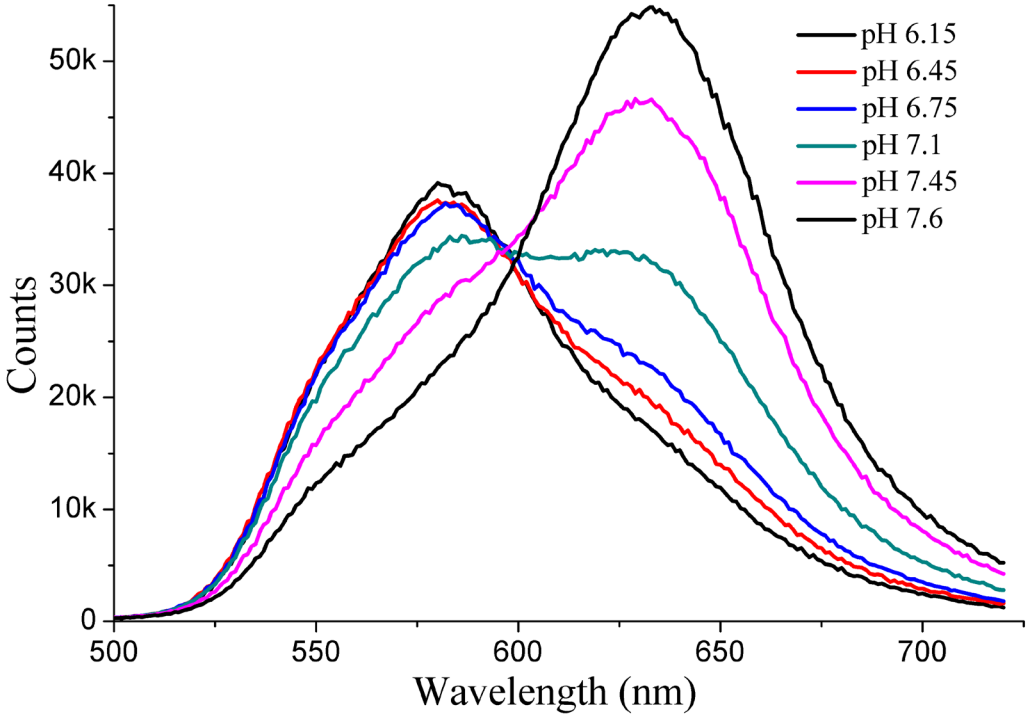

Figure 4-10: Emission spectra of C-SNARF in the pH range 6.15-7.6

The Table 4-3 shows the results of the global analysis performed on the fluorescence decay curves of C-SNARF 1 solutions in the pH range 5.9 to 8.

pH	τ_1 / ns	τ_2 / ns	τ_3 / ns	A_1	A_2	A_3	τ_{av} / ns	χ^2
5.9	0.48	1.45	3.97	0.96	<0.01	0.04	0.62	1.01
6.15	0.48	1.45	3.97	0.92	0.04	0.04	0.65	1.01
6.38	0.48	1.45	3.97	0.87	0.09	0.03	0.69	1.09
6.66	0.48	1.45	3.97	0.81	0.16	0.03	0.74	1.09
7.02	0.48	1.45	3.97	0.67	0.30	0.03	0.87	1.06
7.45	0.48	1.45	3.97	0.47	0.51	0.01	1.03	1.11
7.63	0.48	1.45	3.97	0.39	0.30	0.01	1.11	1.05
7.76	0.48	1.45	3.97	0.30	0.69	<0.01	1.17	1.03
7.93	0.48	1.45	3.97	0.26	0.73	<0.01	1.21	1.07
8.03	0.48	1.45	3.97	0.20	0.80	<0.01	1.27	1.03

Table 4-3: Fluorescence lifetime characteristics of an aqueous solution of C-SNARF in the pH range 5.9 to 8. Individual lifetimes of the different forms (τ_1, τ_2, τ_3) and their corresponding contribution to the fluorescence lifetime (A_1, A_2, A_3). τ_{av} is the average lifetime.

Three lifetime components were identified. τ_1, the lifetime of the acidic form of C-SNARF 1, was calculated to be 0.48 ns. Its contribution is described by A_1. It is the dominant component at pH < 7.4. τ_2 was calculated to be 1.45 ns and is the dominant component at pH > 7.4. The contribution of the basic form is described by A_2. The contribution of the third component is not significant over the range of pH studied. As the product was used as received (without further purification) the third component is attributed to impurities in the dye. Figure 4-11 shows the contribution of each species and the average fluorescence lifetime of C-SNARF solutions in the pH range 5.9 to 8.

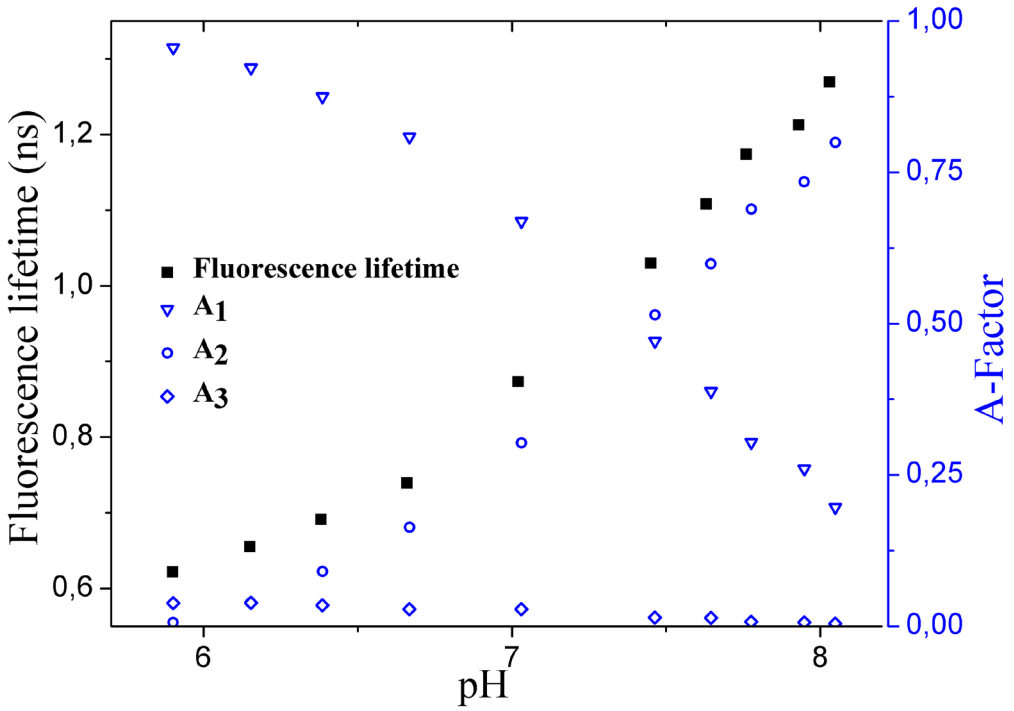

Figure 4-11: C-SNARF average lifetime as function of pH (black squares). Contribution of the monoanion (blue circles) and dianion (blue triangles) species of C-SNARF to the average lifetime.

At pH = pK_a, both species contribute equally to the fluorescence. Figure 4-11 suggests that pH = pK_a at ca. pH 7.4 which is in agreement with previously published work [142].

4.3.4 Quantitative spatial mapping of pH in a microfluidic device using TSCSPC detector and C-SNARF 1

FLIM images using C-SNARF 1 as a pH probe were produced from data recorded using a TSCSPC setup. This system possesses much better time resolution than the time gated system thanks to its 27 ps channels and is capable of resolving much shorter lifetime components due to its short instrument response. Figure 4-12 shows a FLIM image of the T-junction produced using a x20 objectives. Both of the packages used to produce FLIM maps have the capabilities to fit decays with more than one lifetime component. However, in generating FLIM maps, the decay is assumed to approximate to a single lifetime component.

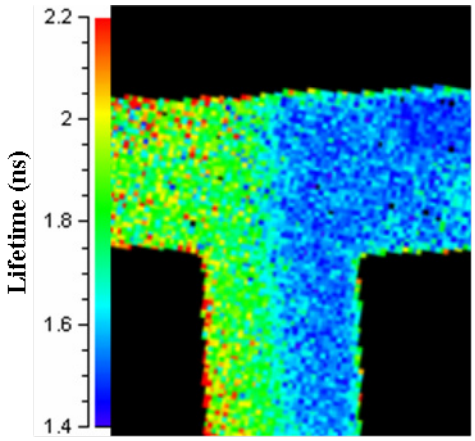

Figure 4-12: Semi-quantitative FLIM image of the T-junction recorded with x20 objective. Change of C-SNARF 1 lifetime across the 6.4-7.6 pH gradient. Flow rate 1µl.min^{-1}.

FLIM images recorded using fluorescein are quantitative because fluorescein fluorescence lifetime decay is simple enough to be reasonably well fitted by a single exponential decay. However, the more complex decay of C-SNARF 1 means that single exponential FLIM maps does not show the pH gradient across the channel. However, A-factor maps can be built using the fluorescence lifetime found in the calibration as fixed parameters. In order to confirm that the three lifetime components τ_1, τ_2 and τ_3 describe well the lifetime decays of the FLIM image, decays from pixels in the channel were extracted and globally analysed using FAST. Table 4-4 shows the comparison between the lifetime components obtained when globally analysing decays collected in a cuvette using TCSPC technique (Table 4-3)

and the results of the global analysis performed on the decays extracted from Figure 4-12.

Collection Method	τ_1 (ns)	τ_2 (ns)	τ_3 (ns)	χ^2
TCSPC	0.483±0.001	1.448±0.004	4.333±0.212	1.03
TSCSPC	0.506±0.002	1.419±0.027	3.671±1.335	1.05

Table 4-4: Lifetime components of C-SNARF obtained by global analysis of data collected using TCSPC and TSCSPC techniques.

Lifetime components obtained by the two methods are in good agreement. The fluorescence lifetime values obtained from the decay curves extracted from Figure 4-12 have been used as fixed lifetime parameters to generate A-factors maps shown Figure 4-13.

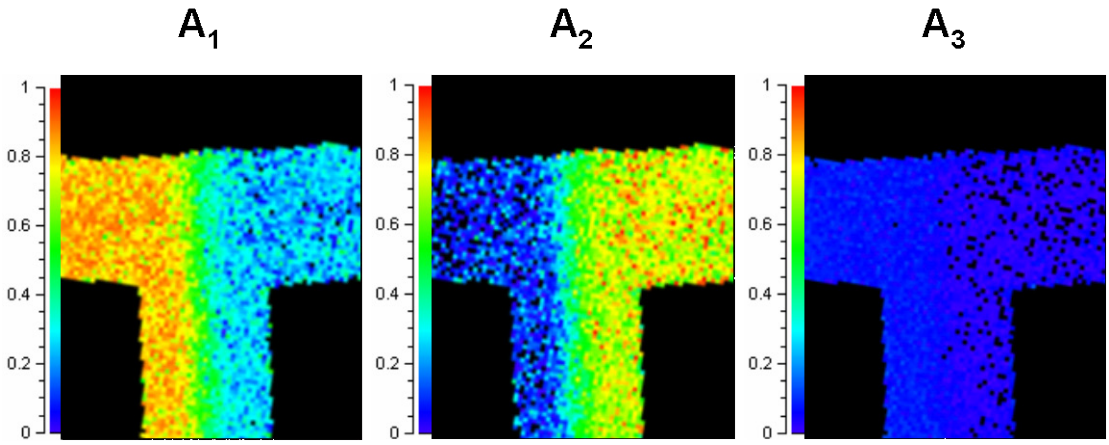

Figure 4-13: A-factors maps of the T-junction of a microfluidic device. A_1, A_2 and A_3 are the normalised amplitude factors corresponding to τ_1, τ_2 and τ_3.

Figure 4-13 shows how quantitative mapping of pH can be obtained by generating A-factor maps. They show the spatial distribution of the normalised pre-exponential factors and therefore spatially resolve the relative contribution to fluorescence decay of each of the C-SNARF 1 species. The use of A-factors to map pH gives a much better resolution than the average lifetime of C-SNARF 1 would do because they change over the pH range mapped by a factor of 8.9 and 4.3 for A_2 and A_1, respectively, whereas the average lifetime changes by a factor of 1.7.

The pH gradient as function of position across the channel was obtained by global analysis of the decays extracted from the raw data of Figure 4-12. The decays were fitted as previously discussed and the pH calculated using Equation (4-2):

$$pH = 8.53 \times \tau_{av}^3 - 28.28 \times \tau_{av}^2 + 33.26 \times \tau_{av} - 6.33 \qquad \textbf{(4-2)}$$

Figure 4-14 shows the distribution of pH across the channel. Each point corresponds to an area of ca. 30(h) x 60(v) μm^2.

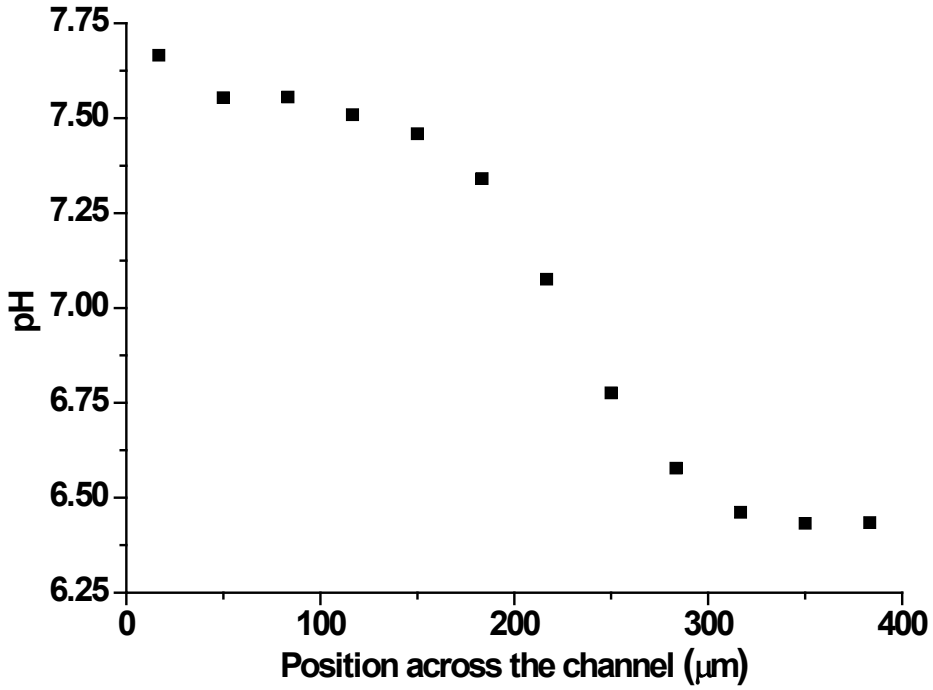

Figure 4-14: pH gradient corresponding to the change in fluorescence lifetime of C-SNARF 1 across the channel.

The 12 measurements across the microchannel relate the distribution of pH with a precision of 0.02 pH units and an accuracy of 0.04 pH units. The spatial and fluorescence lifetime resolutions are limited by the number of photons recorded at each point of the image. In principle, the "number of pixels" in the image is limited by the area needed to integrate over to get enough counts in the maximum channel of the decay. Ultimately, this area is limited by the diffraction limit capabilities of the optical setup. To obtain more points, data would have to be acquired for a longer time. The results shown in this chapter have been obtained for an acquisition time of

ca. 10 min. In the same conditions, with an acquisition time of 100 minutes, 120 points across the microchannel could have been interrogated and would have given accurate measurement of the pH. Compared to the more common time-gated technique, TSCSPC is able to spatially resolve pH in a microfluidic device by measuring the fluorescence lifetime of a probe which exhibits 3 lifetime components.

4.4 Conclusion

To the author's knowledge, this is the first time the TSCSPC technique has been used to probe the environmental properties in microfluidic devices. It is also (to our knowledge) the first use of FLIM to probe pH in microfluidic devices.

A time-gated FLIM system successfully resolved the pH of an aqueous solution with a spatial resolution of 6 μm with an acquisition time of ca. 1 min in a microfluidic device. The fast acquisition of such data was rendered possible by the use of fluorescein as fluorescence lifetime pH probe. Fluorescein exhibits a 2-component exponential fluorescence decay, each component corresponding to the contribution of a fluorescein form. The fluorescence lifetime decay of fluorescein is simple enough to be fitted by a single exponential decay function, hence allowing the time-gated system to generate FLIM images where the pH is quantitatively spatially resolved on each pixel of the camera. Fitting of the fluorescence decay extracted from regions in the device allows measurement of the pH with a precision better than 0.06 pH unit which corresponds to a difference in lifetime of 0.01 ns.

A limitation of the time-gated technique is due to the small dynamic range of the camera. Whereas this limitation was circumvented in this work, it can become critical when the probe exhibits a large change of fluorescence intensity over the environmental gradient generated. Secondly, for the generation of quantitative environmental maps, time-gated FLIM can only work with dyes the fluorescence lifetime of which can be approximate to a single component decay. Finally, in the range of pH used, fluorescein exhibits a change of A-factors of up to 75% whereas its lifetime changes by less than 9%. Therefore, mapping of the A-factors rather than the average lifetime would result in an increased pH resolution.

Thanks to a better time resolution than the time-gated technique, the TSCSPC technique allows spatially resolved fluorescence lifetime decays to be fitted to multi-exponential decay functions. The quadrant anode detects the arrival time and position of single photons resulting in a virtual unlimited dynamic range. TSCSPC has been used in conjunction with C-SNARF 1 to spatially resolve the pH in a microfluidic device. C-SNARF 1 fluorescence lifetime exhibits a 3-component exponential decay in the pH range 5.9 to 8. The shortest component corresponds to the fluorescence of the acid form of C-SNARF and has a lifetime $\tau_1 = 0.5$ ns. The lifetime of the basic form of C-SNARF has a lifetime $\tau_2 = 1.5$ ns.

The 3-component fluorescence decay of C-SNARF did not permit the FLIM images generated by approximation of its lifetime to a single component decay to quantitatively map the pH. The fluorescence lifetime of C-SNARF 1 over the pH gradient generated in the device changes by a factor of 1.7 whereas the relative pre-exponential components change by a factor of up to 8.9. A-factor maps have been generated. They provide direct observation of the fractional contribution of the basic and acidic forms of C-SNARF 1, hence quantitative mapping of the pH in the device.

Decays from points in the image were extracted and successfully fitted to a 3-exponential decay allowing for the average lifetime of C-SNARF to be used to calculate the pH across the microchannel. The calculations have been performed on data extracted from region with an area of 30 x 60 μm^2. The pH has been calculated with a precision and accuracy of 0.02 and 0.04 pH units, respectively, corresponding to a fluorescence lifetime precision and accuracy of 0.01 ns. These features could be significantly improved by increasing the acquisition time of data, which is inversely proportional to the spatial resolution.

The two wide-field FLIM techniques used each have their own advantages and disadvantages. The strong point of the time-gated techniques is its acquisition time. By carefully devising the probing conditions, this technique can be used for quasi-real-time imaging which is a *conditio sine qua non* to image dynamic processes. This is required for *in vivo* or medical imaging. However, when the

acquisition time is not an issue, TSCSPC provides a much better time resolution that allows quantitative mapping of systems that exhibit multi-exponential fluorescence decay.

5 3D MAPPING OF A MICROFLUIDIC DEVICE USING 2-PHOTON EXCITATION FLIM

5.1 Introduction

As has been shown in previous chapters, the advent of time-domain fluorescence imaging techniques and reliable laser sources has provided investigators with a relatively cheap and powerful analytical mapping tool. Furthermore, wide-field time-gated systems have the capability for real-time imaging which promises successful implementation of FLIM in medical imaging systems such as endoscopy [143]. However, one of the limitations of conventional wide-field FLIM is the lack of depth information: an image only reports the lifetime with a colour-coded scale in an x-y plane. The fluorescence lifetime values result from a fluorescence signal collected through part or the entire depth of the sample. This can be a problem when the contribution of fluorescence from out-of-focus is not desired or when depth resolution is required to assess the performance of a microfluidic device. These two cases are examined hereafter. Cases where 3D spatial information is required to assess microfluidic devices have been investigated and the results obtained using 2-photon excitation FLIM are presented in this chapter.

5.1.1 Fluorescence contribution from out-of-focus in wide-field FLIM

Three-dimensional spatial resolution is of particular importance when imaging biological specimens. This is because the contribution from out-of-focus fluorescence blurs the image [144] and can lead to incorrect lifetime values [145, 146]. In dynamic applications, researchers find laser scanning microscopy too slow to correctly map the lifetime of specimen [147]. Instead they use optical sectioning techniques which make use of structural illumination [146, 147] or a Nipkow disk

microscope [148] to resolve depth. Although these techniques have higher intrinsic potential for high-rate FLIM imaging than confocal and 2-photon excitation microscopy, structural illumination requires computation to extract a sectioned image from a set of acquired images [149] and exhibits a reduced signal-to-noise ratio which leads to increased errors when calculating fluorescence lifetimes [148]. The out-of-focus discrimination property of those techniques is also less effective than for confocal and 2-photon excitation. Therefore, although the aforementioned techniques may have superior capabilities for specific applications, the availability of laser scanning techniques and their superiority in spatial and lifetime resolution make them more suitable for three-dimensional quantitative imaging of an established flow in a microfluidic device.

5.1.2 Relative importance of gravity in microflows.

Scaling down is accompanied by an increase in the surface to volume ratio (See chapter 2.4). Gravity forces that scale with mass and therefore with volume, are commonly expected to be negligible in microfluidic devices, and have often been neglected in the study of microflows [150, 151]. However, previous research in the Jones group [7] found that in the case of mixing of two fluids of different properties, gravity had to be accounted for because it is responsible for the reorientation of the interface of the two flows. Whereas in strict laminar conditions two fluids travelling side by side in a microchannel exhibit an interface parallel to the vertical walls of the device, when the two fluids have differing properties gravity affects this parallelism. This phenomenon is responsible for the observation of discrepancies between experimental and simulated results [7], for the loss of flow pattern [151] and obscure measurements caused by the detection of interaction through the horizontal optical window of a device [150, 151]. Applications that require steady laminar flow are numerous (e.g. fuel cells, micromixers, particle separation, DNA diagnostics) and because gravity can affect dramatically the operation of microfluidic devices, its influence on microflows has been investigated by several researchers both theoretically and experimentally [7, 150-155].

5.1.3 Techniques used for 3D mapping of microfluidic devices

Although many techniques have been used to generate 3D maps of microfluidic devices, there is only one publication [150] reporting the interface tilting between two fluids of different characteristics. Optical coherence tomography has been used to evaluate mixing in a 3D structure microfluidic device [156]. The technique has the merit of being able to quantify mixing in deep regions of a device. However, three-dimensional quantitative mapping of mixing fluids represents a big challenge because chemical or physical changes of the properties of the fluids upon mixing induce changes of the scattering profiles. Optical tweezers have been used to probe the flow velocity in the three spatial dimensions of a microchannel [93]. The technique is limited to measuring flow rates and does not allow the gravity effect to be observed. The same limitation applies to confocal μ-PIV measurements of flow within droplets contained in microchannels [157].Two-photon absorption microscopy has been used to generate three-dimensional chemical concentration maps in a microfluidic device [158]. Rhodamine 6G was used to probe the concentration of potassium iodide in the device. Because potassium iodide is quenching the fluorescence of rhodamine 6G, the relative intensity of the latter was used to determine the concentration of the former. The small change of solution density upon addition of potassium iodide (<6% in this case) and the limited number of varying parameters studied (maximum potassium iodide concentration of 500mM and single flow rate) did not permit the observation of gravitational effects.

Two-photon excitation FLIM (2PE-FLIM) has also been used at least twice to generate three-dimensional maps in microfluidic devices prior to the work presented in this thesis. 2PE polarisation-resolved FLIM was used to map glycerol concentration using the change of fluorescence anisotropy of fluorescein in aqueous solution and in a mixture of glycerol and water (50/50) [9]. Under the conditions used (flow rates, density and viscosity gradient), it is very surprising that the work did not lead to an observation of interface tilting between the two flows. Furthermore, the authors explain the asymmetry in the occupation of the two solutions in a plane parallel to the optical window (interface shifted towards one side) by a difference in the applied flow rates (2:1 flow rate ratio between the two

inlets) between the two inlets when a more likely explanation is that the viscosity mismatch between the two flows generate such a flow pattern as predicted theoretically by Stiles et al. [152]. The second paper reports the use of 2PE-FLIM to map temperature in microchannel networks [8]. There seem to be some anomalies in this work. First the use of methanolic solution at 93ºC within devices is surprising since the boiling point of methanol is at 64.7ºC. Secondly, the authors observe that their calibration curve of fluorescence lifetime of rhodamine B in methanol against temperature agrees with what previous researchers have found [159]. Their reported fluorescence lifetime of rhodamine B in methanol at 20ºC is 1.8 ns whereas it has been measured and reported by 8 other groups to be 2.5 ns [160]. Regarding the observation of an interface tilting, the temperature gradients within the devices might have been too small to engender a significant change in methanol properties.

Finally, confocal microscopy has been used to image a section of a microfluidic device [150, 155]. Yamaguchi et al. [150] observed the interface tilting by measuring the angle of the interface formed by a human serum labelled with fluorescein and a PBS buffer originally pumped side-by-side in the device. They introduced a modified dimensionless number, Z, to describe the rotation:

$$Z = \frac{\Delta\rho g a L}{\mu \upsilon} \quad for \quad Z \leq 196 \qquad \textbf{(5-1)}$$

where $\Delta\rho$ is the density difference (kg/m^3), g is the gravitational acceleration (m/s^2), a is the microchannel width and depth (m), L is the microfluidic length (m), μ is the viscosity (Pa.s) and υ is the average velocity (m/s). Z is related to the rotation angle by a second order polynomial. From Equation (5-1), it is clear that tilting due to gravity is proportional to the density difference, gravity, channel size, and is inversely proportional to velocity and viscosity. Using these preliminary results, Yamaguchi *et al.* further investigated the observed phenomenon using computational fluid dynamics modelling and concluded that gravity should be taken into account in microfluidic devices when either interfacial tension or diffusion are small [154].

Although it had been characterised, the effect of gravity on microflows had never been imaged using high spatial resolution quantitative techniques such as 2PE-FLIM. The capacity of this technique to provide high resolution quantitative images of gravitational effects is shown hereafter.

5.1.4 Photophysical properties of ANS

ANS fluorescence has received considerable attention, owing to its extensive use as a biomolecular probe [161]. The photophysics of ANS in pure solvents can be described in terms of a solute-solvent interaction model [162], and in polar solvents is dominated by emission from an intermolecular charge transfer state [163]. The structure of ANS is shown Figure 5-1.

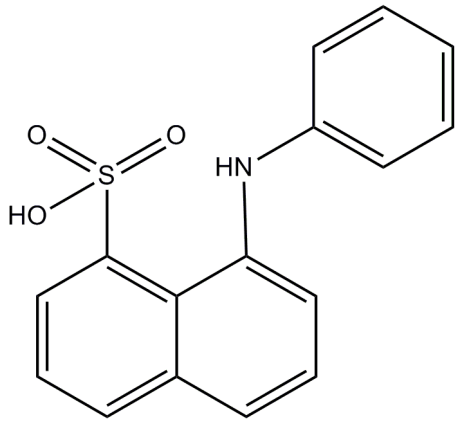

Figure 5-1: Molecular structure of ANS

Upon excitation, ANS exhibits a large increase of its dipole moment. Researchers have assumed a simple competition between the radiative and non-radiative processes, the rate of which is strongly dependent on the solvent dielectric constant. The decrease in radiative transition probability with increasing solvent polarity has been explained by an increase of the weight of the wavefunction corresponding to the charge transfer configuration with increasing solvent polarity [162].

Other explanations have been proposed for the polarity dependence of ANS fluorescence characteristics. The polarity effect has been explain by: solvent quenching due to the creation of an electron trap in water-rich solvents [164]; ring conformation effect [165]; and intersystem crossing mechanisms [166].

5.2 Experimental details

In order to create a situation where gravity has an effect on the orientation of the interface between two flows having different density, the experiment reported by Mendels et al. [7] was repeated using 2PE-FLIM rather than conventional wide-field FLIM. In this experiment, a solution of methanol is brought in contact with a water-methanol mixture at the T-junction of a microfluidic device. The water/methanol content is probed using ANS, a fluorescent dye the fluorescence lifetime of which is extremely sensitive to the composition of water-methanol mixtures [167].

A second system has been studied in which water-glycerol mixtures are used to observe the interface rotation. The glycerol content is probed using Kiton Red (KR) which exhibits a change of fluorescence lifetime as a response to change in the composition of water-glycerol mixtures.

5.2.1 Solution preparation

All measurements of water content in methanol were made with the ammonium salt of 1,8-anilinonaphthalene sulfonate (ANS) obtained from Fluka and used as received. Solutions of ANS (1 mM) in pure methanol and a water-methanol mixture (1:1 molar ratio, which corresponds to 30.8% water v/v) were prepared using HPLC grade methanol and water (Fisher Scientific), used as received. The solutions were kept in brown glass flasks in the fridge.

The change of fluorescence lifetime with change of glycerol content was performed with solutions of KR at 10 μM. First an aqueous solution of KR at 1 mM was prepared, homogenised and kept in the fridge for further dilution. Then glycerol was weighted to the desired amount (0% to 40% vol/vol of the final solution in steps of 2.5%). Deionised water was added to the glycerol for a volume making up 99% of the final solution. Finally, 1% vol/vol of the aqueous solution of KR at 1 mM was added. The solution was homogenised and kept in the fridge until a few hours before measurements were taken.

5.2.2 Microfluidic device and setup

The microfluidic device used in this study was made by etching of a t-shape in a silicon wafer, sealed on one side by a thin silica sheet. Chip-to-world connections were achieved through threaded ports (NanoPorts, Upchurch Scientific) glued at the back of the silicon wafer. The solutions were loaded in syringes (BD 3 ml Syringe Luer-Lok Tip, BD, Belgium) and pumped in the device using syringe pumps (KDScientific, Holliston, MA) through silicone tubing (AlteSil™ High Strength Silicone Tubing, Altec Products Ltd, UK). Typical flow rates were 25 µl/min for each syringe resulting in a flow rate of 50 µl/min in the main channel. Figure 5-2 is a schematic of the device.

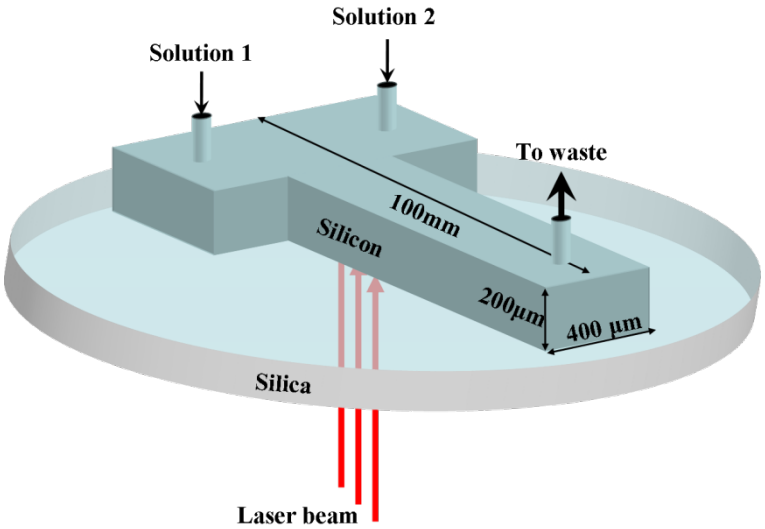

Figure 5-2: Schematic of the microfluidic device used for 2PE-FLIM experiments

5.2.3 Calibration of the probe fluorescence lifetime

The calibration of ANS fluorescence lifetime as a function of water content was obtained from previously published work [3, 7, 167]. The fluorescence lifetimes of the methanol solution and of the water-methanol mixture were measured in the TCSPC setup presented Section 3.2.

5.2.4 Optical and experimental setup (See also Chapter 3.4)

For the water-methanol system, the laser output was set at 720 nm, and focused in the sample using a microscope objective (Nikon, x20, 0.75NA). The

fluorescence signal was filtered using a pair of fluorescence filters (shortpass 680 nm and bandpath 525 nm). The TAC was operated on a 10 ns range. A final image was generated after averaging 10 times the photon arrival times accumulated for 60 s in a 128x128 pixel grid.

For the water-glycerol system, the laser output was set at 785 nm and focused in the sample using a microscope objective (Nikon, x20, 0.75NA). The fluorescence signal was filtered using a pair of fluorescence filters (shortpass 680 nm and bandpath 585 nm). The TAC was operated on a 12.5 ns range. A final image was generated after averaging 5 times the photons arrival times accumulated for 60 s in a 128x128 pixel grid. The temperature of the room was monitored to account for discrepancies in the measurements since the fluorescence lifetime of KR is sensitive to temperature. The temperature of the lab was stable and measured to be 22ºC.

In order to generate a 3D map of the devices, the laser focus was brought manually to the bottom surface of the device (the optical window). It was then moved by 10 μm inside the channel using the computer controlled stepper and an image was recorded. The focus was then moved by steps of 20 μm and images recorded at each step until the top surface of the device was reached resulting in 11 images, each corresponding to a fluorescence map representing the solvent composition in a channel slice.

5.3 Results

5.3.1 Fluorescence properties of ANS

Figure 5-3 shows the excitation and emission spectra of the ANS solutions used in the work presented in this chapter. The excitation maxima were measured at 416 nm for both solutions. Upon addition of 30.8% of water in methanol, a fourfold decrease of the emission intensity was observed. It is not shown on Figure 5-3 because the spectra have been normalised. However, the normalisation allows the observation of the red shift of the maximum emission in the presence of water.

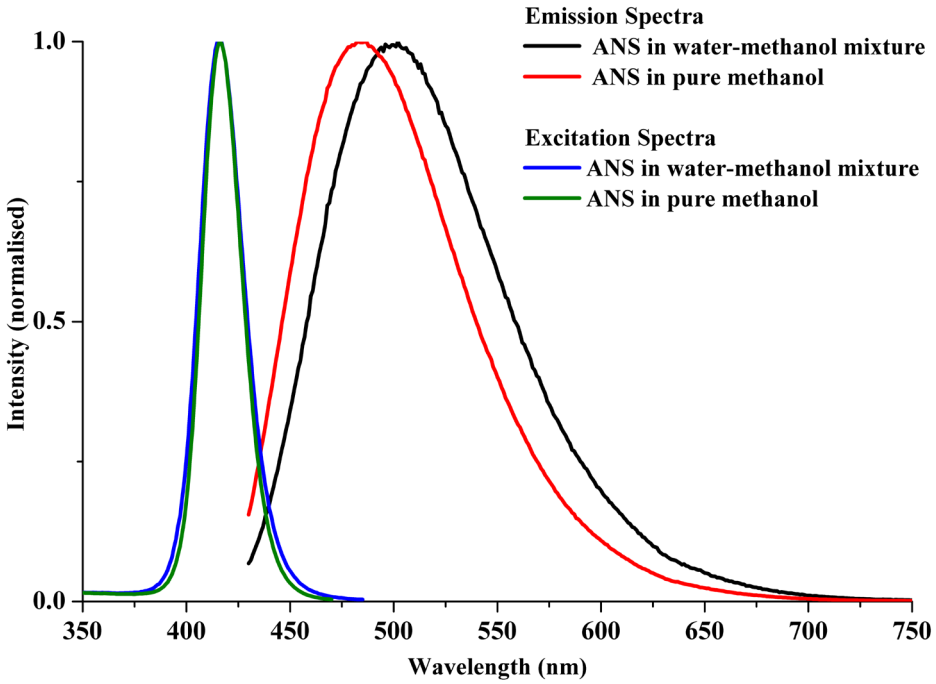

Figure 5-3: Excitation and emission spectra of ANS solutions used for 2PE-FLIM.

The relative difference of emission intensity between the two solutions can be a problem when recording data for FLIM because there is a possibility that the dynamic range of the detector does not allow for the weaker solution to be correctly detected without being saturated in the strongly fluorescent region. The wavelengths of maximum emission are 483 nm and 502 nm for ANS in pure methanol and ANS in the water-methanol mixture, respectively. In the 2PE-FLIM experiment, the use of a bandpass filter centred at 525 nm allows for the fluorescence of ANS in the water-methanol mixture to be spectrally favoured therefore minimising the difference in emission intensity between the two solutions.

In general, the decay curves of a fluorescent dye in mixed solvents show a multi-exponential decay that can be attributed to site-specific solvated species [168] or distribution of the fluorophore environment [21]. A useful characteristic of ANS in a methanol-water mixture is that it exhibits a single exponential decay as shown Figure 5-4.

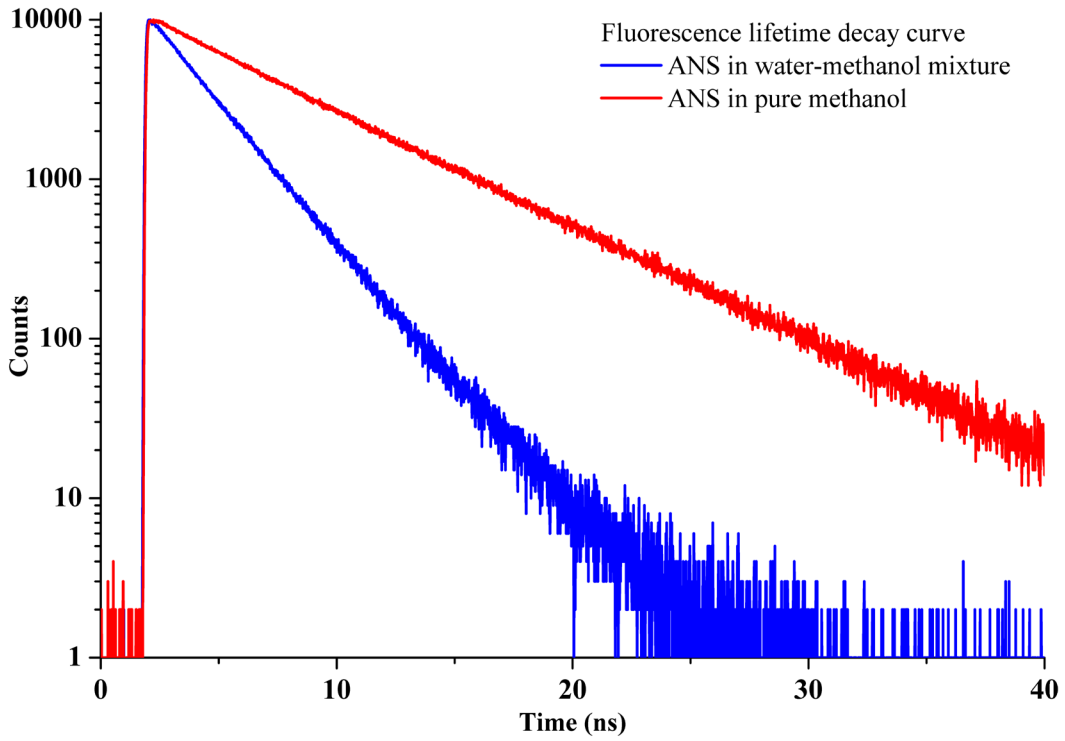

Figure 5-4: Fluorescence lifetime decay curve of ANS solutions used for 2PE-FLIM.

The decay curves shown Figure 5-4 were fitted to a single exponential decay. The fluorescence lifetimes of ANS in pure methanol and in the water methanol mixture were 6.01 ns and 2.42 ns respectively. Those results are in good agreement with previously reported values [3, 7, 167] and measurement of the fluorescence lifetimes was used as a routine check of the purity of the solutions. Figure 5-5 shows the calibration of the percentage of water in water-methanol solutions as a function of the fluorescence lifetime of ANS [3, 7]. The fluorescence lifetime of ANS decreases from 5.97 ns in pure methanol to 2.36 ns in the water-methanol mixture. Although the relation between fluorescence lifetime and water content is quasi-linear, in the range studied it was successfully fitted to a third polynomial function.

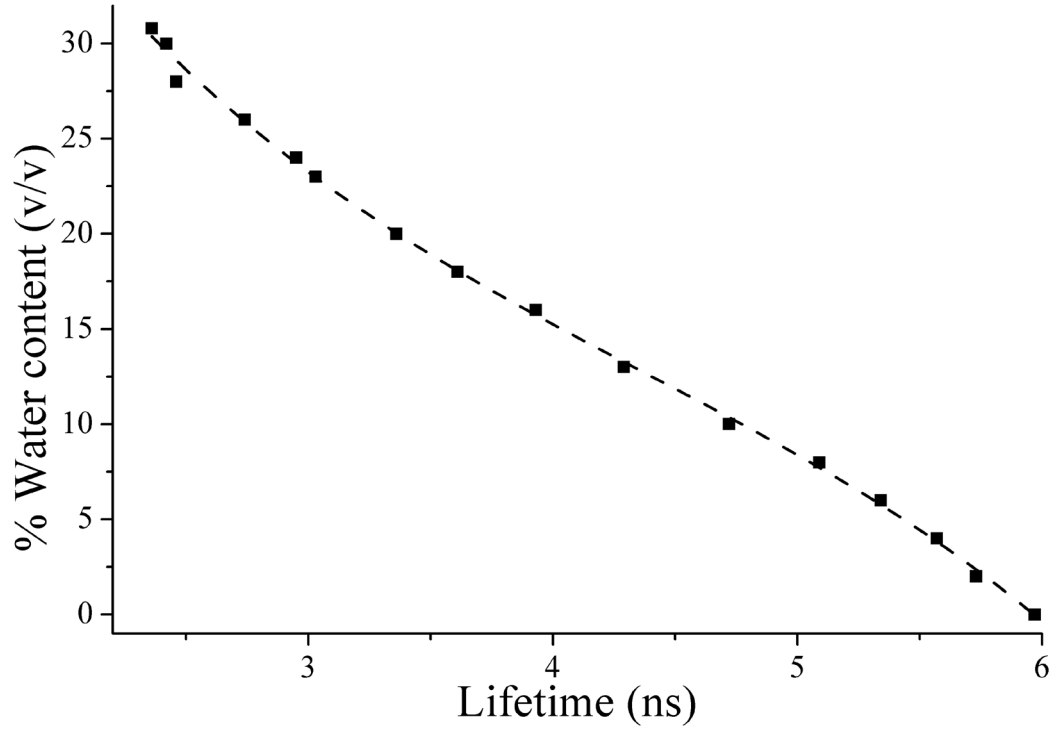

Figure 5-5: Calibration curve showing ANS fluorescence lifetime as a function of the water/methanol ratio in solution. The dashed line is the best fit by the 3rd order exponential function $Y = -0.50 * X^3 + 6.60 * X^2 - 35.64 * X + 84.30$.

The equation $Y = - 0.50 * X^3 + 6.60 * X^2 - 35.64 * X + 84.30$, where Y is the percentage of water volume per volume of solution and X is the fluorescence lifetime. This equation was used in conjunction with the FLIM images, to convert the lifetime value at each pixel to the percentage composition of water, and subsequently to produce composition maps.

5.3.2 FLIM of ANS

In this chapter, the discussion is focused on the rotation of the interface between two flows that have different physical properties. However, the main rationale for using 2PE-FLIM is to combine the superior spatial resolution of 2PE microscopy with the superiority of FLIM to provide quantitative mapping as discussed in Chapter 1. Applied to flow behaviour, these combined properties allow the visualisation of diffusion as well as advection in a device cross-section.

Figure 5-6 shows how 2PE-FLIM is able to produce direct three dimensional reading of the water composition in the microfluidic device. The red colour corresponds to a lifetime of 6 ns and the blue to a lifetime of 2.4 ns denoting a region containing pure methanol and 30.8% water-methanol mixture respectively. Because the relationship between water content and ANS fluorescence lifetime is quasi-linear (Figure 5-5), the false colour scale is quasi-linear with respect to the water content.

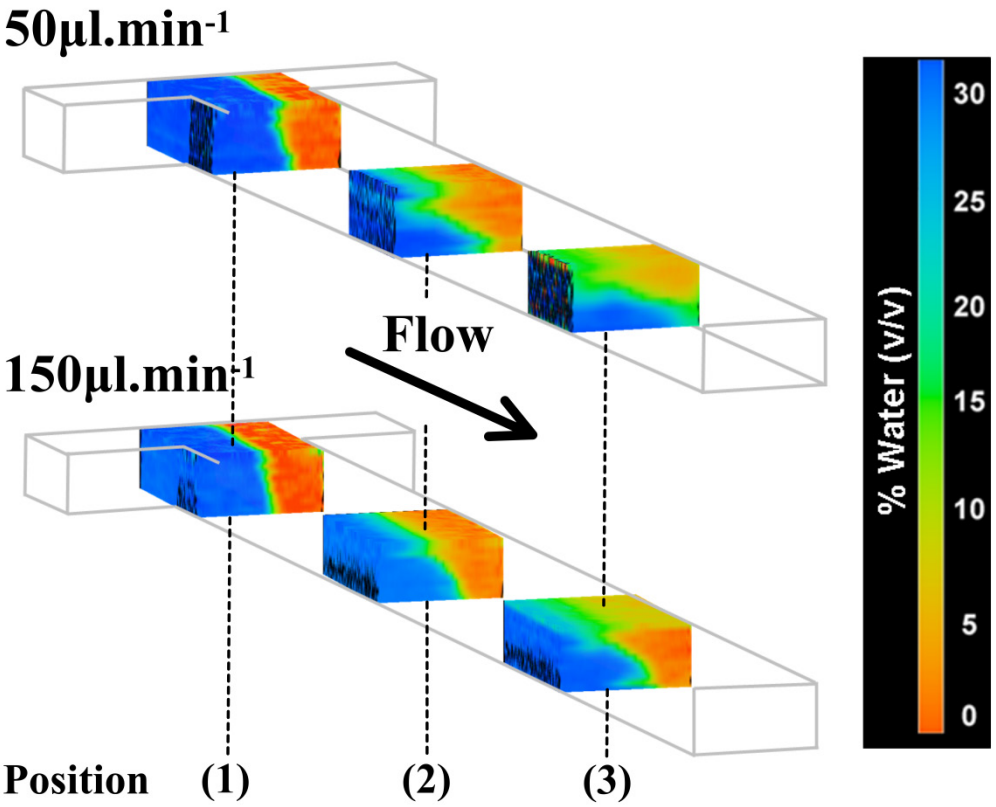

Figure 5-6: 3D images of water/methanol composition at 50 µl/min (top) and 150 µl/min (bottom). Each colour-coded image represent a volumic section of the device at the T-junction (position (1)), in the middle (position (2)), and at the end (position (3)) of the microchannel. The correspondence between colour and water content is given by the colour-coded scale on the right of the figure.

The rotation of the interface between the two fluids of different viscosities is striking in Figure 5-6. The use of high flow rates allows the interface to stay sharp because the mixture does not have time to equilibrate by diffusion during so short a residence time.

With respect to Equation (5-1), the inverse influence of flow rate on the rotation becomes increasingly prominent as the fluid travels down the channel. Whereas at position (1), it is difficult to notice a difference between the top and bottom image, it is clear that the rotation of the interface is more pronounced at position (3) at 50 µl/min than at position (3) at 150 µl/min.

An important observation that was predicted by Stiles *et al.* [152] is the shift of the interface towards the fluid of lower density. This is best observed at the T-junction (position 1) of the device where the water-methanol mixture fluid occupies more space than the pure methanol solution. This effect is not accounted for in the CFD model developed by Yamaguchi *et al.* [154].

Figure 5-7 shows a map of the entire device at three different depths: 40 µm, 100 µm and 160 µm from the device bottom surface. The flow rate was set at 50 µl/min.

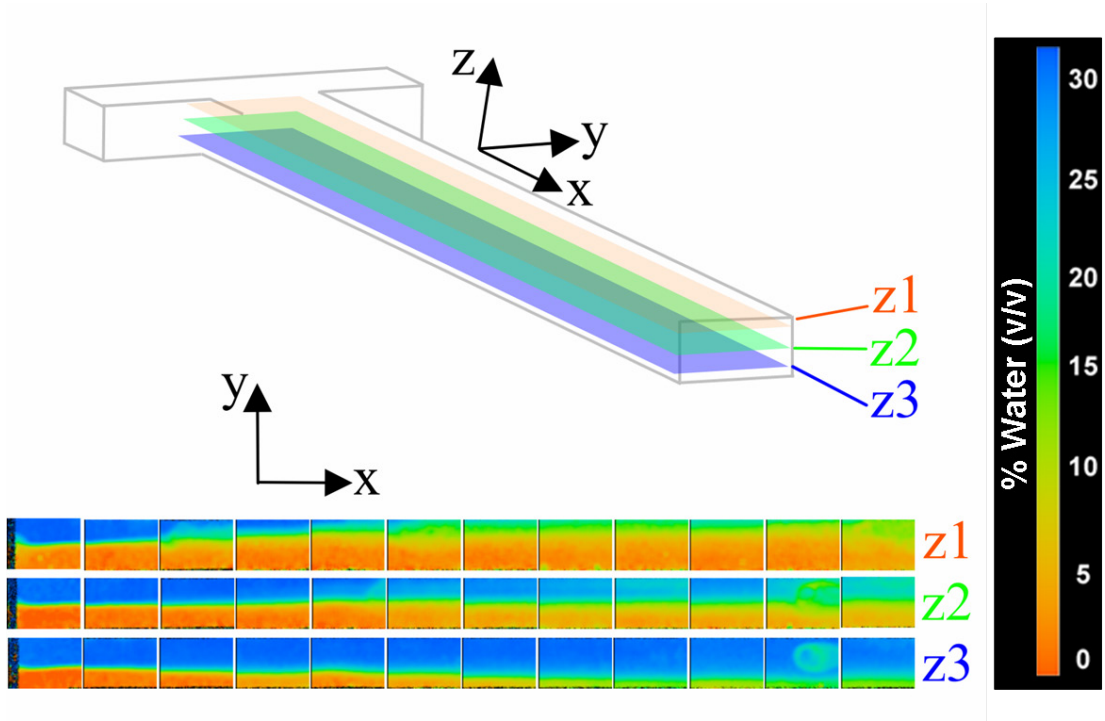

Figure 5-7: Fluorescent lifetime map of the entire device at 40 µm (Z3), 100 µm (Z2) and 160 µm from the optical window.

Mapping of the entire device allows the experimental data to be closely compared with data generated by computer modelling. In the work presented by

Mendels *et al.* [7], although the buoyancy has been accounted for when generating images, the shift of the interface due to the viscosity difference between the two fluids is not ostensible on the computer generated images. As the authors observed, this results in a more efficient mixing than calculated. The fact that the water-methanol mixture occupies more volume in the channel than methanol alone means that advective transport along the channel (x-direction on Figure 5-7) will not be constant. Evidence of the non-constant advective velocity are given in Chapter 6 using μ-PIV.

The discrepancies between computational results and experimental results in the paper from Mendels et al. [7] are more prominent close to the device outlet. The authors concluded that due to the importance of advective phenomena in the assessment of mixing, these discrepancies could be due to back pressure that develop close to the channel outlet and slow the fluid in this region, enhancing the mixing efficiency of the device.

5.3.3 Calibration of the fluorescence lifetime of aqueous solutions of Kiton Red as a function of glycerol content

The fluorescence lifetime of KR in aqueous solutions was measured using the TCSPC setup presented in Section 3.2. It was calibrated over a range of glycerol concentration from 0% (pure water) to 40% vol/mass. Fluorescence decays were accumulated to 10,000 counts in the peak channel on time range of 50 ns and counts were attributed to 4096 channels, each channel corresponding to a time bin of 0.01221 ns. The fluorescence decay curves were analysed by tail-fitting from 0.5 ns after the channel with maximum counts, to meet with the parameters used to generate FLIM images. The analysis was performed with F900. The change in fluorescence lifetime with change of glycerol concentration is shown Figure 5-8.

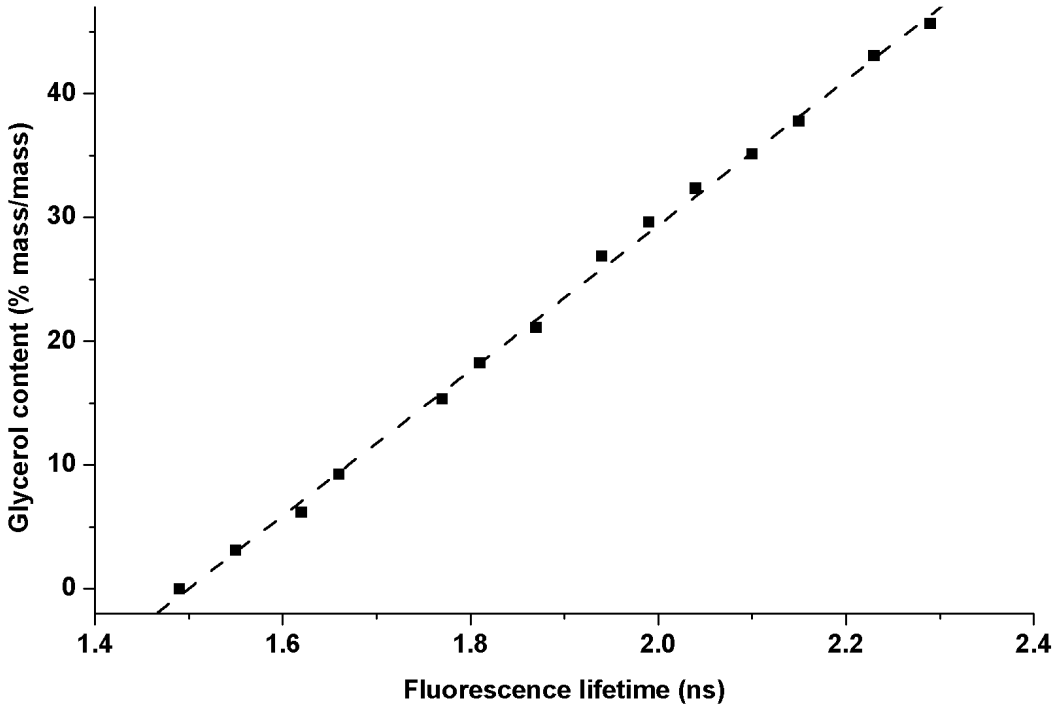

Figure 5-8: Calibration curve showing the linear relationship between glycerol content and fluorescence lifetime of KR. The calibration graph fits well to a linear equation Y=58.63X-87.91

The calibration curve shows the linear change of fluorescence lifetime with changing glycerol concentration in the range studied. The fluorescence lifetime of KR increases from 1.5 ns in water to 2.3 ns in 45% (%mass/mass) glycerol. A linear fit of the measurements generate the equation used to relate the fluorescence lifetime to glycerol concentration and is given by Equation (5-2):

$$Y = 58.63X - 87.91 \qquad \textbf{(5-2)}$$

where Y is the volume fraction of glycerol and X is the fluorescence lifetime. In terms of fluid dynamic studies, the purpose of using glycerol to change the solvent content of aqueous KR solutions is to map the viscosity in microfluidic devices and look at the effect it has on the flow behaviour. However, the fluorescence lifetime sensitivity of KR is not due directly to viscosity but to solvent composition. Nevertheless, with the knowledge of the concentration of glycerol in an aqueous solution, one can know the viscosity of the solution. The viscosity of glycerol

aqueous solutions at 20ºC were obtained from previous publications and are shown Figure 5-9 [169, 170].

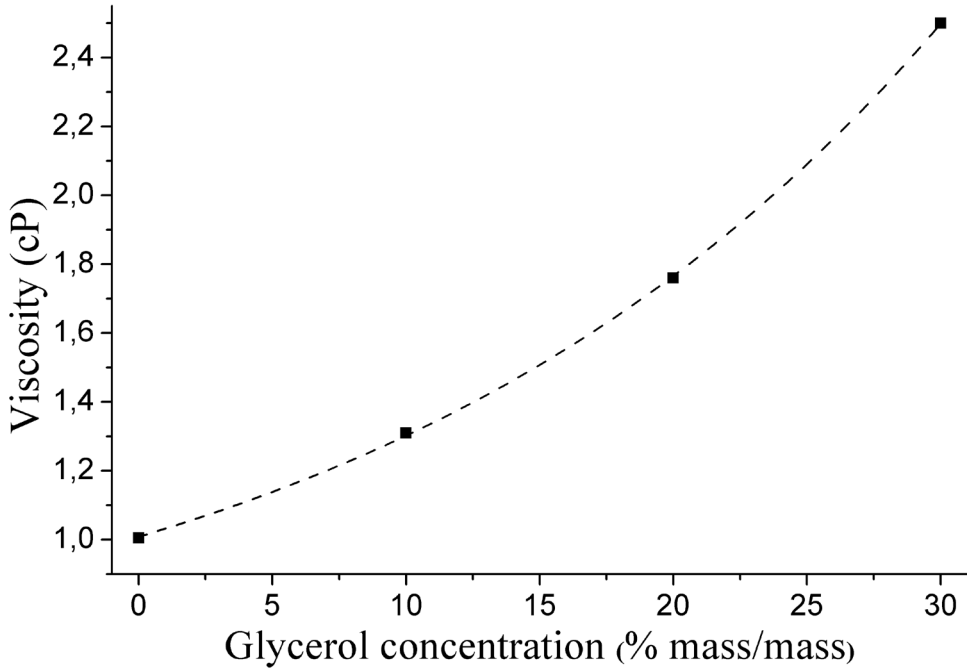

Figure 5-9: Viscosity of aqueous solutions of glycerol as a function of glycerol content (%mass/mass) [169, 170]. The data are fitted to a single exponential growth given by the equation: Y=0.5+0.51exp(X/21.9)

The relationship between glycerol content and viscosity is obtained by fitting the measurements to a single exponential function given by Equation (5-3):

$$Y = 0.5 + 0.51\exp(X/21.9) \qquad \textbf{(5-3)}$$

where Y is the viscosity of the blend (cP) and X is the concentration of glycerol (%mass/mass).

5.3.4 Comparison of methanol-water system with glycerol-water

Figure 5-10 shows the results obtained for the methanolic fluids and compares them with the mixing of pure water with a glycerol-water mixture. The flow rate in both cases is 50 µl/min. Figure 5-10 (a) is a reproduction of Figure 5-6 (top). Figure 5-10 (b) shows mixing of pure water containing KR and a glycerol-water mixture (35.5% glycerol mass/mass %) containing KR. The fluorescence lifetime of KR ranges from 1.5 ns in pure water to 2.1 ns in the mixture. As for ANS

in a methanol-water mixture, the fluorescence lifetime of KR follows a linear relation to the glycerol content in water (See Figure 5-8). The colour-coded scale shows the colours corresponding to changing fluorescence lifetime from 1.5 ns (blue) to 2.1 ns (red). The glycerol content is calculated using Equation (5-2).

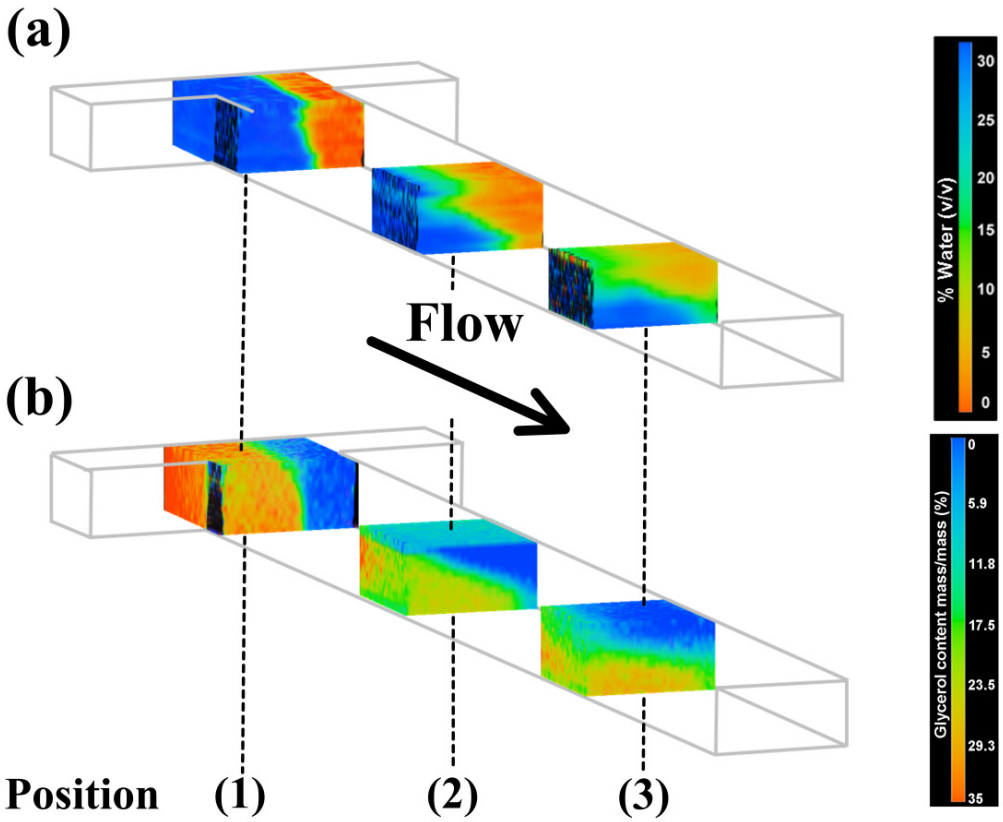

Figure 5-10: 3D images of water/methanol composition at 50 µl/min (a) and glycerol/water composition at 50 µl/min (b). Each colour-coded image represent a volumic section of the device at the T-junction (position (1)), in the middle (position (2)), and at the end (position (3)) of the microchannel. The correspondence between colour and water/glycerol content is given by the colour-coded scale on the right of the figure.

The glycerol-water system exhibits a slightly greater interface rotation than the methanol-water system. The viscosity and density characteristics of the fluids used are detailed in the next section. Briefly, the glycerol-water system exhibits a higher density difference than the methanol-water system and a higher average viscosity. With respect to Equation (5-1), the rotation of the interface is proportional with the density difference and inversely proportional to the viscosity. In other words, the higher density difference in the glycerol-water system enhances the

rotation of the interface when its higher viscosity is working against it. This suggests that the density difference is proportionately more important than the difference in viscosity between the two systems.

5.3.5 Quantification of the rotation

Equation (5-1) was used to calculate values of Z corresponding to the FLIM images presented Figure 5-6 and Figure 5-10. The densities and viscosities of water, methanol, water-methanol mixture (1:1 molar ratio) and glycerol-water mixture (30% glycerol mass/mass) were obtained from previous publications as indicated on Figure 5-11 to Figure 5-13.

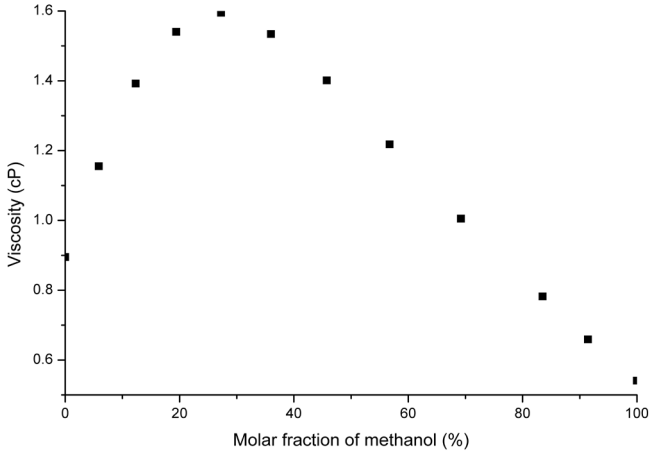

Figure 5-11: Viscosity of water-methanol mixture [171]

The data for the viscosity of water-methanol mixtures Figure 5-11 were fitted to a 6th order polynomial function given by Equation (5-4):

$$\mu = (0.88 + 0.056 \times m - 0.001 \times m^2 + 5.9 \times 10^{-6} \times m^3 + 5.5 \times 10^{-8} \times m^4 - 4.1 \times 10^{-10} \times m^5) \times 10^{-3} \quad \textbf{(5-4)}$$

where μ is the viscosity in Pa.s and m is the molar fraction of methanol.

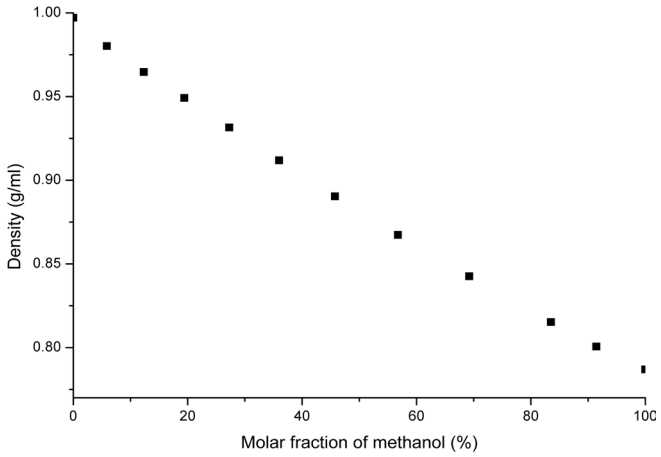

Figure 5-12: Density of water-methanol mixture [171]

The data for the density of water-methanol mixtures Figure 5-12 were fitted to a linear function given by Equation (5-5):

$$\rho = -(0.0021 \times m + 0.99) \times 1000 \qquad \textbf{(5-5)}$$

where ρ is the density in kg/m^3.

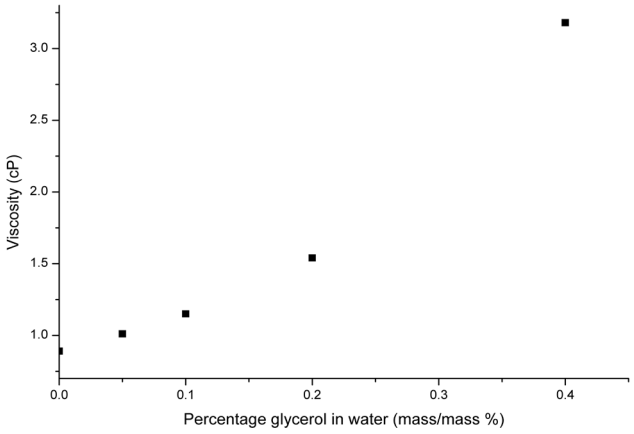

Figure 5-13: Viscosity of water-glycerol mixture[172]

The data for the viscosity of water-glycerol mixtures Figure 5-13 were fitted to an exponential function given by:

$$\mu = (0.5 + 0.51\exp(\mathrm{m}/21.9)) \times 10^{-3} \qquad \textbf{(5-6)}$$

where m is the mass fraction of glycerol.

The data for the density of water-glycerol mixtures Figure 5-14 were fitted to a linear function given by:

$$\rho = -(0.25 \times m + 0.99) \times 1000 \qquad \textbf{(5-7)}$$

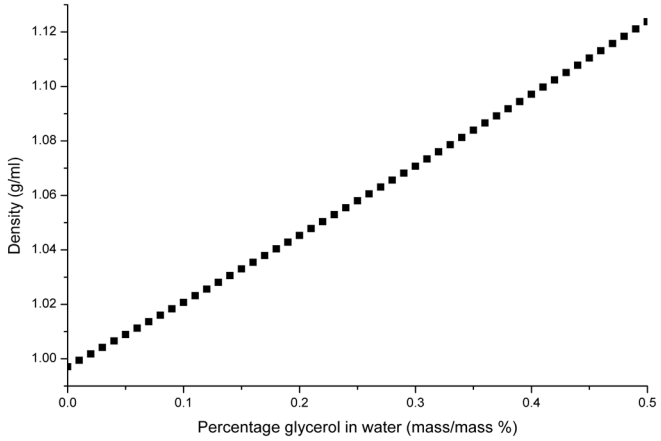

Figure 5-14: Density of water-glycerol mixture [173]

The values for density ρ and viscosity μ used to evaluate Z in Equation (5-1) were calculated using Equation (5-4) to Equation (5-7). They are tabulated in Table 5-1.

	ρ	μ	Δρ	$\mu_{av.}$
Solutions	**kg.m^{-3}**	**Pa.s (x10^{-4})**	**kg.m^{-3}**	**Pa.s (x10^{-4})**
Methanol	**787**	**5.4**	**98**	**9.4**
Water-methanol mixture	**885**	**13.4**		
Water	**997**	**8.9**	**74**	**16.8**
Glycerol-water mixture	**1071**	**24.7**		

Table 5-1: Properties of the solutions, ρ is the density, μ the viscosity, Δ ρ the difference of density between the solutions of a fluidic system, and μ_{av} the average viscosity of the fluidic system.

Table 5-2 tabulates the values for flow rate υ, the typical length of the device cross-section a, the distance at which the measurement were performed L, and the values of Z obtained using Equation (5-1). The angle of rotation, θ, was measured

experimentally from the images in Figure 5-6 and Figure 5-10, and predicted from the value of Z according to Equation (5-8) [155].

$$\theta \approx -2.39Z^2 \times 10^{-3} + 0.91Z \qquad \textbf{(5-8)}$$

The theoretical and observed values of θ are shown in Table 5-2.

	υ	a	L	Z	θ calc.	θ obs.
Fluidic system	**$m.s^{-1}$ ($x10^{-2}$)**	**m ($x10^{-4}$)**			**deg.**	
Water-Methanol	**1.04**	**2.82**	**5**	**13.8**	**12.1**	**25**
			40	**110.8**	**71.5**	**62**
			89	**246.5**	**79.1**	**72**
Water-Methanol	**3.1**	**2.82**	**5**	**4.6**	**4.2**	**14**
			40	**37.1**	**30.4**	**40**
			89	**82.5**	**58.8**	**48**
Water-Glycerol	**1.04**	**2.82**	**5**	**5.8**	**5.21**	**28**
			40	**46.6**	**37.2**	**70**
			89	**103.7**	**68.6**	**79**

Table 5-2: Flow rates ν, typical length of the device a, position in the device L. Values of Z obtained using Equation (5-1), angle of the rotation of the interface, θ, obtained using Equation (5-8) and observed in Figure 5-6 and Figure 5-10.

Discrepancies between calculated and observed values of the interface rotation are evident and arise from numerous reasons. Equation (5-1) is true for channel aspect ratio of 1:1. The wall effect becomes strong when the aspect ratio deviates from unity [150]. In the case of a shallow channel, where the depth is smaller than the width, tilting happens faster at the beginning of the channel and more slowly at the end. This results in θ_{obs} being greater than θ_{calc} at the 1st position in all the cases presented in Table 5-2. As the residence time is increased, θ_{obs} will eventually become smaller than θ_{calc}. This inversion is observed for the methanolic system at position 2 and 3 at flow rates of 1.04 m/s and 3.1 m/s, respectively. It is not observed for the glycerol-water system. However the difference between θ_{obs} and θ_{calc} becomes decreasingly important as the fluid travels down the channel. Finally, Equation (5-1) is true for

$Z \leq 196$. In the case of the methanolic system at 50 µl/min, the third position is out of the range covered by Equation (5-1).

Whereas the enhanced rotation of the interface at the beginning of the channel can be explained by the channel aspect ratio, the fact that at equal flow rate, the glycerol system interface rotation is greater than the methanolic one is a matter of concern for the validity of the model developed by Yamaguchi et al. The model has been validated by a single experiment involving a single fluidic system under one flow rate. Therefore the model does not take into account the effect of diffusion, interfacial tension and viscosity which are characteristics of each individual fluid and its mixtures.

5.4 Conclusion

2PE-FLIM has been used successfully to image the mixing characteristics of water-methanol mixtures and water-glycerol mixtures. The ability of 2PE-FLIM to provide three-dimensional high spatial resolution, quantitative mapping of the solvent composition is unequalled. Whereas confocal FLIM imaging does, in theory, slightly outperform the spatial resolution of two-photon excitation, images generated by the latter technique do not suffer from contribution of out-of-focus fluorescence. The two solvent systems used in the present chapter, in conjunction with their fluorescent probes, were devised to observe the effect of gravity on micromixing. Mixing of methanol and water-methanol mixtures had previously been studied by Mendels et al. [7]. Due to discrepancies between computational and experimental results, the authors became aware of the relative importance of gravity in such a fluidic system. Images obtained by 2PE-FLIM confirm the validity of this hypothesis.

3D imaging of microfluidic devices using 2PE-FLIM has revealed the challenges involved in developing specific CFD models for the microscale. Whereas huge efforts have been made in order to identify relevant forces exerted on fluids contained in microchannels, it is not yet possible to fully model the behaviour of micro-flows. This becomes evident when comparing the observed and calculated

angle of rotation of different fluidic systems using the FLIM images and Equation (5-1). This equation, developed by Yamaguchi et al. to relate rotation angle and density difference between two fluids in a microchannel does not take into account differences in the channel aspect ratio, the effect of viscosity differences, diffusion and interfacial tension. Such considerations would increase the complexity of the problem and would lead to the inability to solve it analytically. The present chapter shows the unique abilities of 2PE-FLIM to simultaneously map the rotation of the interface between two fluids of different densities, provide direct quantitative reading of solvent composition in three spatial dimensions, quantify mixing processes by diffusion through the interface, and observe the effect of the vicinity of the walls of the channel on the flow behaviour. It is the first time 2PE-FLIM has been used to this effect. Thanks to its viscosity characteristics (See Figure 5-11), the water-methanol fluidic system provides good ground for further investigation of the relative importance of density difference independently from viscosity difference and vice-versa.

One characteristic of the flow that FLIM alone cannot resolve is the effect of viscosity gradient on advective forces (flow velocity profile). In Chapter 6, it is shown how FLIM can be combined with μ-PIV to obtain this kind of information.

6 SIMULTANEOUS USE OF MICRO-PARTICLE IMAGING VELOCIMETRY AND FLUORESCENCE LIFETIME IMAGING MICROSCOPY

6.1 Introduction

As the emerging field of microfluidics technology finds new and promising applications, the need to perform accurate measurements of flow parameters increases. Although the flow at the microscale is typically laminar, and may thus, in principle, be readily determined by means of analytical studies and computational analysis, the complex nature of the flow poses a challenge [174]. The ability to perform measurements, not only of bulk quantities such as pH, temperature and flow rate, but also detailed studies of the flow field inside microfluidic systems, becomes essential.

Precise control and detection of chemical reactions and environmental parameters is particularly crucial for the development of microfluidic devices for molecular analysis and molecular biology, also called micro-total analysis system (μ-TAS) or lab-on-a-chip (LOC). In μ-TAS, the full sequence of lab processes at the macroscale is integrated on a chip. Standard analytical operations include sample preparation, injection, fluid and particle handling, reactors and mixers, separation, and detection [175]. Some facets of optical detection in and on μ-TAS are described below.

Assessing the flow field is of primary importance in μ-TAS where dominant transport phenomena can inhibit the device functionality [176], where fluid characteristics such as density and viscosity are sensitive to changing chemical and

environmental factors, and when two fluids of different characteristics are brought in contact. The use of multi-modality simultaneous imaging of the flow field, using μ-PIV, and environmental factors (solvent composition, viscosity and temperature), using FLIM, is described in this chapter.

6.1.1 Importance of optical detection in μ-TAS

The techniques for detection associated with μ-TAS are divided into optical and electrochemical methods. However, the superiority of the former in many respects has encouraged its development and integration for detection in μ-TAS. Microscopic optical methods offer high spatial resolution, real-time detection, and sensitivity down to the single molecule level. They are non-invasive, and are easy to integrate because, as opposed to micro-electrodes, the optical components do not need to be in contact with the sample to provide measurements. Furthermore, the combination of organic or polymer semiconductor devices, that can be fabricated at low cost [177], with microfluidic chip structures, provides a promising route towards disposable, compact and portable devices for environmental, bioanalytical and diagnostic applications [178]. Monitoring a chemical reaction that occurs when two or more fluids come in contact requires the acquisition of information about mixing processes in terms of mass transport, which can be measured using μ-PIV but also requires quantification of the amount of products and reagents in the system, and measurement of the enthalpy of the reaction which can be done using FLIM.

Simultaneous measurements of environmental factors and flow fields would be of particular interest to the study of fuel flow behaviour and the mapping of fuel concentration in fuel cells. It could also allow devices, the functionality of which is based on environmental gradients, to be fully characterised. Such devices are, for example, microfluidic mixers based on temperature-gradient-induced chaotic advection [179] or LOC where concentration gradients and concentration arrays of diffusible samples play important roles in the study of cell biology [180, 181], biochemistry [182, 183], and high-throughput assays for combinational chemistry [184].

6.1.2 Importance of single-photon avalanche photodiode for the miniaturisation of the detection on a chip

Most of the optical detection for chemical analysis in microfluidic devices is performed using conventional apparatus. This result in the mm-size chip sitting on bulky equipment (e.g. microscopes), being illuminated by laser light provided by metre-long cavities (e.g. Ti:S laser module), with the signal being detected by expensive detectors that cannot be miniaturised and that require high voltage supply (e.g. PMT, time-gated cameras). A perfect LOC should be portable, low-cost, automated, and, ultimately, disposable. In terms of optical detection this means miniaturising at least the light source and the light detector, and finding an optical setup that keeps the use of optics to its minimum.

The advent of GaN semiconductor sources 15 years ago [185] has opened a perspective into the miniaturisation of light sources for time-resolved fluorescence analysis. These sources are low cost, reliable and compact, which satisfies the requirement for the development of LOC. Furthermore, their emission wavelengths match the absorption lines of most of the fluorophores used in fluorescence analysis and their relatively short pulses (<1 ns) allows time-resolved fluorescence measurements to be performed. A GaN semiconductor LED has been successfully integrated on a chip and used to measure the fluorescence of microspheres which could be detected at concentration of 0.12 μM [186]. Generally, the work on monolithic integration of light sources for detection in microfluidic systems has been very sparse [187]. However, a few other types of light sources have been integrated on chips. For example, organic LEDs (OLED) have been fabricated on microfluidic glass windows [188, 189]. They were successful at detecting fluorophores at concentration of 1 μM [189].

The choice of integrated detectors is driven by the feasibility of their miniaturisation and by the detection requirements to perform the desired measurements. The most common light detectors for luminescence or fluorescence studies are PMTs and inorganic semiconductor photodiodes. However, due to the large size and high voltage requirement of the former and cost and complex fabrication of the latter, these detectors are not the ideal candidates for the integration

of optical detection in microfluidic devices. Instead, thin film organic photodiodes have been implemented and validated for chemoluminescence based diagnostic tests [178]. The use of a single-photon avalanche diode fabricated on a chip has also been reported. The sensitivity of the device allowed concentration of 6 pM to be detected [190]. The combination of single photon capabilities offer by SPADs and the minute volume handled in microfluidic devices bears promise for detection capability at the extremes of the concentration range. On one hand, this allows the detection of a very few molecules and on the other, at high concentration, it prevents undesirable effects associated with conventional measurements techniques such as re-absorption phenomena. These capabilities can be exploited in forensic analysis where minute volume of sample have to be analysed and in photophysics for the study of fluorescent dye aggregation at high concentration.

The use of a GaN microLED array in combination with a miniaturised SPAD array has led to the fabrication of a fully integrated detection device capable of fluorescence lifetime measurements for LOC applications [191].

6.1.3 Assessment of flow behaviour at the microscale

Correct design of microfluidic devices prior to their assessment in the lab is a quasi-impossible task for several reasons. In the simple case of the operation of a T-mixer, reliable input data of the fluid properties and their mixtures are required. This means finding standards for at least the density, the viscosity, the thermal conductivity, and the diffusion coefficients of the fluids and their mixtures. Gathering this information, when it is available, is tedious and the sources does not always warrant their traceability to standard fluids and methods [7]. Furthermore, whereas the Navier-Stokes equations can be solved exactly in some simple cases [192], solving them becomes an impossible task when two fluids of different densities and viscosities come in contact in a T-mixer configuration. Therefore, in order to validate CFD simulation for the microscale, the models need to be assessed against experimental data. Mendels *et al.* studied the thermal and solutal transport in a T-mixer [7]. Good correlation was found between experimental (FLIM) and modelled results. Whereas their work represents a step towards the full field

monitoring of the chemical reaction, the authors acknowledge the need for the implementation of a particle velocimetry technique to quantify advective transport in the microchannel. Sato *et al.* have compared heat transport due to convection to heat transport due to conduction at a microfluidic T-junction [193]. The temperature map in the microfluidic device was generated by probing the fluorescence intensity of a temperature sensitive dye applied onto the surface cover glass of the device. Such a method will induce measurement errors intrinsic to fluorescence intensity detection. Furthermore, heat transfer properties of the glass cover are very different from the properties of the main substrate (PDMS). Therefore, considering that the temperature of the fluid can be approximated to that of the cover glass is a crude assumption. Convective transport was measured in a decoupled experiment using μ-PIV in only one of the two inlet streams and empirically extended to the whole T-junction. Sato *et al.* found that transport due to heat conduction in microfluidic devices was about 50 times more than that due to heat convection. This figure varies drastically from heat transport at the macroscale which is essentially due to convection alone.

6.1.4 Photophysical properties of Kiton red

Detailed photophysical studies of Kiton red have not been published to date. However, the photophysical properties of its non-sulfonated equivalent rhodamine B has been studied as a function of dye concentration [194], solvent viscosity [195], temperature [196], solvent polarity [197], and pH [198]. Although several models have been proposed to explain the dependence of temperature, viscosity and polarity on the fluorescence of rhodamine B, one explanation is common to the majority of the publications. The torsional dynamics of the diethylamino groups governs the nonradiative processes and is enhanced by solvent polarity and temperature [197, 199]. This effect leads to a decrease of rhodamine B and Kiton red fluorescence lifetime and quantum yield when the temperature or polarity of the solvent is increased. The molecular structure of Rhodamine B and Kiton red are shown Figure 6-1.

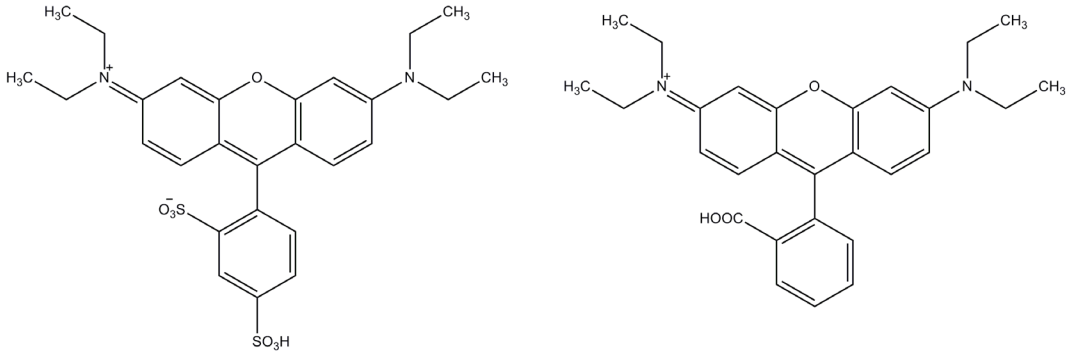

Figure 6-1: Molecular structure of Kiton red and Rhodamine B.

6.2 Experimental setup and procedure

6.2.1 Solution preparation

All solutions were prepared using HPLC grade water (Fisher Scientific), spectrophotometric grade glycerol (Sigma-Aldrich) and laser grade Kiton Red (Kiton Red, acid form, Sigma-Aldrich).

The solution of Rose Bengal (Bengalrosa, Aldrich), used to measure the instrument response of the SPAD on the open-frame microscope, was prepared at 100 μM in HPLC grade water. In order to quench the fluorescence of Rose Bengal, the water contained 5.4 M of potassium iodide (Fisherscientific) and 0.004 M of potassium hydroxide (Fisherscientific). For the temperature calibration on the chip, the concentration of KR was 100 μM.

For FLIM measurements the solution of KR were prepared at 250 μM and further seeded with 1.2 μm diameter polystyrene microbeads. Visual inspection of the solution revealed the density of beads in solution for further adjustment.

6.2.2 Optical setup

A schematic of the experimental setup used to simultaneously record FLIM and μ-PIV measurements is displayed Figure 6-2.

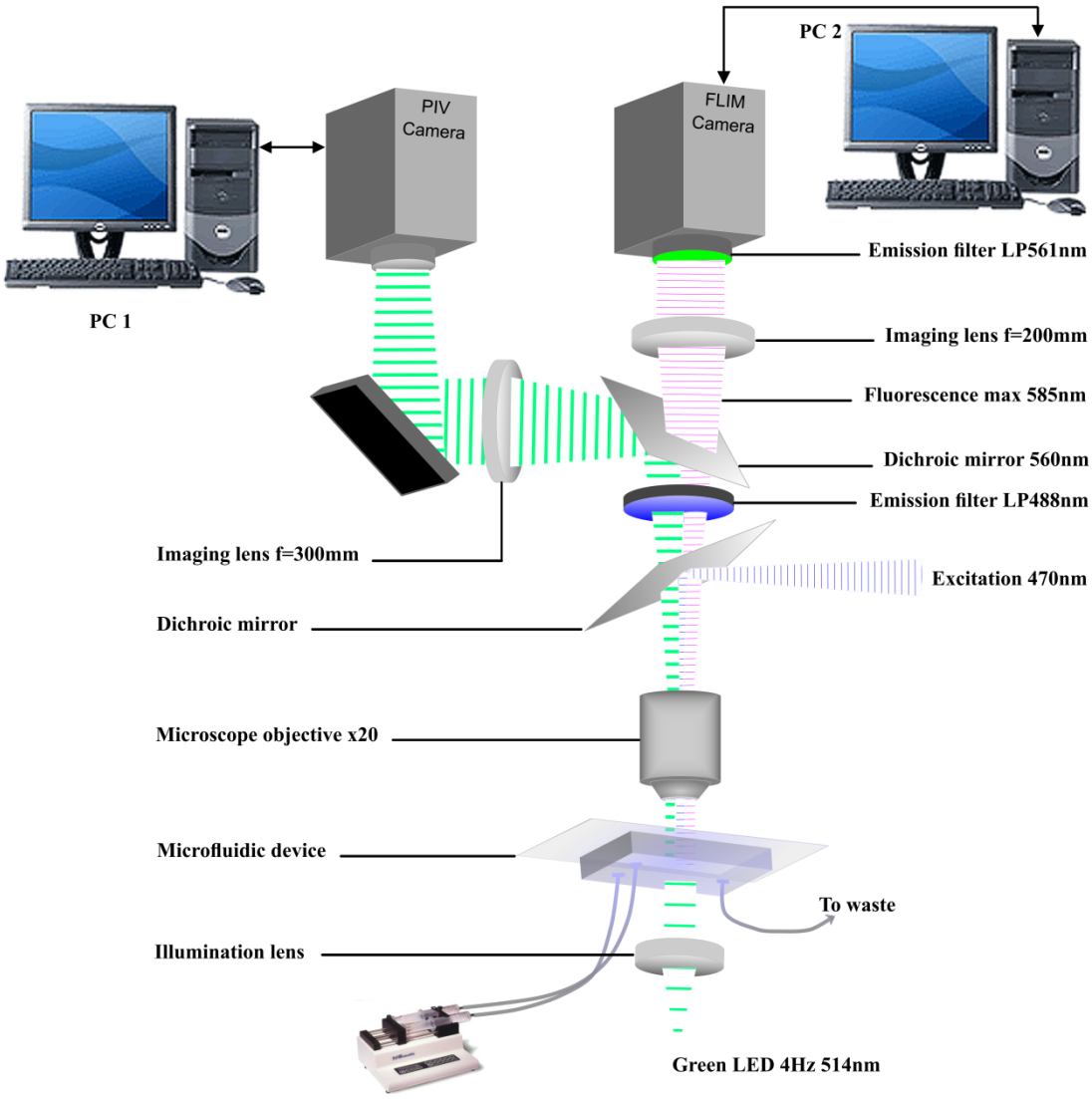

Figure 6-2: Schematic of the experimental setup used to simultaneously record FLIM and µ-PIV measurements.

The excitation light for FLIM was provided by a laser diode (LDH-P-C-470, Picoquant GmbH, Germany) controlled by a picosecond pulsed diode laser driver (PDL800-B, Picoquant GmbH). The laser diode emits at 468 nm and the repetition rate was set to 40 MHz. The beam was spatially reshaped using a pair of semi-cylindrical lenses, expanded and collimated, spatially filtered through an aperture and focused at the back focal plane of the microscope objective (x20, NA0.4, LMPlanFI, Olympus) after reflection off a dichroic beamsplitter (FF505-SDi01-25x36, Semrock). The fluorescence was collected through the same objective while unwanted scattered light from the excitation source and the green LED was removed

using fluorescence filters (LP02-488RS-25 and BLP01-561R-25, Semrock). The sample was imaged onto a gated intensified CCD camera (Picostar HR-12QE, LaVision GmgH, Germany) using an achromatic doublet lens (NT32-917, Edmund Optics Ltd, UK). FLIM images were recorded with 500 ps gate widths at 0.25 ns intervals. Five images were averaged to create the final image. The exposure time (50 to 100 ms) of the camera was set to obtain between 3000 and 4000 counts for the maximum intensity on a pixel. The data were analysed using DaVis 6.2 software running the Picostar DaVis setup.

6.2.3 Microfluidic devices

The microfluidic device used to record simultaneously viscosity using FLIM and flow field with µ-PIV was made from fused silica (LioniX BV, the Netherlands). The solutions were dispensed using PEEK® tubings that were held in place at the inlets and outlet using o-rings. The chip and o-rings were mounted together on a custom-built Perspex holder. A picture of the naked device is shown Figure 6-3. The silica substrate is 0.5 mm high and about 9 mm wide and long. The widths of the channels are 200 µm and 250 µm for the main channel and the inlet channels respectively. The advantage of such a device for flow visualisation and characterisation is its optical transparency across the UV-VIS-NIR spectrum and its rigidity.

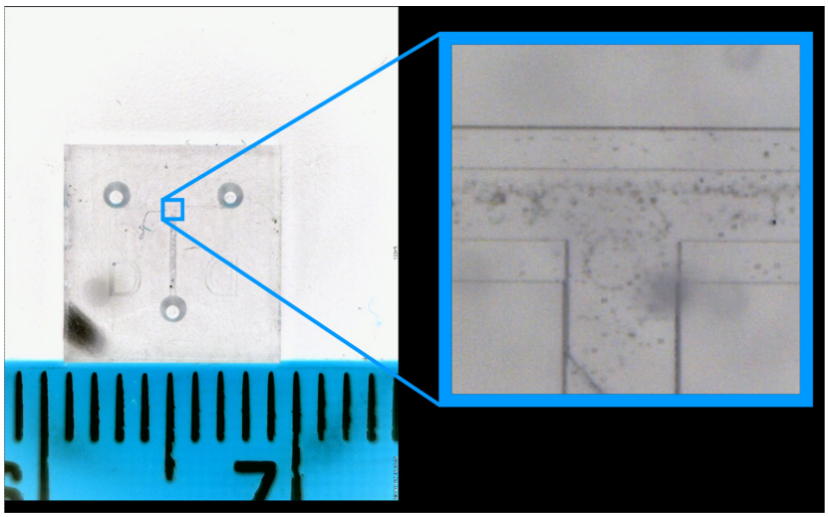

Figure 6-3: Picture of fused silica microfluidic device (left). The ruler is showing millimetre graduations. Enlarged picture of the T-junction (right).

A schematic of the fully mounted device used for the simultaneous measurement of temperature and flow velocity is shown Figure 6-4.

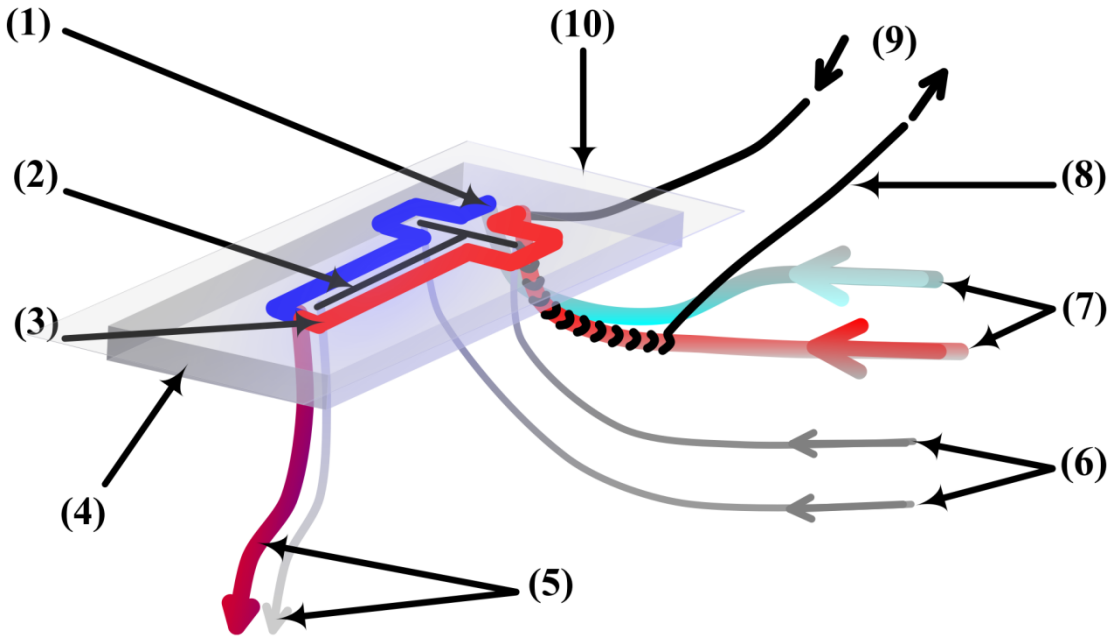

Figure 6-4: Schematic representation of the microfluidic device. Cold sink channel (1); microchannel (2); hot source channel (3); PDMS substrate (4); outlets (5); tubing providing sample to microfluidic channel inlets (6); tubing providing hot (red) and cold (blue) fluid to hot source (red) and cold sink (blue) channels inlets (7); nichrome wire (8) and current provided to it (9); optical window (microscope coverslip, 10).

With reference to Figure 6-4, the microfluidic device comprises two independent channel networks: the microchannel (2) and the channels controlling the temperature (1 and 3). The sample solution was pumped in the microchannel (2) using syringe pumps (KDScientific, Holliston, MA) through PEEK tubing (6) (Tub PEEK™ Yel, Upchurch Scientific, Oak Harbor, WA). The tubing was fitted at one end to syringes (BD 1ml Syringe, BD, Belgium) and at the other end to the microchannel inlets.

In order to generate a temperature gradient, the channels that control the temperature (1 and 3) surround the microchannel (2). They are separated from the microchannel by a PDMS wall 100 μm wide. Hot and cold water were pumped in opposite inlets by syringe pumps (KDScientific, Holliston, MA) through silicon tubing (7) (AlteSil™ High Strength Silicone Tubing, Altec Products Ltd, UK). The

tubing were fitted at one end to the channels inlet and at the other end to a syringe (BD 60 ml Syringe Luer-Lok™ Tip, BD 1ml Syringe, BD, Belgium). In order to provide cold water, one of the syringes was filled with ice and water. The water in the other syringe was heated by a Nichrome wire (9) coil around the tubing, the temperature of the heating coil was controlled by varying the current (ca. 500 mA) supplied by a DC power supply (Thurlby Thandar TS3022S). Typical flow rate was 350 µl/min for the heating/cooling channels.

6.3 Results

6.3.1 *In situ* calibration of the fluorescence lifetime of FLIM probes

Conventionally, the fluorescence lifetime sensitivity of FLIM probes is evaluated in a TCSPC setup, in conditions that differ greatly from their use in an imaging setup. The detection is made at 90º to the excitation beam, the fluorescent solution is contained in a cuvette and held in place in a chamber, and the dye concentration is kept well below the required concentration for imaging techniques. Fluorescence lifetime imaging is performed in an epi-fluorescent fashion and the dye at relatively high concentration is contained in the system under investigation. These differences in experimental configurations can affect the calibration of the fluorescence lifetime versus measurand because the sample chemical and environmental conditions are different. For example, at the concentration used in imaging, the fluorescence lifetime of fluorophores can vary from the fluorescence lifetime of less concentrated solutions used for TCSPC measurements due to aggregation. Furthermore, in microfluidic devices, the short optical path length (tens of microns) of the system allows for the use of high concentration of fluorophores whereas in a cuvette the concentration needs to be kept low to avoid re-absorption effects.

A SPAD has been implemented on the microscope in order to evaluate the potential of *in-situ* calibration. The optical setup used is shown Figure 6-5.

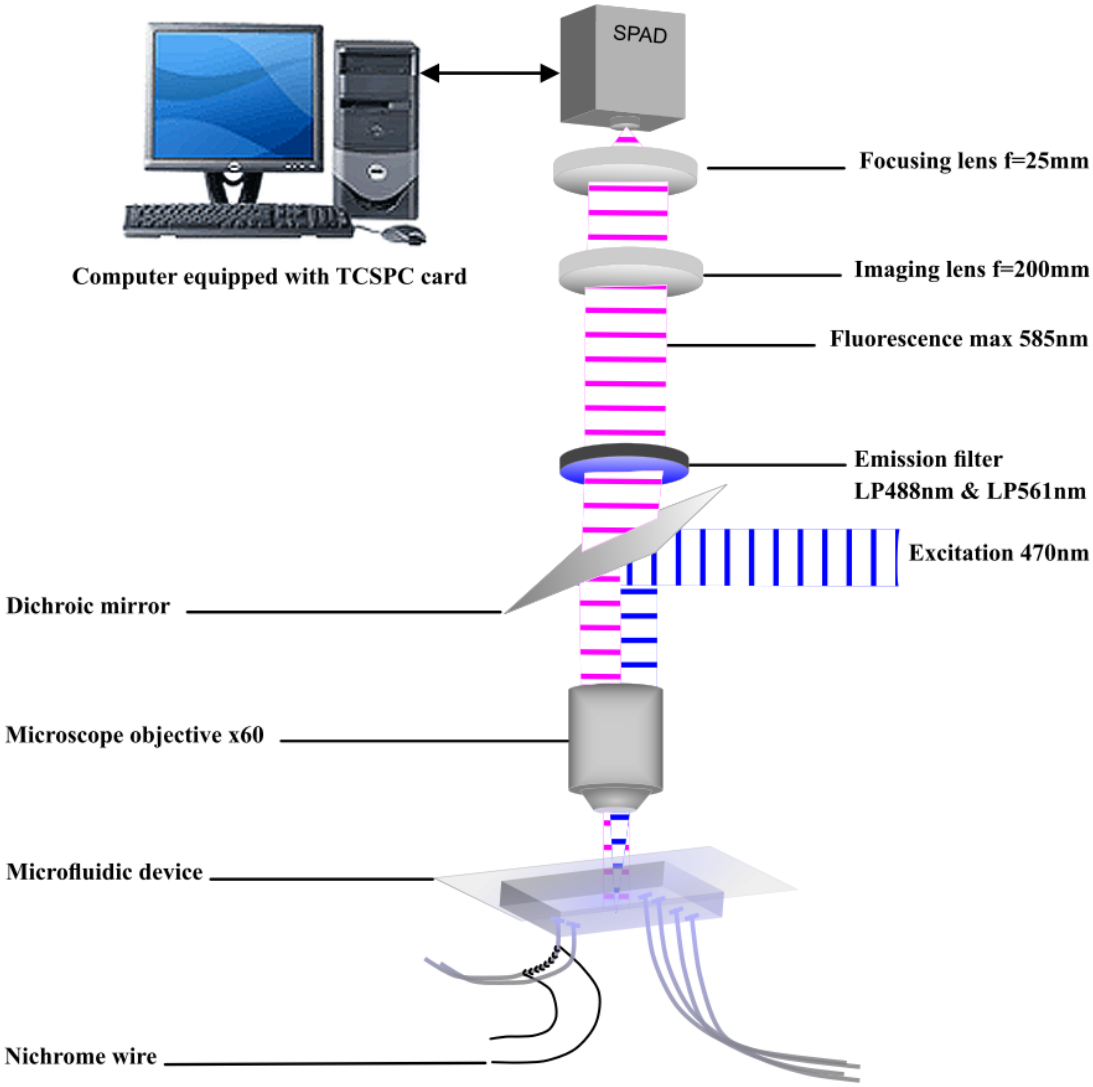

Figure 6-5: Experimental setup used for in-situ calibration of fluorescence lifetime sensitivity.

The main characteristic of the setup presented is the collimated beam illuminating the back aperture of the microscope objective (as opposed to focus in the FLIM setup). It provides the sample with a point excitation which avoids excitation of any fluorescence from unwanted areas. The fluorescence collected is tightly focused on the small detection area (50 x 50 μm^2) of the SPAD.

The instrument response function in time-resolved fluorescence is usually obtained by recording the temporal profile of the excitation source using scattered light from a suspension of colloidal silica (when emission is detected from a cuvette at 90º from incident beam) or by reflection of the signal from a reflective surface

placed on the stage of the microscope. However, single-photon avalanche photodiodes have a time response which is dependent on the wavelength detected. Whereas this has little effect on the processed signal when measuring lifetimes significantly longer than the instrument response of the photodetector, the colour-dependent response becomes particularly worrying when the fluorescence lifetime to be measured becomes more comparable to the time response of the photodetector. Therefore, researchers have looked into finding methods of recording an instrument response at the wavelength of fluorescence emission [29, 30, 37, 200, 201]. In microscopy this method allows the instrument response to be recorded without altering the optical path way, and without changing the filters and the dichroic mirrors [200]. The use of short lifetime dyes that emit at the desired wavelength was proposed more than 20 years ago [37, 201]. However, it is only recently, with the renewed interest in time-resolved fluorescence that this method has been applied in the lab [29, 30, 200]. In the green (530nm-570nm) and red (540nm-610nm) region of the spectrum, the use of erythrosine B (erB) and Rose Bengal (RBl) has been reported [29, 30]. Their molecular structure is presented Figure 6-6. These are short-lifetime fluorescent xanthene dyes with chemical structure similar to fluorescein. The main characteristic of these dyes is the presence of heavy atoms, iodides and chlorides, on the xanthene ring. The fluorescence lifetimes of ErB and RBl in pure water is 89 ps, and 77 ps, respectively [30, 160]. In order to further reduce the fluorescence lifetime of these dyes collisional quenching can be employed.

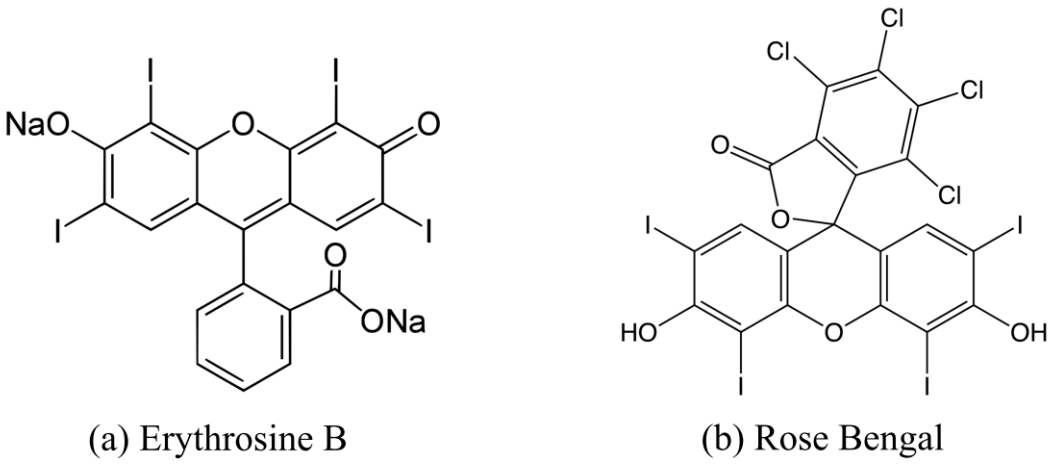

(a) Erythrosine B (b) Rose Bengal

Figure 6-6: Molecular structure of Erythrosine B (a), and Rose Bengal (b)

Collisional quenching involves non-radiative loss of energy from the excited state as a result of collisions with other molecules. Although this process is always present in solutions, some species, such as iodide ions, are particularly efficient in inducing the process and are classified as collisional quenchers [30]. By saturation of the solution with potassium iodide ([KI]>5 M) the fluorescence lifetimes of erB and RBl is shortened to 24 ps and 16 ps, respectively [29, 30].

The instrument response of the SPAD has been recorded at the laser diode wavelength (470 nm) using reflection of a mirror and at the wavelength of emission of KR (585 nm) using quenched RBl contained in a microslide. The mirror and the microslide were held in place on the microscope stage and the instrument response recorded using the setup shown Figure 6-5. The two instrument responses are shown Figure 6-7 on a linear and logarithmic scale.

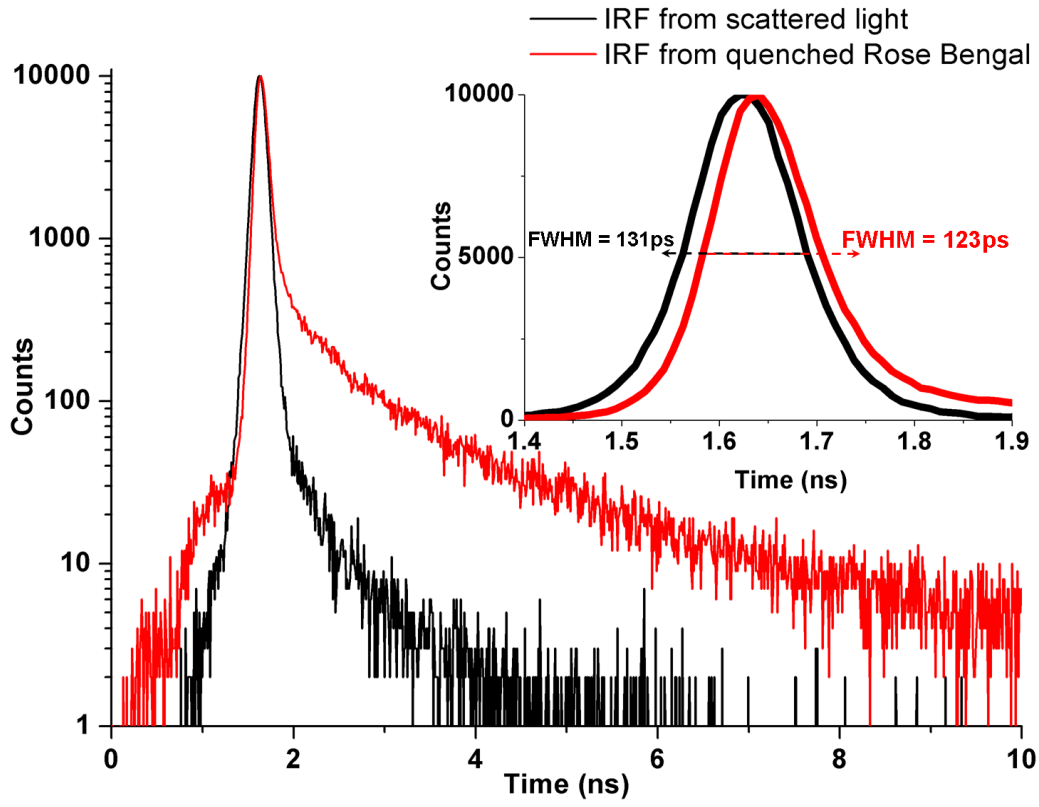

Figure 6-7: Instrument response of the SPAD recorded with scattered light (black line) and with quenched Rose Bengal (red line). The graph presented with the logarithmic y-axis shows the increasing diffusion tail at long wavelength. The FWHM is shown as measured on the graph presented with the linear y-axis.

The response of the SPAD recorded from excitation light (470 nm) reflected off a mirror placed on the microscope stage exhibits a full width half maximum of 131 ps. The instrument response recorded at 570 nm using the fluorescence of quenched RBl shows a narrower full width half maximum (123 ps) but shows a pronounced tail that persists for nanoseconds.

The fluorescence lifetime of KR solutions was measured in a microfluidic device at different temperatures. The calculation of the fluorescence lifetime using different fitting methods and different instrument responses is shown Table 6-1.

Method	Convolution				Tail-fitting	
IRF	Quenched Rose Bengal		Reflection of excitation light		NA	
Power (mW)	τ (ns)	χ^2	τ (ns)	χ^2	τ (ns)	χ^2
0	1.59	1.26	1.84	1.2	1.83	1.06
4.24	1.5	1.17	1.78	1.21	1.79	1.09
15.4	1.42	1.17	1.68	1.4	1.7	1.19
34.7	1.28	1.27	1.56	1.95	1.58	1.6
61.5	1.09	1.17	1.38	2.56	1.41	2.32
93.8	0.913	1.15	1.21	6.33	1.26	4.3
133	0.74	1.25	1.04	12.97	1.11	8.37
183.6	0.58	1.16	0.87	24.47	1	14.95
239	0.44	1.37	0.67	50.03	0.91	23.9
302.4	0.34	1.41	0.42	41.14	0.92	28.63

Table 6-1: Fluorescence lifetime of KR measured in a microfluidic device at different powers supplying the Nichrome wire (P=UI). Results obtained using deconvolution of the signal obtained from measuring the fluorescence of quenched Rose Bengal and reflection of the excitation light. The curves were fitted from the channel with maximum counts down to the channel with 50 counts. The third set of result is obtained by tail-fitting of the decay curves from 0.5ns after the channel with maximum counts. Decay curves background was set fixed to 2.

As observed by other researchers, the fluorescence lifetime of KR decreases with increasing temperature (increasing power supplied to nichrome wire) [7, 8]. The fluorescence lifetime of KR at room temperature (22.5ºC) was calculated to be 1.59 ns by convolution with the instrument response recorded using quenched Rose

Bengal. This value agrees with the lifetime measured by other researchers [8, 202, 203]. The values obtained from the convolution with the reflected excitation light IRF and from tail-fitting are much higher than any values ever reported for the lifetime of KR at room temperature in aqueous solution. The good fits obtained for the decays recorded at the lower temperature with these two methods can be attributed to the fact that the effect of the long tail of the instrument response does not result in a significant deviation from single exponential behaviour. This is because the tail of the instrument response has an exponential decay similar to the lifetime of KR at these temperatures. At higher temperature, the goodness of fit of the decay curves becomes increasingly unacceptable for both the tail-fitting analysis, and the convolution using the instrument response obtained by reflection of the excitation signal. Although the goodness of fit obtained from convolution using the instrument response recorded with quenched Rose Bengal deteriorates to some extent at higher temperature when the lifetime becomes shorter, it is evident that the IRF recorded in this way is a close approximation of the true IRF at the emission wavelength. Figure 6-8 shows the calibration curve obtained for the fluorescence

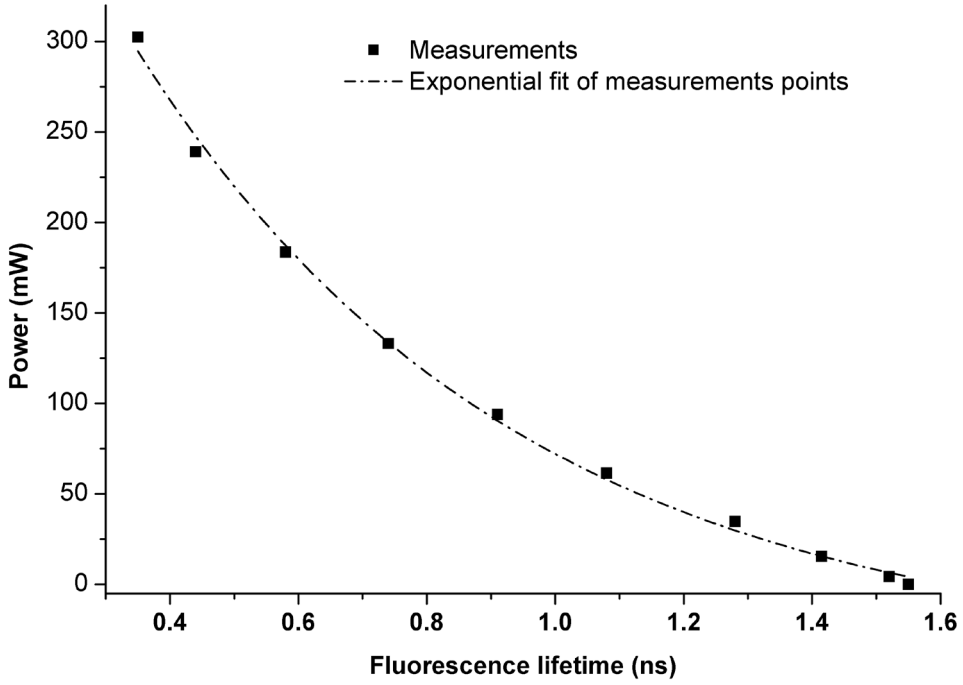

Figure 6-8: Measured fluorescence lifetime (x-axis) at different power supplied to nichrome wire (y-axis) (■). Single exponential fit to the data (-·-). The empirical relation between the power and the fluorescence lifetime is given by P=-40.63 + 602.9*exp(-τ/0.6).

lifetime of KR at different temperatures. In order to generate a calibration curve to analyse the FLIM images, the decays recorded have been convoluted with the IRF obtained with quenched Rose Bengal from 0.5 ns after the channel with maximum counts.

6.3.2 Fluorescence lifetime of Kiton Red in water-glycerol mixtures

The calibration of glycerol content as a function of the fluorescence lifetime of KR was determined Section 5.3.3.

6.3.3 Simultaneous mapping of viscosity and velocity fields

6.3.3.1 FLIM images of viscosity

Figure 6-9 shows how the FLIM images give direct information about the glycerol content across the T-junction of the microfluidic device. The red extreme of the scale corresponds to a fluorescence lifetime of 2 ns and the blue to a fluorescence lifetime of 1.5 ns. With respect to the calibration curve, the blue region corresponds to the aqueous solution and the red region is the 30% mass/mass mixture of glycerol and water.

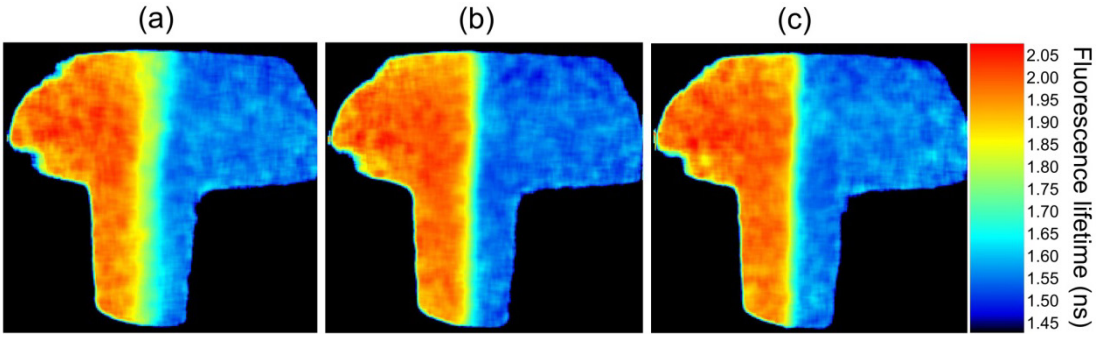

Figure 6-9: FLIM maps of the microfluidic T-junction. Flow rate is 1µl/min (a); 5µl/min (b); 10µl/min (c). Fluorescence lifetime ranges from 1.5ns in the blue region to 2ns in the red region.

The three images Figure 6-9 are FLIM images of the T-junction of the microfluidic device generated at three flow rates: 1 µl/min (a), 5 µl/min (b), 10 µl/min (c). They show how the residence time, which is inversely proportional to the flow rate, influences the mixing of the two solutions. The sharp transition gradient at 10 µl/min becomes less pronounced when the flow rate is reduced to 5 µl/min and a

diffusion zone is clearly formed at 1 µl/min. This is characterised by an extended rainbow like region on Figure 6-9(a).

6.3.3.2 Velocity field maps

Using µ-PIV, velocity field (Figure 6-10) were acquired simultaneously with the FLIM maps (Figure 6-9).

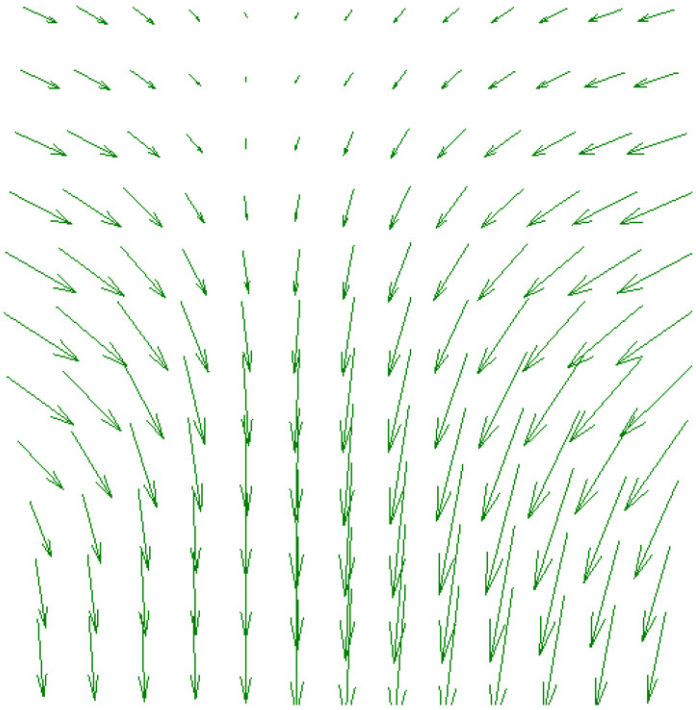

Figure 6-10: Velocity field map of the T-junction of the microfluidic device. The data recorded to generate this map and the FLIM map Figure 6-9(c) have been recorded simultaneously. Each arrow shows the direction and magnitude of the flow in an interrogation area. The water-glycerol mixture is flowing from the top left and the water from top right.

The raw data (images pair) are divided into interrogation areas. The size of the interrogation areas determines the final spatial resolution of the measurement. The interrogation area has to be such that a tracer particle travels no more than 20% of its size. To generate Figure 6-10 a grid was made of interrogation areas of 128 pixels by 128 pixels that overlap by 30% onto each other, resulting in the velocity field map having 11 by 13 interrogation areas. Therefore, the resolution of the measurement is 15x15x47 μm^3. The arrows represent the average displacement of a tracer particle in an interrogation area. Therefore, the velocity field map is an array

of 11 by 13 arrows (vectors). As in Figure 6-9, the right side of the T-junction on Figure 6-10 corresponds to the water inlet and the left side to the mixture of glycerol and water.

The velocity field map gives information about the convection phenomena in fluidic systems. In microfluidic devices, the convection is mainly divided into advection in a direction parallel to the flow and diffusion across the width of the device or at right angles to the flow. Due to enhanced surface effects, the flow in microfluidic devices is in the deep laminar regime (See Section 2.4). Therefore, the velocity field maps of the T-junction exhibit a wall-like separation of the streams coming from opposite inlets. At low flow rate, two fluids with the same chemical and physical properties would exhibit perfectly symmetrical and laminar transport behaviour. However, a gradient of the fluid properties across the device induces heterogeneity in the flow behaviour of the incoming streams. In the case presented Figure 6-10, water and the mixture of water and glycerol have different densities and viscosities. These properties are associated with advection and diffusion phenomena. Therefore, one can expect a flow behaviour that is non-symmetrical across the channel. Actually, it can be seen on Figure 6-10 how the convection is more important (longer arrows) on the right side of the channel. Furthermore, the component of the vector perpendicular to the channel seems more important in the right side of the channel than on the left side.

6.3.3.3 Correlation between FLIM images and velocity field maps

In order to correlate the results obtained by μ-PIV and FLIM, the magnitude of the velocity field and the fluorescence lifetime decay across the channel were extracted from the region of interest shown Figure 6-11.

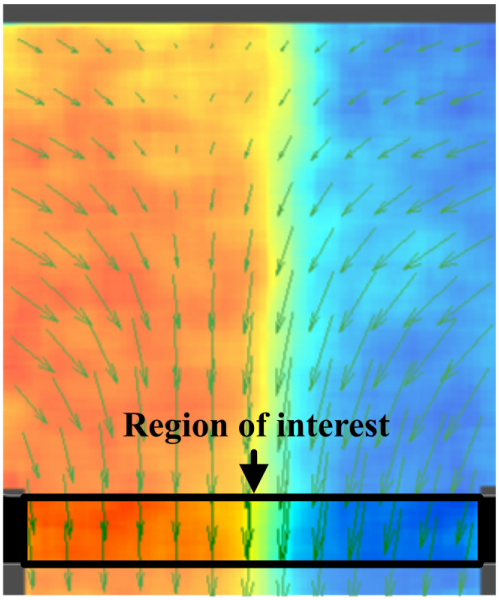

Figure 6-11: Velocity field map of the T-junction at flow rate of 10 µl.min^{-1} superimposed on the corresponding FLIM image. The data shown in Figure 6-12, Figure 6-13, and Figure 6-14 are extracted from the black rectangle labelled 'region of interest'.

The fluorescence decay curves were tail-fitted using F900, the calculated lifetimes converted into glycerol content using Equation (5-2), and viscosity using Equation (5-3). The resulting viscosity profiles are shown Figure 6-12. These show how varying the flow rate induces a displacement of the sharp gradient transition. It has to be noted here that the glycerol concentration does not scale linearly with viscosity. Therefore, whereas concentration profiles can provide quantitative information about mixing processes, Figure 6-12 strictly reports the physical characteristic of the fluid across the channel, not its composition. However, the displacement of the transition gradients and the extension of the diffusion region reflect changes in the relative importance of the different transport effects.

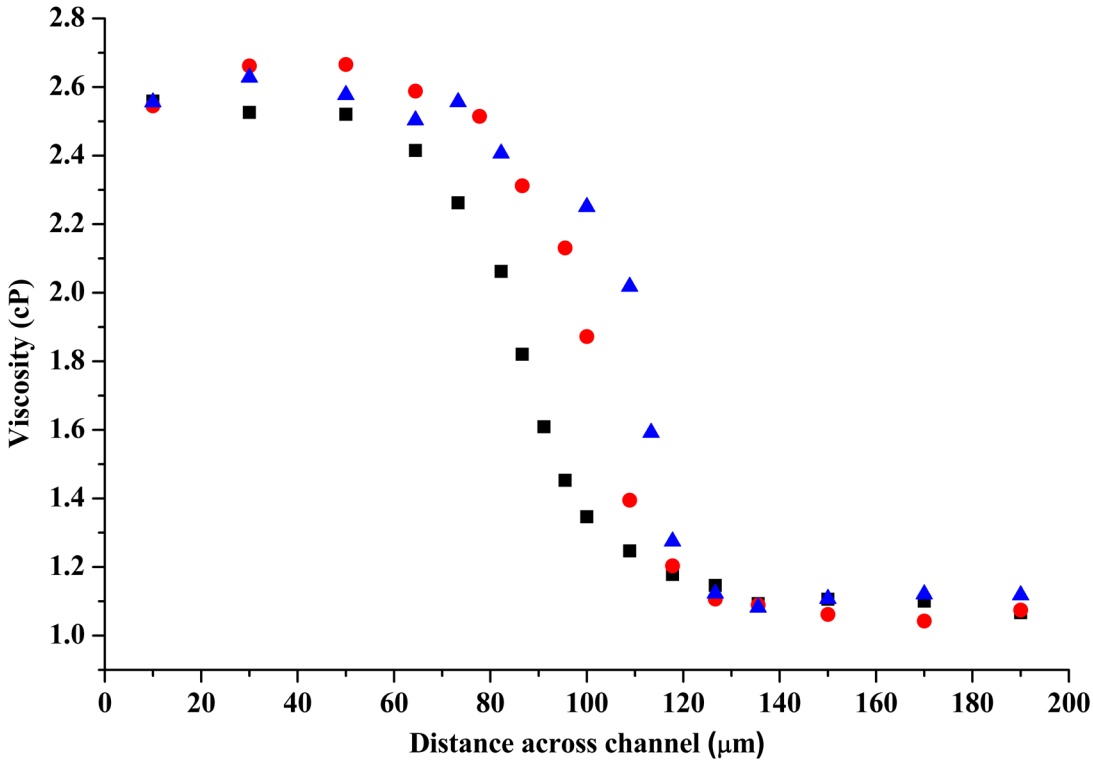

Figure 6-12: Viscosity profiles calculated from data extracted from FLIM images (Figure 6-9). Flow rates are 1 µl/min (black squares); 5 µl/min (red dots); and 10 µl/min (blue triangles).

The extension of the diffusion region observed in Figure **6-12** at low flow rates results from an increase in the residence time of the solutions. At high flow rates, the displacement of the viscosity gradient to the right of Figure **6-12** is due to advective forces scale linearly with flow rate and fluid density. When increasing the flow rate, those forces will be favoured and the denser fluid will induce a displacement of the interface between two streams toward the least dense fluid. In Figure 6-12, this is observed by a displacement of the interface between the water and glycerol mixture (left) and pure water (right) toward the less dense fluid, water (right). This phenomenon has been predicted by CFD calculations [152].

The change of viscosity profile at different flow rates induces a change of the velocity field in the microfluidic device. Figure 6-13 and Figure 6-14 show the velocity profile of the flow in the region of interest associated with the viscosity gradients at 1 µl/min and 10 µl/min, respectively.

The overall shapes of the two velocity profiles shown Figure 6-13 and Figure 6-14 are different. At 1 µl/min (Figure 6-13) the flow has a characteristic Poisseuille profile with a maximum slightly shifted towards the water side which is less viscous, offering less resistance to the pressure-driven flow.

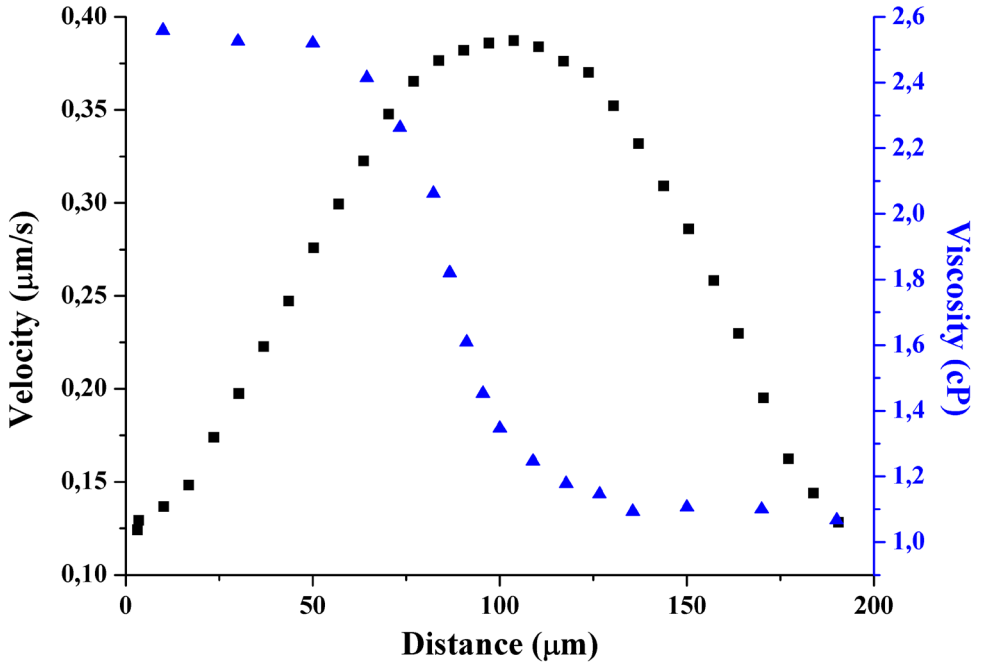

Figure 6-13: Velocity profile (black squares) and viscosity profile (blue triangles) of the microfluidic device across the section shown in Figure 6-11, at a flow rate of 1 µl/min.

At 10 µl/min (Figure 6-14), the decreased diffusion and increased longitudinal advection results in a step-like viscosity profile at the interface between the two fluids. The two incoming streams seem to travel independently from each other, separated by the wall behaviour of the viscosity step. This behaviour results in the observation of two flow fronts forming the velocity profile observed in Figure 6-14. However, this observation would need to be supported by a thorough statistical assessment of the experimental results in order to conclude on the degree of independency of the two flows.

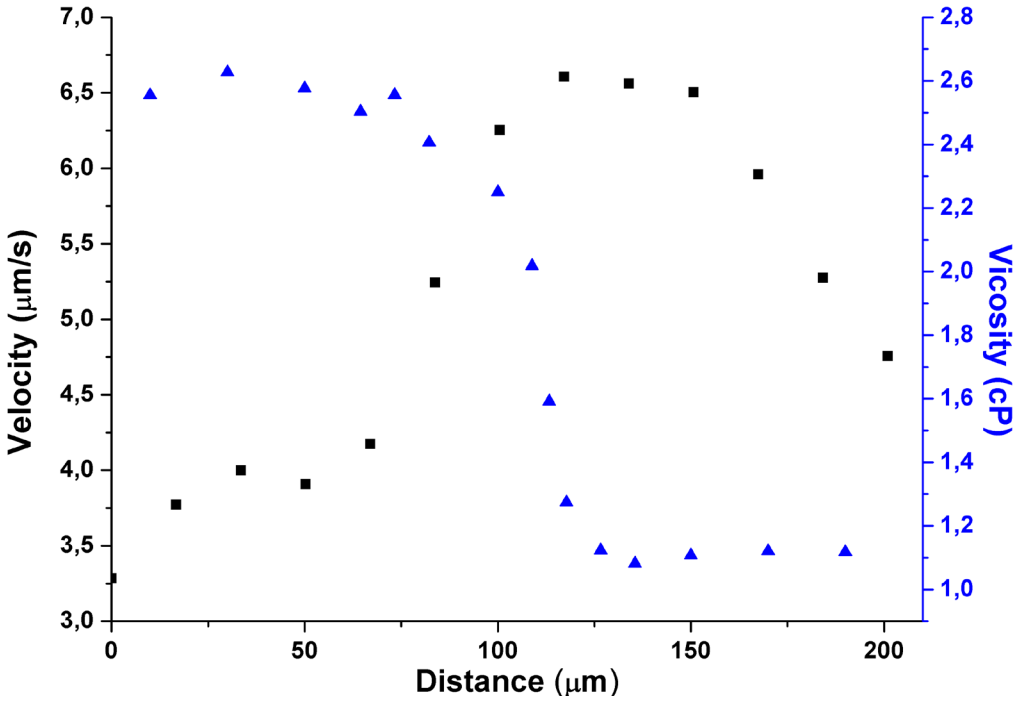

Figure 6-14 Velocity profile (black squares) and viscosity profile (blue triangles) of the microfluidic device across the section shown in Figure 6-11 at a flow rate of 10 µl/min.

6.3.4 Simultaneous mapping of temperature and velocity fields

6.3.4.1 FLIM images of temperature

FLIM images of the T-junction of a microfluidic device were generated in order to investigate possible alteration of the flow behaviour due to a temperature gradient generated across the microchannel. Figure 6-15 shows the fluorescence lifetime gradient at the T-junction of the microfluidic device. The low lifetime values (~0.8 ns) correspond to the higher temperature. They are associated with the red colour on the image. The long lifetime values (~1 ns) correspond to the lower temperature and are associated with the blue colour.

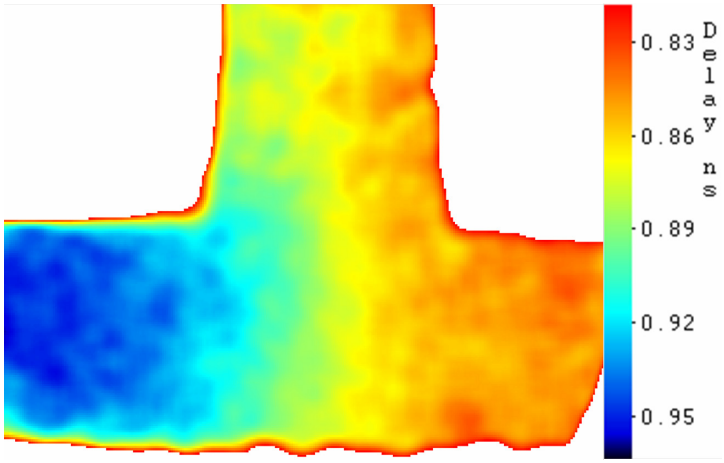

Figure 6-15: FLIM image of the T-junction of a microfluidic device subjected to an axial temperature gradient. The fluorescence lifetime scale ranges from 0.95 ns which corresponds to the lower temperature inlet (blue region) to 0.80 ns which corresponds to the higher temperature region (red region).

Whereas at the macroscale the dominant heat flux is due to convection, at the microscale the heat flux due to conduction has been found to be 50 times that due to convection [193]. This results in a rapid thermal equilibrium reached at low flow rates. It is clearly visible on Figure 6-15 where the gradient of temperature across the inlets vanishes almost as soon as the two streams come in contact. In a previous publication [193], one of the inlet channels was heated with a Pt thin-film heater before the T-junction. Therefore, the heat fluxes between the two incoming streams at the T-junction were observed in a thermally non-controlled environment and highly subjected to heat losses due to thermal contact with the surrounding environment. In the case studied here, the temperature gradient is imposed by a cold sink and a hot source that run from the left inlet and right inlet respectively and along the left and right wall of the main microchannel down to the outlet. In such a microfluidic device, where the flow is laminar and convection occurs mainly parallel to the channel, dominance of convective heat transport would result in a sharp gradient of temperature across the channel. However, as opposed to heat transfer at the macroscale which mainly occurs by convection, the small distances associated with microscale promote heat transfer due to conduction that scales with $1/l^2$.

6.3.4.2 Correlation between temperature gradient and flow profile

Figure 6-16 shows the velocity profile extracted at the T-junction.

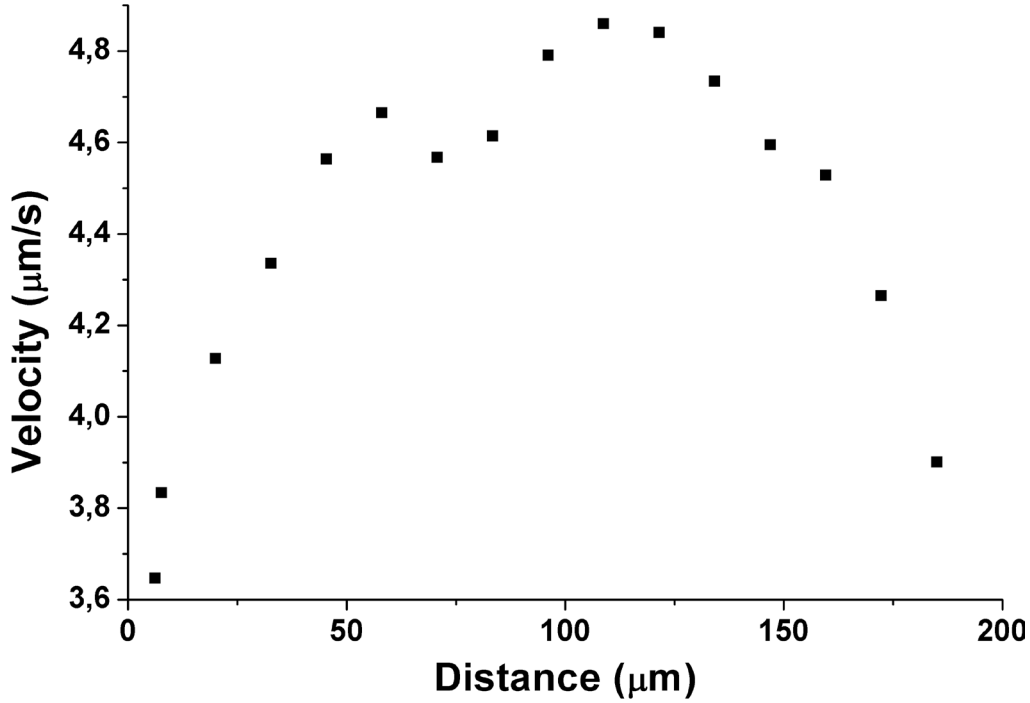

Figure 6-16: Velocity profile across the microchannel at the T-junction. Flow rate 7 µl/min.

As observed in Figure 6-16, the temperature gradient across the channel has a similar effect on the velocity profile as the viscosity gradient. The introduction of a temperature gradient affects the same physical and chemical properties as the gradient generated with pure water and the water/glycerol mixture. Water has a density and viscosity which are temperature-dependent. When the temperature of water is increased, it becomes less viscous and less dense. Therefore, it can be expected that the heated side of the channel exhibits higher velocity than the cooled side in the same way that the pure water exhibit higher velocity than the water/glycerol mixture in Figure 6-13 and Figure 6-14. It is indeed the case as shown Figure 6-16 where the appearance of two flow fronts with a velocity maximum on the side of the less viscous fluid is observed.

6.4 Conclusion

For the first time, FLIM has been combined with μ-PIV. The two techniques have been used simultaneously to quantitatively map complementary properties in a microfluidic device.

The effect a viscosity gradient has on the velocity profile across a microfluidic channel, has been investigated using a water-glycerol fluidic system. At 1 μl/min, the typical Poiseuille profile was observed with a velocity maximum slightly shifted towards the less viscous stream. At higher flow rates, the residential time of the sample in the device is reduced and transport by diffusion no longer irons out the interface between the two streams. The two incoming streams travel independently of each other as if the sharp viscosity gradient generated a wall to separate them. This results in the observation of two flow fronts.

The fluorescence lifetime of Kiton Red as a function of temperature has been calibrated *in situ* using TCSPC technique and a SPAD. The wavelength effect on the response of SPADs has been circumvented by using the quenched fluorescence of Rose Bengal to record an instrument response. Using the special fixtures of a custom-made microfluidic device, a temperature gradient has been generated across a channel. As for the water and glycerol system, the temperature gradient across the channel also affects the profile of the flow that deviates from the typical Poiseuille profile. The velocity maximum is on the heated side of the channel where the fluid has a lower viscosity and the apparition of two flow fronts is noticeable at 7 μl/min.

7 MICROTHERMOMETRY: FLIM OF OPTICALLY TRAPPED PROBES IN A MICROFLOW

7.1 Introduction

Precise control of temperature is a key requirement in many microfluidic applications, for example, in biology for polymerase chain reaction amplification of DNA [204-206], in medicine for drug delivery [111], in electronics for heat dissipation [207] and in chemistry for control of reaction rates, determination of phase transition temperatures and activation energies [208]. However, the measurement of temperature on such a small scale is challenging. To date, attempts to measure temperature within microfluidic devices have been based on a number of different mechanical and optical approaches.

7.1.1 Measurements of temperature in microfluidic devices

Conventionally, temperature in microfluidics is measured via micro-thermocouples integrated within each chip. However, a major drawback to this approach is that it can only report the temperature of a very small volume of solution close to the thermocouple itself. It is well known that rapid heat dissipation within microfluidic devices can lead to significant non-uniformity of the temperature over the small intra-channel length scales, and thus, micro-thermocouples can, at best, only provide an approximate spatial temperature map. Additionally, the necessity of implanting the thermocouple within the device reduces measurement flexibility, and requires complex fabrication routes coupled with shortened device lifespans.

As an alternative, optical techniques are currently being developed to overcome some of the limitations of micro-thermocouples. Common approaches utilise the temperature sensitivity of the commercially available fluorescent dye Rhodamine B (RhB) combined with fluorescence intensity techniques [209-214].

However, such approaches are also beset with problems, for example, the adsorption of RhB on the internal surfaces of the device, which affects intensity and lifetime, photobleaching of the fluorescent probe [9], and variations in the excitation and detection efficiencies across the field of view of the microscope can all result in local artefacts in the measurement [215]. The use of methods based on the measurement of the fluorescence lifetime of a dye, such as fluorescence lifetime imaging microscopy (FLIM), overcomes some of these problems, and FLIM has been used successfully to generate high spatial resolution maps of temperature distribution in microfluidic devices [7, 8, 216]. Use of a customised polymer based temperature-sensitive fluorescent probe allowed the temperature in a microfluidic device to be mapped with a resolution of less than 0.1ºC [6]. While FLIM offers high spatial resolution and accurate mapping of the temperature in devices, the technique also exhibits some drawbacks since the fluorescent dye pervades the whole measurement volume. Although this may not be problematic for measurements on prototype devices during design and development, it precludes applications in functioning microfluidic systems where the presence of the dye would interfere with their functions. Such applications include microreactors, where the presence of the dye could interfere with chemical reactions, and biological application involving permeable cells where toxicity of the dye molecules can be problematic. Cells can be damaged or killed by direct chemical toxicity of the dye and also through dye-induced photosensitisation [217].

7.1.2 Non-invasive measurement of temperature in microfluidic devices

Attempts to overcome the problem of dye toxicity, by incorporating RhB into the polymer of the device [9], suffered the same shortcomings as both microthermocouples and fluorescence intensity-based methods, namely local artefacts and inaccurate measurement of the temperature in the channel.

The Brownian motion of nanoparticles has been proposed as an alternative technique to perform three dimensional measurement in microsystems and avoid toxicity effects [215]. While the nanoparticles used were not toxic to the system

studied in the published work, using Brownian motion is only feasible when there is no fluid motion. The requirement to measure the temperature while the device is in operation without introducing perturbations is, therefore, only fulfilled in the case of stop-flow operation with biological objects not sensitive to the nanoparticles tracked.

To date, techniques that have been used to measure temperature in microfluidic devices all have drawbacks. To address these drawbacks, an alternative method which permits the use of FLIM without the disadvantageous use of an intrusive fluorescent dye has been developed. This has been achieved by encapsulating the temperature sensitive Kiton Red (KR) fluorophore within a chemically inert microdroplet, which can be held and manipulated in the flow using optical tweezers.

7.1.3 Micro-emulsions in microfluidics

Micro-emulsions have been used to compartmentalise individual assays. They were first developed for directed evolution [218] and have found many applications in molecular evolution [219]. The fabrication and manipulation of micro-droplets have greatly benefited from microfluidic technologies. They allow for the high-throughput fabrication of highly monodisperse micro-droplets that can be fused, subdivided and used for the control of picoliter scale biochemical assays [220]. Therefore, much effort has been put into developing microfluidic platforms for the fabrication of micro-emulsions [221-223] for their use in biochemistry. In the work presented in this chapter, a temperature-sensitive fluorescent dye has been encapsulated in a double micro-emulsion. A single microdroplet was trapped using optical tweezers and used to locally probe the temperature in a microfluidic channel.

7.1.4 Manipulating objects in microfluidic devices

Optical tweezers have been used previously to manipulate objects within microfluidic devices, for example, to analyse flow fields by measuring the displacement of trapped beads [93, 224, 225], as micropumps or microvalves [226-228], for cell manipulation alone [229] or associated with a visualisation technique such as fluorescence microscopy [230], super resolution microscopy [231] or Raman

spectroscopy [232]. A fluorescein-labelled polymer bead has been trapped in a microfluidic device and its fluorescence intensity measured to determine the local pH [130]. In principle, a similar approach using a RhB-labelled bead might be used to measure temperature. However, immobilisation of RhB on a polymer bead inhibits the intramolecular torsional motion that is the origin of the temperature sensitivity of the fluorophore [233].

Commercially available RhB-loaded polystyrene beads and custom-synthesised surface-functionalised beads in which the fluorophore is tethered to the surface by an alkyl amino chain were investigated [106]. For both types of bead the RhB lifetime was independent of temperature. To overcome this problem, a water-oil-water emulsification method was used [13] to produce microdroplets in which the KR fluorophore is encapsulated but remains in a fluid environment. In these 'double bubbles' an aqueous droplet of the fluorescent dye is surrounded by an oil shell which serves both to contain the fluorophore and to provide the refractive index differential required for optical trapping of the droplet in an external aqueous medium.

The novel method presented in this chapter combines the capability of optical tweezers to manipulate objects with the capacity of FLIM to provide quantitative temperature measurement. It allows the temperature to be measured locally, with micron-scale spatial resolution while the microsystem is in operation without introducing artefacts or toxicity to the continuous flowing medium.

7.2 Materials and methods

7.2.1 Optical tweezers setup

The combination of FLIM and optical tweezers was made possible via the custom-built multi-parameter microscope platform described in Section 3.6. Details of the optical setup are given Figure 7-1.

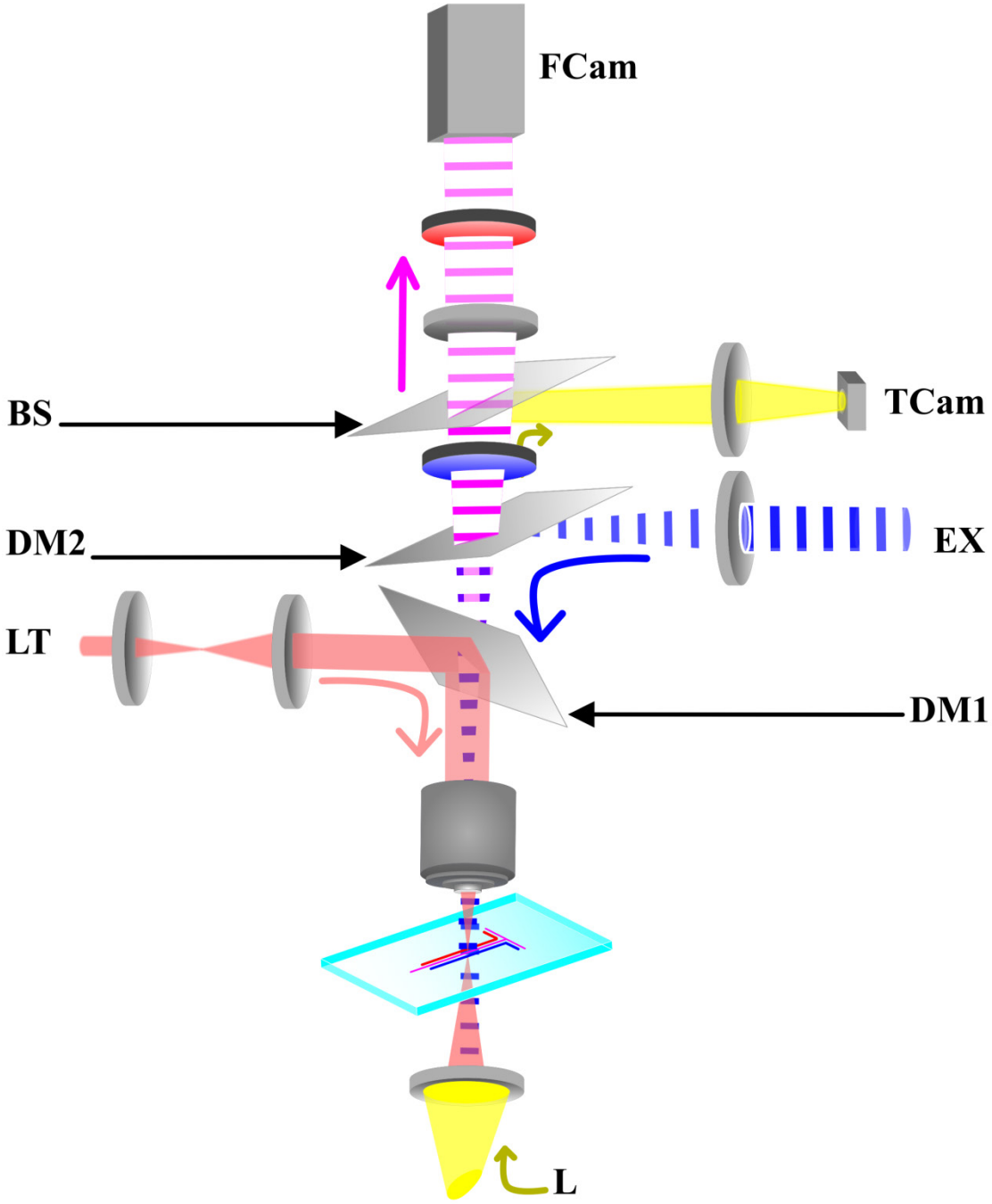

Figure 7-1: Schematic diagram of the optical setup in which optical trapping and fluorescence lifetime imaging microscopy (FLIM) are combined. CW Laser tweezers (LT, 785nm) beam (Red line); dichroic mirror 1 (DM1, transmission below 780nm); white illumination light (L); fluorescence signal (pink dashed line); excitation source (EX, 40MHz, 470nm), blue dashed line; dichroic mirror 2 (DM2, transmission above 505nm); beam splitter (BS); Tweezer control camera (TCam); FLIM Camera (FMCam)

The custom-built optical tweezers system [234] allows trapping and manipulation of micron-sized particles using an intuitive 'click and trap' computer interface. The optical trap is formed by a tightly focussed beam from a circularised diode laser (VPSL-0785-070-x-5-A, Blue Sky Research) providing up to 70 mW output power at a wavelength of 785 nm. The laser beam is expanded and then coupled into the back of the microscope objective (60x, NA 1.2 Plan Apo WI, Nikon), using a 780-nm short-pass dichroic mirror. The high numerical aperture of the water immersion objective ensured a tight focus leading to strong trapping while at the same time minimising aberrations when trapping deep inside the sample. The laser beam can be steered using a pair of galvanometric mirrors located in the conjugate plane of the back aperture of the objective as shown Figure 7-2:

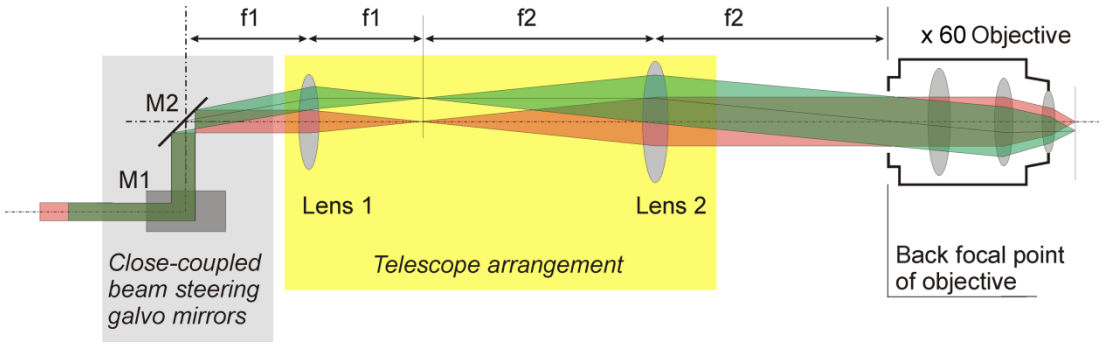

Figure 7-2: Galvo mirrors and optical setup used to steer the beam focus in the sample [112].

The graphical user interface (written in Labview 7.1, National Instruments) displays live images of the sample captured on a CCD camera and adjusts the trap position by controlling the galvanometric mirrors in response to mouse movement.

7.2.2 Fluorescence lifetime imaging microscopy

A 468-nm diode laser (LDH-P-C-470, Picoquant GmbH, Germany) controlled by a picosecond pulsed driver (PDL800-B, Picoquant GmbH) operating at 40 Mhz was used as the excitation source for FLIM. The beam was reshaped using a pair of semi-cylindrical lenses, expanded and collimated, spatially filtered through an aperture and focused at the back focal plane of the microscope objective following reflection off a dichroic mirror (FF505-SDi01-25x36, Semrock). The fluorescence was collected through the same objective. Unwanted scattered light from the

excitation source and the laser tweezers was removed using filters (LP02-488RS-25 and FF01-680/SP-25, Semrock). The fluorescence was imaged onto a gated intensified CCD camera (Picostar HR-12QE, LaVision GmgH, Germany) using an achromatic doublet lens (NT32-917, Edmund Optics Ltd, UK). FLIM images were recorded with 1 ns gate widths at 1 ns intervals. Five images were averaged to create the final image. The exposure time of the camera was set (in the range 340 ms to 680 ms) to obtain a maximum intensity per pixel of between 3000 and 4000 counts. FLIM images were produced and analysed using DaVis 6.2 software.

7.2.3 Preparation and Characterisation of Fluorescent Microdroplets

The fluorescent microdroplets consisted of an aqueous solution of the fluorescent dye encapsulated inside an oil bubble, which in turn was suspended in an external water phase. Similar water-oil-water emulsions have been used for *in-vitro* compartmentalisation [13, 218, 219, 235]. The internal water phase (W1) was an aqueous solution of 0.3 mM Kiton Red (Sulforhodamine B, acid form, laser grade, Sigma-Aldrich) and 0.3 mM NaCl. The oil phase (O) consisted of paraffin oil (Fisher Scientific) and a surfactant 3.2% wt/wt (ABIL EM 90, Degussa). The external water phase (W2) was an aqueous solution of 1% wt/wt of a surfactant (Triton X-102, Sigma-Aldrich) and 0.75% of carboxymethyl added at room temperature and shaken regularly for 1 hour, then cooled on ice. Over ice, 25 µl of W1 was added to 2 ml of O, and homogenised (Disperser, Ultra-Turrax T25 basic, Ika®) for 2 min at 13500 rpm, to create a water in oil (W1/O) emulsion. Over ice, 2.4 ml of W2 was added to the emulsion W1/O, and homogenised for 2 min at 11500 rpm, to form the final W1/O/W2 emulsion.

A sample of the emulsion in a 1 cm path-length cuvette was held in a thermostatically controlled cuvette holder in the setup described Chapter 3.2. The temperature was measured with a thermocouple (Hanna Instruments HI93530) immersed directly in the emulsion. Fluorescence was excited at 400 nm and detected at 580 nm, via a 488-nm long-pass filter (Semrock) and a monochromator which was set to a bandpass of 18 nm to mimic the bandpass filter used in the FLIM setup.

Decay curves were recorded over a 50 ns time range resolved into 4096 channels and accumulated to give 10000 counts in the peak channel.

7.3 Results and discussion

7.3.1 The response of microdroplet fluorescence lifetime to temperature

The fluorescence decay of a dilute solution of KR microdroplets (50 µl of initial recipe into 10 ml of W2) was measured as a function of temperature over the range of 27 ºC to 61 ºC. At each temperature, the fluorescence decay was described by a bi-exponential function. The decay parameters together with the average lifetimes, $\langle\tau\rangle$, as defined by Equation (7-1), are given in Table 7-1.

$$\langle\tau\rangle = \frac{A_1\tau_1 + A_2\tau_2}{A_1 + A_2} \qquad \textbf{(7-1)}$$

The predominant shorter lifetime component, τ_1, accounts for 80% of the emitting population at 27 ºC, increasing to 97% at 61.4 ºC. This lifetime corresponds to that of KR in bulk aqueous solution, where the decay is mono-exponential. The second, minor component with longer lifetime, τ_2, suggests the presence of dye aggregates in the microdroplet.

Temp. / ^{o}C	τ_1 / ns	τ_2 / ns	A_1	A_2	$\langle\tau\rangle$ /ns
27.0	1.23	2.32	0.80	0.20	1.45
35.2	1.04	2.17	0.87	0.13	1.19
44.0	0.86	2.29	0.93	0.07	0.96
52.7	0.69	2.53	0.96	0.04	0.77
61.4	0.57	3.17	0.97	0.03	0.64

Table 7-1: Temperature-dependence of the fluorescence decay parameters of Kiton Red microdroplets, the fluorescence lifetimes, τ_i, and the corresponding fractional amplitudes, A_i, are given, together with the average lifetime, $\langle\tau\rangle$.

The less soluble parent fluorophore, Rhodamine B, readily forms aggregates in water even at micro-molar concentrations, characterised by the appearance of a longer lifetime component in the fluorescence decay [160]. It is, therefore, not surprising to

observe a small amount of aggregation of KR at a concentration of 0.3 mM. Furthermore, the decrease of the amplitude of this component (A_2) with increasing temperature is consistent with disaggregation at higher temperature, as observed previously [236].

The bi-exponential decay of the microdroplets can be conveniently represented by a single parameter, the average lifetime $<\tau>$, as defined by Equation (7-1. The values of $<\tau>$ are given in Table 7-1. The dependence of $<\tau>$ on temperature is shown graphically in Figure 7-3, together with the corresponding curve for KR in bulk water.

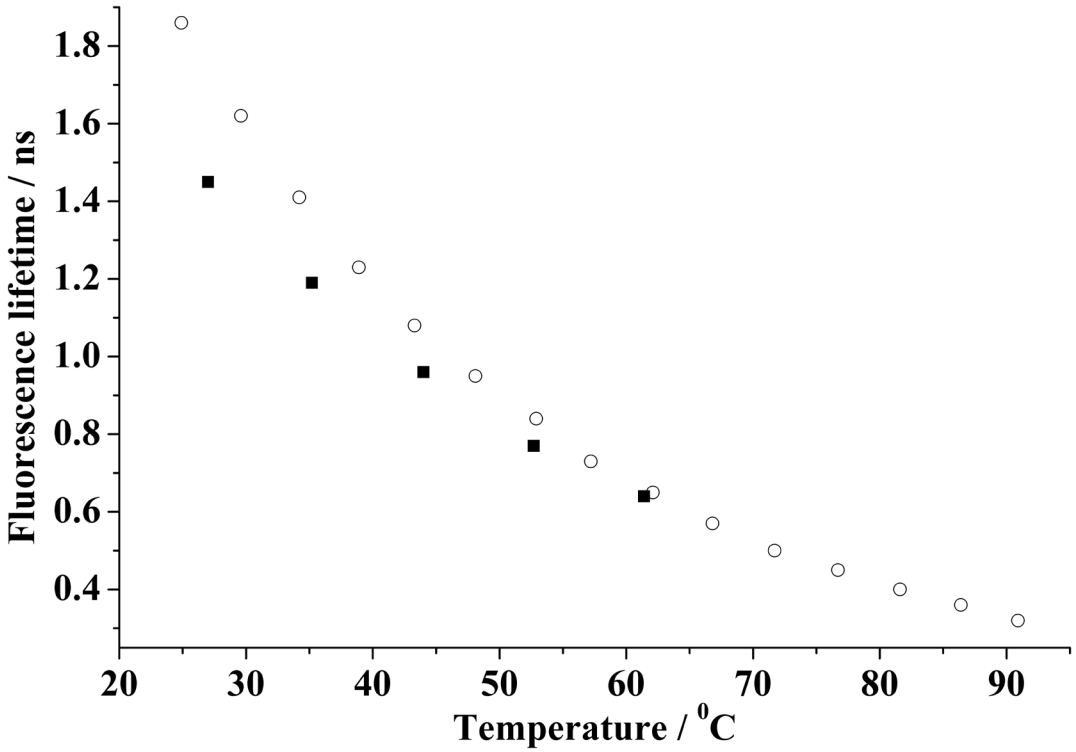

Figure 7-3: Temperature dependence of the average fluorescence lifetime of Kiton Red microdroplets. The corresponding temperature dependence in bulk aqueous solution (○) [7], is shown for comparison.

The lifetime-temperature response of the microdroplets closely resembles that of the bulk solution [7, 8], confirming that containment of KR in the microdroplet does not inhibit its conformational freedom. The small decrease in lifetime of KR in the microdroplets compared with bulk aqueous solution may be accounted for by the

effect of the local environment (presence of NaCl and surfactants and the proximity of an oil/water interface) on the non-radiative decay rate and the effect of increased refractive index, which increases the radiative rate [237].

7.3.2 Calibration curve for FLIM temperature measurement

In order to construct a calibration curve to apply to the FLIM data it was necessary to determine fluorescence lifetimes by tail fitting the fluorescence decay curves over the same time range used to analyse the FLIM data. The decay times obtained are presented Table 7-2.

Temp. / ^{o}C	Single exponential fit		Bi-exponential fit	
	τ_s /ns	χ^2	$<\tau>$ /ns	χ^2
27.0	1.51	1.00	1.54	0.91
35.2	1.26	1.19	1.27	0.96
44.0	1.06	1.59	1.10	1.08
52.7	0.90	2.14	0.91	0.98
61.4	0.79	2.77	0.84	0.97

Table 7-2: Fluorescence lifetime calculated by tail fitting the decay curves recorded using TCSPC. The fluorescence lifetime calculated using a single exponential fitting function τ_s are reported with the average lifetime calculated from a bi-exponential function.

The lifetime calculated by tail-fitting from 1 ns after the maximum are consistently longer that the lifetime values presented Table 7-1 because the fitting neglects the early part of the decay where the short lifetime component τ_1 is the most significant; hence it is overweighting the long lifetime component τ_2, resulting in longer lifetime values. As shown in Table 7-2, over this truncated fitting range, a single exponential function provides a very good fit to the data for temperatures up to 44 ^{o}C. Above 44^{o}C, the quality of the fit deteriorates somewhat, as indicated by the higher χ^2 values. Nevertheless the latter decays are still adequately fitted by a single exponential function as indicated by the similarity of the lifetime to the average lifetime obtained from the bi-exponential fit. Over the temperature range relevant to the present FLIM measurements (~15 to 35 ^{o}C) a single exponential fit is entirely satisfactory. The temperature-lifetime calibration curve derived from the data in Table 7-2 is shown in Figure 7-4.

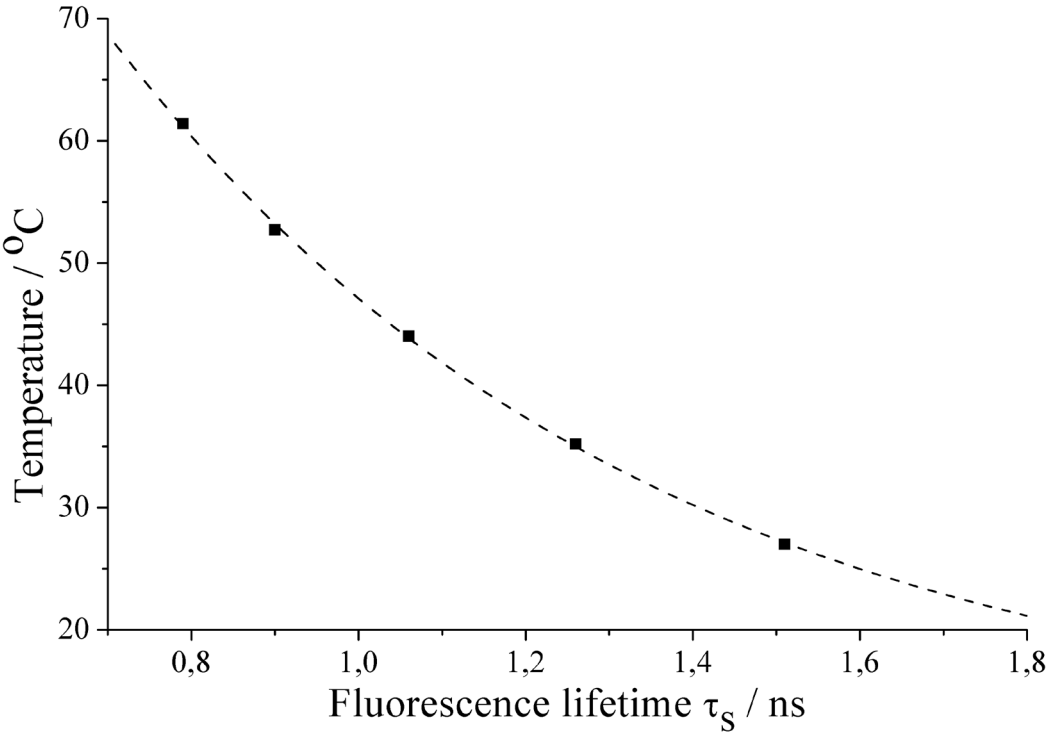

Figure 7-4: Fluorescence lifetime of the microdroplet obtained by mono-exponential fitting of the curves recorded at different temperatures (Black square). The dashed line shows the exponential decay function fitted to the data, T = 172.exp(-τ/0.645)+10.5 used as a calibration for subsequent analysis of the FLIM images.

The empirical relation used hereafter as calibration equation to calculate the temperature from FLIM data is given by:

$$T = 172 \times \exp\left(-\frac{\tau}{0.645}\right) + 10.5 \qquad \textbf{(7-2)}$$

7.3.3 Fluorescence lifetime imaging microscopy of optically trapped microdroplets in the microchannel

The use of optical tweezers necessitates high magnification and large numerical apertures to produce a very tightly focused beam, in combination with moderate optical powers, in order to enable the capture of an object subject to Brownian motion and flow. This naturally raises concerns about heating effects, which may perturb device operation or damage biological samples. Previous work has shown that heating due to the tweezer beam is wavelength-dependent and scales linearly with power [238-241]. The temperature increase due to a 800-nm tweezer

beam was reported to be 1.7ºC/W [241]. The 780-nm laser, used in these experiments, has a maximum output power of 60 mW, which, assuming no loss along the optical path, would induce a maximum temperature increase of 0.1ºC. This small temperature increase should not perturb the device operation, would not damage biological samples and does not introduce any artefact into the temperature measurement since 0.1ºC is below the temperature resolution of KR FLIM (*vide infra*). The absence of a discernible heating effect was confirmed by FLIM of microdroplets in the absence and presence of the tweezer laser beam.

Microdroplets could be trapped at powers just above the lasing threshold (ca. 3 mW) in the absence of flow, whilst at maximum output optical power droplets could be trapped in a flow velocity of up to 1 mm/s. Once trapped, a microdroplet was moved to the desired position and a series of time-gated images recorded in order to generate a FLIM image. Figure 7-5 shows a series of frames from the tweezer-control camera illustrating the capture and positioning of a droplet in the microchannel.

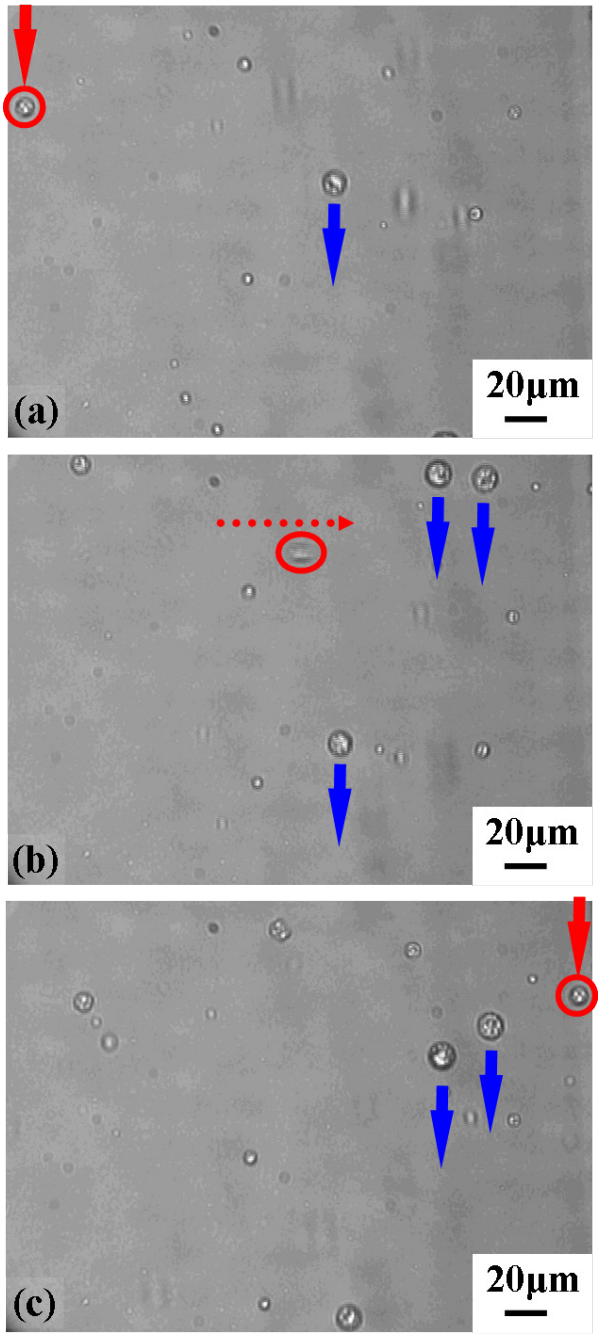

Figure 7-5: A series of frames from the tweezer-control camera showing the trapping and manoeuvring of a microdroplet. Frame (a) shows the position at which the microdroplet was initially trapped (red arrowhead) at the LH edge of the channel. Frame (b) shows the movement of the microdroplet in the middle of the channel (red arrow). Frame (c) shows movement of the microdroplet to its final position at the RH edge of the channel. For spatial reference the position and motion of some other microdroplets are indicated by blue arrowheads.

Figure 7-6 shows the characteristics of a droplet trapped close to the cooling channel of the microfluidic device. The intensity image (Figure 7-6(a)) is shown

together with the corresponding intensity profile (Figure 7-6(b)). In order to generate the FLIM image, the fluorescence lifetimes have been calculated for pixels that have intensity higher than the half maximum intensity. The FLIM map of the droplet generated is shown Figure 7-6(c) together with the decay, corresponding to the intensity at each gate integrated over the droplet image. The curve is fitted to a single exponential decay.

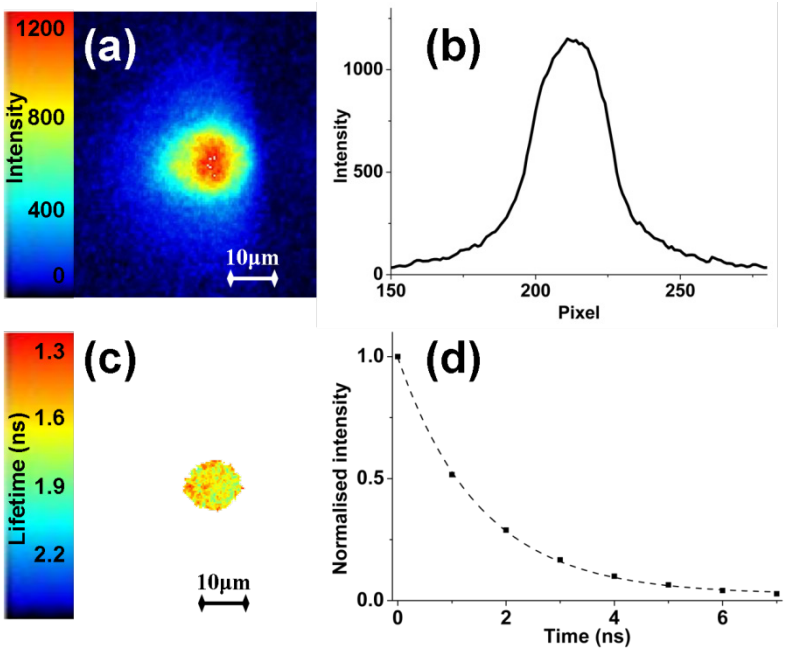

Figure 7-6: Fluorescence image of a microdroplet trapped in the microfluidic device (a); Intensity profile across the droplet (b); FLIM image of the droplet (c); Average intensity of the microdroplet in the 8 gates used to build the fluorescence decay (Black dots), the dashed line shows the fitted single exponential decay: I=0.97exp(-t/1.52)+0.02 (d).

The decay curve Figure 7-6(d) results from the data extracted from the FLIM image Figure 7-6(c). The single exponential fit gives a lifetime value of 1.52 ± 0.03 ns corresponding to a temperature of 26.9 ± 0.8ºC.

After recording the images of the droplet trapped in the cooled side of the channel, the droplet was moved to the heated side of the channel and images recorded to construct a FLIM image at this position. The resulting FLIM image is shown Figure 7-7(a). It has been displayed alongside the FLIM image of the droplet trapped in the cooled side Figure 7-7(b).

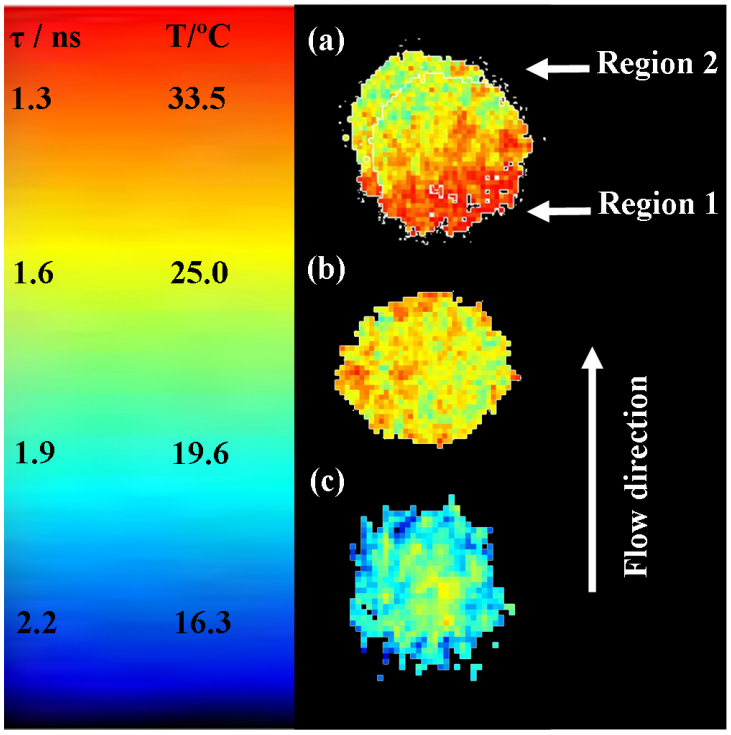

Figure 7-7: FLIM images of a droplet in the heated side of the channel (a); the same droplet in the cooled side of the channel (b); and a droplet trapped at room temperature (c). The colour coded scale illustrates the fluorescence lifetime calculated at each pixel.

The FLIM images Figure 7-7 clearly show the change of fluorescence lifetime of the droplet associated with the change of local temperature. The average fluorescence lifetime of the droplet changes from 1.37 ± 0.04 ns in Figure 7-7(a) to 1.52 ± 0.03 ns in Figure 7-7(b), indicating a change in temperature from 31.1 ± 1.3ºC to 26.9 ± 0.8ºC across the channel. For comparison, the FLIM image of a droplet trapped at room temperature is shown Figure 7-7(c). It exhibits a lifetime of 1.80 ± 0.07 ns corresponding to a temperature of 21.1 ± 1.1 ºC.

The spatial distribution of the fluorescence lifetime across the FLIM image of the droplet in Figure 7-7(a) is different to that in Figure 7-7(b). Whereas in Figure 7-7(b), the spatial distribution of lifetimes is fairly uniform, in Figure 7-7(a) there is a gradient of fluorescence lifetime values across the microdroplet. We believe that this effect is due to a slight movement of the microdroplet during the image acquisition. The degradation of FLIM images by motion artefacts has been studied by Elson et al. [143]. They showed that the movement of a fluorescent bead during

the acquisition time can cause a change of the intensity of a pixel between time-gated images and hence affect the measured fluorescence decay. In the work presented in this chapter, data at the shortest delay time (earliest time gate) were acquired first. In the region of the FLIM image at the upstream edge of the droplet (i.e. region 1 in Figure 7-7(a)), movement of the droplet in the direction of flow will result in a decrease in pixel intensity during the acquisition time (because the intensity maximum is moving away from this region) and the late gates (gates recorded with long delay) will have an anomalously low intensity. Therefore, the observed lifetime in the upstream region will be shorter than the true lifetime value. Conversely, in the region facing downstream (i.e. region 2 in Figure 7-7(a)), the late gates will have a higher intensity than that expected because the intensity maximum is moving towards this region and the observed lifetime will be longer than the true value. The size of the optical trap is much smaller than the microdroplet and it is possible that the microdroplet has moved due to forces exerted by the flow without going out of the trap. This artefact could be problematic if the spatial distribution of the fluorescence lifetimes were being used to quantify local environmental characteristics. However, in the present case, the lifetime value used to determine the temperature is calculated from intensity data integrated over the entire droplet. Therefore, the intensity lost in region 1 of the droplet is compensated by the intensity gained in region 2 and the lifetime calculated is the same whether the droplet has moved or not.

The spatial resolution obtained with the microdroplet probes is limited by the size of the microdroplets themselves. Their diameter is adjustable by varying the emulsification procedure used during fabrication. Stable microdroplets can be produced down to around 70 nm in diameter [13]. However, in order to produce droplets that were both tweezable and detectable, a droplet diameter larger than ca. 5 μm was used in the present work. The maximum size of droplet which could be tweezed was ca. 20 μm.

Both the spatial and temperature resolution could be greatly improved. The use of a more sensitive detector or a temperature-sensitive probe with a higher

quantum yield would allow smaller droplets to be detected and, hence, produce a better spatial resolution. An improved lifetime resolution can be obtained using time-correlated single photon detection, which would provide a better quality of the decay data and, therefore, a much better resolution of the temperature.

Whereas the purchase or implementation of more sensitive detectors can constitute an expensive and time consuming task, the flexibility in the microdroplet fabrication offers a cheap alternative. For example, using the recently reported thermo-responsive polymer would permit a temperature resolution of less than 0.1ºC [6].

To the author's knowledge, this is the first time that FLIM has been used in combination with optical tweezers. Further development/customisation of local probes, together with the implementation of multi-trap laser tweezers would allow a full environmental and chemical mapping at the tip of a laser.

7.4 Conclusion

It is the first time that the simultaneous use of optical tweezers and FLIM has been demonstrated. Two microscopic techniques have been combined on a custom-built open-frame multimodal microscope and used in conjunction with a specially developed temperature-sensitive fluorescent microdroplet to probe temperature profiles in a microfluidic device.

The microdroplets are based on a water-oil-water emulsion, with KR solvated in the inner water phase, enabling it to maintain its classic fluorescence lifetime response to temperature. The fluorescence lifetime of KR within the microdroplet decreases with increasing temperature from 1.45 ns at 27ºC to 0.64 ns at 61.4 ºC. Microdroplets with diameters between 5 and 20 μm have been shown to be fully tweezable within the constraints of a microfluidic device.

FLIM images of optically trapped microdroplets held at selected positions across a temperature gradient within the microfluidic device have demonstrated the

ability to locally measure the temperature in a microchannel with micron-scale resolution.

The ease of fabrication and the control of the droplet characteristics should appeal to other researchers interested in non-invasive at the microscale and micromanipulation.

8 Conclusions

For the first time, FLIM has been used in simultaneous combination with other microscopic tools and techniques to gain further insights into flow behaviour at the microscale and spatially resolve environmental and chemical characteristics in microfluidic devices.

Throughout the work presented in this thesis, three FLIM techniques have been used. A summary of their respective advantages and disadvantages are given in the table below. More details are given in the subsequent paragraphs.

Techniques	Pros	Cons
Time-Gated	• Real-time imaging capabilities • Relatively simple setup • Established technique	• Poor temporal resolution • Intensifier induces a slight blur in the image • Small dynamic range
TSCSPC	• Good spatial and temporal resolution • Virtually infinite dynamic range	• Slow acquisition • Analysing software not user-friendly and not fully developed
2PE-FLIM	• 3-spatial dimensions • Unequalled spatial resolution • Good temporal resolution • Elimination of the out-of-focus fluorescence	• High laser power can damage biological sample • Slow acquisition • Scanning unit and high power short-pulsed laser are expensive

Table 8-1: Summary of the relative advantages and disadvantages of the different FLIM techniques used in this thesis.

In wide-field FLIM, the choice of the detector/camera must be informed by the complexity of the fluorescence decay of the probe and the resolution required. We have shown that appropriate combinations of detector and probe can achieve

spatially-resolved pH measurements at the microscale with pH resolution approaching that of commercial pH meters for the macroscale.

In this work, the pH measurements were limited to the pH range over which the fluorescent probe is partially protonated/deprotonated. However, even though it has not been demonstrated to date, it is possible to use a combination of fluorescent dyes the transition from protonated to deprotonated form of which occurs at different pH to develop a fluorescent system capable of covering a larger pH range. A combination of fluorescent probes would also allow simultaneous mapping of various chemical characteristics. This would require the use of a FLIM system the time resolution of which allows multi-exponential decays to be fitted. To that extent, TSCSPC in the ideal candidate thanks to its high time resolution and ability to acquire data with a high signal-to-noise ratio.

In some cases, the main requirement for the development of a quantitative mapping system is driven by the need for real-time imaging. The use of a time-gated system in conjunction with a probe the fluorescence lifetime of which can be determined by a minimum number of measurements (2 points are sufficient to draw a line characterising a single exponential decay) can provide the capabilities required for FLIM to be developed for applications requiring real-time imaging such as imaging of dynamic systems, *in vivo* imaging and medical imaging. The use of time-gated detection in conjunction with fluorescein is the ideal starting point for the development of a system that would allow real-time quantitative mapping of pH of most of the biological and body fluids.

The influence of gravity in microfluidic devices is significantly weaker than that of surface effects, and as a result it has often been neglected. Therefore, the mixing of two fluids is generally treated as a 2-dimensional case where diffusion happens through a stable vertical interface. Previously it had been shown that quantitative agreement between computational fluid and experimental data obtained using wide-field FLIM could only be achieved by including the effect of gravity. However, substantiating the importance of gravity forces in microflows using wide-field FLIM is difficult because of the long depth of focus of the microscope

objectives used and the contribution from out-of-focus fluorescence. To circumvent the shortcomings inherent to wide-field illumination and detection, 2-photon excitation was used to quantitatively map the mixing of fluidic systems in three spatial dimensions. The density mismatch of two solutions in the device generates a rotation of the interface between two streams. 2PE-FLIM combines the capabilities of wide-field FLIM and confocal microscopy. The technique provides quantitative information about gravitational effects and diffusion processes at the microscale. Furthermore, 2PE-FLIM gives quantitative insight into the fluid behaviour close to the boundary (wall) of the device that can be obtained neither by wide-field FLIM, because of the lack of depth resolution, nor by confocal microscopy, because of illumination/detection artefacts due to the proximity of the wall of the device. The development of a reliable computational fluid dynamics model for the microscale would therefore greatly benefit if the simulated results were compared with experimental data obtained using 2PE-FLIM.

The advent of technologies that require the expertise from various scientific backgrounds benefits from the development of tools that facilitate the use of techniques that are alien to a particular discipline. As such, the work presented in this thesis has benefited from an engineering technique, soft lithography, which allows the fabrication of microfluidic prototypes by scientists from any discipline. Likewise, the design and development of an open-frame microscope has permitted the implementation of different microscopic techniques and their simultaneous use, overcoming the inflexibility of commercial microscopes without the technical difficulties encountered in constructing an optical setup from scratch on a conventional optical table.

FLIM and μ-PIV, two complementary flow characterisation techniques, were implemented on the open-frame microscope. The two techniques were, for the first time, used simultaneously to map the fluid characteristics, using FLIM, and the flow velocity fields, using μ-PIV. Mismatch of viscosity or temperature between two streams was responsible for the deviation of the advective transport across the channel from the typical Poiseuille profile. More generally, the combination of FLIM

and μ-PIV provides a total analytical tool for fluidic systems because these two techniques used simultaneously can gather all the parameters required by computational fluid dynamics modellers to validate models: solvent composition, temperature and flow velocity fields.

A temperature-sensitive fluorescent microdroplet has been trapped using laser tweezers in a microfluidic device. The microdroplet was used to locally measure the temperature in the device using FLIM. Microdroplets are already extensively used in microfluidic devices for the study of molecular evolution. Incorporating the probe fabricated in this thesis into such devices would be straightforward and could report on the micro-environment in a chemically non-invasive way. The microdroplets could also be used for multi-parameter mapping of micro-environment using FLIM. For example, Kiton Red, encapsulated in microdroplets could be used to probe the temperature, while fluorescein dissolved in the continuous water phase, could be used to probe the pH. They could also be used as fluorescent tracers for μ-PIV experiments.

FLIM has three characteristics that have allowed its successful implementation for the study of fluid in microfluidic devices: it provides investigators with high-quality quantitative spatial information at the microscale; it can be used in different configurations to satisfy the spatial and temporal resolution required for different applications; it can be combined with other microscopic techniques and optical tools. Therefore, FLIM has the potential to play a role in every facet of the development of microfluidic technology: in engineering to assess the performance of devices; in fluid dynamics to study mass transport phenomena at the microscale; in chemistry to spatially resolve the state of molecules; in biotechnology to control the environment of samples; and in medical applications for diagnostics.

References

[1] J. G. Santiago, S. T. Wereley, C. D. Meinhart, D. J. Beebe, and R. J. Adrian, "A particle image velocimetry system for microfluidics," *Experiments in Fluids,* vol. 25, pp. 316-319, 1998.

[2] D. Sinton, "Microscale flow visualization," *Microfluidics and Nanofluidics,* vol. 1, pp. 2-21, 2004.

[3] S. W. Magennis, E. M. Graham, and A. C. Jones, "Quantitative spatial mapping of mixing in microfluidic systems," *Angewandte Chemie-International Edition,* vol. 44, pp. 6512-6516, 2005.

[4] J. R. Lakowicz, H. Szmacinski, K. Nowaczyk, and M. L. Johnson, "Fluorescence Lifetime Imaging of Free and Protein-Bound Nadh," *Proceedings of the National Academy of Sciences of the United States of America,* vol. 89, pp. 1271-1275, 1992.

[5] S. M. Matthews, A. D. Elder, K. Yunus, C. F. Kaminski, C. M. Brennan, and A. C. Fisher, "Quantitative kinetic analysis in a microfluidic device using frequency-domain fluorescence lifetime imaging," *Analytical Chemistry,* vol. 79, pp. 4101-4109, Jun 1 2007.

[6] E. M. Graham, K. Iwai, S. Uchiyama, A. P. de Silva, S. W. Magennis, and A. C. Jones, "Quantitative mapping of aqueous microfluidic temperature with sub-degree resolution using fluorescence lifetime imaging microscopy," *Lab on a Chip,* vol. 10, pp. 1267-1273.

[7] D. A. Mendels, E. M. Graham, S. W. Magennis, A. C. Jones, and F. Mendels, "Quantitative comparison of thermal and solutal transport in a T-mixer by FLIM and CFD," *Microfluidics and Nanofluidics,* vol. 5, pp. 603-617, 2008.

[8] R. K. P. Benninger, Y. Koc, O. Hofmann, J. Requejo-Isidro, M. A. A. Neil, P. M. W. French, and A. J. deMello, "Quantitative 3D mapping of fluidic temperatures within microchannel networks using fluorescence lifetime imaging," *Analytical Chemistry,* vol. 78, pp. 2272-2278, 2006.

[9] R. K. P. Benninger, O. Hofmann, J. McGinty, J. Requejo-Isidro, I. Munro, M. A. A. Neil, A. J. deMello, and P. M. W. French, "Time-resolved fluorescence imaging of solvent interactions in microfluidic devices," *Optics Express,* vol. 13, pp. 6275-6285, 2005.

[10] T. Robinson, P. Valluri, H. B. Manning, D. M. Owen, I. Munro, C. B. Talbot, C. Dunsby, J. F. Eccleston, G. S. Baldwin, M. A. A. Neil, A. J. de Mello, and P. M. W. French, "Three-dimensional molecular mapping in a microfluidic mixing device using fluorescence lifetime imaging," *Optics Letters,* vol. 33, pp. 1887-1889, 2008.

[11] A. D. Elder, S. M. Matthews, J. Swartling, K. Yunus, J. H. Frank, C. M. Brennan, A. C. Fisher, and C. F. Kaminski, "The application of frequency-domain Fluorescence Lifetime Imaging Microscopy as a quantitative

analytical tool for microfluidic devices," *Optics Express,* vol. 14, pp. 5456-5467, 2006.

[12] G. M. Whitesides, "Soft lithography," *Abstracts of Papers of the American Chemical Society,* vol. 212, pp. 31-INOR, 1996.

[13] O. J. Miller, K. Bernath, J. J. Agresti, G. Amitai, B. T. Kelly, E. Mastrobattista, V. Taly, S. Magdassi, D. S. Tawfik, and A. D. Griffiths, "Directed evolution by in vitro compartmentalization," *Nature Methods,* vol. 3, pp. 561-570, 2006.

[14] B. Herman and H. J. Tanke, *Fluorescence microscopy*, 2nd ed.: BIOS Publisher Ltd, 1998.

[15] E. U. Condon, "Nuclear Motions Associated with Electron Transitions in Diatomic Molecules," *Physical Review,* vol. 32, p. 858, 1928.

[16] J. Yguerabide, "Nanosecond fluorescence spectroscopy of macromolecules," *Methods Enzymol,* vol. 26 PtC, pp. 498-578, 1972.

[17] D. V. O'Connor and D. Phillips, *Time-correlated Single Photon Counting*: ACADEMIC PRESS, INC. (LONDON) LTD., NW1 7DX 1984.

[18] *Steady State and Time Resolved Fluorescence Spectrometers*. Available: http://www.edinst.com/pdf/920%20Series%20Brochure.pdf

[19] W. Becker, *The bh TCSPC Handbook*: Becker & Hickl Gmbh, 2006.

[20] J. L. Wiza, "Microchannel Plate Detectors," *Nuclear Instruments & Methods,* vol. 162, pp. 587-601, 1979.

[21] J. R. Lakowicz, *Principle of Fluorescence Spectroscopy*, 2nd ed.: Kluwer Academic/Plenum Publishers, 1999.

[22] S. Cova, G. Ripamonti, and A. Lacaita, "Avalanche semiconductor detector for single optical photons with a time resolution of 60 ps," *Nuclear Instruments and Methods in Physics Research Section A: Accelerators, Spectrometers, Detectors and Associated Equipment,* vol. 253, pp. 482-487, 1987.

[23] R. H. Haitz, "Model for Electrical Behavior of Microplasma," *Journal of Applied Physics,* vol. 35, pp. 1370-&, 1964.

[24] S. Cova, A. Longoni, and A. Andreoni, "Towards Picosecond Resolution with Single-Photon Avalanche-Diodes," *Review of Scientific Instruments,* vol. 52, pp. 408-412, 1981.

[25] T. Louis, G. H. Schatz, P. Kleinbolting, A. R. Holzwarth, G. Ripamonti, and S. Cova, "Performance Comparison of a Single-Photon Avalanche-Diode with a Microchannel-Plate Photomultiplier in Time-Correlated Single-Photon Counting," *Review of Scientific Instruments,* vol. 59, pp. 1148-1152, 1988.

[26] G. S. Buller, R. D. Harkins, A. McCarthy, P. A. Hiskett, G. R. MacKinnon, G. R. Smith, R. Sung, A. M. Wallace, R. A. Lamb, K. D. Ridley, and J. G. Rarity, "Multiple wavelength time-of-flight sensor based on time-correlated

single-photon counting," *Review of Scientific Instruments,* vol. 76, pp. 083112-083112-7, 2005.

[27] A. McCarthy, R. J. Collins, N. J. Krichel, V. Fernandez, A. M. Wallace, and G. S. Buller, "Long-range time-of-flight scanning sensor based on high-speed time-correlated single-photon counting," *Applied Optics,* vol. 48, pp. 6241-6251, 2009.

[28] S. Cova, A. Longoni, A. Andreoni, and R. Cubeddu, "A Semiconductor Detector for Measuring Ultraweak Fluorescence Decays with 70 Ps Fwhm Resolution," *Ieee Journal of Quantum Electronics,* vol. 19, pp. 630-634, 1983.

[29] M. Szabelski, R. Luchowski, Z. Gryczynski, P. Kapusta, U. Ortmann, and I. Gryczynski, "Evaluation of instrument response functions for lifetime imaging detectors using quenched Rose Bengal solutions," *Chemical Physics Letters,* vol. 471, pp. 153-159, 2009.

[30] M. Szabelski, D. Ilijev, P. Sarkar, R. Luchowski, Z. Gryczynski, P. Kapusta, R. Erdmann, and I. Gryczynski, "Collisional Quenching of Erythrosine B as a Potential Reference Dye for Impulse Response Function Evaluation," *Applied Spectroscopy,* vol. 63, pp. 363-368, 2009.

[31] C. E. Webb and J. D. C. Jones, *Handbook of laser technology and applications*: Institute of Physics Publishing, 2003.

[32] M. Ghioni, A. Gulinatti, I. Rech, F. Zappa, and S. Cova, "Progress in silicon single-photon avalanche diodes," *Ieee Journal of Selected Topics in Quantum Electronics,* vol. 13, pp. 852-862, 2007.

[33] G. Ripamonti and S. Cova, "Carrier diffusion effects in the time-response of a fast photodiode," *Solid-State Electronics,* vol. 28, pp. 925-931, 1985.

[34] A. Lacaita, M. Ghioni, and S. Cova, "Double Epitaxy Improves Single-Photon Avalanche-Diode Performance," *Electronics Letters,* vol. 25, pp. 841-843, 1989.

[35] A. Lacaita, S. Cova, M. Ghioni, and F. Zappa, "Single-Photon Avalanche-Diode with Ultrafast Pulse Response Free from Slow Tails," *Ieee Electron Device Letters,* vol. 14, pp. 360-362, 1993.

[36] A. Spinelli, M. A. Ghioni, S. D. Cova, and L. M. Davis, "Avalanche detector with ultraclean response for time-resolved photon counting," *Ieee Journal of Quantum Electronics,* vol. 34, pp. 817-821, 1998.

[37] M. Vandenzegel, N. Boens, D. Daems, and F. C. Deschryver, "Possibilities and Limitations of the Time-Correlated Single Photon-Counting Technique - a Comparative-Study of Correction Methods for the Wavelength Dependence of the Instrument Response Function," *Chemical Physics,* vol. 101, pp. 311-335, 1986.

[38] P. L. Becker, "Quantitative fluorescence measurements," in *Fluorescence Imaging Spectroscopy and Microscopy* vol. 137, J. D. Winefordner, Ed., ed: Wiley & Sons, inc., 1996, pp. 1-29.

[39] J. R. Lakowicz and H. Szmacinski, "Imaging applications of time-resolved fluorescence spectroscopy " in *Fluorescence Imaging Spectroscopy and Microscopy* vol. 137, J. D. Winefordner, Ed., ed: Wiley & Sons, inc., 1996, pp. 273-311.

[40] J. E. Whitaker, R. P. Haugland, and F. G. Prendergast, "Spectral and Photophysical Studies of Benzo[C]Xanthene Dyes - Dual Emission Ph Sensors," *Analytical Biochemistry,* vol. 194, pp. 330-344, 1991.

[41] J. R. Lakowicz, "Frequency-Domain Lifetime Measurements," in *Principles of Fluorescence Spectroscopy*, ed: Springer US, 2006, pp. 157-204.

[42] *Picostar HR 12 Operation Manual,* G. LaVision GmbH, 1998.

[43] M. Göppert-Mayer, "Über Elementarakte mit zwei Quantensprüngen," *Annalen der Physik,* vol. 401, pp. 273-294, 1931.

[44] P. T. C. So, T. French, W. M. Yu, K. M. Berland, C. Y. Dong, and E. Gratton, "Two-photon fluorescence microscopy: time-resolved and intensity imaging," in *Fluorescence Imaging Spectroscopy and Microscopy* vol. 137, J. D. Winefordner, Ed., ed: Wiley & Sons, inc., 1996, pp. 351-374.

[45] A. Diaspro, G. Chirico, and M. Collini, "Two-photon fluorescence excitation and related techniques in biological microscopy," *Quarterly Reviews of Biophysics,* vol. 38, pp. 97-166, 2005.

[46] J. R. Lakowicz, "Multiphoton Excitation and Microscopy," in *Principles of Fluorescence Spectroscopy*, ed: Springer US, 2006, pp. 607-621.

[47] R. M. Williams, D. W. Piston, and W. W. Webb, "2-Photon Molecular-Excitation Provides Intrinsic 3-Dimensional Resolution for Laser-Based Microscopy and Microphotochemistry," *Faseb Journal,* vol. 8, pp. 804-813, 1994.

[48] H. A. Stone, A. D. Stroock, and A. Ajdari, "Engineering flows in small devices: Microfluidics toward a lab-on-a-chip," *Annual Review of Fluid Mechanics,* vol. 36, pp. 381-411, 2004.

[49] S. Hardt, F. Schönfeld, and N.-T. Nguyen, "Mixing in Microscale," in *Microfluidic Technologies for Miniaturized Analysis Systems*, ed: Springer US, 2007, pp. 117-155.

[50] A. D. Stroock, S. K. W. Dertinger, A. Ajdari, I. Mezic, H. A. Stone, and G. M. Whitesides, "Chaotic mixer for microchannels," *Science,* vol. 295, pp. 647-651, 2002.

[51] N. T. Nguyen and Z. G. Wu, "Micromixers - a review," *Journal of Micromechanics and Microengineering,* vol. 15, pp. R1-R16, 2005.

[52] S. Hardt, F. Schönfeld, S. Hardt, and F. Schönfeld, "Microfluidics: Fundamentals and Engineering Concepts," in *Microfluidic Technologies for Miniaturized Analysis Systems*, ed: Springer US, 2007, pp. 1-58.

[53] M. E. Erdogan, "On the flows produced by sudden application of a constant pressure gradient or by impulsive motion of a boundary," *International Journal of Non-Linear Mechanics,* vol. 38, pp. 781-797, 2003.

[54] S. Hoffmann, Raebiger, Norbert, "Microscale flow visualization," in *Micro Process Engineering*. vol. 1, ed: Wiley VCH, 2009, pp. 93-115.

[55] R. J. Adrian, "Particle-Imaging Techniques for Experimental Fluid-Mechanics," *Annual Review of Fluid Mechanics,* vol. 23, pp. 261-304, 1991.

[56] B. P. Mosier, J. I. Molho, and J. G. Santiago, "Photobleached-fluorescence imaging of microflows," *Experiments in Fluids,* vol. 33, pp. 545-554, 2002.

[57] J. I. Molho, A. E. Herr, B. P. Mosier, J. G. Santiago, T. W. Kenny, R. A. Brennen, G. B. Gordon, and B. Mohammadi, "Optimization of turn geometries for microchip electrophoresis," *Analytical Chemistry,* vol. 73, pp. 1350-1360, 2001.

[58] P. H. Paul, M. G. Garguilo, and D. J. Rakestraw, "Imaging of pressure- and electrokinetically driven flows through open capillaries," *Analytical Chemistry,* vol. 70, pp. 2459-2467, 1998.

[59] D. Maynes and A. R. Webb, "Velocity profile characterization in sub-millimeter diameter tubes using molecular tagging velocimetry," *Experiments in Fluids,* vol. 32, pp. 3-15, 2002.

[60] I. Yamamoto, Sato, Hishida, Maeda, "Measurements in microchannel by laser induced molecular tagging amd micro-PIV.," in *11th Symposium on Aplications of laser technology to fluid mechanics*, Lisbon, Portugal.

[61] J. W. Chung, C. P. Grigoropoulos, and R. Greif, "Infrared thermal velocimetry for nonintrusive flow measurement in silicon microfluidic devices," *Review of Scientific Instruments,* vol. 74, pp. 2911-2917, 2003.

[62] A. K. Tieu, M. R. Mackenzie, and E. B. Li, "Measurements in Microscopic Flow with a Solid-State Lda," *Experiments in Fluids,* vol. 19, pp. 293-294, 1995.

[63] J. A. Taylor and E. S. Yeung, "Imaging of Hydrodynamic and Electrokinetic Flow Profiles in Capillaries," *Analytical Chemistry,* vol. 65, pp. 2928-2932, 1993.

[64] C. D. W. S. Meinhart, *Micro/Nano Technology Systems for Biomedical Applications: Microfluidics, Optics, and Surface Chemistry*. Oxford: Oxford University Press.

[65] S. J. Williams, C. Park, and S. T. Wereley, "Advances and applications on microfluidic velocimetry techniques," *Microfluidics and Nanofluidics,* vol. 8, pp. 709-726.

[66] S. T. Wereley and C. D. Meinhart, "Recent Advances in Micro-Particle Image Velocimetry," *Annual Review of Fluid Mechanics,* vol. 42, pp. 557-576.

[67] M. Raffel, C. E. Willert, S. T. Wereley, J. Kompenhans, M. Raffel, C. Willert, S. Wereley, and J. Kompenhans, "PIV Recording Techniques," in *Particle Image Velocimetry*, R. J. Adrian, M. Gharib, W. Merzkirch, D. Rockwell, and J. H. Whitelaw, Eds., ed: Springer Berlin Heidelberg, 2007, pp. 97-121.

[68] A. Einstein, "Über die von der molekularkinetischen Theorie der Wärme geforderte Bewegung von in ruhenden Flüssigkeiten suspendierten Teilchen," *Annalen der Physik,* vol. 322, pp. 549-560, 1905.

[69] M. G. Olsen and R. J. Adrian, "Out-of-focus effects on particle image visibility and correlation in microscopic particle image velocimetry," *Experiments in Fluids,* vol. 29, pp. S166-S174, 2000.

[70] C. D. Meinhart, S. T. Wereley, and J. G. Santiago, "A PIV algorithm for estimating time-averaged velocity fields," *Journal of Fluids Engineering-Transactions of the Asme,* vol. 122, pp. 285-289, 2000.

[71] S. J. Lee and G. B. Kim, "Synchrotron microimaging technique for measuring the velocity fields of real blood flows," *Journal of Applied Physics,* vol. 97, 2005.

[72] B. J. Jones, P. S. Lee, and S. V. Garimella, "Infrared micro-particle image velocimetry measurements and predictions of flow distribution in a microchannel heat sink," *International Journal of Heat and Mass Transfer,* vol. 51, pp. 1877-1887, 2008.

[73] C. M. Zettner and M. Yoda, "Particle velocity field measurements in a near-wall flow using evanescent wave illumination," *Experiments in Fluids,* vol. 34, pp. 115-121, 2003.

[74] J. S. Park, C. K. Choi, and K. D. Kihm, "Optically sliced micro-PIV using confocal laser scanning microscopy (CLSM)," *Experiments in Fluids,* vol. 37, pp. 105-119, 2004.

[75] R. Lindken, J. Westerweel, and B. Wieneke, "Stereoscopic micro particle image velocimetry," *Experiments in Fluids,* vol. 41, pp. 161-171, 2006.

[76] M. Speidel, A. Jonas, and E. L. Florin, "Three-dimensional tracking of fluorescent nanoparticles with subnanometer precision by use of off-focus imaging," *Optics Letters,* vol. 28, pp. 69-71, 2003.

[77] Y. Sugii, S. Nishio, and K. Okamoto, "In vivo PIV measurement of red blood cell velocity field in microvessels considering mesentery motion," *Physiological Measurement,* vol. 23, pp. 403-416, 2002.

[78] J. S. Park, C. K. Choi, and K. D. Kihm, "Temperature measurement for a nanoparticle suspension by detecting the Brownian motion using optical

serial sectioning microscopy (OSSM)," *Measurement Science & Technology,* vol. 16, pp. 1418-1429, 2005.

[79] A. Ashkin, "Acceleration and Trapping of Particles by Radiation Pressure," *Physical Review Letters,* vol. 24, pp. 156-&, 1970.

[80] A. Ashkin, J. M. Dziedzic, J. E. Bjorkholm, and S. Chu, "Observation of a Single-Beam Gradient Force Optical Trap for Dielectric Particles," *Optics Letters,* vol. 11, pp. 288-290, 1986.

[81] J. E. Molloy and M. J. Padgett, "Lights, action: optical tweezers," *Contemporary Physics,* vol. 43, pp. 241-258, 2002.

[82] W. Chester, D. R. Breach, and I. Proudman, "On Flow Past a Sphere at Low Reynolds Number," *Journal of Fluid Mechanics,* vol. 37, pp. 751-&, 1969.

[83] M. E. J. Friese, T. A. Nieminen, N. R. Heckenberg, and H. Rubinsztein-Dunlop, "Optical alignment and spinning of laser-trapped microscopic particles," *Nature,* vol. 394, pp. 348-350, 1998.

[84] E. Higurashi, R. Sawada, and T. Ito, "Optically induced angular alignment of trapped birefringent micro-objects by linearly polarized light," *Physical Review E,* vol. 59, p. 3676, 1999.

[85] E. Higurashi, H. Ukita, H. Tanaka, and O. Ohguchi, "Optically Induced Rotation of Anisotropic Micro-Objects Fabricated by Surface Micromachining," *Applied Physics Letters,* vol. 64, pp. 2209-2210, 1994.

[86] S. Hardt, F. Schönfeld, and S. Maruo, "Manipulation of Microobjects by Optical Tweezers," in *Microfluidic Technologies for Miniaturized Analysis Systems*, ed: Springer US, 2007, pp. 275-314.

[87] K. Sasaki, M. Koshioka, H. Misawa, N. Kitamura, and H. Masuhara, "Pattern-Formation and Flow-Control of Fine Particles by Laser-Scanning Micromanipulation," *Optics Letters,* vol. 16, pp. 1463-1465, 1991.

[88] F. Arai, K. Yoshikawa, T. Sakami, and T. Fukuda, "Synchronized laser micromanipulation of multiple targets along each trajectory by single laser," *Applied Physics Letters,* vol. 85, pp. 4301-4303, 2004.

[89] C. Mio, T. Gong, A. Terray, and D. W. M. Marr, "Design of a scanning laser optical trap for multiparticle manipulation," *Review of Scientific Instruments,* vol. 71, pp. 2196-2200, 2000.

[90] V. Garces-Chavez, D. McGloin, H. Melville, W. Sibbett, and K. Dholakia, "Simultaneous micromanipulation in multiple planes using a self-reconstructing light beam," *Nature,* vol. 419, pp. 145-147, 2002.

[91] J. Leach, G. Sinclair, P. Jordan, J. Courtial, M. J. Padgett, J. Cooper, and Z. J. Laczik, "3D manipulation of particles into crystal structures using holographic optical tweezers," *Optics Express,* vol. 12, pp. 220-226, 2004.

[92] M. Pitzek, R. Steiger, G. Thalhammer, S. Bernet, and M. Ritsch-Marte, "Optical mirror trap with a large field of view," *Optics Express,* vol. 17, pp. 19414-19423, 2009.

[93] H. Mushfique, J. Leach, H. B. Yin, R. Di Leonardo, M. J. Padgett, and J. M. Cooper, "3D mapping of microfluidic flow in laboratory-on-a-chip structures using optical tweezers," *Analytical Chemistry,* vol. 80, pp. 4237-4240, 2008.

[94] T. Ota, T. Sugiura, and S. Kawata, "Surface-force measurement with a laser-trapped microprobe in solution," *Applied Physics Letters,* vol. 80, pp. 3448-3450, 2002.

[95] J. Guck, R. Ananthakrishnan, H. Mahmood, T. J. Moon, C. C. Cunningham, R. Hallworth, and J. Kas, "The optical stretcher - A novel laser tool to micromanipulate cells," *Biophysical Journal,* vol. 80, p. 1138, 2001.

[96] S. R. Quake, H. Babcock, and S. Chu, "The dynamics of partially extended single molecules of DNA," *Nature,* vol. 388, pp. 151-154, 1997.

[97] I. Inc., *Model 5-050 Ultrafast Harmonic Generation System, USER MANUAL*, 1994.

[98] http://jp.hamamatsu.com/products/sensor-etd/pd002/pd394/R3809U-50/index_en.html.

[99] TCC900, *Computer module for Time-correlated Single Photon Counting*, 2nd ed.: Edinburgh Instrument Ltd, 2002.

[100] FAST, *Advanced Analysis of Fluorescence Time Courses*, 1st ed.: Edinburgh Instrument Ltd., 2006.

[101] J. R. Lakowicz, "Time-Domain Lifetime Measurements," in *Principles of Fluorescence Spectroscopy*, ed: Springer US, 2006, pp. 97-155.

[102] V. Emiliani, D. Sanvitto, M. Tramier, T. Piolot, Z. Petrasek, K. Kemnitz, C. Durieux, and M. Coppey-Moisan, "Low-intensity two-dimensional imaging of fluorescence lifetimes in living cells," *Applied Physics Letters,* vol. 83, pp. 2471-2473, 2003.

[103] M. Lampton and R. F. Malina, "Quadrant Anode Image Sensor," *Review of Scientific Instruments,* vol. 47, pp. 1360-1362, 1976.

[104] Y. E. Chen and A. Periasamy, "Characterization of two-photon excitation fluorescence lifetime imaging microscopy for protein localization," *Microscopy Research and Technique,* vol. 63, pp. 72-80, 2004.

[105] W. S. Rasband, "ImageJ," ed: U. S. National Institutes of Health, Bethesda, Maryland, USA., 1997-2008.

[106] R. M. Sanchez-Martin, M. Muzerelle, N. Chitkul, S. E. How, S. Mittoo, and M. Bradley, "Bead-based cellular analysis, sorting and multiplexing," *Chembiochem,* vol. 6, pp. 1341-1345, 2005.

[107] C. Dedeugd, M. Wankhede, and B. S. Sorg, "Multimodal optical imaging of microvessel network convective oxygen transport dynamics," *Applied Optics,* vol. 48, pp. D187-D197, 2009.

[108] R. P. Trivedi, T. Lee, K. A. Bertness, and Smalyukh, II, "Three dimensional optical manipulation and structural imaging of soft materials by use of laser tweezers and multimodal nonlinear microscopy," *Optics Express,* vol. 18, pp. 27658-27669.

[109] R. R. Gullapalli, T. Tabouillot, R. Mathura, J. H. Dangaria, and P. J. Butler, "Integrated multimodal microscopy, time-resolved fluorescence, and optical-trap rheometry: toward single molecule mechanobiology," *Journal of Biomedical Optics,* vol. 12, 2007.

[110] C. A. DiMarzio, "Three-dimensional multi-modal microscopy," in *Complex Medical Engineering, 2009. CME. ICME International Conference on*, 2009, pp. 1-4.

[111] J. Li and C. Kleinstreuer, "Microfluidics analysis of nanoparticle mixing in a microchannel system," *Microfluidics and Nanofluidics,* vol. 6, pp. 661-668, 2009.

[112] A. McCarthy, "Personal communication," ed, 2010.

[113] E. Delamarche, H. Schmid, B. Michel, and H. Biebuyck, "Stability of molded polydimethylsiloxane microstructures," *Advanced Materials,* vol. 9, pp. 741-746, 1997.

[114] D. Bodas and C. Khan-Malek, "Hydrophilization and hydrophobic recovery of PDMS by oxygen plasma and chemical treatment - An SEM investigation," *Sensors and Actuators B-Chemical,* vol. 123, pp. 368-373, 2007.

[115] X. L. Luo, D. L. Berlin, J. Betz, G. F. Payne, W. E. Bentley, and G. W. Rubloff, "In situ generation of pH gradients in microfluidic devices for biofabrication of freestanding, semi-permeable chitosan membranes," *Lab on a Chip,* vol. 10, pp. 59-65.

[116] H. Jung, A. D. Robison, and P. S. Cremer, "Detecting Protein-Ligand Binding on Supported Bilayers by Local pH Modulation," *Journal of the American Chemical Society,* vol. 131, pp. 1006-1014, 2009.

[117] A. Abou-Hassan, J. F. Dufreche, O. Sandre, G. Meriguet, O. Bernard, and V. Cabuil, "Fluorescence Confocal Laser Scanning Microscopy for pH Mapping in a Coaxial Flow Microreactor: Application in the Synthesis of Superparamagnetic Nanoparticles," *Journal of Physical Chemistry C,* vol. 113, pp. 18097-18105, 2009.

[118] K. Shinohara, Y. Sugii, K. Okamoto, H. Madarame, A. Hibara, M. Tokeshi, and T. Kitamori, "Measurement of pH field of chemically reacting flow in microfluidic devices by laser-induced fluorescence," *Measurement Science & Technology,* vol. 15, pp. 955-960, 2004.

[119] A. R. Thete, G. A. Gross, T. Henkel, and J. M. Koehler, "Microfluidic arrangement with an integrated micro-spot array for the characterization of pH and solvent polarity," *Chemical Engineering Journal,* vol. 135, pp. S327-S332, 2008.

[120] W. Drenckhan, "Generation of Superstable, Monodisperse Microbubbles Using a pH-Driven Assembly of Surface-Active Particles," *Angewandte Chemie-International Edition,* vol. 48, pp. 5245-5247, 2009.

[121] E. Verpoorte, "Microfluidic chips for clinical and forensic analysis," *Electrophoresis,* vol. 23, pp. 677-712, 2002.

[122] C. F. Lin, G. B. Lee, C. H. Wang, H. H. Lee, W. Y. Liao, and T. C. Chou, "Microfluidic pH-sensing chips integrated with pneumatic fluid-control devices," *Biosensors & Bioelectronics,* vol. 21, pp. 1468-1475, 2006.

[123] E. S. Douglas, S. C. Hsiao, H. Onoe, C. R. Bertozzi, M. B. Francis, and R. A. Mathies, "DNA-barcode directed capture and electrochemical metabolic analysis of single mammalian cells on a microelectrode array," *Lab on a Chip,* vol. 9, pp. 2010-2015, 2009.

[124] F. Sassa, K. Morimoto, W. Satoh, and H. Suzuki, "Electrochemical techniques for microfluidic applications," *Electrophoresis,* vol. 29, pp. 1787-1800, 2008.

[125] Y. Cheng, P. Xiong, C. S. Yun, G. F. Strouse, J. P. Zheng, R. S. Yang, and Z. L. Wang, "Mechanism and Optimization of pH Sensing Using SnO2 Nanobelt Field Effect Transistors," *Nano Letters,* vol. 8, pp. 4179-4184, 2008.

[126] K. Abe, K. Suzuki, and D. Citterio, "Inkjet-printed microfluidic multianalyte chemical sensing paper," *Analytical Chemistry,* vol. 80, pp. 6928-6934, 2008.

[127] S. Lee, B. L. They, G. L. Cote, and M. V. Pishko, "Measurement of pH and dissolved oxygen within cell culture media using a hydrogel microarray sensor," *Sensors and Actuators B-Chemical,* vol. 128, pp. 388-398, 2008.

[128] P. Mela, S. Onclin, M. H. Goedbloed, S. Levi, M. F. Garcia-Parajo, N. F. van Hulst, B. J. Ravoo, D. N. Reinhoudt, and A. van den Berg, "Monolayer-functionalized microfluidics devices for optical sensing of acidity," *Lab on a Chip,* vol. 5, pp. 163-170, 2005.

[129] K. Fa, J. J. Tulock, J. V. Sweedler, and P. W. Bohn, "Profiling pH gradients across nanocapillary array membranes connecting microfluidic channels," *Journal of the American Chemical Society,* vol. 127, pp. 13928-13933, 2005.

[130] N. Klauke, P. Monaghan, G. Sinclair, M. Padgett, and J. Cooper, "Characterisation of spatial and temporal changes in pH gradients in microfluidic channels using optically trapped fluorescent sensors," *Lab on a Chip,* vol. 6, pp. 788-793, 2006.

[131] V. K. Yadavalli and M. V. Pishko, "Biosensing in microfluidic channels using fluorescence polarization," *Analytica Chimica Acta,* vol. 507, pp. 123-128, 2004.

[132] R. Sanders, A. Draaijer, H. C. Gerritsen, P. M. Houpt, and Y. K. Levine, "Quantitative Ph Imaging in Cells Using Confocal Fluorescence Lifetime Imaging Microscopy," *Analytical Biochemistry,* vol. 227, pp. 302-308, 1995.

[133] C. Hille, M. Berg, L. Bressel, D. Munzke, P. Primus, H. G. Lohmannsroben, and C. Dosche, "Time-domain fluorescence lifetime imaging for intracellular pH sensing in living tissues," *Analytical and Bioanalytical Chemistry,* vol. 391, pp. 1871-1879, 2008.

[134] T. French, P. T. C. So, D. J. Weaver, T. CoelhoSampaio, E. Gratton, E. W. Voss, and J. Carrero, "Two-photon fluorescence lifetime imaging microscopy of macrophage-mediated antigen processing," *Journal of Microscopy-Oxford,* vol. 185, pp. 339-353, 1997.

[135] A. Tamulis, J. Tamuliene, M. L. Balevicius, Z. Rinkevicius, and V. Tamulis, "Quantum mechanical studies of intensity in electronic spectra of fluorescein dianion and monoanion forms," *Structural Chemistry,* vol. 14, pp. 643-648, 2003.

[136] J. E. Whitaker, R. P. Haugland, and F. G. Prendergast, "SPECTRAL AND PHOTOPHYSICAL STUDIES OF BENZO C XANTHENE DYES - DUAL EMISSION PH SENSORS," *Analytical Biochemistry,* vol. 194, pp. 330-344, 1991.

[137] J. M. Alvarez-Pez, L. Ballesteros, E. Talavera, and J. Yguerabide, "Fluorescein excited-state proton exchange reactions: Nanosecond emission kinetics and correlation with steady-state fluorescence intensity," *Journal of Physical Chemistry A,* vol. 105, pp. 6320-6332, 2001.

[138] N. Klonis and W. H. Sawyer, "Spectral properties of the prototropic forms of fluorescein in aqueous solution," *Journal of Fluorescence,* vol. 6, pp. 147-157, 1996.

[139] M. Yassine, J. M. Salmon, J. Vigo, and P. Viallet, "C-SNARF-1 as a pHi fluoroprobe: Discrepancies between conventional and intracellular data do not result from protein interactions," *Journal of Photochemistry and Photobiology B-Biology,* vol. 37, pp. 18-25, 1997.

[140] H. Szmacinski and J. R. Lakowicz, "Optical Measurements of Ph Using Fluorescence Lifetimes and Phase-Modulation Fluorometry," *Analytical Chemistry,* vol. 65, pp. 1668-1674, 1993.

[141] A. C. Ribou, J. Vigo, and J. M. Salmon, "C-SNARF-1 as a fluorescent probe for pH measurements in living cells: Two-wavelength-ratio method versus whole-spectral-resolution method," *Journal of Chemical Education,* vol. 79, pp. 1471-1474, 2002.

[142] M. Salerno, J. J. Ajimo, J. A. Dudley, K. Binzel, and P. Urayama, "Characterization of dual-wavelength seminaphthofluorescein and seminapthorhodafluor dyes for pH sensing under high hydrostatic pressures," *Analytical Biochemistry,* vol. 362, pp. 258-267, 2007.

[143] D. S. Elson, I. Munro, J. Requejo-Isidro, J. McGinty, C. Dunsby, N. Galletly, G. W. Stamp, M. A. A. Neil, M. J. Lever, P. A. Kellett, A. Dymoke-Bradshaw, J. Hares, and P. M. W. French, "Real-time time-domain fluorescence lifetime imaging including single-shot acquisition with a segmented optical image intensifier," *New Journal of Physics,* vol. 6, 2004.

[144] J. G. White, W. B. Amos, and M. Fordham, "An Evaluation of Confocal Versus Conventional Imaging of Biological Structures by Fluorescence Light-Microscopy," *Journal of Cell Biology,* vol. 105, pp. 41-48, 1987.

[145] A. Squire and P. I. H. Bastiaens, "Three dimensional image restoration in fluorescence lifetime imaging microscopy," *Journal of Microscopy-Oxford,* vol. 193, pp. 36-49, 1999.

[146] J. Siegel, D. S. Elson, S. E. D. Webb, D. Parsons-Karavassilis, S. Leveque-Fort, M. J. Cole, M. J. Lever, P. M. W. French, M. A. A. Neil, R. Juskaitis, L. O. Sucharov, and T. Wilson, "Whole-field five-dimensional fluorescence microscopy combining lifetime and spectral resolution with optical sectioning," *Optics Letters,* vol. 26, pp. 1338-1340, 2001.

[147] M. J. Cole, J. Siegel, S. E. D. Webb, R. Jones, K. Dowling, P. M. W. French, M. J. Lever, L. O. D. Sucharov, M. A. A. Neil, R. Juskaitis, and T. Wilson, "Whole-field optically sectioned fluorescence lifetime imaging," *Optics Letters,* vol. 25, pp. 1361-1363, 2000.

[148] D. M. Grant, D. S. Elson, D. Schimpf, C. Dunsby, J. Requejo-Isidro, E. Auksorius, I. Munro, M. A. A. Neil, P. M. W. French, E. Nye, G. Stamp, and P. Courtney, "Optically sectioned fluorescence lifetime imaging using a Nipkow disk microscope and a tunable ultrafast continuum excitation source," *Optics Letters,* vol. 30, pp. 3353-3355, 2005.

[149] M. A. A. Neil, R. Juskaitis, and T. Wilson, "Method of obtaining optical sectioning by using structured light in a conventional microscope," *Opt. Lett.,* vol. 22, pp. 1905-1907, 1997.

[150] Y. Yamaguchi, T. Honda, M. P. Briones, K. Yamashita, M. Miyazaki, H. Nakamura, and H. Maeda, "Influence of gravity on a laminar flow in a microbioanalysis system," *Measurement Science & Technology,* vol. 17, pp. 3162-3166, 2006.

[151] S. K. Yoon, M. Mitchell, E. R. Choban, and P. J. A. Kenis, "Gravity-induced reorientation of the interface between two liquids of different densities flowing laminarly through a microchannel," *Lab on a Chip,* vol. 5, pp. 1259-1263, 2005.

[152] P. J. Stiles and D. F. Fletcher, "Hydrodynamic control of the interface between two liquids flowing through a horizontal or vertical microchannel," *Lab on a Chip,* vol. 4, pp. 121-124, 2004.

[153] P. J. Stiles and D. F. Fletcher, "Effects of gravity on the steady state of a reaction in a liquid-state microreactor-deviations from Poiseuille flow," *Physical Chemistry Chemical Physics,* vol. 5, pp. 1219-1224, 2003.

[154] Y. Yamaguchi, T. Honda, M. P. Briones, K. Yamashita, M. Miyazaki, H. Nakamura, and H. Maeda, "Influence of gravity on two-layer laminar flow in a microchannel," *Chemical Engineering & Technology,* vol. 30, pp. 379-382, Mar 2007.

[155] Y. Yamaguchi, F. Takagi, K. Yamashita, H. Nakamura, H. Maeda, K. Sotowa, K. Kusakabe, Y. Yamasaki, and S. Morooka, "3-D simulation and visualization of laminar flow in a microchannel with hair-pin curves," *AIChE Journal,* vol. 50, pp. 1530-1535, 2004.

[156] C. W. Xi, D. L. Marks, D. S. Parikh, L. Raskin, and S. A. Boppart, "Structural and functional imaging of 3D microfluidic mixers using optical coherence tomography," *Proceedings of the National Academy of Sciences of the United States of America,* vol. 101, pp. 7516-7521, 2004.

[157] H. Kinoshita, S. Kaneda, T. Fujii, and M. Oshima, "Three-dimensional measurement and visualization of internal flow of a moving droplet using confocal micro-PIV," *Lab on a Chip,* vol. 7, pp. 338-346, 2007.

[158] D. Schafer, E. A. Gibson, W. Amir, R. Erikson, J. Lawrence, T. Vestad, J. Squier, R. Jimenez, and D. W. M. Marr, "Three-dimensional chemical concentration maps in a microfluidic device using two-photon absorption fluorescence imaging," *Optics Letters,* vol. 32, pp. 2568-2570, 2007.

[159] N. Kitamura, Y. Hosoda, K. Ueno, and S. Iwata, "An application of plastic microchannel-microheater chips to a thermal synthetic reaction," *Analytical Sciences,* vol. 20, pp. 783-786, May 2004.

[160] N. Boens, W. W. Qin, N. Basaric, J. Hofkens, M. Ameloot, J. Pouget, J. P. Lefevre, B. Valeur, E. Gratton, M. Vandeven, N. D. Silva, Y. Engelborghs, K. Willaert, A. Sillen, G. Rumbles, D. Phillips, A. Visser, A. van Hoek, J. R. Lakowicz, H. Malak, I. Gryczynski, A. G. Szabo, D. T. Krajcarski, N. Tamai, and A. Miura, "Fluorescence lifetime standards for time and frequency domain fluorescence spectroscopy," *Analytical Chemistry,* vol. 79, pp. 2137-2149, 2007.

[161] J. Slavik, "ANILINONAPHTHALENE SULFONATE AS A PROBE OF MEMBRANE-COMPOSITION AND FUNCTION," *Biochimica Et Biophysica Acta,* vol. 694, pp. 1-25, 1982 1982.

[162] Chakraba.Sk and W. R. Ware, "NANOSECOND TIME-RESOLVED EMISSION SPECTROSCOPY OF 1-ANILINO-8-NAPHTHALENE SULFONATE," *Journal of Chemical Physics,* vol. 55, pp. 5494-&, 1971 1971.

[163] E. M. Kosower and H. Kanety, "INTRAMOLECULAR DONOR-ACCEPTOR SYSTEMS," *Journal of Molecular Structure,* vol. 84, pp. 259-267, 1982 1982.

[164] P. J. Sadkowski and G. R. Fleming, "THE INFLUENCE OF SOLVENT-SOLUTE INTERACTION ON RADIATIONLESS PROCESSES - EXCITED-STATE DYNAMICS OF 1,8-ANILINONAPHTHALENE SULFONATE AND RELATED MOLECULES," *Chemical Physics,* vol. 54, pp. 79-89, 1980 1980.

[165] W. Kirk, E. Kurian, and W. Wessels, "Photophysics of ANS V. Decay modes of ANS in proteins: The IFABP-ANS complex," *Biophysical Chemistry,* vol. 125, pp. 50-58, Jan 2007.

[166] C. J. T. Seliskar, D; Gohlke, J.R.; Brand, L, in *Molecular Luminescence*, E. Lim, Ed., ed: Benjamin, New

York, 1969, p. 677.

[167] L. Dougan, J. Crain, H. Vass, and S. W. Magennis, "Probing the liquid-state structure and dynamics of aqueous solutions by fluorescence spectroscopy," *Journal of Fluorescence,* vol. 14, pp. 91-97, Jan 2004.

[168] T. Molotsky and D. Huppert, "Site specific solvation statics and dynamics of coumarin dyes in hexane-methanol mixture," *Journal of Physical Chemistry A,* vol. 107, pp. 2769-2780, 2003.

[169] J. B. Segur and H. E. Oberstar, "Viscosity of Glycerol and Its Aqueous Solutions," *Industrial and Engineering Chemistry,* vol. 43, pp. 2117-2120, 1951.

[170] N. S. Cheng, "Formula for the viscosity of a glycerol-water mixture," *Industrial & Engineering Chemistry Research,* vol. 47, pp. 3285-3288, 2008.

[171] S. Z. Mikhail and W. R. Kimel, "Densities and Viscosities of Methanol-Water Mixtures," *Journal of Chemical & Engineering Data,* vol. 6, pp. 533-537, 1961.

[172] D. R. Lide, "Fluid properties," in *Handbook of Chemistry and Physics*

74th ed, 1993-1994, p. 198.

[173] E. W. Flick, "Polyhydric Alcohols " in *Industrial solvents handbook*, 5th ed: Noyes, 1998, p. 435.

[174] M. M. S. L. R. Mielnik, "Micro Particle Image Velocimetry - an overview. ," *Turbulence,* vol. 10, pp. 83-90, 2004.

[175] P. S. Dittrich, K. Tachikawa, and A. Manz, "Micro total analysis systems. Latest advancements and trends," *Analytical Chemistry,* vol. 78, pp. 3887-3907, 2006.

[176] E. Berthier, J. Warrick, H. Yu, and D. J. Beebe, "Managing evaporation for more robust microscale assays - Part 2. Characterization of convection and diffusion for cell biology," *Lab on a Chip,* vol. 8, pp. 860-864, 2008.

[177] D. Braun, "Semiconducting polymer LEDs," *Materials Today,* vol. 5, pp. 32-39, 2002.

[178] X. H. Wang, M. Amatatongchai, D. Nacapricha, O. Hofmann, J. C. de Mello, D. D. C. Bradley, and A. J. de Mello, "Thin-film organic photodiodes for integrated on-chip chemiluminescence detection - application to antioxidant capacity screening," *Sensors and Actuators B-Chemical,* vol. 140, pp. 643-648, 2009.

[179] A. A. Darhuber, J. P. Valentino, J. M. Davis, S. M. Troian, and S. Wagner, "Microfluidic actuation by modulation of surface stresses," *Applied Physics Letters,* vol. 82, pp. 657-659, 2003.

[180] S. J. Wang, W. Saadi, F. Lin, C. M. C. Nguyen, and N. L. Jeon, "Differential effects of EGF gradient profiles on MDA-MB-231 breast cancer cell chemotaxis," *Experimental Cell Research,* vol. 300, pp. 180-189, 2004.

[181] N. L. Jeon, H. Baskaran, S. K. W. Dertinger, G. M. Whitesides, L. Van de Water, and M. Toner, "Neutrophil chemotaxis in linear and complex gradients of interleukin-8 formed in a microfabricated device," *Nature Biotechnology,* vol. 20, pp. 826-830, 2002.

[182] X. Y. Jiang, J. M. K. Ng, A. D. Stroock, S. K. W. Dertinger, and G. M. Whitesides, "A miniaturized, parallel, serially diluted immunoassay for analyzing multiple antigens," *Journal of the American Chemical Society,* vol. 125, pp. 5294-5295, 2003.

[183] H. B. Mao, T. L. Yang, and P. S. Cremer, "Design and characterization of immobilized enzymes in microfluidic systems," *Analytical Chemistry,* vol. 74, pp. 379-385, 2002.

[184] M. A. Holden, S. Kumar, E. T. Castellana, A. Beskok, and P. S. Cremer, "Generating fixed concentration arrays in a microfluidic device," *Sensors and Actuators B-Chemical,* vol. 92, pp. 199-207, 2003.

[185] M. I. Nathan, "The blue laser diode. GaN based light emitters and lasers - Nakamura,S, Fasol,G," *Science,* vol. 277, pp. 46-47, 1997.

[186] J. A. Chediak, Z. S. Luo, J. G. Seo, N. Cheung, L. P. Lee, and T. D. Sands, "Heterogeneous integration of CdS filters with GaN LEDs for fluorescence detection microsystems," *Sensors and Actuators a-Physical,* vol. 111, pp. 1-7, Mar 2004.

[187] K. B. Mogensen, H. Klank, and J. P. Kutter, "Recent developments in detection for microfluidic systems," *Electrophoresis,* vol. 25, pp. 3498-3512, 2004.

[188] S. Camou, M. Kitamura, J. P. Gouy, H. Fujita, Y. Arakawa, and T. Fujii, "Organic Light Emitting Device as a fluorescence spectroscopy's light source : one step towards the lab-on-a-chip device," *Applications of Photonic Technology 5,* vol. 4833, pp. 1-8, 2002.

[189] J. B. Edel, N. P. Beard, O. Hofmann, J. C. DeMello, D. D. C. Bradley, and A. J. deMello, "Thin-film polymer light emitting diodes as integrated excitation sources for microscale capillary electrophoresis," *Lab on a Chip,* vol. 4, pp. 136-140, 2004.

[190] I. Rech, A. Restelli, S. Cova, M. Ghioni, M. Chiari, and M. Cretich, "Microelectronic photosensors for genetic diagnostic microsystems," *Sensors and Actuators B-Chemical,* vol. 100, pp. 158-162, 2004.

[191] B. R. Rae, C. Griffin, J. McKendry, J. M. Girkin, H. X. Zhang, E. Gu, D. Renshaw, E. Charbon, M. D. Dawson, and R. K. Henderson, "CMOS driven micro-pixel LEDs integrated with single photon avalanche diodes for time resolved fluorescence measurements," *Journal of Physics D-Applied Physics,* vol. 41, 2008.

[192] H. Lee, R. Westervelt, D. Ham, and H. Stone, "Introduction to Fluid Dynamics for Microfluidic Flows," in *CMOS Biotechnology*, ed: Springer US, 2007, pp. 5-30.

[193] Y. Sato, G. Irisawa, M. Ishizuka, K. Hishida, and M. Maeda, "Visualization of convective mixing in microchannel by fluorescence imaging," *Measurement Science & Technology,* vol. 14, pp. 114-121, 2003.

[194] J. E. Selwyn and Steinfel.Ji, "AGGREGATION EQUILIBRIA OF XANTHENE DYES," *Journal of Physical Chemistry,* vol. 76, pp. 762-&, 1972 1972.

[195] R. S. Moog, M. D. Ediger, S. G. Boxer, and M. D. Fayer, "VISCOSITY DEPENDENCE OF THE ROTATIONAL REORIENTATION OF RHODAMINE-B IN MONO-ALCOHOL AND POLY-ALCOHOL - PICOSECOND TRANSIENT GRATING EXPERIMENTS," *Journal of Physical Chemistry,* vol. 86, pp. 4694-4700, 1982 1982.

[196] R. F. Kubin and A. N. Fletcher, "FLUORESCENCE QUANTUM YIELDS OF SOME RHODAMINE DYES," *Journal of Luminescence,* vol. 27, pp. 455-462, 1982 1982.

[197] M. J. Snare, F. E. Treloar, K. P. Ghiggino, and P. J. Thistlethwaite, "THE PHOTOPHYSICS OF RHODAMINE-B," *Journal of Photochemistry,* vol. 18, pp. 335-346, 1982 1982.

[198] P. J. Sadkowski and G. R. Fleming, "PHOTOPHYSICS OF ACID AND BASE FORMS OF RHODAMINE-B," *Chemical Physics Letters,* vol. 57, pp. 526-529, 1978 1978.

[199] K. G. Casey and E. L. Quitevis, "EFFECT OF SOLVENT POLARITY ON NONRADIATIVE PROCESSES IN XANTHENE DYES - RHODAMINE-B IN NORMAL ALCOHOLS," *Journal of Physical Chemistry,* vol. 92, pp. 6590-6594, Nov 17 1988.

[200] R. Luchowski, Z. Gryczynski, P. Sarkar, J. Borejdo, M. Szabelski, P. Kapusta, and I. Gryczynski, "Instrument response standard in time-resolved fluorescence," *Review of Scientific Instruments,* vol. 80, 2009.

[201] M. Zuker, A. G. Szabo, L. Bramall, D. T. Krajcarski, and B. Selinger, "Delta-Function Convolution Method (Dfcm) for Fluorescence Decay Experiments," *Review of Scientific Instruments,* vol. 56, pp. 14-22, 1985.

[202] K. Ray, H. Nakahara, and A. Sakamoto, "Time-resolved fluorescence spectroscopic and scanning near-field optical microscopic studies of rhodamine dye adsorbed in cationic Langmuir-Blodgett films," *Spectrochimica Acta Part a-Molecular and Biomolecular Spectroscopy,* vol. 61, pp. 103-107, 2005.

[203] P. Lavallard, M. Rosenbauer, and T. Gacoin, "Influence of surrounding dielectrics on the spontaneous emission of sulforhodamine B molecules," *Physical Review A,* vol. 54, pp. 5450-5453, 1996.

[204] C. S. Liao, G. B. Lee, J. J. Wu, C. C. Chang, T. M. Hsieh, F. C. Huang, and C. H. Luo, "Micromachined polymerase chain reaction system for multiple DNA amplification of upper respiratory tract infectious diseases," *Biosensors & Bioelectronics,* vol. 20, pp. 1341-1348, 2005.

[205] H. C. Chang, S. N. Leaw, A. H. Huang, T. L. Wuk, and T. C. Chang, "Rapid identification of yeasts in positive blood cultures by a multiplex PCR method," *Journal of Clinical Microbiology,* vol. 39, pp. 3466-3471, 2001.

[206] L. Gui and C. L. Ren, "Numeric simulation of heat transfer and electrokinetic flow in an electroosmosis-based continuous flow PCR chip," *Analytical Chemistry,* vol. 78, pp. 6215-6222, 2006.

[207] P. Chamarthy, S. V. Garimella, and S. T. Wereley, "Measurement of the temperature non-uniformity in a microchannel heat sink using microscale laser-induced fluorescence," *International Journal of Heat and Mass Transfer,* vol. 53, pp. 3275-3283.

[208] H. B. Mao, T. L. Yang, and P. S. Cremer, "A microfluidic device with a linear temperature gradient for parallel and combinatorial measurements," *Journal of the American Chemical Society,* vol. 124, pp. 4432-4435, 2002.

[209] U. Seger, M. Panayiotou, S. Schnydrig, M. Jordan, and P. Renaud, "Temperature measurements in microfluidic systems: Heat dissipation of negative dielectrophoresis barriers," *Electrophoresis,* vol. 26, pp. 2239-2246, 2005.

[210] G. Y. Tang, D. G. Yan, C. Yang, H. Q. Gong, J. C. Chai, and Y. C. Lam, "Assessment of Joule heating and its effects on electroosmotic flow and electrophoretic transport of solutes in microfluidic channels," *Electrophoresis,* vol. 27, pp. 628-639, 2006.

[211] D. Ross, M. Gaitan, and L. E. Locascio, "Temperature measurement in microfluidic systems using a temperature-dependent fluorescent dye," *Analytical Chemistry,* vol. 73, pp. 4117-4123, 2001.

[212] D. Ross and L. E. Locascio, "Microfluidic temperature gradient focusing," *Analytical Chemistry,* vol. 74, pp. 2556-2564, 2002.

[213] J. Sakakibara, K. Hishida, and M. Maeda, "Measurements of Thermally Stratified Pipe-Flow Using Image-Processing Techniques," *Experiments in Fluids,* vol. 16, pp. 82-96, 1993.

[214] R. Samy, T. Glawdel, and C. L. Ren, "Method for microfluidic whole-chip temperature measurement using thin-film poly(dimethylsiloxane)/Rhodamine B," *Analytical Chemistry,* vol. 80, pp. 369-375, 2008.

[215] K. Chung, J. K. Cho, E. S. Park, V. Breedveld, and H. Lu, "Three-Dimensional in Situ Temperature Measurement in Microsystems Using Brownian Motion of Nanoparticles," *Analytical Chemistry,* vol. 81, pp. 991-999, 2009.

[216] F. Gielen, F. Pereira, A. J. deMello, and J. B. Edel, "High-Resolution Local Imaging of Temperature in Dielectrophoretic Platforms," *Analytical Chemistry,* vol. 82, pp. 7509-7514.

[217] H. M. Shapiro and H. M. Shapiro, "Practical flow cytometry, Third edition," *Practical flow cytometry, Third edition,* p. xxxviii+542p, 1995.

[218] D. S. Tawfik and A. D. Griffiths, "Man-made cell-like compartments for molecular evolution," *Nature Biotechnology,* vol. 16, pp. 652-656, 1998.

[219] A. D. Griffiths and D. S. Tawfik, "Miniaturising the laboratory in emulsion droplets," *Trends in Biotechnology,* vol. 24, pp. 395-402, 2006.

[220] J. Clausell-Tormos, D. Lieber, J. C. Baret, A. El-Harrak, O. J. Miller, L. Frenz, J. Blouwolff, K. J. Humphry, S. Koster, H. Duan, C. Holtze, D. A. Weitz, A. D. Griffiths, and C. A. Merten, "Droplet-based microfluidic platforms for the encapsulation and screening of mammalian cells and multicellular organisms," *Chemistry & Biology,* vol. 15, pp. 427-437, 2008.

[221] N. Pannacci, H. Bruus, D. Bartolo, I. Etchart, T. Lockhart, Y. Hennequin, H. Willaime, and P. Tabeling, "Equilibrium and Nonequilibrium States in Microfluidic Double Emulsions," *Physical Review Letters,* vol. 101, 2008.

[222] K. L. Lao, J. H. Wang, and G. B. Lee, "A microfluidic platform for formation of double-emulsion droplets," *Microfluidics and Nanofluidics,* vol. 7, pp. 709-719, 2009.

[223] L. Frenz, J. Blouwolff, A. D. Griffiths, and J. C. Baret, "Microfluidic Production of Droplet Pairs," *Langmuir,* vol. 24, pp. 12073-12076, 2008.

[224] B. A. Nemet and M. Cronin-Golomb, "Microscopic flow measurements with optically trapped microprobes," *Optics Letters,* vol. 27, pp. 1357-1359, 2002.

[225] G. Knoner, S. Parkin, N. R. Heckenberg, and H. Rubinsztein-Dunlop, "Characterization of optically driven fluid stress fields with optical tweezers," *Physical Review E,* vol. 72, 2005.

[226] A. Terray, J. Oakey, and D. W. M. Marr, "Microfluidic control using colloidal devices," *Science,* vol. 296, pp. 1841-1844, 2002.

[227] K. Ladavac and D. G. Grier, "Microoptomechanical pumps assembled and driven by holographic optical vortex arrays," *Optics Express,* vol. 12, pp. 1144-1149, 2004.

[228] J. Leach, H. Mushfique, R. di Leonardo, M. Padgett, and J. Cooper, "An optically driven pump for microfluidics," *Lab on a Chip,* vol. 6, pp. 735-739, 2006.

[229] J. Enger, M. Goksor, K. Ramser, P. Hagberg, and D. Hanstorp, "Optical tweezers applied to a microfluidic system," *Lab on a Chip,* vol. 4, pp. 196-200, 2004.

[230] G. P. McNerney, W. Hubner, B. K. Chen, and T. Huser, "Manipulating CD4(+) T cells by optical tweezers for the initiation of cell-cell transfer of HIV-1," *Journal of Biophotonics,* vol. 3, pp. 216-223.

[231] M. Capitanio, D. Maggi, F. Vanzi, and F. S. Pavone, "FIONA in the trap: the advantages of combining optical tweezers and fluorescence," *Journal of Optics a-Pure and Applied Optics,* vol. 9, pp. S157-S163, 2007.

[232] K. Ramser, W. Wenseleers, S. Dewilde, S. Van Doorslaer, L. Moens, and D. Hanstorp, "Micro-resonance Raman study of optically trapped Escherichia coli cells overexpressing human neuroglobin," *Journal of Biomedical Optics,* vol. 12, 2007.

[233] M. J. Snare, F. E. Treloar, K. P. Ghiggino, and P. J. Thistlethwaite, "The photophysics of rhodamine B," *Journal of Photochemistry,* vol. 18, pp. 335-346, 1982.

[234] G. D. Wright, J. Arlt, W. C. K. Poon, and N. D. Read, "Optical tweezer micromanipulation of filamentous fungi," *Fungal Genetics and Biology,* vol. 44, pp. 1-13, 2007.

[235] F. Gao, Z. G. Su, P. Wang, and G. H. Ma, "Double Emulsion Templated Microcapsules with Single Hollow Cavities and Thickness-Controllable Shells," *Langmuir,* vol. 25, pp. 3832-3838, 2009.

[236] J. Ghasemi, A. Niazi, and M. Kubista, "Thermodynamics study of the dimerization equilibria of rhodamine B and 6G in different ionic strengths by photometric titration and chemometrics method," *Spectrochimica Acta Part a-Molecular and Biomolecular Spectroscopy,* vol. 62, pp. 649-656, 2005.

[237] R. A. Lampert, S. R. Meech, J. Metcalfe, D. Phillips, and A. P. Schaap, "The refractive index correction to the radiative rate constant in fluorescence lifetime measurements," *Chemical Physics Letters,* vol. 94, pp. 137-140, 1983.

[238] Y. Liu, D. K. Cheng, G. J. Sonek, M. W. Berns, C. F. Chapman, and B. J. Tromberg, "Evidence for Localized Cell Heating Induced by Infrared Optical Tweezers," *Biophysical Journal,* vol. 68, pp. 2137-2144, 1995.

[239] A. Schonle and S. W. Hell, "Heating by absorption in the focus of an objective lens," *Optics Letters,* vol. 23, pp. 325-327, 1998.

[240] E. J. G. Peterman, F. Gittes, and C. F. Schmidt, "Laser-induced heating in optical traps," *Biophysical Journal,* vol. 84, pp. 1308-1316, 2003.

[241] S. Ebert, K. Travis, B. Lincoln, and J. Guck, "Fluorescence ratio thermometry in a microfluidic dual-beam laser trap," *Optics Express,* vol. 15, pp. 15493-15499, 2007.

Conferences, meetings and workshops

- Presentation given at conferences and meetings

PHOTON 10, **Oral Presentation,** Southampton (UK)…….Aug 2010
Simultaneous Multi-Parameter Mapping of Microfluidic Devices using FLIM, μ-PIV, Optical Tweezers and TCSPC

Edinburgh Microfluidics Prototyping Initiative, Oral Presentation, Scottish Microelectronic Centre, Edinburgh (UK).....Apr 2010
Simultaneous Multi-Parameter Mapping of Microfluidic Devices using FLIM, μ-PIV, Optical Tweezers and TCSPC

PhD final year talk, Awarded best talk of the physical chemistry section …….....Mar 2010
Quantitative imaging of microfluidic devices

RASOR LAOC Symposium 2010, Poster Presentation, Glasgow (UK)..... Mar 2010
Towards Lab-on-a-Chip, Simultaneous Quantitative Multi-Parameter Mapping of Microfluidic Devices

MAF 11, Oral Presentation, Budapest (Hungary).....Sep 2009
Simultaneous Multi-Parameter Mapping of Microfluidic Devices using FLIM, μ-PIV, Optical Tweezers and TCSPC

42nd IUPAC congress, Poster & flash oral presentation, Glasgow (UK).....Aug 2009
Simultaneous Multi-Parameter Mapping of Microfluidic Devices using FLIM, μ-PIV, Optical Tweezers and TCSPC

IONS-5, Poster presentation, ICFO Barcelona (Spain).....Feb 2009
Use of FLIM for Mapping pH in Microfluidic Systems

36th Scottish Microscopy Symposium, Poster presentation, Edinburgh (UK) …….Nov 2008
Use of FLIM for Mapping pH in Microfluidic Systems

PHOTON 08, Poster presentation, Edinburgh (UK).....Aug 2008
Use of FLIM for Mapping pH in Microfluidic Systems

- Contribution to conference papers

MAF 12, Oral Presentation, Strasbourg (France).....Sep 2011
Optically trapped microsensors for microfluidic temperature measurement by fluorescence lifetime imaging microscopy
Mathieu A. Bennet, Patricia R. Richardson, Jochen Arlt, Aongus McCarthy, Gerald S.Buller and Anita C. Jones

EMPC2011, Oral Presentation, Brighton (England).....…..…Sep 2011
Characterisation of ion transportation during electroplating of high aspect ratio microvias using megasonic agitation
S.Costello, N.Strusevich, M.K.Patel, C.Bailey, D.Flynn, R.W. Kay, D. Price, M.Bennet, A.C.Jones, R. Habeshaw, C. Demore, S. Cochran and M.P.Y. Desmulliez

- Workshop attended

Introduction to research funding; Managing Bibiliographies, Thesis Writing, Web Publishing, Researcher and the Media.....2010

Paper writing course.....2009

Peer reviewing, Metrology in Microfluidics.....2008

Reprints of publications

Mathieu A. Bennet, Patricia R. Richardson, Jochen Arlt, Aongus McCarthy, Gerald S. Buller and Anita C. Jones . *Optically trapped microsensors for microfluidic temperature measurement by fluorescence lifetime imaging microscopy*, Lab on a Chip, August 2011, DOI: 10.1039/c1lc20391f.